Phonon Anharmonicity of Ionic Compounds and Metals

Thesis by

Chen W. Li

In Partial Fulfillment of the Requirements

for the Degree of

Doctor of Philosophy

California Institute of Technology

Pasadena, California

2012

(Defended May 4th, 2012)

To my lovely wife, Jun, whose support is indispensable through the years,

and

my son, Derek

Acknowledgments

First and foremost, I would like to thank my advisor, Brent Fultz, for his guidance and support throughout my graduate student years at Caltech, and especially for his efforts to offer me a second chance at admission after the visa difficulty. I am very fortunate to have had him as a mentor and collaborator during these years. Without his insightful advice, this work would not have been possible.

I owe many thanks to all current and former members of the Fultz group, who have been a constant source of thoughts and support. In particular, I would like to thank Mike McKerns for his guidance on the Raman and computational work. Special thanks to my officemates, Olivier Delaire (now at Oak Ridge National Lab), Max Kresch (now at IDA), Mike Winterrose (now at MIT Lincoln Lab), and Jorge Muñoz, who made the work much more enjoyable. Thanks to the former DANSE postdocs: Nikolay Markovskiy, Xiaoli Tang, Alexander Dementsov, and J. Brandon Keith. You helped me a lot on programming and calculations. Also thanks to other former group members: Matthew Lucas (now at Air Force Research Laboratory), Rebecca Stevens, Hongjin Tan (now at Contour Energy Systems), and Justin Purewal (now at Ford Motor/University of Michigan); as well as other current group members: Hillary Smith, Tian Lan, Lisa Mauger, Sally Tracy, Nick Stadie, and David Abrecht. It is fun to work and travel with you. I would like to extend my special thanks to Jiao Lin for his relentless help on computation matters, and Channing Ahn for his help on experiments using his expertise. I also wish current and future members of the Fultz group the best of luck and hope you to continue to make the group an exciting and fruitful place to work in.

I also wish to thank all the members of the Caltech community who have

helped me over the years: especially, Bill Johnson and other people in his group, for his illuminating thermodynamics lectures, and sharing their equipment; Mike Vondrus, for his help on building the weird things I designed, and fixing the things I had trouble with; Pam Albertson and many other former Materials Science staff, for their efforts to keep everything running; Avalon Johnson, for keeping the group cluster, where I did most of my work here, up and running.

I wish to acknowledge the generous help and support of our collaborators at Oak Ridge National Laboratory: Doug Abernathy, Matthew Stone, Mark Loguillo, and Matthew Lucas (again), as well as Lee Robertson, Karol Marty, and Mark Lumsden, among many others. They made our inelastic neutron scattering experiments possible through their unrelenting support during many sleepless nights, and were always willing to share their deep knowledge and understanding of neutron scattering.

I wish to take this opportunity to also thank several people in the neutron scattering community for their advice and help on my career: Rob McQueeney, Guangyong Xu, Genda Gu, and Ben Larson.

Finally, I wish to express my gratitude to my parents and my wife, Jun, for their unconditional love and support through the years. It is your encouragement and understanding that kept me up in the darkest days: I would not have made it without you. And Derek, you brought us the paramount joy.

Financial support for this thesis was provided by the United States Department of Energy (DOE) and by the National Science Foundation (NSF).

Abstract

Vibrational studies of materials at elevated temperatures are relatively rare, and most phonon work also has emphasized harmonic behavior. Non-harmonic effects are often unexplored. These non-harmonic effects can be important for many properties of the material, such as thermal transport and phase stability.

Phonon theory and computational methods are briefly reviewed, and the experimental techniques for phonon study, such as Raman spectroscopy and inelastic neutron scattering, are discussed. Several experiments on phonon anharmonicity were performed, and interpreted with these computational methods.

In Raman spectroscopy studies on the phonon dynamics of hafnia and zirconia, Raman line positions, and shapes of temperatures to 1000 K were measured and the types of modes that exhibit the most anharmonicity were characterized and correlated to the vibrational displacements of individual atoms in the unit cell. It was found that anharmonicity in these systems is rich in information and strongly mode dependent.

Using time-of-flight inelastic neutron scattering, we found purely quartic transverse modes with an anomalous mode stiffening with temperature, and related these modes to the enormous negative thermal expansion of the DO_9 structure of scandium fluoride.

Using second-order perturbation theory, phonon linewidths from the third-order anharmonicity were calculated from first-principles density functional theory with the supercell finite-displacement method. For face-centered cubic aluminum, the good agreement between calculations and the phonon density of states up to 750 K indicates that the third-order phonon-phonon interactions

calculated can account for the lifetime broadenings of phonons in aluminum to at least 80% of its melting temperature.

Contents

List of Figures

List of Tables

Part I

Introduction

Chapter 1

Introduction

1.1 Motivations

Vibrational studies of materials at elevated temperatures are relatively rare. Most phonon work also has emphasized harmonic behavior—non-harmonic effects are often unexplored. However, these non-harmonic effects can be important for many properties of the material, such as thermal transport, phase stability, and thermal expansion.

Harmonic and quasiharmonic models are good approximations for many materials, but anharmonic behaviors are also quite common. Recent work by our group found that adiabatic electron-phonon interactions can have a considerable effect on the vibrational entropy of vanadium metal and A15 vanadium compounds, because of their high electronic density of states near the Fermi level. [1, 2] When electron-phonon interactions are not playing major roles, such as in aluminum metal, the phonon-phonon interactions are believed to be the dominant component of the phonon anharmonicity, especially at elevated temperatures. Combined experimental and computational studies on metals and alloys can give insights about the anharmonicity and their effects on phonon dynamics.

Ionic compounds such as oxides or fluorides have dramatic differences from metals and alloys. Firstly, they have much greater variety in structures, many of which have low symmetry. Secondly, most ionic compounds have low electrical conductivity. As a result, electrons are more locally confined, and phonon dynamics generally has a larger impact on many properties of these materials. A good understanding of the high-temperature vibrational behavior of these materials can have major benefits for their applications in thermoelectrics, fuel cells, and thermal barrier coating, for example.

1.2 Present Work

Basic concepts in phonon theory and computational methods are briefly reviewed, and key experimental techniques for phonon study, Raman spectroscopy, and

inelastic neutron scattering are discussed. Several experiments on phonon anharmonicity were performed with these experimental methods, and interpreted with computational methods. Aside from the phonon frequency shift, which is typically used to understand vibrational thermodynamics, high-resolution measurements of phonon energy broadening allows for an assessment of the origin of the anharmonic behavior.

In Raman spectroscopy studies on the phonon dynamics of hafnia and zirconia, Raman line positions, and shapes of temperatures to 1000 K were measured, and the temperature-dependent Raman peak shifts and broadenings were reported and compared with each other. The modes that exhibit the most anharmonicity were characterized and correlated to the vibrational displacements of individual atoms in the unit cell using both a shell model and density functional theory. It was found that anharmonicity in these systems is rich in information and strongly mode dependent. The discrepancy between the temperature and pressure Grüneisen parameters is surprisingly large. Previous studies have largely neglected these effects and further exploration will definitely advance the understanding of phonons and vibrational entropy.

Cubic scandium fluoride (ScF_3) has an enormous negative thermal expansion over a wide range of temperature. Using time-of-flight inelastic neutron scattering, we found purely quartic transverse modes with an anomalous mode stiffening with temperature, and related these modes to the negative thermal expansion of the DO_9 structure using phonon and frozen phonon calculations with first-principles methods. The vibrational entropy contribution from these soft phonon modes may help to stabilize the cubic phase over a wide range of temperature.

The thermal phonon broadening in aluminum was studied by theoretical and experimental methods. Using second-order perturbation theory, phonon linewidths from the third-order anharmonicity were calculated from first-principles density functional theory with the supercell finite-displacement method. The importance of all three-phonon processes were assessed, and individual phonon broadenings are presented. For face-centered cubic aluminum, the good agreement between

calculations and prior measurements of phonon linewidths at 300 K, and new measurements of the phonon density of states from 7 to 750 K, indicates that the third-order phonon-phonon interactions calculated from DFT can account for the lifetime broadenings of phonons in aluminum to at least 80% of its melting temperature.

For reference, the publications related to the current work are listed in Appendix A.

Part II

Theory

Even though the theory part of the current work is divided into separate chapters on on theory and computational techniques, in reality, it becomes more and more difficult to draw a clear line between those two. Benefiting from the ever-growing power of computers and improved computational methods, modern physical science heavily relies on computational science for both experimental and theoretical studies. It is relatively easy to determine the computational part of the the experimental work because it will involve either experimental design/simulation or data acquisition and post-processing. Theoretical work, however, sometimes becomes so convolved with computational techniques that the two are inseparable. Here we put the part of the theory that is directly associated with the materials simulations in the calculation chapter, and the rest in the phonon theory chapter.

Chapter 2

Phonon Theory

2.1 Introduction

In physical science, a phonon is a **collective** excitation of atoms or molecules in condensed matter phases such as solids and liquids. The name "phonon" comes from the Greek word "$\varphi\omega\nu\acute{\eta}$", which translates as "sound" or "voice" because sound is just long-wavelength accoustic phonons. First introduced in 1932 by Russian physicist Igor Tamm, a phonon is referred to as a "quasiparticle", which represents an excited state in the quantization of the modes of vibrations of elastic structures of interacting particles. [3, 4]

Phonons play major roles in solid state physics. They often determine the thermal and electrical conductivities of materials, and sometime have a large impact on a material's crystal structure as well. A phonon is a quantum mechanical description of a special type of vibrational motion, in which a lattice uniformly oscillates at the same frequency. In classical mechanics this is commonly known as a normal mode, but in quantum mechanical treatments phonons are considered nearly-free particles.

This work will mostly be focused on the dynamics of nuclei in crystals because for phonon dynamics, most of the moving mass is in the nuclei. Theoretical and computational principles of phonons have been elaborated extensively elsewhere. [4–9] This chapter will only briefly restate the basic questions regarding the theory of phonon lattice dynamics, and the following chapter will discuss in more detail the techniques for phonon-related calculations.

2.2 Crystal Lattice

The formalism for phonons is usually developed for solids with long-range periodicity: crystal lattices. A perfect crystal lattice can be generated by the infinite repetition in 3-dimensional space of a unit cell defined by three noncoplanar vectors: $\mathbf{a}_1$, $\mathbf{a}_2$, and $\mathbf{a}_3$, which are called the primitive lattice vectors of the crystal. [8, 10, 11] Labeling each unit cell by a triplet of integers $l = (l_1, l_2, l_3)$, the

equilibrium position of the origin of the unit cell l is

$$\mathbf{r}_l = l_1\mathbf{a}_1 + l_2\mathbf{a}_2 + l_3\mathbf{a}_3. \tag{2.1}$$

The number of possible arrangements of the lattice vectors are limited, and they are called Bravais lattices. There are 5 Bravais lattices in 2 dimensions (Fig. 2.1) and 14 Bravais lattices in 3 dimensions. A Braivais lattice looks exactly the same from any of the lattice points $\mathbf{r}_l$.

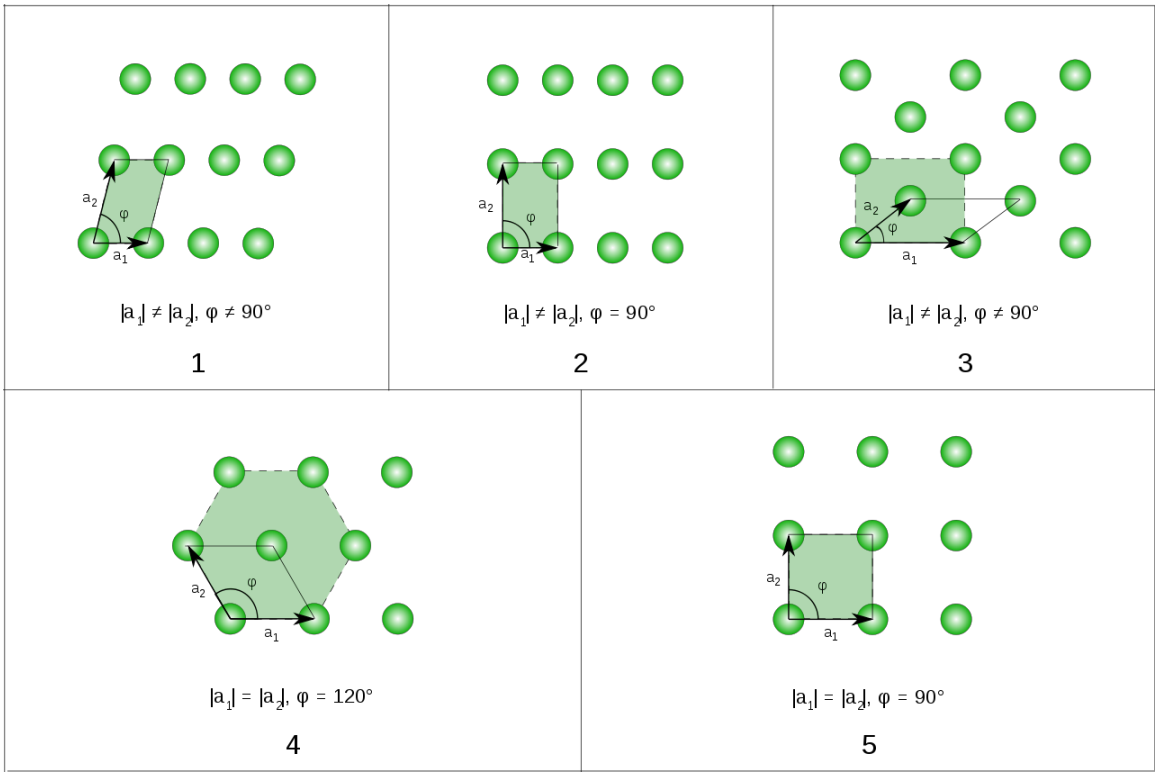

Figure 2.1: The five two-dimensional Bravais lattices: oblique, rectangular, rhombic, hexagonal, and square [12]

Each of the $\mathcal{R}$ atoms in one unit cell is assigned an index $\kappa = 1, 2...\mathcal{R}$. The equilibrium positions of the atoms with respect to the origin of a unit cell are defined as the site vectors $\mathbf{r}_\kappa, \kappa = 1, 2...\mathcal{R}$, and the equilibrium position of atom κ in cell l is a combination of the two vectors

$$\mathbf{r}_{l\kappa} = \mathbf{r}_l + \mathbf{r}_\kappa. \tag{2.2}$$

At finite temperatures the atoms vibrate around their equilibrium positions, adding another time-dependent vector to the instantaneous position of the atoms.

Sometimes it is convenient to study Bravais lattices by their reciprocal lattices, which are the Fourier transform of the spatial function of the original lattice, now in k-space (momentum space). Detailed mathematical and physical descriptions can be found in any solid state physics textbook. [9, 10, 13] Because of the periodicity of the reciprocal lattice, it is sufficient to study only one primitive cell (Brillouin zone) of reciprocal space. Defined similar to the Wigner-Seitz cell in real space, the volume included by surfaces at the same distance from one site of the reciprocal lattice and its neighbors is the first Brillouin zone. Higher-order Brillouin zones with the same volumes could also be defined. Using the symmetry in the point group of the lattice, the first Brillouin zone can be further reduced to the irreducible Brillouin zone, which is commonly used in computations to reduce to the amount of work.

2.3 Normal Modes

Before discussing normal modes in periodic lattices, first we have a look at vibrations in systems of just a few particles (for example, a CO_2 molecule). Suppose the system is made of n point-mass-like particles interconnected by harmonic springs. There will be $3n$ equations of motions and $3n$ degrees of freedom, including 3 translational and $3n-3$ vibrational degrees of freedom. The system is completely solvable, albeit extremely difficult to tackle directly when the number of particles becomes large.

However, through a coordinate transformation, it is possible to transform the single problem with many coupled variables into many problems, each with a single, uncoupled variable. This transformation is well known for mechanical systems and commonly done through diagonalizing the dynamical matrix from the equations of motions. [14, 15] For a system with n particles, there are generally $3n-3$ normal modes (with the exception of some geometric arrangements) and

the general motions of the system are a superpositions of these normal modes. The modes are "normal" in the sense that they are uncoupled. That is to say, in a perfectly harmonic system, an excitation of one mode will never cause motion of a different mode, i.e, there is no energy transfer between these (harmonic) normal modes.

The same idea applies to solids with periodic lattices as detailed in Section 2.6.3. The evenly spaced energy levels of these harmonic normal modes are exactly how phonons are defined. Solids with more than one type of atom in the unit cell have two types of phonons: acoustic phonons and optical phonons. Acoustic phonons are long-wavelength, coherent movements of atoms out of their equilibrium positions and are named after their close relation to sound waves. They can be both longitudinal (LA, in the direction of propagation) or transverse (TA, perpendicular to the propagation direction). Acoustic phonons mostly have a linear dispersion relationship between frequency and phonon wavevector, in which the frequency goes to zero in the limit of long wavelength. On the contrary, optical phonons are short-wavelength, out-of-phase movements of the atoms in the lattice and only occur if the lattice is made of atoms of different charge or mass. [5] They are named optical because in some ionic crystals, they can be excited by electromagnetic radiation (light) through infrared absorption or Raman scattering. Optical phonons have a nonzero frequency at the Brillouin zone center and because of the symmetry, they show no dispersion near that long-wavelength limit. Similar to acoustic phonons, longitudinal and transverse optical phonons are often abbreviated as LO and TO phonons, respectively.

2.4 Phonon Thermodynamics

Phonons are defined to facilitate the understanding of the collective motions of atoms in crystals as normal modes of a solid. They are treated independently, giving independent contributions to thermodynamic functions, simplifying analyses of the vibrational partition function and vibrational entropy. Here we use the

notations of Fultz. [16].

Phonons are bosons, so there is no limit to how many phonons can be present in each normal mode. Consider a set of N coupled modes with the same energy ε and suppose m phonons are free to distribute between these modes. Using the entropy equation of Boltzmann, the phonon entropy can be written as:

$$S = k_{\mathrm{B}} \ln \Omega, \tag{2.3}$$

where Ω is the number of ways to place the m phonons in the N modes. Notice that the phonons are indistinguishable. Using the binomial result of the combinatorial rule, Ω can be written as:

$$\Omega = \frac{(N-1+m)!}{(N-1)!\, m!}. \tag{2.4}$$

In macroscopic systems where the numbers of modes N are large, $N-1$ can be replaced by N:

$$\Omega = \frac{(N+m)!}{N!\, m!}. \tag{2.5}$$

Substituting (2.5) into (2.3), and expanding the factorial using the Stirling approximation of $\ln x! \simeq x \ln x - x$:

$$S = k_{\mathrm{B}}\Big[(N+m)\ln(N+m) - N\ln N - m\ln m\Big]. \tag{2.6}$$

Assuming the occupancy of each mode is $n \equiv m/N$, the entropy per mode can be written as:

$$\frac{S}{N} = k_{\mathrm{B}}\Big[(1+n)\ln(1+n) - n\ln n\Big]. \tag{2.7}$$

As a comparison, the entropy per site for fermions is

$$\frac{S_{\text{fermi}}}{N} = -k_{\text{B}}\Big[(1-c)\ln(1-c) + c\ln c\Big], \tag{2.8}$$

where c is the occupancy of each site. This happens to be the same as the entropy of mixing (where c is the site occupancy) due to the nature of the Pauli exclusion principle.

With the vibrational entropy per mode (Eq. 2.7), the Helmholtz free energy per mode for a system of oscillators is

$$\frac{F}{N} = \frac{E}{N} - T\frac{S}{N} = n\,\varepsilon - T\,k_{\text{B}}\Big[(1+n)\ln(1+n) - n\ln n\Big], \tag{2.9}$$

where $E = n\,\varepsilon$ is the total phonon energy in the mode.

The equilibrium phonon occupancy n at temperature T can be calculated by minimizing the free energy F with respect to n. The result:

$$n(T) = \frac{1}{\mathrm{e}^{\frac{\varepsilon}{k_{\text{B}}T}} - 1}, \tag{2.10}$$

is the Planck distribution for phonons, or the Bose-Einstein distribution. It is common practice to simplify the expression using $\beta = (k_{\text{B}}\,T)^{-1}$.

In a crystalline system, there are a variety of phonon modes with different energies. Using the results above, the phonon entropy of the system can be calculated with the partition function.

For a harmonic crystal, the total vibrational energy capacity is calculated as contributions from a system of independent oscillators. The partition function for a single quantum harmonic oscillator (mode) i at energy $\epsilon_i = \hbar\omega_i$, where ω_i is the vibrational frequency, is:

$$\mathcal{Z}_i = \sum_n^{\infty} \mathrm{e}^{-\beta(n+1/2)\epsilon_i} = \frac{\mathrm{e}^{-\beta\epsilon_i/2}}{1-\mathrm{e}^{-\beta\epsilon_i}}. \tag{2.11}$$

For a harmonic solid with N atoms, there are $3N$ independent oscillators. The

total partition function is the product of these single oscillator partition functions,

$$\mathcal{Z}_N = \prod_i^{3N} \frac{\mathrm{e}^{-\beta\epsilon_i/2}}{1-\mathrm{e}^{-\beta\epsilon_i}}. \tag{2.12}$$

Using the thermodynamics relation of the partition function, the phonon free energy and entropy can be calculated as:

$$F_{\mathrm{ph}} = \frac{1}{2}\sum_i^{3N} \epsilon_i \ + k_{\mathrm{B}}T \sum_i^{3N} \ln\left(1-\mathrm{e}^{-\beta\epsilon_i}\right), \tag{2.13}$$

$$S_{\mathrm{ph}} = k_{\mathrm{B}} \sum_i^{3N} \left[-\ln\left(1-\mathrm{e}^{-\beta\epsilon_i}\right) + \frac{\beta\epsilon_i}{\mathrm{e}^{\beta\epsilon_i}-1}\right]. \tag{2.14}$$

It is often useful to work with a phonon density of states (DOS), $g(\epsilon)$, where $3Ng(\epsilon)\mathrm{d}\epsilon$ phonon modes are in an energy interval $\mathrm{d}\epsilon$. Note that the phonon DOS $g(\epsilon)$ here is assumed to be normalized to unity. For a discrete phonon DOS in m intervals of bin width $\Delta\epsilon$ each, the partition function can be computed numerically as:

$$\mathcal{Z}_N = \prod_{j=1}^{m} \left(\frac{\mathrm{e}^{-\beta\epsilon_j/2}}{1-\mathrm{e}^{-\beta\epsilon_j}}\right)^{3Ng(\epsilon_j)\Delta\epsilon}. \tag{2.15}$$

It is interesting that the only material parameter relevant to the thermodynamic partition function is the phonon DOS, $g(\epsilon)$.

Using a measured or calculated phonon DOS, the phonon entropy of a harmonic crystal at temperature T can be written as

$$S_{\mathrm{ph}} = 3k_{\mathrm{B}} \int_0^\infty g(\epsilon) \left[(n(\epsilon)+1)\ln\left(n(\epsilon)+1\right) - n(\epsilon)\ln\left(n(\epsilon)\right)\right] \mathrm{d}\epsilon, \tag{2.16}$$

where $n(\epsilon)$ is the Planck distribution for phonon occupancy of Eq. 2.10. In the high-temperature limit, the difference in phonon entropy between two harmonic

phases, α and β becomes independent of temperature and can be written as

$$\Delta S_{\mathrm{ph}}^{\beta-\alpha} = 3k_{\mathrm{B}} \int_0^\infty (g^\alpha(\epsilon) - g^\beta(\epsilon)) \ln(\epsilon)\, \mathrm{d}\epsilon. \tag{2.17}$$

It has been known for a while that phonon entropy is important for crystal stability [17, 18] but obtaining an accurate phonon DOS to calculate differences in vibration entropy like $\Delta S_{\mathrm{ph}}^{\beta-\alpha}$ turns out to be difficult and became possible only recently. [19, 20] More details will be discussed in later chapters on these computational and experimental techniques. Although the temperature effects on phonon thermodynamics are also important and will be discussed in subsequent sections, the phonon spectra of solids are mostly determined by phases and compositions. The dominant factors for phonon entropy are the atomic masses M, and the spring constants k from the interatomic force constants, as in a classic harmonic oscillator:

$$\omega = \sqrt{\frac{k}{M}}, \tag{2.18}$$

where ω is the vibrational frequency. For atoms of similar size, it is found that in a solid solution of atoms A and B, with their atomic masses M_A and M_B, respectively, the phonon entropy upon alloying tends to scale with $\ln(M_A/M_B)$, [16,21] although there is a large scatter in this correlation especially for some of the alloys. This is possibly a consequence of the difference in atom sizes, which cause local stress and as a result, drastically alter the interatomic force constants.

Phonon entropy trends due to the changes of interatomic force constants may be robust for transition metal alloys. As shown in the study of vanadium alloys [22], there is a linear relation between the phonon entropy and the difference in electronegativity, in spite of large differences in atomic mass and atomic size. Increased charge transfers between the first-near-neighbor atoms caused by a larger difference in electronegativity reduce the charge screening by reducing the metallic-like states near the Fermi level, and in turn, stiffen the interatomic force

constants.

2.5 Temperature Effects

2.5.1 Harmonic Phonons

In the simplest approximation, where all the oscillators in a solid are harmonic and have fixed frequencies (Einstein model [7]), the heat capacity could be derived from Planck distribution (Eq. 2.10). The heat capacity at constant volume $C_{V,i}$ for the mode i is

$$C_{\mathrm{V},i}(T) = k_{\mathrm{B}} \left(\frac{\varepsilon_i}{k_{\mathrm{B}}T}\right)^2 \frac{\exp(\varepsilon_i/k_{\mathrm{B}}T)}{(\exp(\varepsilon_i/k_{\mathrm{B}}T)-1)^2}, \tag{2.19}$$

where the temperature derivative of the occupancy distribution is weighted by the energy of the phonon mode. In the high-temperature limit, the result becomes the classic one: one k_{B} per mode.

A Debye model, [7] which treats the vibrations as phonons in a box, assumes a phonon DOS that is a quadratic function of energy, and increases monotonically up to a cutoff energy. (The actual DOS often has a more abrupt rise at low energies that comes from the lower sound velocity of the low transverse modes and a complex structure at higher energies.) The Debye model does predict some general features of the heat capacity a little better, especially in the low-temperature limit. A useful result from this model is the Debye temperature

$$\theta_{\mathrm{D}} = \frac{h\nu_{\mathrm{m}}}{k}, \tag{2.20}$$

where ν_{m} is the vibrational frequency at the cutoff energy. Above this temperature, the vibrations in the solid are approaching the classical limit and quantum effects become less important. For pure elements, θ_{D} varies from less than 100 K (soft metals) to over 2000 K (carbon).

The ideal harmonic crystal model is nice and simple. However, it cannot

account for even some of the most basic behaviors of solids. Typically, materials expand when heated, their elastic constants change with temperature and pressure, their specific heats at constant volume or pressure are not equal, and their thermal conductivity is not infinite. We have to go beyond the harmonic approximation to understand these properties. [5, 20, 23]

2.5.2 Quasiharmonic Thermodynamics

Experimentally, the heat capacity at constant pressure C_p is most useful because it can be measured directly by calorimetry:

$$C_p(T) = T \left.\frac{dS}{dT}\right|_p. \tag{2.21}$$

The difference between C_p and C_V is a classical thermodynamic relationship [10]

$$C_p - C_V = 9Bv\alpha^2 T, \tag{2.22}$$

where B is bulk modulus, α is the linear coefficient of thermal expansion, and v is specific volume.

Eq. 2.22 can be derived by assuming that the free energy of a crystal comes only from phonons and thermal expansion. The total free energy can be written as

$$F(T) = E_{elas}(T) + E_{ph}(T) - TS_{ph}. \tag{2.23}$$

Phonon energies fall significantly, but thermal occupancy compensates, leading to small net changes in E_{ph}.

The elastic energy of thermal expansion is

$$E_{elas} = \frac{1}{2}B\frac{(\delta V)^2}{V_0} = \frac{9}{2}BV_0\,\alpha^2 T^2, \tag{2.24}$$

and the phonon energy and entropy in the classical limit are

$$E_{\rm ph}(T) = 3Nk_{\rm B}T, \tag{2.25}$$

$$S_{\rm ph}(T) = k_{\rm B}\sum_{j}^{3N}\ln\left(\frac{k_{\rm B}T}{\hbar\omega_j}\right). \tag{2.26}$$

Assume a linear phonon frequency shift with respect to the change of volume:

$$\omega_j = \omega_j^0(1-3\alpha T\gamma), \tag{2.27}$$

$$\ln(\omega_j) \simeq \ln(\omega_j^0) - 3\alpha T\gamma, \tag{2.28}$$

where γ is the Grüneisen parameter. The phonon entropy can be written as

$$S_{\rm ph}(T) = \left[k_{\rm B}\sum_{j}^{3N}\ln\left(\frac{k_{\rm B}T}{\hbar\omega_j^0}\right)\right] + 9N\gamma\alpha k_{\rm B}T \tag{2.29}$$

$$= S_{\rm ph}^0 + S_{\rm q}, \tag{2.30}$$

where the first term, $S_{\rm ph}^0$, is the harmonic phonon entropy at $T=0$, and the second term, $S_{\rm q}$, is the quasiharmonic part:

$$S_{\rm q} = 9BV_0\alpha^2 T. \tag{2.31}$$

Typical quasiharmonic effects on the heat capacity are shown in Fig. 2.2.

Using these results, the total free energy in a quasiharmonic crystal is

$$F(T) = \frac{9}{2}BV_0\alpha^2T^2 + 3Nk_{\rm B}T - TS_{\rm ph}^0(T) - 9N\alpha\gamma k_{\rm B}T^2. \tag{2.32}$$

The equilibrium thermal expansion coefficient, α, can be calculated by minimizing the free energy with respect to α, giving

$$\alpha = \frac{C_V\gamma}{3BV_0}. \tag{2.33}$$

This quasiharmonic phonon entropy, $S_{\rm q}$, should always be considered when

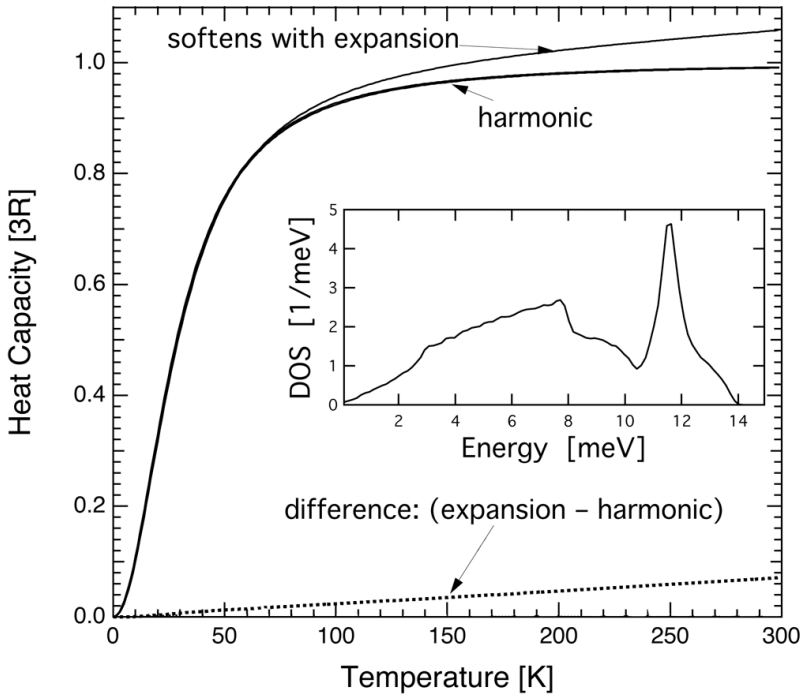

Figure 2.2: Heat capacity versus temperature for a simple harmonic model with a phonon DOS unchanged with temperature, and a typical case where the solid expands against its bulk modulus. Inset is the phonon DOS at 0 K. From [16]

comparing the vibrational thermodynamics of different materials at elevated temperatures because it often gives a good accounting of the phonons and thermal expansion, but many exceptions are known. This quasiharmonic approximation assumes that the oscillations in the system are harmonic-like and they change only modestly and predictably with changes in temperature and pressure. Also the phonon lifetimes are long enough so that their frequencies are well defined.

2.5.3 Anharmonic Thermodynamics

Typically, the word “anharmonic” describes any oscillator with generalized forces that deviate from linearity with respect to generalized coordinates. This definition includes the quasiharmonic effects from the thermal expansion. However, we will follow the more restrictive usage in modern thermodynamics, where “anharmonic” effects only account for the behavior beyond the harmonic and quasiharmonic theory of Eq. 2.30.

It is possible to experimentally determine if a solid is “quasiharmonic” or “anharmonic”. The thermal softening of the phonon modes can give a mode-averaged Grüneisen parameter γ. The phonon DOS can be used to calculate C_V, and conventional measurements can provide B, V_0, and α, accounting for all unknowns in Eq. 2.30. If the γ from Eq. 2.30 matches the γ from phonon shifts, the solid is “quasiharmonic”.

When phonon softening or stiffening is inconsistent with the Grüneisen parameter γ needed for equality in Eq. 2.30, the solid is anharmonic. The anharmonicity may be a result of electron-phonon interactions, changes in electronic structure with temperature, or higher-order phonon-phonon interactions. It is generally difficult to determine the sources of non-harmonic behavior and their contributions to the entropy. [7] Usually the effects of electron-phonon interactions are important only at low temperatures and are often ignored as a source of anharmonicity when the temperature is higher. Substantial deviations from quasiharmonic behavior are known for many metal [16] and non-metal systems.

2.5.4 Phonon Entropy

The logarithm definition of the entropy makes it easy to split the total entropy into uncorrelated subsystems

$$S = k_B \ln \Omega = k_B \ln \left(\prod_i \Omega_i \right) = k_B \sum_i \ln \Omega_i = \sum_i S_i, \tag{2.34}$$

where i denotes the index of subsystems. It may be necessary to correct for the interactions between these subsystems (cross terms) but they are usually small enough to be treated as perturbations. The total entropy of a crystal then can be written as the sum of configurational, phonon, electron, electron-phonon interaction, magnetic, and nuclear contributions

$$S = S_{cf} + S_{ph} + S_{el} + S_{el-ph} + S_m + S_n. \tag{2.35}$$

We will ignore other effects, such as electronic, magnetic, and nuclear ones, and only consider phonon harmonic, quasiharmonic, and anharmonic contributions

$$S_{\mathrm{ph}} = S^0_{\mathrm{ph}} + + S_{\mathrm{q}} + S_{\mathrm{anh}} \tag{2.36}$$

for now. The temperature dependence of the entropy can be written as:

$$\frac{\mathrm{d}S(T,V)}{\mathrm{d}T} = \frac{\partial S}{\partial T}\bigg|_V + \frac{\partial S}{\partial V}\bigg|_T \frac{\mathrm{d}V}{\mathrm{d}T}. \tag{2.37}$$

The harmonic part of the vibrational entropy can be calculated with a phonon DOS from low temperature measurement or calculation. The harmonic phonons undergo no change with respect to the temperature or volume, and as a result the temperature dependence of harmonic entropy only occurs because of the change in the Planck occupancy with temperature.

For quasiharmonic phonons, their frequencies depend on volume only and they make a contribution only through the second term on the right-hand side of Eq. 2.37.

$$\Delta S_{\mathrm{q}} = \frac{\partial S}{\partial V}\bigg|_T \frac{\mathrm{d}V}{\mathrm{d}T}\Delta T \tag{2.38}$$

Using the Grüneisen parameter to describe the frequency change with temperature, the quasiharmonic contribution is

$$\Delta S_{\mathrm{q}} = 9B\upsilon\alpha^2\Delta T. \tag{2.39}$$

The problem is more difficult for anharmonic entropy because it may contribute through either of the two terms on the right-hand side of Eq. 2.37. The first term, the temperature-dependence of the vibrational entropy at fixed volume, is caused by changes in the interatomic force constants with temperature. For example in an interatomic potential with a quartic term, the force constants change with the amplitude of thermal displacements. This quartic term happens to have no effect

on the thermal expansion, but it does change the phonon frequencies by 4-phonon process. The second term is associated with changes of the interatomic force constants with volume. Although the quasiharmonic contribution is expected to account for most of this effect, it is only correct to first order [20]. For example, the phonon linewidth broadening from the cubic term in the interatomic potential alters the vibrational entropy. The quasiharmonic contribution accounts for shifting of the phonon frequencies but misses those higher-order terms.

2.5.5 Electronic Entropy

Unlike phonons, which are bosons, electrons fill the states up to the Fermi level, even at absolute zero temperature. The electronic entropy arises from the thermal excitation of electrons around the Fermi level and can be written as:

$$S_{\mathrm{el}} = -k_{\mathrm{B}} \int_{-\infty}^{\infty} [(1-f)\ln(1-f) + f \ln f] n(\varepsilon) \mathrm{d}\varepsilon, \tag{2.40}$$

where $f(\varepsilon, T)$ is the Fermi distribution function and $n(\varepsilon)$ is the electronic density of states. Similar to the phonon entropy, the total electronic entropy can be split into contributions from the ground state and the thermal expansion (lattice dilation):

$$S_{\mathrm{el}} = S_{\mathrm{el}}^{G} + S_{\mathrm{el}}^{D}. \tag{2.41}$$

S_{el} can be as large as 1 kB/atom at elevated temperatures but S_{el}^{D} is usually an order of magnitude smaller, so the major of the electronic entropy comes from the thermal excitations of electrons near the Fermi surface.

2.6 Lattice Dynamics

2.6.1 Interatomic Force-Constants

For atom vibrations in crystals, only the motions of the nucleus are relevant because the mass of the electron is negligible in comparison. Ignoring the detailed mechanism of these interactions [8, 20], the Hamiltonian for nuclear motions can be written as [24, 25]

$$H_{\mathrm{n}} = \sum_{l,\kappa} \frac{\mathbf{p}_{l\kappa}^2}{2m_\kappa} + \Phi, \tag{2.42}$$

where Φ is the potential energy, $\mathbf{p}$ is the momentum vector, and l and κ are the labels of atom and unit cell, respectively. The instantaneous position $\mathbf{R}_{l\kappa}(t)$ of atom $l\kappa$ at time t is

$$\mathbf{R}_{l\kappa}(t) = \mathbf{r}_l + \mathbf{r}_\kappa + \mathbf{u}_{l\kappa}(t), \tag{2.43}$$

where the atom κ in the unit cell l vibrates about its equilibrium with the displacement $\mathbf{u}_{l\kappa}(t)$.

We expand the total potential energy Φ in a Taylor series about these equilibrium positions

$$\begin{aligned} \Phi &= \Phi_0 + \sum_{\alpha l\kappa} \Phi_{\alpha l\kappa}\, u_{\alpha l\kappa} \\ &\quad + \frac{1}{2} \sum_{\alpha l\kappa} \sum_{\alpha' l'\kappa'} \Phi_{\alpha\alpha' l\kappa l'\kappa'}\, u_{\alpha l\kappa}\, u_{\alpha' l'\kappa'} + \ldots, \end{aligned} \tag{2.44}$$

where $\alpha = \{x, y, z\}$ are the Cartesian components, the coefficients of the Taylor series are the derivatives of the potential with respect to the displacements

$$\Phi_{\alpha l\kappa} = \left.\frac{\partial \Phi}{\partial u_{\alpha l\kappa}}\right|_0, \tag{2.45}$$

$$\Phi_{\alpha\alpha' l\kappa l'\kappa'} = \left.\frac{\partial^2 \Phi}{\partial u_{\alpha l\kappa}\, \partial u_{\alpha' l'\kappa'}}\right|_0, \tag{2.46}$$

and Φ_0 is the static potential energy of the crystal. Because the force on any atom must vanish in the equilibrium configuration,

$$\Phi_{\alpha l\kappa} = 0. \tag{2.47}$$

As an approximation that we will revisit in the next section, we neglect terms of order three and higher in the displacements in Eq. 2.44. The Hamiltonian can be written as

$$H_{\mathrm{n}} = \sum_{l\kappa} \frac{\mathbf{p}_{l\kappa}^2}{2m_\kappa} + \Phi_0 + \frac{1}{2} \sum_{\alpha l\kappa} \sum_{\alpha' l'\kappa'} \Phi_{\alpha\alpha' l\kappa l'\kappa'}\, u_{\alpha l\kappa}\, u_{\alpha' l'\kappa'}. \tag{2.48}$$

This is the harmonic approximation of lattice dynamics.

It is possbile to rewrite the Hamiltonian in matrix form

$$H_{\mathrm{n}} = \sum_{l\kappa} \frac{\mathbf{p}_{l\kappa}^2}{2m_\kappa} + \Phi_0 + \frac{1}{2} \sum_{l\kappa} \sum_{l'\kappa'} \mathbf{u}_{l\kappa}^T\, \Phi_{l\kappa l'\kappa'}\, \mathbf{u}_{l'\kappa'}, \tag{2.49}$$

where $\Phi_{l\kappa l'\kappa'}$ is a 3×3 force-constant matrix defined for each atom pair $l\kappa$ and $l'\kappa'$ ($(l,\kappa) \neq (l',\kappa')$):

$$\Phi_{l\kappa l'\kappa'} = [\Phi_{\alpha\alpha' l\kappa l'\kappa'}]. \tag{2.50}$$

This is the famous Born-von Kármán model. [8, 26] If $(l,\kappa) = (l',\kappa')$, $\Phi_{\alpha\alpha' l\kappa l\kappa}$ is a "self-force constant", determined by the requirement of no overall translation of the crystal

$$\Phi_{l\kappa l\kappa} = - \sum_{(l',\kappa') \neq (l,\kappa)} \Phi_{l\kappa l'\kappa'}. \tag{2.51}$$

Because equal and opposite forces act between each atom of a pair, the matrix

$\Phi_{l\kappa l'\kappa'}$ must be real and symetric.

$$\Phi_{l\kappa l'\kappa'} = \begin{pmatrix} a & b & c \\ b & d & e \\ c & e & f \end{pmatrix} \tag{2.52}$$

To satisfy the translational symmetry, the force constant matrices must also have the following property

$$\Phi_{l\kappa l'\kappa'} = \Phi_{0\kappa(l'-l)\kappa'} = \Phi_{(l-l')\kappa 0\kappa'}. \tag{2.53}$$

It should be noted that the interatomic force constants, such as $\Phi_{\alpha\alpha' l\kappa l'\kappa'}$, are in fact not constant but functions of temperature and lattice parameters.

2.6.2 Equations of Motion

Using the the harmonic approximation and the potential above, the equations of motion for nuclei are

$$m_\kappa \mathbf{u}_{l\kappa}(t) = -\sum_{l',\kappa'} \Phi_{l\kappa l'\kappa'}\, \mathbf{u}_{l'\kappa'}(t). \tag{2.54}$$

There are $3 \times \mathcal{R} \times N^{\text{cell}}$ equations of motion for a finite crystal containing N^{cell} unit cells, each containing $\mathcal{R}$ atoms. [8]

It is easily calculated that for any crystal of reasonable size (on the order of 10^{23} atoms) the atoms on the surface account for only a very small fraction of all atoms. Typical atom in that crystal has many, many atoms in any direction extending beyond the distance that interatomic forces can reach. As a result, it is convenient to apply the approximation that displacements separated by a certain number of cells are equal. Imposing these periodic boundary conditions on the crystal, the solutions to the equation of motions can be written in the form of

plane waves of wavevector $\mathbf{k}$, angular frequency $\omega_{\mathbf{k}j}$, and "polarization" $\mathbf{e}_{\kappa j}(\mathbf{k})$

$$\mathbf{u}_{l\kappa\mathbf{k}j}(t) = \sqrt{\frac{2\hbar}{N m_\kappa \omega_{\mathbf{k}j}}}\,\mathbf{e}_{\kappa j}(\mathbf{k})\,\mathrm{e}^{\mathrm{i}(\mathbf{k}\cdot\mathbf{r}_l-\omega_{\mathbf{k}j}t)}, \tag{2.55}$$

$$= \hbar\sqrt{\frac{2n(\varepsilon_{\mathbf{k}j},T)+1}{N m_\kappa \varepsilon_{\mathbf{k}j}}}\,\mathbf{e}_{\kappa j}(\mathbf{k})\,\mathrm{e}^{\mathrm{i}(\mathbf{k}\cdot\mathbf{r}_l-\omega_{\mathbf{k}j}t)}, \tag{2.56}$$

where we take the real part to obtain physical displacements. The phase factor, $\mathrm{e}^{\mathrm{i}\mathbf{k}\cdot\mathbf{r}_l}$, provides all the long-range spatial modulation, while the dependence on κ, a short-range basis vector index, is placed in the complex constant $\mathbf{e}_{\kappa j}(\mathbf{k})$. It is convenient for this constant and the exponential to have modulus unity. j is the "branch index" discussed below and there are $3\mathcal{R}$ different such branches from symmetry.

2.6.3 The Eigenvalue Problem of the Phonon Modes

The polarization vectors, $\mathbf{e}_{\kappa j}(\mathbf{k})$, contain all information on the excursion of each atom κ in the unit cell for the phonon mode $\mathbf{k}, j$, including the displacement direction of the atom and its relative phase with respect to the other atoms. These "polarization" vectors and their associated angular frequencies $\omega_{\mathbf{k}j}$ (normal modes) can be calculated by diagonalizing the "dynamical matrix" $D(k)$. The detailed descriptions can be found elsewhere. [8, 23–25]

The dynamical matrix can be obtained by substituting Eq. 2.56 into 2.54. It has the dimensions $3N \times 3N$ and is constructed from 3×3 submatrices $D_{\kappa\kappa'}(\mathbf{k})$

$$D(\mathbf{k}) = \begin{pmatrix} D_{11}(\mathbf{k}) & \dots & D_{1N}(\mathbf{k}) \\ \vdots & \ddots & \vdots \\ D_{N1}(\mathbf{k}) & \cdots & D_{NN}(\mathbf{k}) \end{pmatrix}, \tag{2.57}$$

where each sub-matrix $D_{\kappa\kappa'}(\mathbf{k})$ is the Fourier transform of the force-constant

matrix $\Phi_{l\kappa l'\kappa'}$

$$D_{\kappa\kappa'}(\mathbf{k}) = \frac{1}{\sqrt{m_\kappa m_{\kappa'}}} \sum_{l'} \Phi_{0\kappa l'\kappa'}\, e^{i\mathbf{k}\cdot(\mathbf{r}_{l'}-\mathbf{r}_0)}. \tag{2.58}$$

To simplify, the equations of motions (Eq. 2.54) with the plane wave solutions (Eq. 2.56) can be represented as an eigenvalue problem:

$$D(\mathbf{k})\,\mathbf{e}_j(\mathbf{k}) = \omega^2_{\mathbf{k}j}\,\mathbf{e}_j(\mathbf{k}), \tag{2.59}$$

where

$$\mathbf{e}_j(\mathbf{k}) = \begin{pmatrix} e_{x1j}(\mathbf{k}) \\ e_{y1j}(\mathbf{k}) \\ e_{z1j}(\mathbf{k}) \\ e_{x2j}(\mathbf{k}) \\ \vdots \\ e_{zNj}(\mathbf{k}) \end{pmatrix} \tag{2.60}$$

is the eigenvector(s).

It can be shown that the dynamical matrix $D(\mathbf{k})$ is hermitian for any value of $\mathbf{k}$. As a result it is thus fully diagonalizable and the eigenvalues $\omega^2_{\mathbf{k}j}$ are real. The eigenvectors and eigenvalues of the dynamical matrix evaluated at a particular wavevector $\mathbf{k}$ correspond to the $3\mathcal{R}$ eigenmodes of vibration of the crystal for that wavevector. It should be noted that the angular frequency ($\omega_{\mathbf{k}j}$) dependence on the wavevector ($\mathbf{k}$), called a dispersion relation, can be quite complicated. The speed of propagation of phonons in solids (speed of sound) is given by the group velocity as the slope of this relation

$$v_{\text{sound}} = v_{\text{g}} = \frac{\partial \omega_{\mathbf{k}j}}{\partial \mathbf{k}}, \tag{2.61}$$

instead of the phase velocity

$$v_{\mathrm{p}} = \frac{\omega_{\mathbf{k}j}}{\mathbf{k}}. \tag{2.62}$$

2.6.4 The Phonon Density of States

With the phonon vibrations calculated above, it is straightforward to calculate the phonon density of states (DOS) of a crystal. This is done by diagonalizing the dynamic matrix $D(\mathbf{k})$ at a large number of $\mathbf{k}$ points in the first Brillouin zone, and then binning them into the DOS histogram.

Similarly, a phonon partial DOS $g_d(\varepsilon)$, which gives the spectral distribution of motions by one atom species d in the unit cell, can be obtained through weighting the vibrational contribution

$$g_d(\varepsilon) = \sum_{\mathbf{k}|} \sum_{\alpha\kappa j} \delta_{d\kappa} |e_{\alpha\kappa j}(\mathbf{k})|^2 g(\varepsilon). \tag{2.63}$$

Because the eigenvalues of the dynamical matrix are normalized for each $\mathbf{k}$ as

$$\sum_{\alpha\kappa j} |e_{\alpha\kappa j}(\mathbf{k})|^2 = 1, \tag{2.64}$$

the total DOS is the sum of the partial DOSs of all atoms in the unit cell,

$$g(\varepsilon) = \sum_{d} g_d(\varepsilon). \tag{2.65}$$

This seems simple but some software for phonon calculations does not implement it correctly. As a result, the partial DOSs do not add up to the total DOS, and the total DOS may also have an incorrect weighting on the different atom species.

2.6.5 Group Theory

With group theory, it is possible to find eigenvectors and eigenvalues without diagonalizing the dynamical matrix. [8] Maradudin and Vosko's review showed how group theory can be used to understand the normal modes of crystal vibrations and classify them. [27] In their work, the degeneracies of the different normal modes were addressed rigorously, and their association with the symmetry elements of the crystal were used to label them. In the same issue of the journal, Warren discussed the point group of the bond, [28] which refers to the real space symmetries of the interatomic interactions, i.e., how the force constants transform under the point group operations at a central atom.

2.7 Phonon-Phonon Interactions

Due to the huge mass ratio ($1 : 10^5$), it is often reasonable to assume that the nuclear motions are slow enough so that the electron levels adapt continuously to the evolving structure (Born–Oppenheimer approximation or adiabatic approximation). [4, 8, 10] This assumes that the electronic and nuclear systems are well separated and any interactions can be accounted for as perturbations. The full Hamiltonian of the crystal can be written as

$$H = H_{\mathrm{n}} + H_{\mathrm{e}} + H_{\mathrm{ep}}, \tag{2.66}$$

where H_{e} and H_{ep} are the contributions from the electron, including electron-electron interactions and thermal electronic excitations, and from electron-phonon interactions (EPI), respectively.

Phonon-phonon interactions originate from the third- and higher-order terms

in the Taylor series of Eq. 2.44:

$$\begin{aligned} H_{\mathrm{n}} = \Phi_0 \quad &+ \quad \sum_{\kappa} \frac{\mathbf{p}_\kappa^2}{2m} + \frac{1}{2!} \sum_{\kappa\alpha} \sum_{\kappa'\alpha'} \Phi_{\alpha\alpha'\kappa\kappa'}\, u_{\alpha\kappa}\, u_{\alpha'\kappa'} \\ &+ \quad \frac{1}{3!} \sum_{\kappa\alpha} \sum_{\kappa'\alpha'} \sum_{\kappa''\alpha''} \Phi_{\alpha\alpha'\alpha''\kappa\kappa'\kappa''}\, u_{\alpha\kappa}\, u_{\alpha'\kappa'}\, u_{\alpha''\kappa''} \\ &+ \quad \frac{1}{4!} \sum_{\kappa\alpha} \sum_{\kappa'\alpha'} \sum_{\kappa''\alpha''} \sum_{\kappa'''\alpha'''} \Phi_{\alpha\alpha'\alpha''\alpha'''\kappa\kappa'\kappa''\kappa'''}\, u_{\alpha\kappa}\, u_{\alpha'\kappa'}\, u_{\alpha''\kappa''}\, u_{\alpha'''\kappa'''} + \ldots \end{aligned} \tag{2.67}$$

where we assume one atom per unit cell.

The transformation to normal coordinates for an infinite periodic crystal is

$$\mathbf{U}_{\mathbf{k}_i} = \frac{1}{\sqrt{N\,m}} \sum_{\mathbf{r}_\kappa} \mathbf{u}_{\mathbf{r}_\kappa} \mathrm{e}^{-\mathrm{i}\mathbf{k}_i \cdot \mathbf{r}_\kappa}, \tag{2.68}$$

and by Fourier inversion

$$\mathbf{u}_{\vec{r}_\kappa} = \frac{1}{\sqrt{N\,m}} \sum_{\mathbf{k}_i} \mathbf{U}_{\mathbf{k}_i} \mathrm{e}^{+\mathrm{i}\mathbf{k}_i \cdot \mathbf{r}_\kappa}. \tag{2.69}$$

Substituting this into Eq. 2.67, we identify the Fourier transform of $\Phi_{\alpha\alpha'\kappa\kappa'}$, and use it to define the dynamical matrix.

It is usually easier to work with the quantized phonon field using the second quantization formalism. The phonon field operator is

$$A_{\mathbf{k}_i} = a_{\mathbf{k}_i} + a^\dagger_{-\mathbf{k}_i} = A^\dagger_{-\mathbf{k}_i}. \tag{2.70}$$

Constructed from the momentum and position operators of the Hamiltonian, the raising and lowering operators $a^\dagger_{\mathbf{k}_i}$ and $a_{\mathbf{k}_i}$ create and annihilate the phonon $\mathbf{k}_i$, respectively, similar to raising and lowering operators for a simple quantum harmonic oscillator. [29]

This is the occupation number representation, where n phonons of wavevector $\mathbf{k}_i$ are created with n raising operations as $\left(a^\dagger_{\mathbf{k}}\right)^n |0\rangle_{\mathbf{k}} = (n!)^{-1/2} |n\rangle_{\mathbf{k}}$. The

displacement operators in this representation are

$$\mathbf{u}(\mathbf{r}_\kappa) = \sum_{\mathbf{k}_i} \sqrt{\frac{\hbar}{2N\,m\,\omega_{\mathbf{k}_i}}}\,\mathbf{e}(\mathbf{k}_i)\,\mathrm{e}^{\mathrm{i}\mathbf{k}_i\cdot\mathbf{r}_\kappa}\,A_{\mathbf{k}_i}. \tag{2.71}$$

By substituting this into Eq. 2.67, we have

$$\begin{aligned}\hat{H}_\mathrm{n} &= \Phi_0 + \sum_{\mathbf{k}_i} \hbar\,\omega_{\mathbf{k}_i}\left(a^\dagger_{\mathbf{k}_i}\,a_{\mathbf{k}_i} + \frac{1}{2}\right) \\ &+ \sum_{\mathbf{k}_i}\sum_{\mathbf{k}_j}\sum_{\mathbf{k}_k} V(\mathbf{k}_i,\mathbf{k}_j,\mathbf{k}_k)\;A_{\mathbf{k}_i}\,A_{\mathbf{k}_j}\,A_{\mathbf{k}_k} \\ &+ \sum_{\mathbf{k}_i}\sum_{\mathbf{k}_j}\sum_{\mathbf{k}_k}\sum_{\mathbf{k}_l} V(\mathbf{k}_i,\mathbf{k}_j,\mathbf{k}_k,\mathbf{k}_l)\;A_{\mathbf{k}_i}\,A_{\mathbf{k}_j}\,A_{\mathbf{k}_k}\,A_{\mathbf{k}_l} + \ldots,\end{aligned} \tag{2.72}$$

where the first sum on the right-hand side includes both the kinetic energy and the harmonic part of the potential energy, and the V are related to the Fourier transforms of Φ. For example, the cubic term is

$$\begin{aligned}V(\mathbf{k}_i,\mathbf{k}_j,\mathbf{k}_k) &= \frac{1}{3!}\sqrt{\frac{1}{N\,m^3}\left(\frac{\hbar}{2}\right)^3\frac{1}{\omega_{\mathbf{k}_i}\omega_{\mathbf{k}_j}\omega_{\mathbf{k}_k}}}\,\delta(\mathbf{k}_i+\mathbf{k}_j+\mathbf{k}_k-\mathbf{g}) \\ &\times \sum_{\vec{r}_\kappa}\mathbf{e}(\mathbf{k}_i)\mathbf{e}(\mathbf{k}_j)\mathbf{e}(\mathbf{k}_k)\mathrm{e}^{+\mathrm{i}(\mathbf{k}_i+\mathbf{k}_j+\mathbf{k}_k)\cdot\mathbf{r}_\kappa}\Phi_{\alpha,\alpha',\alpha''\kappa,\kappa',\kappa''},\end{aligned} \tag{2.73}$$

where the factor δ signifies that the conservation of lattice momentum $\mathbf{k}_i+\mathbf{k}_j+\mathbf{k}_k = \mathbf{g}$, where $\mathbf{g}$ is a reciprocal lattice vector. [9] The cubic ($V(\mathbf{k}_i,\mathbf{k}_j,\mathbf{k}_k)$) and quartic ($V(\mathbf{k}_i,\mathbf{k}_j,\mathbf{k}_k,\mathbf{k}_l)$) terms give the energies of "phonon-phonon interactions" because they alter the phonon energies when larger vibrational displacements are present in the crystal.

Although not obvious at first sight, details of the phonon dispersions are crucial for an attempt to calculate anharmonic behavior because of the conservation of energy and momentum. For example, for three phonon process, $\mathbf{k}+\mathbf{k}' = \mathbf{k}'' + \mathbf{g}$ and $\varepsilon+\varepsilon' = \varepsilon''$ must be satisfied simultaneously. Most phonon dispersions are curved and phonon processes that satisfy momentum and energy conservation depend on the symmetry of the dispersion relations, and on the crystal structure.

For larger phonon wavevectors **k**, momentum conservation is possible by adding a reciprocal lattice vector **g**, and the idea is that the momentum transferred to the entire crystal occurs with zero energy because of the large mass of the crystal. Such "umklapp" processes allow many more three-phonon interactions, but the phonon wavevectors must be of length comparable to the reciprocal lattice vector for this to be possible.

It is important to determine how many terms are needed in Eq. 2.72 to account accurately for anharmonic behavior. The higher-order terms become progressively smaller, but the requirement of energy and momentum conservation restricts the allowable three-phonon processes, so fourth-order anharmonicity can be as significant as the third. Also, four-phonon processes can be generated from two three-phonon processes.

For systems where the electron-phonon interaction (EPI) has little role, such as ionic isolators, the anharmonic phonon effects are solely from phonon-phonon interactions. These cause the energies of phonons to be shifted and broadened. Treating all the components as perturbations, the energy shifts can be written as

$$\Delta\omega(\mathbf{q}) = \Delta\omega^{q}(\mathbf{q}) + \Delta\omega^{3}(\mathbf{q}) + \Delta\omega^{4}(\mathbf{q}), \tag{2.74}$$

where the terms on the right-hand side are quasiharmonic, third-, and fourth-order contributions, respectively. On the other hand, the energy broadening is believed to be usually dominated by the third-order contribution. The related theory has been discussed in detail. [4, 15, 23, 30–33]

2.8 Electron-Phonon Interactions

There are large energy differences between the phonon and electron systems in the crystal. As a result, the Hamiltonian of the solid is commonly separated into phonon and electron contributions. The energy of the crystal deformation caused by a phonon originates with the electrons, of course, but although this potential

energy of deformation is electronic in origin, it transfers to kinetic energy in the motion of the nuclei. In a perfectly harmonic system, the electron-phonon interaction affects equally the energies of the electrons and the phonons. If the electrons were always in their ground states, all this energy of deformation would be associated with phonons only. Treating the electron system and the phonon system as two independent thermodynamic systems becomes inconsistent at finite temperature, however, because the presence of phonons alters the thermal excitations of electrons. [4]

Classically, the electron-phonon interaction (EPI) requires the coordinates of the electrons $\{\mathbf{r}_\lambda^{\mathrm{el}}\}$, and the coordinates of the nuclei $\{\mathbf{r}_j^{\mathrm{n}}\}$ [22]

$$H_{\mathrm{ep}} = \sum_{\lambda,j} v\,(\mathbf{r}_\lambda^{\mathrm{el}}, \mathbf{r}_j^{\mathrm{n}}). \tag{2.75}$$

The EPI in the "adiabatic approximation" does not allow the nuclear kinetic energy to alter the electron states. The "non-adiabatic" electron-phonon interaction accounts for how the electronic states are altered by the nuclear kinetic energy, not the potential energy of displaced nuclei, as for the adiabatic case. The non-adiabatic EPI requires no thermal activation, and can be responsible for superconductivity.

In the adiabatic picture, unique electron eigenstates exist for a snapshot of the nuclear thermal displacements, which evolve continuously as the nuclei move. For a given electronic structure, the adiabatic electron-phonon interaction is proportional to the number of phonons, $n(\varepsilon, T) + 1/2$, times the difference of electron occupancy with respect to the ground state, $f(T) - f(0)$, where $f(T)$ is the Fermi-Dirac distribution. When there are sharp features in the electronic DOS near the Fermi level, there will be other temperature dependences associated with the thermal sampling of the excited electron states.

To illustrate how the electron eigenstates change with nuclear displacements, a simple approach is to consider an electronic band formed from isotropic s-electrons, and a uniform dilation, as may be associated with longitudinal phonons

of long wavelength,

$$H_{\mathrm{ep}}^{\mathrm{D}} = -\sum_{\lambda} D\Delta(\mathbf{r}_{\lambda}^{\mathrm{el}}) \tag{2.76}$$

where $\Delta(\mathbf{r}_{\lambda}^{\mathrm{el}})$ is the fractional change in volume at $\mathbf{r}_{\lambda}^{\mathrm{el}}$, and D is a "deformation potential", typically a few eV. This simple approach is convenient because $\Delta(\mathbf{r}_{\lambda}^{\mathrm{el}})$ is related to the displacement $\mathbf{u}$ as through its divergence: $\Delta(\mathbf{r}_{\lambda}^{\mathrm{el}}) = \nabla \cdot \mathbf{u}$, so

$$H_{\mathrm{ep}}^{\mathrm{D}} = -D\sum_{\lambda} \nabla \cdot \mathbf{u}(\mathbf{r}_{\lambda}^{\mathrm{el}}). \tag{2.77}$$

For longitudinal phonons

$$\vec{e}(\mathbf{k}_i) = \frac{\mathbf{k}_i}{k_i}, \tag{2.78}$$

and Eq. 2.76 can be written as

$$\hat{H}_{\mathrm{ep}}^{\mathrm{D}} = -\mathrm{i}D\sum_{\mathbf{r}_{\lambda}^{\mathrm{el}}}\sum_{\mathbf{k}_i}\sqrt{\frac{\hbar}{2N\,m\,\omega_{\mathbf{k}_i}}}\,|\mathbf{k}_i|\,\mathrm{e}^{\mathrm{i}\mathbf{k}_i\cdot\mathbf{r}_{\lambda}^{\mathrm{el}}}\,A_{\mathbf{k}_i}. \tag{2.79}$$

Similar to the second quantization of phonons, fermion field operators for the electron are

$$\Psi^{\dagger}(\mathbf{r}_{\lambda}^{\mathrm{el}}) = \sum_{\mathbf{k}_{\lambda}} C_{\mathbf{k}_{\lambda}}^{\dagger}\,\mathrm{e}^{-\mathrm{i}\mathbf{k}_{\lambda}\cdot\mathbf{r}_{\lambda}^{\mathrm{el}}}, \tag{2.80}$$

which when applied to a multi-electron state, places an electron in the state $\mathbf{k}_{\lambda}$. When small, $\hat{H}_{\mathrm{ep}}^{\mathrm{D}}$ is a perturbation that mixes electronic states and can be evaluated by using the fermion field operators C and $C^{\dagger}$, where the exponential phase factors cancel the k-space integration unless there is a conservation of wavevector. This forces the same total $\mathbf{k}_{\lambda} + \mathbf{k}_i$ for the creation operators as for

the annihilation operators

$$\hat{H}_{\mathrm{ep}}^{\mathrm{D}} = -\mathrm{i}D\sqrt{\frac{\hbar}{2N\,m}}\sum_{\mathbf{k}_\lambda}^{\text{electron}}\sum_{\mathbf{k}_i}^{\text{phonon}}\sqrt{\frac{k_i}{c_L}}A_{\mathbf{k}_i}C^{\dagger}_{\mathbf{k}_\lambda+\mathbf{k}_i}C_{\mathbf{k}_\lambda}, \tag{2.81}$$

plus an analogous term with $A^{\dagger}_{\mathbf{k}_i}C_{\mathbf{k}_\lambda+\mathbf{k}_i}C^{\dagger}_{\mathbf{k}_\lambda}$ for phonon creation. Here we used a linear dispersion relationship $\omega_L = c_L k_i$ for long-wavelength, longitudinal acoustic phonons.

In general, there are two lower-order terms that are used to describe the electron-phonon interaction. The first is a generalization of the previous result for the deformation potential with long-wavelength, longitudinal acoustic phonons

$$\hat{H}_{\mathrm{ep}}^{1} = \sum_{\mathbf{k}_i}\sum_{\mathbf{k}_\lambda} V^{\mathrm{ep}}(\mathbf{k}_i,\mathbf{k}_\lambda)\,A_{\mathbf{k}_i}C^{\dagger}_{\mathbf{k}_\lambda+\mathbf{k}_i}C_{\mathbf{k}_\lambda}, \tag{2.82}$$

which accounts for the processes where an electron is excited from state $\mathbf{k}_\lambda$ to $\mathbf{k}_\lambda + \mathbf{k}_i$, simultaneously with the annihilation of a phonon in state $\mathbf{k}_i$, or creation of a phonon in state $-\mathbf{k}_i$. The second low-order term for electron-phonon coupling ($\hat{H}_{\mathrm{ep}}^{2}$) includes a factor from second-order perturbation theory, $\sum_{\mathbf{k}'}\langle\mathbf{k}|\Omega|\mathbf{k}'\rangle\langle\mathbf{k}'|\Omega|\mathbf{k}\rangle$. There is no change of electron state by this process, nevertheless, the scattering into the virtual states alters the self-energy of the electron.

Calculating the thermodynamic effects of electron-phonon coupling requires averaging over all electron states near the Fermi surface separated by $\mathbf{k}_j$ and differing in energy by a selected $\hbar\omega$. Most work on electron-phonon coupling has focused on superconductivity, where $\hbar\omega$ is rather small, and the electron states are close enough to the Fermi surface that it is reasonable to use ground-state Fermi surface properties. The Éliashberg coupling function $\alpha^2 g(\omega)$, where $g(\omega)$ is the phonon DOS, accounts for all scattering between electron states on the Fermi surface. The "electron-phonon coupling parameter" λ is calculated by weighting by ω^{-1}

$$2\int_0^{\omega_{\max}}\frac{\alpha^2 g(\omega)}{\omega}\mathrm{d}\omega = \lambda, \tag{2.83}$$

which describes the overall strength of the electron-phonon coupling.

Chapter 3

Computational Techniques

3.1 Introduction

While the advances in computational tools and techniques made possible many, things believed impractical only a couple of decades ago, one still has to make many approximations when doing most computational work. For computational solid state physics, it is the task of theoretical studies to decide on the best approximations to reduce the computational difficulties while preserving as much information as possible about the objects of study. Improvements in the power of computers rarely make sudden breakthroughs, so simulations often need breakthroughs in theory.

Computational science on atomic and subatomic scales benefits all disciplines of science, such as chemistry and bio sciences, but it is especially important for physical sciences. In materials science, we are mostly interested in the simulations on the level of the electronic structure and the levels of crystals or molecules. Predicting the properties of known materials, especially under extreme conditions such as high temperatures, high pressure, or high radiation, and designing materials with desired properties under these conditions, are the ultimate goals of computational materials science. We will only briefly review the computational techniques used for phonon studies in this chapter. More detailed discussion can be found in many books. [5, 34–38]

As for all computational problems, there is always a compromise between accuracy and speed or time. It is important to select the right tools for the problem at hand, often depending on the size of the systems.

3.2 First-Principle Methods

3.2.1 Many-Body Problem

All the interatomic forces in solid state materials are intrinsically electromagnetic interactions—the other three fundamental forces are irrelevant at this scale. The

exact Hamiltonian of such as a system can be written precisely as:

$$\mathbf{H} = -\sum_i \frac{\hbar^2}{2m_\mathrm{e}}\nabla_i^2 + \frac{1}{2}\sum_{i\neq j}\frac{e^2}{|\mathbf{r}_i-\mathbf{r}_j|} - \sum_{I,i}\frac{Z_I e^2}{|\mathbf{r}_i-\mathbf{R}_I|} - \sum_I \frac{\hbar^2}{2M_I}\nabla_I^2 + \frac{1}{2}\sum_{I\neq J}\frac{Z_I Z_J e^2}{|\mathbf{R}_I-\mathbf{R}_J|}, \tag{3.1}$$

where the terms on the right-hand side correspond to the kinetic energy of electrons, potential energy between electrons, potential energy between electrons and nuclei, kinetic energy of nuclei, and potential energy between nuclei, respectively. All the potential energies are from Coulumbic interactions. The uppercase and lowercase subscripts label the nuclei and electrons, respectively. M is the nuclear mass, m_e is the electronic mass, Z is the atomic number of nuclei, and R and r donate positions of nuclei and electrons, respectively.

Because electrons have to be considered as quantum particles, the problem comes down to solving the many-body wave functions from the Schrödinger equation. This problem is extremely difficult to tackle directly, even with a system made of only a couple of particles. It is even difficult numerically. The computational cost scales as $O(e^N)$, where N is the size of the system. For any other system of practical size, it is necessary to resort to a few approximations.

3.2.2 Hartree-Fock Method

Using the Born-Oppenheimer approximation as discussed in last chapter, it is possible to solve problems at the electronic structure level by isolating the electronic degrees of freedom and placing the nuclei in fixed configurations. In 1928, Hartree suggested an approximation in which the system is reduced to one-electron model where the interactions from other electrons are treated as a mean field. As a result, the total wave function is just the product of the many one-electron wave functions. This is a good starting point, however, it missed some important effects, such as the Pauli exclusion principle and the exchange and correlation energies from the many-body nature of the system.

Fock improved Hartree's work by approximating the wave functions as linear

combinations of non-interacting one-electron wave functions in the form of a Slater determinant

$$\Psi(\mathbf{r}_i) = \frac{1}{\sqrt{n!}} \begin{vmatrix} \Psi_1(\mathbf{r}_1) & \Psi_2(\mathbf{r}_1) & \dots & \Psi_n(\mathbf{r}_1) \\ \Psi_1(\mathbf{r}_2) & \Psi_2(\mathbf{r}_2) & \dots & \Psi_n(\mathbf{r}_2) \\ \vdots & \vdots & \ddots & \vdots \\ \Psi_1(\mathbf{r}_n) & \Psi_2(\mathbf{r}_n) & \cdots & \Psi_n(\mathbf{r}_n) \end{vmatrix}, \tag{3.2}$$

where n is the number of electrons in the system. It solves the problem of antisymmetry, ensuring that the sign of the total wave function will change when two electrons are switched, and no electrons will share a same state.

Under the Hartree-Fock approximation, the total energy can be written as a sum of kinetic, electron-nuclear, Hartree, and exchange energies

$$E = E_{\mathrm{k}} + E_{\mathrm{e-n}} + E_{\mathrm{H}} + E_{\mathrm{x}}, \tag{3.3}$$

where the Hartree energy E_{H} is determined by the mean-field Hartree treatment and the exchange energy E_{x} corrects for the energy difference as a result of the antisymmetry. Note that we are still missing the correlation energies from the interactions of the spins between electrons, but they can be treated similarly. The computational cost of Hartree-Fock model scales as $O(N^4)$, where N is the size of the system.

3.2.3 Variational Principle and Self-Consistent Field Method

Because electrons are indeed not independent but correlated, their wave functions need to be optimized to obtain exact solutions. One of the basic foundations of the first principle theory is the variational principle, which states that in a quantum system without degeneracy, there is only one ground-state. So by minimizing the total energy with respect to the wave function, it is possible to achieve a unique ground state.

In practice, the wave functions are usually optimized iteratively using a self-consistent field (SCF) method. A random or a typical wave function is used as the starting point. The electron densities are calculated with these wave functions and then used to obtain the total energy. Using these results, it is possible to solve the equations to have a new set of energies and wave functions for each electron. This process is done iteratively until the changes to wave functions are below a certain threshold.

3.3 Density Functional Theory

3.3.1 Hohenberg-Kohn Theorems

It was not until the 1960s when Hohenberg and Kohn showed by their two theorems that it is possible to solve the problem using only the electronic density $\rho(\mathbf{r})$, that first principles calculations on systems larger than a couple of dozen atoms were made possible. This electron density of states is defined as the sum of all occupied orbitals (i)

$$\rho(\mathbf{r}) = \sum_i |\phi_i(\mathbf{r})|^2, \tag{3.4}$$

which is normalized to the total number of electrons, n,

$$\int \rho(\mathbf{r}) \mathrm{d}\mathbf{r} = n. \tag{3.5}$$

The first HK theorem states that the external (electron-nuclear) potential $V_{\mathrm{e-n}}$ is uniquely determined by the ground state electron density $\rho_0(\mathbf{r})$. Because $V_{\mathrm{e-n}}$ determines the Hamiltonian, and thus the ground state and its density $\rho_0(\mathbf{r})$, the conclusion is that there is a one-to-one relationship between the ground-state density $\rho_0(\mathbf{r})$ and the external potential $V_{\mathrm{e-n}}$ for the electrons. As a consequence, the Hamiltonian and every property of the system is determined from $\rho_0(\mathbf{r})$.

The second HK theorem addresses the problem of finding such a ground state. It states that given the external potential $V_{\mathrm{e-n}}$ there exists a uniquely defined

functional for the energy $E[\rho(\mathbf{r})]$. The density that minimizes this functional is the ground-state density and the energy at the minimum is the ground-state energy

$$E[\rho(\mathbf{r})] = F[\rho(\mathbf{r})] + E_{\text{ext}}[\rho(\mathbf{r})] \geq E_{\text{gs}}. \tag{3.6}$$

This is also the variational principle. It is still, however, necessary to know the functional $F[\rho(\mathbf{r})]$. This difficulty was overcome by Kohn and Sham.

3.3.2 Kohn-Sham Theory

To solve the problem mentioned above, Kohn and Sham introduced the exchange-correlation energy E_{XC}, defined as the difference in energy between the independent electron system and the true system. As a result, the functional can be written as:

$$F = T + E_{\text{HF}} + E_{\text{XC}}, \tag{3.7}$$

where T and E_{HF} are kinetic and Hartree-Fock Coulomb interaction energies, respectively.

This exchange-correlation energy E_{XC} contains all the difficult parts about the interactions between electrons in the real system, and its exact form is unknown. Nevertheless, several approximations for exchange and correlation functionals have been developed, and among them are the local density approximation (LDA) and several generalized gradient approximations (GGA). Using these approximations, it is possible to obtain the variational minimization as an eigenvalue problem using the Rayleigh-Ritz method.

The single-particle Kohn-Sham (KS) Hamiltonian can be written as

$$\mathbf{H} = \mathbf{T}_{\text{ni}} + \mathbf{V}_{\text{HF}} + \mathbf{V}_{\text{XC}} + \mathbf{V}_{\text{ext}}, \tag{3.8}$$

in which ni means “non-interacting”. For an N-particle system, the problem is solved as a one-particle system in its N lowest eigenstates, also called Kohn-Sham orbitals. These N equations of the eigenvalue problem are the celebrated

Kohn-Sham equations and can be solved by expanding the single electron wave functions in a basis, and diagonalizing the related KS Hamiltonian matrix. This needs to be done iteratively using a self-consistency method, similar to the one discussed in last section. Alternatively, the problem can also be solved using a variational approach by minimizing with, for example, a conjugate gradient method, thanks to the orthonormalization of the Kohn-Sham orbitals. [39]

3.3.3 Exchange and Correlation

In detail, the exchange-correlation energy can be written as the sum of the exchange energy, interacting kinetic energy, and the interacting correlation energy

$$E_{\mathrm{XC}} = E_{\mathrm{X}} + T_{\mathrm{int}} + E_{\mathrm{int,C}} = E_{\mathrm{X}} + E_{\mathrm{C}}, \tag{3.9}$$

where the later two add up to the correlation energy E_{C}, which accounts for the correlating part of the kinetic and electron-electron interaction terms. E_{X} comes from the electrons with the same spin, while E_{C} comes form the electrons with a different spin. Both are Coulumbic in origin.

It is informative to check the relative magnitude of the these energies in a real system to understand their contributions. For a helium atom, whose exact solution is available, E_{ext}, T_{ni}, E_{H}, and E_{XC} account for about 53%, 23%, 16%, and 8% of the total energy, respectively. [34] The contribution from exchange-correlation energy may seem small, but it is actively involved in the chemical changes in the system and a accurate description of it is crucial to the success of density functional theory (DFT). Further details on DFT theory can be found in many books. [40–42]

The first question when performing a density functional calculation is probably the choice of exchange and correlation functionals. One of the first and still widely used approximations is the so-called local density approximation (LDA). The LDA's exchange and correlation energy is a function only of the homogeneous electron density. The exchange and correlation energy of a non-uniform system

is simply a sum over small finite volumes in which the electronic density is approximately constant. As a result, the functional depends only on the local information on the electronic density of states, and it works well for systems with small or smooth variations of the electronic density over distance (read: covalent materials and simple metals). LDA usually overestimates the exchange energy, while underestimating the correlation energy. The calculated lattice parameters are generally smaller and the approximation does not work well for strongly correlated systems, transition metals, van der Waals interactions, and hydrogen bonds. LDA can be extended to include spin-polarized calculations, called the local spin-polarized density approximation (LSDA).

Most of the other approximations fall into the category of generalized gradient approximations (GGA), which work better for systems with stronger gradients in electronic density of states because, as its name suggests, it not only takes into account the local electron density but also its gradient (and maybe higher-order terms). Unlike LDA, there is no one general form for the exchange-correlation function, but some forms are well accepted, including PW91 and PBE. Some hybrid functionals, such as B3LYP, include either a higher-order density gradient or a certain amount of nonlocal HF exchange energy. They seem to work better for systems with large oscillations of electron density and long-range interactions, but not without an increase in computational cost. GGA usually overestimates the lattice parameters, although it generally yields better results than LDA. While better, GGA still may not work well with strongly correlated systems, and a $+U$ method was proposed to compensate for the localized electron states by adding a repulsive energy term U. It should be noted that both LDA and GGA tend to severely underestimate the band gap because of the noninteracting nature and the partial removal of self-interaction in DFT. Some remedies include: using hybrid functionals mentioned above, using Green function techniques (e.g., GW approximation), and using some self-interaction correction methods.

3.3.4 Choice of Basis Sets and Pseudopotentials

To solve the Kohn-Sham equations numerically, it is necessary to select a basis set to decompose the wave functions. In practice, a finite set must be used, so the basis must be truncated somehow. The best choice of basis sets demands that a minimal number of basis vectors should be used (fast convergence), and projections can be calculated efficiently while the representation is as accurate as possible. The choice is always a compromise between speed and accuracy.

One common approach is using a plane wave basis set, such as the ones in Bloch's theorem. The problem is solved on the k-grid mesh in the irreducible Brillouin zone, which helps to cut down the number of points. For larger systems, the irreducible Brillouin zones are smaller, and a couple of k-points may give a very good description. In some massive calculations, calculations only at the center of the Brillouin zone (Γ point) may even be sufficient.

A cutoff energy must also be selected to limit the number of reciprocal lattice vectors in the series. This seems straightforward, but one has to realize that the electron wave functions oscillate wildly near the nuclei, so the required cutoff energy can be quite large. However, because the wave functions near the nuclei are mostly irrelevant to the bonding, it is possible to modify the external potential so that the wave functions only vary smoothly inside some core radius. These modified potentials are called pseudopotentials. When well executed, this approach can achieve very good accuracy with a much smaller cutoff energy and, as a result, a much smaller matrix to diagonalize.

There are three common types of pseudopotentials. In a norm-conserving pseudopotential, the electron charge within the core part is equal to that of the actual atom. Ultrasoft pseudopotentials do not conserve the charge but instead reduce the peak height of the potentials to reduce the number of plane waves needed to represent the wave functions. It is also possible to keep the core part of the wave functions as a frozen atomic configuration, and these potentials are called projector-augmented wave (PAW) potentials.

The so-called augmented plane wave method (APW) is a step further. The wave functions take a hybrid form with the core part using a basis of atomic orbitals and the valence part using standard plane waves basis. While more complicated, the APW method can describe the wave functions in the core part better. It is also an all-electron method, so information about the core electrons is accessible.

3.3.5 More on DFT

The success of DFT is partially attributable to its computational cost of $O(N) \sim O(N^3)$, where N is the size of the system. Although the low $O(N)$ cost is only possible for systems without much long range interaction, such as wide-gap insulators, it is a remarkable achievement considering the complexity of a n-electron interacting system. It is possible to extend the DFT calculations to study the excited-states, using Green's function or time-dependent DFT (TDDFT). [43]

The success of DFT is also attributable to its ability to reliably calculate the electronic energy from a set configuration of the atoms, no matter if they are at equilibrium positions or not. This makes it possible to minimize the energy and solve the ground state with good accuracy. Frozen phonon calculations, in which atoms are displaced in certain phonon modes, can provide details about the anharmonicity of the phonons. Using supercell displacement or density functional perturbation theory (DFPT) methods, it is possible to calculate the phonon DOS and dispersion relations using lattice dynamics analysis as discussed in last chapter.

Unlike insulators or semiconductors, whose charge densities have a smooth decaying edge at the gap, metals have sharp edges of charge densities at their Fermi levels at 0 K. These edges create problems for the plane wave expansion, and usually a smearing near the Fermi surface is necessary. A few smearing schemes are commonly used: Gaussian smearing, Fermi smearing, and Methfessel-Paxton smearing. The smearing may seem like an analog to electronic excitations at a finite temperature, but it is introduced for computational reasons instead of

physical reasons. The amount of smearing needs to be selected carefully to reduce the computational cost while retaining a reasonable accuracy. Sometimes, the results are obtained by extrapolating to the zero smearing limit.

DFT may look like a "do-everything" tool, but one still needs to understand its limitations to avoid possible mistakes. A large number of both theoretical and numerical approximations are used in any DFT calculations, and it is important to understand that all the results are based on those approximations. It is also easy to make mistakes when executing the method. One of the common mistakes is the failure to perform a careful convergence test on the parameters used in the calculation. Care must be taken and it is almost always the case that the convergence tests cost as much computational time, if not more than, the production runs.

3.4 Molecular Dynamics (MD)

Contrary to what its name may suggest, the molecular dynamics method uses classical mechanics (including a classical approach for quantum mechanics) to simulate atomic movements and predict both static and dynamic properties of not only molecules but also solid materials. Because the motions of atoms at an atomic scale are still well within the classical mechanics limit, there is no problem using Newton's equations to describe the trajectories of atoms. Even in the case of first-principle MD, in which the inter-atomic forces are calculated by quantum mechanical approaches, the motions of the nuclei can still be safely considered as classical.

3.4.1 Principles

As the Born-Oppenheimer approximation suggests, the electrons' response to the motions of nuclei is so fast that their rearrangement can be considered as instantaneous. Newton's equations of the system have nothing to do with the

electrons. It should be noted that, in a Newtonion view of the world, everything is deterministic: with the exact knowledge of the positions and velocities of the atoms inside the system plus the exact interatomic forces, the future and past trajectories can be calculated precisely. This is not true, however, in the real quantum world, where the time-reversal symmetry is broken.

In the molecular dynamics method, the classical equations of motion are solved as according to the time evolution:

(1) Assume the initial positions and velocities of every atom in the system are known, using the interatomic potentials, the forces on each atom can be calculated;

(2) Under these forces, the positions and velocities of the atoms are updated toward a time step (Δt);

(3) Repeat the steps above.

It is immediately obvious there are many problems regarding the choices of initial conditions, approximations of using finite time steps, adding up of truncation and round-up errors. We will discuss them briefly in the following sections. More detailed explanation can be found in many textbook and review articles. [44–52]

What can we learn from molecular dynamics? The most important information obtained directly are the positions and the velocities (which can be calculated from the former) of all the atoms in the system. All the other raw data, such as energies and forces, may be saved during the calculation, but they are easily calculated from the positions.

In principle, the trajectories contain all the information about the phonons in the system (within the sampling and numerical resolution). Thermodynamic properties that can be calculated directly or by analysis are basic energy, structure, mechanical properties, thermal expansion, phase diagram, defect, grain, thermal conductivity, radial distribution functions, diffusion, and many others. With enough resolution, phonon DOS and phonon dispersions can be calculated with MD, too.

3.4.2 Potentials

Molecular dynamics simulations can be only as good as the potentials used. Interatomic potentials can be attractive or repulsive. Molecular dynamics are commonly classified according to the potentials used or, more generally, how the interatomic forces are calculated. Classical MD uses simple pair or multiple-particle potentials in analytical forms. First-principles MD, on the other hand, uses DFT methods to obtain the interatomic forces. [44]

First-principles MD include two common categories: Born-Oppenheimer MD (BOMD) or Car-Parrinello MD (CPMD). BOMD uses the same minimization method with standard DFT calculations. For every MD time step, the electronic states are relaxed to the ground states and the interatomic forces are calculated from there. CPMD couples the electronic degrees of freedom into the classical coordinate system and a set of coefficients of the plane wave basis set is treated classically as an additional set of coordinates. To do this, these orbitals are assigned a fictitious mass. The main benefit of a CPMD approach is the reduction in computational expense but at a cost that electronic states are not relaxed to ground states. This approach may work well for some systems, in which interatomic forces can be estimated with approximate electronic structure, such as insulators and semiconductors, but less so for other systems such as metals. The convergence of CPMD is also poorer compared to BOMD, so a smaller time step is often required, and this partially undermines the cost benefit.

The first way to generate classical potentials is by fitting certain functions to the structural and/or thermodynamical properties of the system, such as lattice parameters, bulk modulus, elastic modulus, thermal expansion, and vibrational spectrum, among many others. Classical potentials can also be calculated from first principles methods, and there are some good codes to do that. One thing that needs to be noticed about these potentials is their transferability: how well the potentials can be used for other systems or systems under other conditions. Classical potentials tend not to be easily transferable, and it is necessary to find

or generate the right potentials for the systems of interest.

Consider a system of N particles. The potential energy can be expanded into two-particle, three-particle, ..., and n-particle terms:

$$U(\mathbf{r}_1, \mathbf{r}_2, \ldots \mathbf{r}_n) = \sum_{i<j}^{N} U(\mathbf{r}_i, \mathbf{r}_j) + \sum_{i<j<k}^{N} U(\mathbf{r}_i, \mathbf{r}_j, \mathbf{r}_k) + \ldots. \tag{3.10}$$

In systems where near-range interactions dominate, it is possible to ignore all higher-order potentials and only consider pair potential $U(\mathbf{r}_i, \mathbf{r}_j)$.

Tens of pair potentials are well known, and many of them are widely used. As a typical example, the Lennard-Jones (LJ) potential is:

$$U_{\mathrm{LJ}}(r) = 4\varepsilon \left[\left(\frac{\sigma}{r}\right)^{12} - \left(\frac{\sigma}{r}\right)^{6} \right], \tag{3.11}$$

where r is the interatomic distance and ε and σ are parameters. LJ potentials are commonly used for free noble gas atoms. For solid state materials, the Buckingham potential is often used. It is

$$U_{\mathrm{Buck}}(r) = A \exp(-Br) - \frac{C}{r^6}, \tag{3.12}$$

where r is the interatomic distance and A, B, and C are parameters. These two potential models are isotropic, and the energy only depends on interatomic distance. In general, however, potentials can be directional. When describing some covalent solids, such as diamond, the highly directional bonds require a directional potential model, such as Tersoff potential.

In systems such as metals and their alloys, where electrons are delocalized and long-range interactions are more important, pair potentials usually cannot give a good description of the system. Other classical potentials using the mean-field concept, such as the embedded atom method (EAM), work better.

The field of classical interatomic potentials is still making active progress. Many new ideas are being developed.

3.4.3 Solving Equations of Motion

As we mentioned earlier in this chapter, solving the Newton's equation of motions involves the finite-difference method in time step (Δt). Assuming we have a complete knowledge of the system at time t, the position at time $t + \Delta t$ can be calculated from the Taylor expansion as

$$\mathbf{r}(t + \Delta t) = \mathbf{r}(t) + \mathbf{v}(t)\Delta t + \frac{1}{2!}\mathbf{a}(t)\Delta t^2 + \frac{1}{3!}\frac{\mathrm{d}^3\mathbf{r}(t)}{\mathrm{d}t^3}\Delta t^3 + \ldots. \tag{3.13}$$

Note that everything up to the second order on the right-hand side is either known, or can be calculated directly. This may seem enough but it turns out that it is not, and the system is unstable. Fortunately, it is possible to achieve resolution on the order of $O(\Delta t^4)$ using some simple algorithms, and more importantly, achieve good stability.

We will not go in to details about the problem of stability, as it has been well described elsewhere. The basic idea, however, is quite simple. In a stable system, these equations capture the trajectories of the atoms "well enough" (although with errors) when compared to a real system (or a system simulated with much better resolution and finer time step). On the contrary, a system is unstable when a change in these parameters lead to a catastrophic different in the trajectories after only a few time steps.

The first trick is called the Verlet algorithm. Writing Eq. 3.13 for a step forward and backward

$$\mathbf{r}(t + \Delta t) = \mathbf{r}(t) + \mathbf{v}(t)\Delta t + \frac{1}{2!}\mathbf{a}(t)\Delta t^2 + \frac{1}{3!}\frac{\mathrm{d}^3\mathbf{r}(t)}{\mathrm{d}t^3}\Delta t^3, \tag{3.14}$$

$$\mathbf{r}(t - \Delta t) = \mathbf{r}(t) - \mathbf{v}(t)\Delta t + \frac{1}{2!}\mathbf{a}(t)\Delta t^2 - \frac{1}{3!}\frac{\mathrm{d}^3\mathbf{r}(t)}{\mathrm{d}t^3}\Delta t^3, \tag{3.15}$$

and adding them up

$$\mathbf{r}(t + \Delta t) = 2\mathbf{r}(t) - \mathbf{r}(t - \Delta t) + \mathbf{a}(t)\Delta t^2. \tag{3.16}$$

We have eliminated the first-order (velocity) and third-order terms. Other slightly more complex algorithms, such as velocity-verlet and predictor-corrector algorithms are more frequently used because of their increased accuracy, stability, and energy conservation.

Directly solving these equations of motion requires a computation time scale of $O(N^2)$. To achieve the desired performance of $O(N)$, the number of interacting neighbors must be limited. This is commonly implemented by choosing a cutoff radius r_{cut}, beyond which the interatomic forces are ignored. (Note that this approach does not work for systems with long-range Coulumbic interactions.) During the calculation, a list of neighbors is often maintained for each atom. By doing so, the calculation of interatomic forces is only necessary when the changes in the interatomic distances are larger than a preset tolerance.

To simulate the bulk properties of materials, it is also necessary to use periodic boundary conditions with the supercell. The same principle also applies to simulations of surfaces and thin films.

Last but not the least, the size of time steps has to be determined. A time step that is too small unnecessarily wastes computational time without improving the resolution, while a time-step that is too large will render a system unstable. The choice of time steps is also sensitive to the system and its environment, such as temperature and pressure. There has been much theoretical work on the balance of the time step sizes, but "trial-and-error" is still the most trouble-free method. Convergence testing with different time-step sizes is necessary to determine the ideal choice. The actual resolution of the simulations is determined mostly by the size of the system and the number of time steps, although the size of time steps is also relevant.

3.4.4 Initial Conditions

The initial positions of the atoms are usually taken from a cryptography database or a DFT calculation. The initial velocities are often set randomly using a Maxwell-

Boltzmann distribution at the temperature of the set point, while keeping the total translational momentum as zero.

Sometimes, the experimental lattice parameters are not well reproduced by the potentials used by the MD simulations. In those cases, the MD can go unstable if it starts with these initial conditions, so it is preferable to do an optimization first using either a steepest-descent or some conjugate-gradient methods. Unlike MD, the optimization is performed in a static "frozen" state, and the excessive kinetic energies are "damped" to help the system relax to its lowest energy state, using a method such as simulated annealing. This is by no means as simple a task as it may sound, but fortunately the starting point (experimental lattice structure and lattice parameters) is usually very close to this lowest energy state, and the optimization can be straightforward (at least when the potentials are of good quality).

3.4.5 Ensembles and Thermostats

In statistical physics and thermodynamics, an ensemble is an idealization consisting of a large (or infinite) number of copies of a system, considered all at once, each of which represents a possible state that the real system might be in. [13] A MD simulation creates a large number of such copies and thus an ensemble.

Defined with different fixed variables, there are a number of different types of ensembles. Some of the most commonly used ones are microcanonical (NVE) ensemble, canonical (NVT) ensemble, and grand canonical (VTμ) ensemble. The first two are commonly used for molecular dynamics, and NVE ensemble is the simplest to implement. The NVT ensemble is probably the ideal ensemble because it reproduces the system in a more realistic way, but it is also more complex because the energy of the system has to be modulated by a thermostat. The use of isothermal-isobaric (NPT) ensembles is on the rise, thanks to the variable cell method which is implemented in more and more first-principles codes.

A few thermostats are commonly used for MD in a NVT ensemble and a

thermostat also helps to correct for energy drifting from the accumulation of numerical errors. The difficulty is how to maintain the correct ensemble while doing energy exchange. Simple velocity scaling is the most intuitive way, but it breaks the ensemble. A Berendsen thermostat, which weakly couples the system with a heat bath, is a better choice, but it still disturb the ensemble. The Andersen thermostat uses a stochastic approach to couple the particle in the system to a heat beat. While it reproduces the canonical ensemble, it is believed that the dynamic quantities, such as diffusion properties, are disturbed and not usable.

The current state-of-the-art technique for temperature control is the Nosé-Hoover thermostat. In this method, a fictitious mass Q and its related degree of freedom is added to the system to simulate the coupling with the heat bath by scaling the timescale and adding a potential term. It can be proved that this thermostat will reproduce a canonical ensemble in the real system, but the choice of Q is essential. Small Q will cause high-frequency oscillations and large Q makes the system approach a microcanonical ensemble.

Sometimes it is beneficial to use multiple thermostats. It may first be advantageous to use a thermostat that achieves the equilibrium faster, and then switch back to the thermostat with the correct ensemble for the production run.

3.4.6 Data Analysis

As we mentioned earlier, all the information that a molecular dynamics simulation gives is contained in the trajectories of the particles. A fair number of time steps need to be discarded before the system is in an equilibrium state and all the information from the initial condition is lost by that point, due to the numerical errors.

To determine when the system reaches equilibrium, it is often useful to look at the changes of total energy (potential plus kinetic) versus time. For a system in an NVE ensemble, it is often necessary to achieve an energy fluctuation less than 0.1%. For a system in an NVT ensemble, it is common to have a temperature fluctuation

of a large amplitude, but one must ensure that the frequency of fluctuation agrees well with the one predicted by the size and components of the system. A velocity distribution function is also helpful to determine if the system is in equilibrium (the distribution should be close to the Maxwell-Boltzmann distribution at the corresponding temperature).

While the phase of the system can be found from the instantaneous positions of the atoms in an equilibrium state, one has to remember that the atoms are vibrating around their equilibrium positions, so to get accurate lattice parameters, time averages of the positions must be calculated. Some thermodynamic properties of the system can be obtained by taking derivatives of the results from a set of different environments. For example, the bulk modulus can be obtained by running an NVE MD under a few different volumes, and comparing the calculated pressures. The same method also applies to the thermal expansion coefficient.

A radial distribution function (RDF), calculated by binning the distances between atom-atom pairs, gives useful information about the distribution of atoms around each other. A RDF is particularly useful for amorphous or other disordered materials. Pair distribution functions (PDF) measured from X-ray scattering can be converted to RDFs, and directly compared to the ones from molecular dynamics, sometimes with very good agreement. The mean square displacement (MSD) over time t tells how far atoms travel from their original positions. It is useful to check for solid-liquid phase changes because in liquid systems, the MSD tends to increase linearly with time.

We are mostly interested in obtaining phonon dynamics information from these trajectories. In principle, with a system of sufficient size, small enough time step, and long enough run-time, it is possible to reproduce all the phonon properties to good resolution within the limit of the interatomic potentials. To calculate the vibrational spectrum from the trajectories, we need to define a velocity autocorrelation function (VAF) first:

$$C(t) = \frac{\langle \mathbf{v}(0) \cdot \mathbf{v}(t) \rangle}{\langle \mathbf{v}(0) \cdot \mathbf{v}(0) \rangle}, \tag{3.17}$$

where $\mathbf{v}(t)$ is the velocity of atoms and $\langle\rangle$ denotes the average over all atoms, and is normalized to the velocities at $t = 0$. Partial VAFs for certain atoms (for example, one species in a multi-element compound), or velocities at certain symmetry directions can also be defined accordingly.

The VAF gives the information on the dynamics of an "average" atom. It always starts at unity and usually decays to zero in the long-time limit because eventually all the information about the initial state is lost and so is the "correlation".

In a solid material, the VAF contains all information on the vibrational spectrum. [53] The square of the Fourier transform of a VAF yields the phonon density of states

$$g(\omega) = \frac{1}{2\pi}\left(\int_{-\infty}^{\infty} C(t)\exp(i\omega t)\mathrm{d}t\right)^2. \tag{3.18}$$

Because of the discrete nature of the MD simulations, it is convenient to calculate discrete VAFs

$$C_m = \frac{\langle \mathbf{v}_m \cdot \mathbf{v}_0 \rangle}{\langle \mathbf{v}_0 \cdot \mathbf{v}_0 \rangle}, \tag{3.19}$$

and use a fast Fourier transform to obtain the phonon DOS. One problem remains: the VAF often goes to zero eventually and as a result, when using Eq. 3.17, late time steps in longer MD simulations will not contribute to the statistical quality of the result because the VAF has decayed to zero there. One way to solve this problem is breaking up long MD runs into shorter ones, and using an averaged VAF. A smarter way to do it is using an average of all possible VAFs that can be constructed from the trajectories [53]

$$C_m = \frac{1}{M-m}\sum_{n=0}^{M-m-1}\frac{\langle \mathbf{v}_{n+m} \cdot \mathbf{v}_n \rangle}{\langle \mathbf{v}_0 \cdot \mathbf{v}_0 \rangle}. \tag{3.20}$$

For a MD simulation with m steps, there are $m-1$ different VAFs with different ranges. The smaller t parts always have better statistical quality and they happen to be the parts that contain the most information. It is important to have the correct weighting factor here.

The resolution of the phonon DOS is mostly determined by the size and the

number of time steps, but the sizes of the system also matters. There are some rules on the choice of the size and the number of time steps for achieving a desired resolution. Using a partial VAF, partial phonon DOS functions for specific atoms and phonon dispersion relations can also be calculated similarly. Although the vibrational information at the Γ point is always missing because it corresponds to the correlations with atoms at infinite distances, it is possible to approximate it with a q point that is close enough to the center of the Brillouin zone.

In practice, any direct Fourier transform of the VAF gives noisy results. It is best to append the VAF with a trailing series of zeros several times larger in size. Because a steep step function causes oscillations after Fourier transformation, it is also necessary to smooth the interface between the VAF and the zeros in case the VAF does not drop very close to zero there (as is usually the case).

An integration of the VAF over time gives the diffusion coefficient D

$$D = \frac{1}{3}\int_0^\infty \langle \mathbf{v}(0) \cdot \mathbf{v}(t) \rangle \mathrm{d}t, \tag{3.21}$$

which is related to the MSD.

3.4.7 More on MD

Molecular dynamics, especially when performed using first-principles DFT methods, is very capable of reproducing the vibrational properties of materials. It can account for many of the effects that will be neglected when using other methods. For a example, anharmonic effects in crystal lattices have contributions from intrinsic and extrinsic terms. The first one comes from the shapes of the interatomic potentials and the second one comes from the thermally induced lattice distortion. While frozen phonon calculations using the DFT method can address the first one correctly, they totally miss the extrinsic contribution.

With that said, one must always be cautious when using classical MD. As we mentioned before, these potentials are fitted to the properties of materials.

Sometimes they are directly generated from the vibrational properties, such as a measured phonon dispersion. So it is not surprising if it happens to give ideal results for some of the properties while it completely fails for others. It cannot be emphasized more that any calculation, molecular dynamics or lattice dynamics, is only as good as the potentials it uses, at best.

It is possible to use molecular dynamics to simulate systems in nonequilibrium states, such as for thermal transport and radiation damage, but these simulations usually require larger system sizes, and so in most cases only classical MD is practical.

3.5 Packages

There are a good number of open-source and commercial packages for performing computational simulations. The choice of package sometimes depends on the available functionality that is necessary for the work, but most of the time it is a personal preference. Here is an incomplete list of the packages that may be most widely used for solid state studies, although some other packages that orient toward chemistry and bio sciences may also work for solid state materials.

3.5.1 DFT Codes

Vienna Ab initio Simulation Package (VASP), [54, 55] commercial

DFT, HF, hybrid, Green's function methods, BOMD

It has a reliable set of potentials (density functionals).

Quantum Espresso, [56] open source

DFT, HF, DFPT, Wannier, CPMD, BOMD, phonon DOS/dispersion

It has a fast k-point parallelization and broad selection of potentials (density functionals).

ABINIT, [57] open source

DFT, DFPT, TDDFT, BOMD

WIEN2k, [58] commercial

DFT

It is an all-electron (L)APW+lo code.

3.5.2 Classical Lattice Dynamics Codes

General Utility Lattice Program (GULP), [59] open source

Lattice dynamics, MD

Gulp has a broad selection of pair and multi-particle potential functions.

Large-scale Atomic/Molecular Massively Parallel Simulator (LAMMPS), [60]

open source

MD

It handles large systems well and also has a lot of potential functions.

3.5.3 Phonon Lattice Dynamics Codes

Many DFT codes do not have the capacity of performing phonon lattice dynamics calculation to obtain phonon DOS and dispersion relations. Some external codes can perform phonon calculations by supercell or DFPT methods using one of the DFT codes to calculated the interatomic forces.

PHONON, [61] commercial

It works with VASP, WIEN2k, and many other DFT codes.

Phonopy, [62] open source

It is python based and works with VASP (super lattice and DFPT modes), WIEN2k.

PHON, [63] open source

It works with VASP.

Part III

Scattering Experiment

There are a wide range of different types of scattering techniques, among which the most used are IR and Raman spectroscopy, x-ray diffraction, inelastic x-ray scattering, nuclear resonant inelastic scattering, neutron diffraction, and inelastic neutron scattering. There are similarities and differences between the techniques. Most of the diffraction techniques are primarily used for studying static structures, although it is possible to extend them into the dynamics domain by the so-called "total scattering". Phonon dynamics studies generally need inelastic scattering techniques.

Thermal neutrons have wavelengths close to the lattice parameters of crystals, and thus their wave vectors have about the same size as the width of the Brillouin zone. Their energy scale also corresponds well to phonon energies in many materials.

In infrared and Raman spectroscopy, photons also match excitation energies in molecules or crystals but, due to their small wave vector, they can only sample vibration modes very close to the Γ point at the center of the Brillouin zone. Besides, the modes accessible by IR and Raman spectroscopy are limited by respective selection rules, which sometimes are complementary between the two techniques.

In nuclear resonant inelastic scattering and conventional X-ray photon inelastic x-ray scattering, the photons have much higher energies and wave vector, and thus are able to probe the whole Brillouin zone, making the measurements of phonon dispersions and densities of states possible.

In this part of the thesis, the experimental techniques and data reduction processes on neutron scattering and Raman scattering are discussed.

Chapter 4

Neutron Scattering

4.1 Introduction

The neutron is a hadron and an essential part of the nuclei of all atoms except hydrogen. Neutrons help to bind protons together with strong force, and as a result, neutrons and protons are called nucleons. Together, they make up the majority of the mass in the universe we can see. The neutron has a unique combination of properties, as listed in Table 4.1.

Table 4.1: Properties of the neutrons [64]

Property	Value
Mass	$1.674927351(74) \times 10^{-27}$ kg
Electric charge	0
Spin	$-\hbar/2$
Magnetic moment	$9.6623647(23) \times 10^{-27}$ J/T
Lifetime	881.5 ± 1.5 s
Composition	udd

The mass of neutrons make their energies and momenta match those of phonons and magnons in crystals, and their Broglie wavelength close to interatomic distances in solids. Charge neutrality gives neutrons great penetrating power and makes them interact directly with nuclei, thus the lattices, via strong force. In addition, the spin and magnetic moment of neutrons makes them useful for studying magnetic behavior of the matter by magnetic scattering. All these make free neutrons a valuable probe for structural and dynamical studies of condensed matter.

For their pioneering work in neutron scattering, Brockhouse and Shull shared the 1994 Nobel Prize in physics for their contributions to neutron spectroscopy and neutron diffraction, respectively. Nowadays, neutron scattering techniques are flourishing and provide indispensable tools for research topics ranging from biology and medicine to renewable energy and electronics. Neutron scattering is still one of the best experimental techniques to study dynamics, such as phonon and magnons in condensed matter.

For scattering research, free neutrons are usually generated by nuclear fission in reactors or by spallation processes, in which high-energy protons bombard a heavy metal target. Fission provides a constant flow of neutrons, while the spallation produces high-intensity, albeit short, neutron pulses. The neutrons are then thermalized by a moderator, which can be water, heavy water (D_2O), or liquid hydrogen depending on the desired range of neutron energy. A neutron guide and maybe some neutron optics then direct the neutrons to the samples in each individual instrument, where the actual scattering takes place.

The neutron scattering may involve both magnetic and nuclear (strong) interactions. For phonon studies in this thesis, only the latter will be considered. Nuclear scattering can be "elastic" or "inelastic". Diffraction studies of the structure usually use only the "elastic" part of the scattering, in principle similar to x-ray diffraction. If there is a change in energy after the scattering, the process is "inelastic". Furthermore, the scattering can be classified as "coherent" or "incoherent", depending on whether the scattering preserves the relative phase of the wavelets scattered from different locations. In the end, scattering will fall into one of the four types: "coherent elastic", "coherent inelastic", "incoherent elastic", or "incoherent inelastic". More detailed explanation of the concepts can be found in the book by Fultz [16].

General experimental setups for inelastic neutron scattering can be illustrated as shown in Fig. 4.1. Incident neutrons with energy E_i and momentum $\mathbf{Q}_\mathrm{i}$ will be scattered by the sample, and the final energies E_f and momenta $\mathbf{Q}_\mathrm{f}$ of the neutrons are picked up by detectors. With the knowledge of the energies and momenta before and after the scattering, the energy transfer and momentum transfer can be calculated: $\Delta E = E_\mathrm{f} - E_\mathrm{i}$ and $\Delta\mathbf{Q} = \mathbf{Q}_\mathrm{f} - \mathbf{Q}_\mathrm{i}$. As a side note, the energy and momentum of neutrons are related by the relation: $E = \hbar^2\mathbf{Q}^2/2m$, in which m is the mass of the neutron. This leads to the kinematic limits of scattering. Usually the incident energy and direction are known, to figure out the energy and momentum transfer, all one needs to measure are the scattering angle (θ) and energy. There are many approaches to making these measurements but

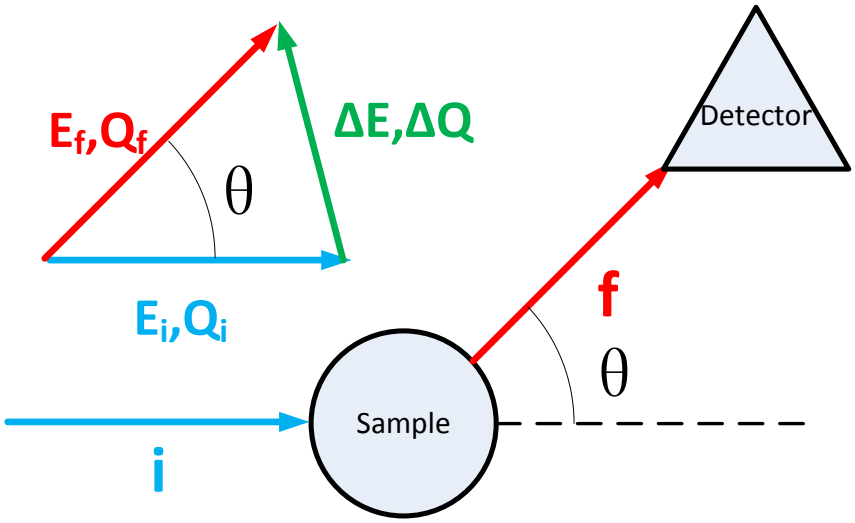

Figure 4.1: The geometry of inelastic neutron scattering. Blue: incident beam; Red: scattered beam; Green: energy and momentum transfer

the most common are those of time-of-flight and triple-axis spectrometers.

4.2 Scattering Theory

4.2.1 Scattering Cross Section

Detailed accounts of the theory and experiments of neutron scattering can be found in the books by Squires [65], Lovesey [66], and Fultz [16]. Here is a brief summary. The cross section is the key concept of any scattering experiment. For neutrons and photons, which are quantized particles, scattering happens with certain probabilities. The cross section (σ) essentially defines the "area" "seen" by the particles at each scattering center. Knowing the cross section and density of these scatterers, one can calculate the scattering probability of the particles passing through the sample of a certain size. This overall probability does not depend on the structure of the sample, which will only redistribute the intensity of the scattering through interference.

The total, coherent, and incoherent scattering cross section and absorption

cross section of all the elements, including their isotopes, are found in publications or databases, such as the one at the NIST Center for Neutron Research (NCNR) [67]. These data are handy information for planning experiments, especially for determining appropriate quantities of samples.

To describe anisotropic scattering, the differential scattering cross section ($d\sigma/d\Omega$) is defined as the piece of the area ($d\sigma$) for scattering the particles into a particular increments in solid angle ($d\Omega$), as shown in Fig. 4.2,

$$\frac{d\sigma}{d\Omega} = \frac{\begin{array}{c}\text{number of neutrons scatterred per second into} \\ \text{a small solid angle d}\Omega \text{ in specific direction}\end{array}}{\Phi d\Omega}, \tag{4.1}$$

in which Φ is the neutron flux. When integrated over all solid angles, the differential cross section adds up to the total cross section,

$$\sigma = \int_{4\pi} \frac{d\sigma}{d\Omega} d\Omega. \tag{4.2}$$

The differential scattering cross section can be further defined with respect to final energy if needed.

4.2.2 Fermi's Golden Rule

In a scattering process, the state of the neutron changes from $\mathbf{Q}_\mathrm{i}$ to $\mathbf{Q}_\mathrm{f}$, and the state of the sample changes from λ_i to λ_f. The differential scattering cross section can be written as

$$\left(\frac{d\sigma}{d\Omega}\right)_{\lambda_\mathrm{i}\to\lambda_\mathrm{f}} = \frac{1}{\Phi d\Omega} \sum_{\mathbf{Q}_\mathrm{f} \text{ in } \mathrm{d}\Omega} W_{\mathbf{Q}_\mathrm{i},\lambda_\mathrm{i}\to\mathbf{Q}_\mathrm{f},\lambda_\mathrm{f}} \tag{4.3}$$

in which $W_{\mathbf{Q}_\mathrm{i},\lambda_\mathrm{i}\to\mathbf{Q}_\mathrm{f},\lambda_\mathrm{f}}$ is the number of transitions from the initial to final state per second. According to Fermi's golden rule,

$$\sum_{\mathbf{Q}_\mathrm{f} \text{ in } \mathrm{d}\Omega} W_{\mathbf{Q}_\mathrm{i},\lambda_\mathrm{i}\to\mathbf{Q}_\mathrm{f},\lambda_\mathrm{f}} = \frac{2\pi}{\hbar} \rho_{\mathbf{Q}_\mathrm{f}} |\langle \mathbf{Q}_\mathrm{i}, \lambda_\mathrm{i} | V | \mathbf{Q}_\mathrm{f}, \lambda_\mathrm{f} \rangle|^2 \tag{4.4}$$

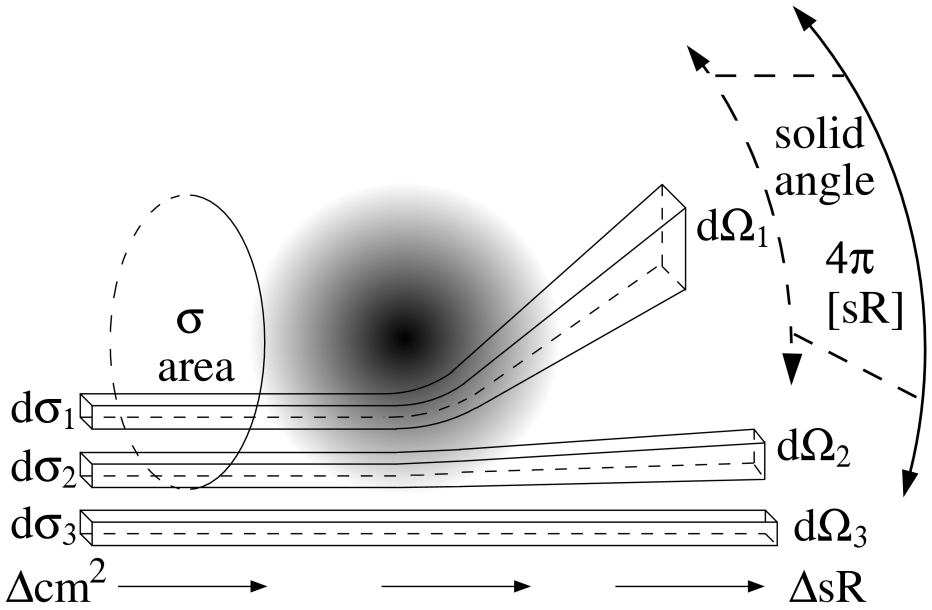

Figure 4.2: The differential scattering cross sections for three paths past a scatterer. From [16]

in which V is the scattering potential, and $\rho_{\mathbf{Q}_f}$ is the density of final states in $d\Omega$ per unit energy. Assuming one neutron in volume Y,

$$\rho_{\mathbf{Q}_f} = \frac{Y}{(2\pi)^3}\mathbf{Q}_f\frac{m}{\hbar^2}d\Omega \tag{4.5}$$

$$\Phi = \frac{1}{Y}\frac{\hbar}{m}\mathbf{Q}_i. \tag{4.6}$$

After substituting, Eq. 4.3 can be written as

$$\left(\frac{d\sigma}{d\Omega}\right)_{\lambda_i\to\lambda_f} = \frac{Q_f}{Q_i}\left(\frac{m}{2\pi\hbar^2}\right)^2 |\langle \mathbf{Q}_i, \lambda_i | V | \mathbf{Q}_f, \lambda_f \rangle|^2. \tag{4.7}$$

Adding the dependence on the final energy and considering energy conservation, the double differential cross section can be written as

$$\left(\frac{\mathrm{d}^2\sigma}{\mathrm{d}\Omega \mathrm{d}E_f}\right)_{\lambda_i\to\lambda_f} = \frac{Q_f}{Q_i}\left(\frac{m}{2\pi\hbar^2}\right)^2 |\langle \mathbf{Q}_i, \lambda_i | V | \mathbf{Q}_f, \lambda_f \rangle|^2 \delta(E_{\lambda_i} - E_{\lambda_f} + E_i - E_f). \tag{4.8}$$

4.2.3 Scattering by Crystal

In a crystal, the scattering potential (V) is the sum of the potentials (V_j) from nuclei at locations ($\mathbf{R}_j$)

$$V = \sum_j V_j(\mathbf{r} - \mathbf{R}_j). \tag{4.9}$$

The difficulty is in finding a suitable function form for these potentials. Since the strong force is short-ranged, an isotropic three-dimensional Dirac delta function called Fermi pseudopotential

$$V(\mathbf{r}) = a\delta(\mathbf{r}) \tag{4.10}$$

is probably the simplest but still realistic model. The constant a could be calculated from the scattering length b by integrating the delta functions for the differential cross section. The result is

$$V(\mathbf{r}) = \frac{2\pi\hbar^2}{m} b\delta(\mathbf{r}). \tag{4.11}$$

By Fourier transforming the scattering potentials (V_j) to reciprocal space, the matrix elements in Eq. 4.8 can be written as $\sum_j b_j \langle \lambda_\mathrm{i} \left| \exp\left(i(\mathbf{Q}_\mathrm{i} - \mathbf{Q}_\mathrm{f}) \cdot \mathbf{R}_j\right) \right| \lambda_\mathrm{f} \rangle$. Then we sum over λ_f, average over λ_i, and rewrite the positions $\mathbf{R_j}$ as Heisenberg operators. This result is

$$\begin{aligned} \frac{\mathrm{d}^2\sigma}{\mathrm{d}\Omega \mathrm{d}E_\mathrm{f}} &= \frac{Q_\mathrm{f}}{Q_\mathrm{i}} \frac{1}{2\pi\hbar} \sum_{jj'} b_j b_{j'} \\ &\times \int_{-\infty}^{\infty} \left\langle \exp\left(i(\mathbf{Q}_\mathrm{f} - \mathbf{Q}_\mathrm{i}) \cdot \mathbf{R}_{j'}(0)\right) \exp\left(i(\mathbf{Q}_\mathrm{i} - \mathbf{Q}_\mathrm{f}) \cdot \mathbf{R}_j(t)\right) \right\rangle \exp(-i\omega t) dt, \end{aligned} \tag{4.12}$$

in which $\omega = (E_\mathrm{i} - E_\mathrm{f})/\hbar$ is determined by the energy transferred to the sample.

The scattering cross section can be divided into coherent and incoherent parts

$$\left(\frac{\mathrm{d}^2\sigma}{\mathrm{d}\Omega \mathrm{d}E_\mathrm{f}}\right)_\mathrm{coherent} = \frac{\sigma_{coh}}{4\pi}\frac{Q_\mathrm{f}}{Q_\mathrm{i}}\frac{1}{2\pi\hbar}\sum_{jj'} \times \int_{-\infty}^{\infty} \left\langle \exp\left(i(\mathbf{Q}_\mathrm{f}-\mathbf{Q}_\mathrm{i})\cdot\mathbf{R}_{j'}(0)\right)\exp\left(i(\mathbf{Q}_\mathrm{i}-\mathbf{Q}_\mathrm{f})\cdot\mathbf{R}_j(t)\right)\right\rangle \exp(-i\omega t)dt \quad (4.13)$$

and

$$\left(\frac{\mathrm{d}^2\sigma}{\mathrm{d}\Omega \mathrm{d}E_\mathrm{f}}\right)_\mathrm{incoherent} = \frac{\sigma_{inc}}{4\pi}\frac{Q_\mathrm{f}}{Q_\mathrm{i}}\frac{1}{2\pi\hbar}\sum_{j} \times \int_{-\infty}^{\infty} \left\langle \exp\left(i(\mathbf{Q}_\mathrm{f}-\mathbf{Q}_\mathrm{i})\cdot\mathbf{R}_{j}(0)\right)\exp\left(i(\mathbf{Q}_\mathrm{i}-\mathbf{Q}_\mathrm{f})\cdot\mathbf{R}_j(t)\right)\right\rangle \exp(-i\omega t)dt, \quad (4.14)$$

in which, $\sigma_\mathrm{coh} = 4\pi(\bar{b})^2$, $\sigma_\mathrm{inc} = 4\pi\left(\overline{b^2} - (\bar{b})^2\right)$. It is obvious from these expressions that coherent scattering depends on the correlations between different scatterers and the same scatterer at different times, while the incoherent scattering involves only the latter. In practice, the coherent and incoherent scattering for different elements can be quite different, as determined by the disorder of different spin states and isotopes. For example, the scattering is mostly coherent for vanadium-50 and incoherent for vanadium-51. It is the abundance of the isotopes (V^{50} : 0.25%; V^{51} : 99.75%) that makes the regular vanadium largely incoherent.

4.2.4 Scattering by Phonons

In a crystal at finite temperature, atoms are not static. Instead, they are vibrating in phonon modes, as described in Chapter 2. The instantaneous positions of atoms can be written as $\mathbf{R}_j(t) = \mathbf{x}_j + \mathbf{u}_j(t)$, in which $\mathbf{x}_j$ is the time-independent equilibrium position and $\mathbf{u}_j(t)$ is the deviation from the equilibrium position for atom j.

For simplification, it is traditional to define two operators:

$$U = -\left(i(\mathbf{Q}_\mathrm{i} - \mathbf{Q}_\mathrm{f}) \cdot \mathbf{u}_0(t)\right), \tag{4.15}$$

$$V = i(\mathbf{Q}_\mathrm{i} - \mathbf{Q}_\mathrm{f}) \cdot \mathbf{u}_j(t). \tag{4.16}$$

As a result, the cross sections of both Eqs. 4.13 and 4.14 can be expressed by the correlation function $\langle \exp U \exp V \rangle$. For a Bravais lattice in which all atoms are equivalent, and harmonic oscillators in which the probability functions are Gaussian

$$\langle \exp U \exp V \rangle = \exp \langle U^2 \rangle \exp \langle UV \rangle, \tag{4.17}$$

in which, by Taylor expansion,

$$\exp \langle UV \rangle = 1 + \langle UV \rangle + \frac{1}{2}\langle UV \rangle^2 + \ldots . \tag{4.18}$$

Here on the right side the first term corresponds to elastic scattering, the second term corresponds to the one-phonon process, and so on. For a p-phonon process, this term can be written as $(1/p!)\langle UV \rangle^p$, which can be justified by analyzing the expressions for each term in the Taylor expansion of both sides of Eq. 4.17.

The factor $\exp \langle -2W \rangle = \exp \langle U^2 \rangle$ is the well-known Debye-Waller factor, named after Peter Debye and Ivar Waller. It quantifies the attenuation of elastic scattering caused by thermal motion.

By expressing the displacement operator ($\mathbf{u}_j$) in terms of the phonon creation and annihilation operators ($\hat{b}^\dagger_{\mathbf{q},j}$, $\hat{b}_{\mathbf{q},j}$)

$$\mathbf{u}_j = \left(\frac{\hbar}{2MN}\right)^{1/2} \sum_{\mathbf{q},j} \frac{\mathbf{e}_{\mathbf{q},j}}{\sqrt{\omega_{\mathbf{q},j}}} \left(\hat{b}_{\mathbf{Q},j} \exp\left(i\mathbf{q} \cdot \mathbf{R}_j\right) + \hat{b}^\dagger_{\mathbf{Q},j} \exp\left(-i\mathbf{q} \cdot \mathbf{R}_j\right)\right), \tag{4.19}$$

the one-phonon scattering term in Eq. 4.18 can be written as

$$\left(\frac{\mathrm{d}^2\sigma}{\mathrm{d}\Omega \mathrm{d}E}\right)_{\mathrm{inc},1} = \frac{\sigma_{inc}}{4\pi}\frac{Q_\mathrm{f}}{Q_\mathrm{i}}\frac{1}{2M}\exp\langle U^2\rangle \sum_{\mathbf{q},j}\frac{\left((\mathbf{Q}_\mathrm{i}-\mathbf{Q}_\mathrm{f})\cdot\mathbf{e}_{\mathbf{q},j}\right)^2}{\omega_{\mathbf{q},j}} \times \left(\langle n_{\mathbf{q},j}+1\rangle\,\delta\left\langle\omega-\omega_{\mathbf{q},j}\right\rangle + \langle n_{\mathbf{q},j}\rangle\,\delta\left\langle\omega+\omega_{\mathbf{q},j}\right\rangle\right), \quad (4.20)$$

in which the two terms correspond to phonon creation and annihilation and $\langle n_{\mathbf{q},j}\rangle$ is the Planck distribution. It can also be written in the form of the phonon density of states ($g(\hbar\omega)$), as first derived by Placzek and van Hove [68]

$$\left(\frac{\mathrm{d}^2\sigma}{\mathrm{d}\Omega \mathrm{d}E}\right)_{\mathrm{inc},1} = \frac{\sigma_{inc}}{4\pi}\frac{Q_\mathrm{f}}{Q_\mathrm{i}}\frac{3N}{2M}\exp\langle U^2\rangle\,\frac{Q^2}{3\omega}g(\hbar\omega)\,\langle n(\omega)+1\rangle\,. \quad (4.21)$$

In a more general form, the scattering can also be described by the van Hove correlation function $G(\mathbf{r},t)$, [69] which is the space-time correlation function for the scattering centers. The scattering function $S(\mathbf{Q},E)$ is the Fourier transform in time and space

$$S(\mathbf{Q},E) = \frac{1}{2\pi\hbar}\int G(\mathbf{r},t)\exp(i((\mathbf{Q}_\mathrm{i}-\mathbf{Q}_\mathrm{f})\cdot\mathbf{r}-\frac{E}{\hbar}t))d\mathbf{r}dt. \quad (4.22)$$

The cross sections for coherent and incoherent scattering can then be written as

$$\left(\frac{\mathrm{d}^2\sigma}{\mathrm{d}\Omega \mathrm{d}E}\right) = \frac{\sigma_\mathrm{coh}}{4\pi}\frac{Q_\mathrm{f}}{Q_\mathrm{i}}S_\mathrm{coh}(\mathbf{Q},E), \quad (4.23)$$

$$\left(\frac{\mathrm{d}^2\sigma}{\mathrm{d}\Omega \mathrm{d}E}\right)_\mathrm{incoherent} = \frac{\sigma_\mathrm{inc}}{4\pi}\frac{Q_\mathrm{f}}{Q_\mathrm{i}}S_\mathrm{inc}(\mathbf{Q},E) \quad (4.24)$$

in which $S_\mathrm{inc}(\mathbf{Q},E)$ is the incoherent scattering function with only self intermediate terms. [65]

4.3 Time-of-Flight Neutron Chopper Spectrometer

4.3.1 Concept and Setup

For a complete study of phonon density of states for materials, time-of-flight (TOF) instruments are usually the best choice. TOF instruments are installed at both reactor sources (e.g., NG-6 at the NIST Center for Neutron Research) and spallation sources (e.g., ARCS, SEQUOIA, and CNCS at the Spallation Neutron Source). But because of the intrinsic character of pulsed operation, the latter are better suited for this type of instrument and generally able to achieve higher effective neutron fluxes.

As an example of a spallation source, a schematic illustration of the Spallation Neutron Source (SNS) at the Oak Ridge National Laboratory is shown in Fig. 4.3. Firstly, negatively charged hydrogen ions (H^-) are produced by an ion source, formed into a pulsed beam, and accelerated to an energy of 2.5 MeV by the front-end systems. The beam is then accelerated by the linear accelerator (linac) to 1 GeV. After passing through a stripper foil, which removes the electrons from ions to produce protons, the beam is bunched and intensified by the accumulator ring to produce short and sharp (1 μs) pulses at 60 Hz. These proton pulses bombard a liquid mercury target to produce neutrons, which are then modulated with water or liquid hydrogen to produce thermal or cold neutrons for use with different instruments.

In a direct-geometry, time-of-flight chopper spectrometer, as shown in Fig. 4.4, each neutron pulse leaves the moderator at a known time. Then neutrons pass through T_0 and Fermi choppers, which are fast-rotating cylinders with slits designed for letting through neutrons at desired timings. The T_0 chopper is aimed to stop very fast neutrons leaked from moderators and the γ-rays. The Fermi chopper, on the other hand, provides the chromatization. The two-chopper design cuts down the slow or fast neutrons from the preceding or subsequent proton pulses, which otherwise would pass through the chopper (Fig. 4.5). With proper

Figure 4.3: Spallation Neutron Source is a collaborative effort of six national laboratories

settings, the initial energy (E_i) and wavevector ($\mathbf{Q}_\mathrm{i}$) are known.

In an desired experimental configuration, most of the neutrons selected by the choppers will pass through the sample unscattered and be absorbed by the beam stop. For the ones that do get scattered and arrive at the detectors, their arrival times and locations will be recorded. Detectors are usually ^{3}He-filled long tubes, bundled as packs. By measuring the intensity of the signals on the two ends of the tubes, the location of the event within the tube can be calculated. Until recently, the raw data were binned to histograms of detector pack, detector, pixel, and time channel. With more modern data acquisition and storage, the raw data are stored in event mode, in which each neutron registered by the detectors is identified by its detector pack, detector, pixel, and arrival time (τ).

With the above information we can determine the final energies and wavevectors of the neutrons

$$E_\mathrm{f} = \frac{m_\mathrm{n}}{2}\left(\frac{L}{\tau}\right)^2, \tag{4.25}$$

$$Q_\mathrm{f} = \frac{m_n L}{\hbar\tau}, \tag{4.26}$$

in which L is the distance from the sample to the detector pixel. The direction of $\mathbf{Q}_\mathrm{f}$ is unit vector from the sample to the pixel. The energy and wavevector

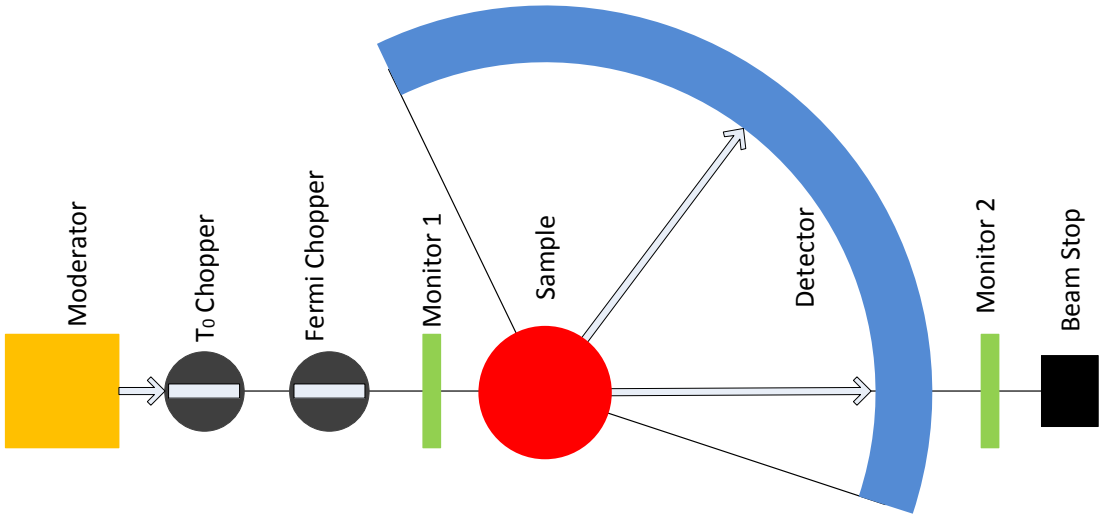

Figure 4.4: Schematic of a direct geometry a time-of-flight neutron chopper spectrometer.

transferred to the sample are

$$E = E_{\mathrm{i}} - E_{\mathrm{f}}, \tag{4.27}$$

and

$$\mathbf{Q} = \mathbf{Q}_{\mathrm{i}} - \mathbf{Q}_{\mathrm{f}}. \tag{4.28}$$

The direction of $\mathbf{Q}$ is only relevant for single crystal samples. For polycrystalline samples the neutron scattering is averaged over all directions that have the same $Q = |\mathbf{Q}|$.

4.3.2 Kinematic Limit

One of the major advantages of time-of-flight techniques is the simultaneous coverage of large regions of reciprocal space (**q**-space). For a particular scattering angle Φ and incident energy E_{i}, the relation between maximum momentum transfer

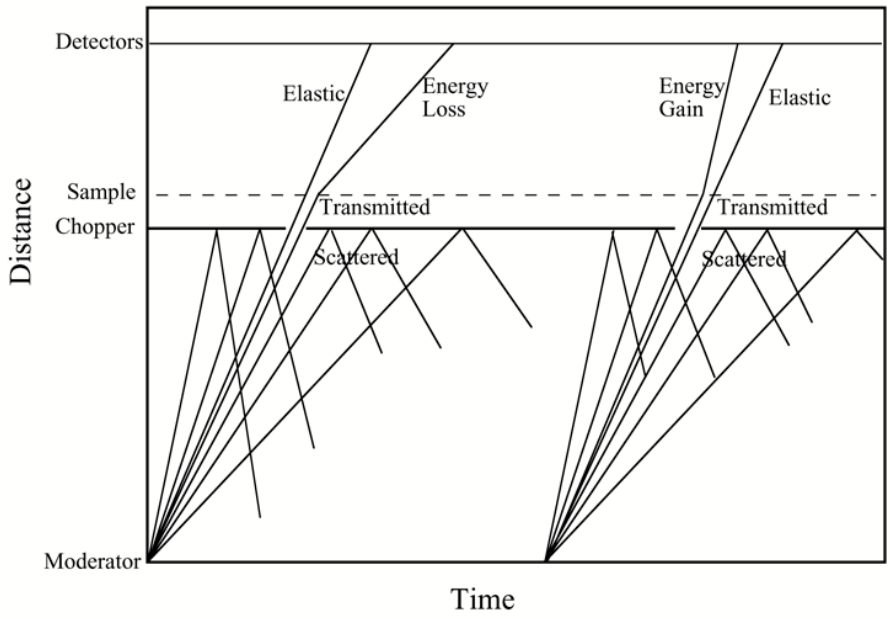

Figure 4.5: Distance-time diagram of the chopper timing of a direct-geometry time-of-flight neutron chopper spectrometer. From [16]

Q_{max} and energy transfer is

$$Q_{max} = \left(\frac{1}{2.072} \left(2E_i(1 - \cos\Phi\sqrt{1 - \frac{E}{E_i}}) - E \right) \right)^{\frac{1}{2}}, \tag{4.29}$$

in which Q is in $Å^{-1}$ and the energies are in meV. This is called the kinematic limit, as shown in Fig. 4.6.

Usually dozens or hundreds of Brillouin zones are covered by the Q range, but it is always wise to calculate the volume of the covered reciprocal space and compare it to that of the Brillouin to ensure a good average is achieved, which is essential for a good phonon density of states study. Large momentum transfer (Q) can be achieved by using higher incident energies or measuring phonons at larger scattering angles, but the former will degrade the energy resolution and the latter is limited by the instrument. Also, at high Q, the multiphonon and multiple scatterings are stronger, and the signal-to-noise ratio can be substantially lower after correction.

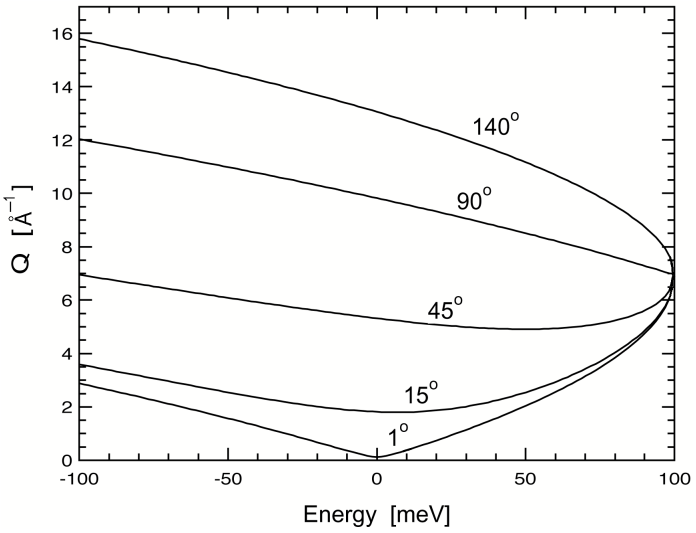

Figure 4.6: Kinematic limit for a time-of-fight chopper spectrometer, calculated using 4.29 for five values of scattering angle Φ. Incident energy was E_{inc} = 100 meV. Positive E corresponds to phonon creation, negative to phonon annihilation. From [16]

4.3.3 Time-of-Flight Chopper Spectrometers at the SNS

Time-of-flight chopper spectrometers are useful for a variety of measurements, and instruments are designed with different purposes in mind. Four inelastic spectrometers at the Spallation Neutron Source (SNS), Oak Ridge National Laboratory, use time-of-flight in design: ARCS (Wide Angular-Range Chopper Spectrometer), SEQUOIA (Fine-Resolution Fermi Chopper Spectrometer), CNCS (Cold Neutron Chopper Spectrometer), and HYSPEC (Hybrid Spectrometer). Their major specifications are listed in Table 4.2.

Using ambient water moderators, ARCS and SEQUOIA are better suited for studying phonon dynamics and magnetic dynamics. CNCS and HYSPEC, on the other hand, are engineered toward studies of molecules, nanostructure, superconductivity, and magnetism, which benefit from long-wavelength cold neutrons from coupled cryogenic hydrogen moderators.

Most of the time-of-flight neutron scattering work in this thesis was performed on ARCS. A schematic sketch of the ARCS instrument is shown in Fig. 4.7.

Table 4.2: Time-of-flight chopper spectrometers at SNS

Property	ARCS	SEQUOIA	CNCS	HYSPEC
moderator	ambient H_2O	ambient H_2O	20 K hydrogen	20 K hydrogen
E_i	20 ~ 1500 meV	10 ~ 2000 meV	0.5 ~ 80 meV	3.6 ~ 90 meV
energy resolution	2 ~ 5%	1 ~ 5%	10 ~ 500 μeV	2 ~ 20%
moderator-to-sample	13.6 m	20 m	36.2 m	40.4 m
sample-to-detector	3.0 ~ 3.4 m	5.5 ~ 6.3 m	3.5 m	4.5 m
detector coverage (h)	$-28 \sim 135^\circ$	$-30 \sim 60^\circ$	$-50 \sim 135^\circ$	$2 \sim 135^\circ$
detector coverage (v)	$-27 \sim 26^\circ$	$-18 \sim 18^\circ$	$-16 \sim 16^\circ$	N/A

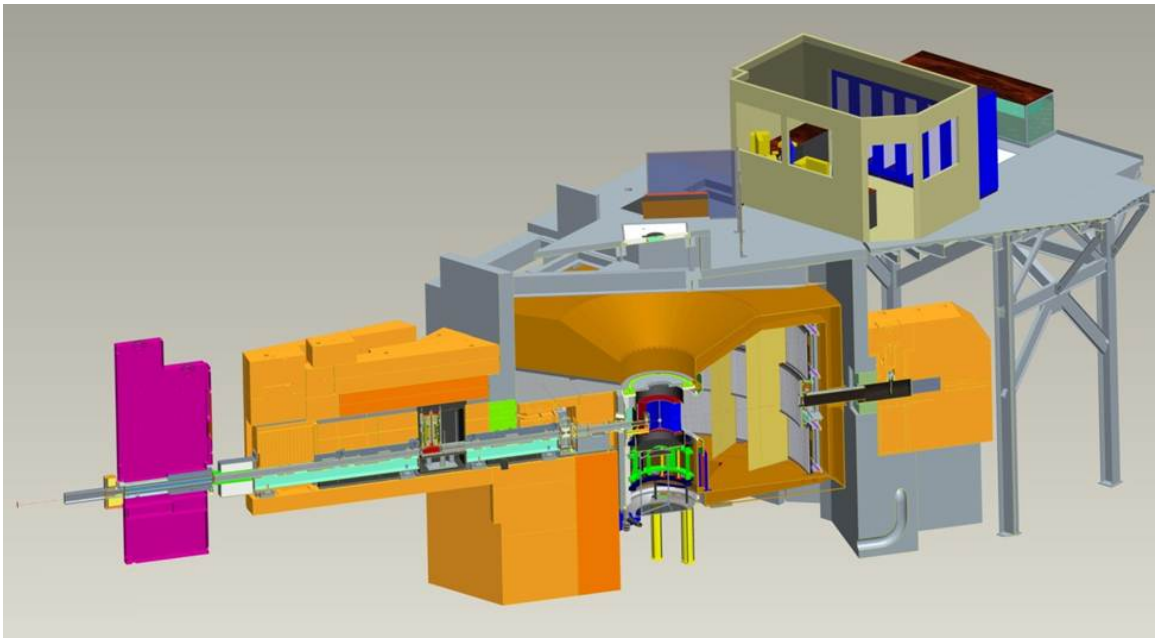

Figure 4.7: Schematic of the Wide Angular-Range Chopper Spectrometer (ARCS) at Spallation Neutron Source (SNS)

4.3.4 Data Reduction to $S(Q,E)$

Data from a time-of-flight chopper spectrometer must be “reduced” to an intensity as a function of momentum and energy transfers $S(Q,E)$. This is always a daunting task, not only due to the difficulty of binning a large amount of data, but also due to the complexity of multiphonon and multiple scattering corrections. The principles and procedures are detailed elsewhere. [15, 16] For the ARCS instrument, most of the data reduction functions are provided by the software package *DrChops*. [70]

^{3}He detectors are the most commonly used type of detectors for neutron instruments. In practice, some of the detectors may not working properly all the time; some may become "noisy", and some may go "silent" completely. These bad detectors need to be identified and masked. This is usually done by setting a threshold of maximum and minimum neutron counts for each pixel, and those pixels receiving extremely high or low counts are discredited and removed by the mask. This is a trial-and-error approach. The maximum and minimum counts must be chosen carefully to throw out the bad detectors without losing any useful ones.

The efficiency γ_{dpt} varies from detector to detector, and also depends on the incident energy (d, p, and t denote detector, pixel, and time-of-flight.). Usually the data were corrected for detector efficiency using a measurement from vanadium, which is a highly incoherent neutron scatterer with coherent and incoherent neutron scattering cross sections of $\sigma^{\text{coh}} = 0.0184$ and $\sigma^{\text{inc}} = 5.08$, respectively. The incident neutron beam can be monochromatic or "white". The latter can be achieved by de-phasing the Fermi chopper. This provides a larger flux for better counting statistics in a given time of measurement. Lately, the calibrations are done at the pixel level to compensate for variations of efficiency within each detector, but this requires a much longer exposure time to ensure statistical quality. It is possible only recently due to the high flux from the recent generation of spallation neutron sources. The calibrated intensity is

$$I_{dpt} = \frac{I^0_{dpt}}{\gamma_{dpt}}, \tag{4.30}$$

where I^0_{dpt} is the measured intensity.

For ARCS, the detectors are straight tubes, arranged in multiple banks to cover a large solid angle of approximately π steradian. ARCS has three detector banks, as shown in Fig. 4.8. As a result, pixels at different detectors and different locations within each detector cover different amounts of solid angle, which must be calculated and corrected for analytically. This correction is more important for instruments with multiple detector banks such as ARCS, where the differences in solid angles are significant.

The incident energy of the neutrons is known from the setting of the T_0 and Fermi chopper, but it is always more accurate to calculate this E_{i} from the data. This can be done using the timings of neutrons arriving at the two monitors located before and after the sample. At ARCS it is more commonly performed using the scattering data by fitting the elastic peak to a Gaussian or other function. The difference from the nominal incident energy can be as large as 5% in some cases.

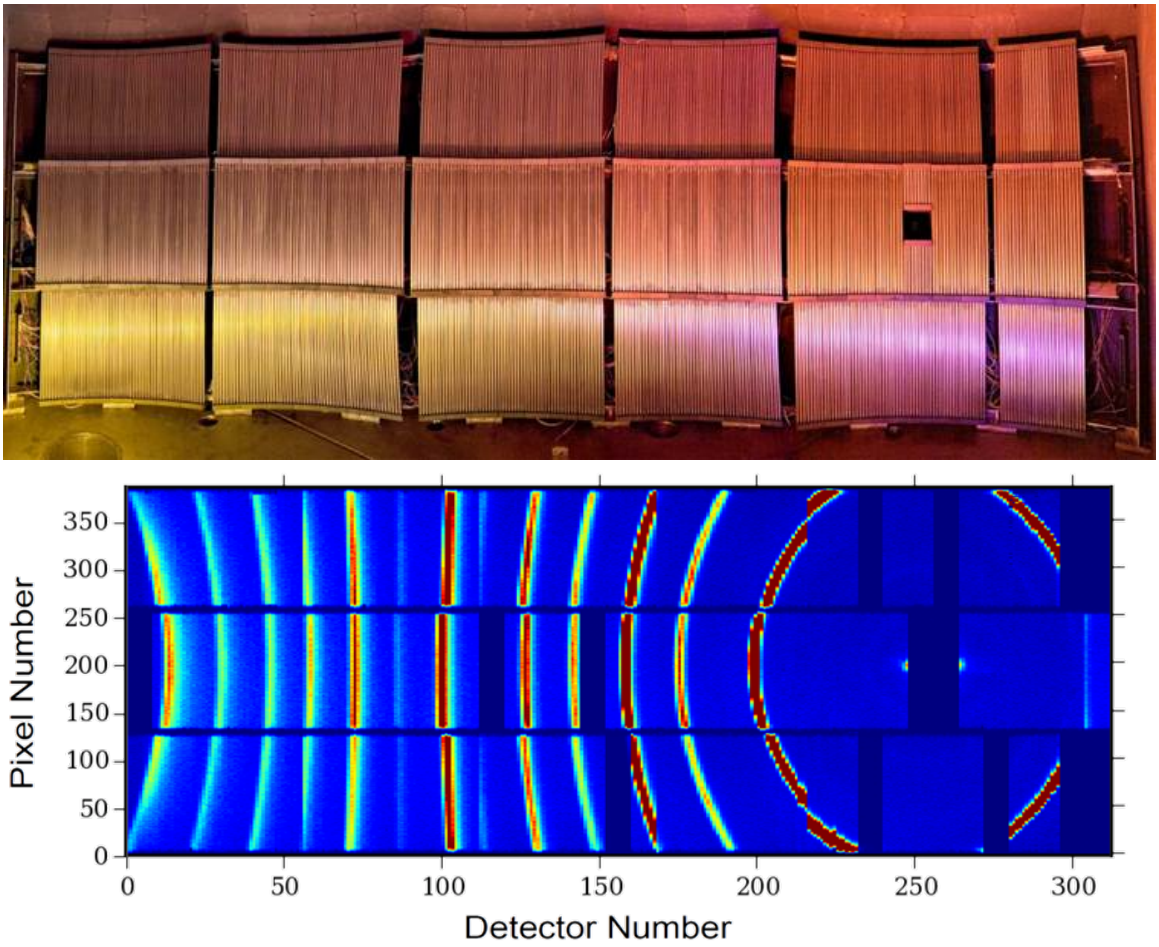

Figure 4.8: Detector banks at ARCS and the signal from a polycrystalline sample. The detector tubes are grouped into different banks and packs.

For the polycrystalline samples, the raw event data of individual neutron detections were first binned to get $I(E, 2\theta)$, where 2θ is the scattering angle and E is the energy transfer, and normalized by either the monitor counts or the proton current on target. The $I(E, 2\theta)$ was then rebinned into intensity, $I(Q, E)$, where $\hbar Q$ is the momentum transfer to the sample.

Before further processing, the background intensity I_B measured from the sample container, the sample environment (if applicable), and the instrument itself must be removed from $I(Q, E)$. The intensity after background correction is

$$I = I_S - f I_B, \tag{4.31}$$

in which

$$f = 1 - p \tag{4.32}$$

is a correction factor for the background that is shadowed by the sample. p is less than the percentage of the neutrons scattered by the sample, and is usually less than 20%.

4.3.5 Reduction to Phonon DOS

Polycrystalline samples are well suited for direct measurements of the phonon density of states (DOS). First, the elastic peak is removed below a certain energy transfer and replaced by a function of energy determined from the inelastic scattering just past the elastic peak. [15]

The one-phonon DOS we seek must be obtained after corrections for multiphonon and multiple scattering. The former involves in the simultaneous creation or annihilation of multiple phonons by one neutron, whereas the latter means that one neutron is scattering multiple times by the sample, the instrument, the sample container, or the sample environment. To minimize the multiphonon and multiple scattering while making good use of available neutrons, the sample thickness is usually chosen so that about 5% $\sim$ 10% of the neutrons that hit the sample are scattered. The formula to calculate the sample thickness is documented in Appendix B.

A common way to correct for multiphonon scattering is the Fourier-log method. Although it does not correct for the multiple scattering, it is a direct method and works well when a simple resolution function exists, as for nuclear resonant inelastic x-ray scattering. [71] For time-of-flight chopper neutron spectrometers, an iterative method is necessary. For both multiple scattering and multiphonon scattering, a two-scattering profile involves a convolution of two single-scattering profiles. An n-phonon-scattering profile $P^n(E)$, is related to the one-phonon-

scattering profile $P^1(E)$ through a recursion relation

$$P^n(E) = \int_{-\infty}^{\infty} P^{n-1}(E')P^1(E-E')dE'. \tag{4.33}$$

It is believed that the multiple scattering is related to the multiphonon scattering through slowly varying functions of Q and E. [72] If these functions are assumed to be constants a_n, the total scattering is given by

$$I(Q,E) = N'\left(\sum_{n=1}^{\infty}(1+a_n)S^n(Q,E)\right), \tag{4.34}$$

in which $S^n(Q,E)$ is the n-phonon-scattering and the N' is a normalization constant. An example using nickel is shown in Fig. 4.9.

Assuming a_ns are the same for all $n > 2$ and the incoherent approximation is valid,

$$I(Q,E) = N\left(S^1_{\text{inc}}(Q,E) + (1+C_{\text{ms}})S^{2+}_{\text{inc}}(Q,E)\right), \tag{4.35}$$

where

$$S^{j+}(Q,E) = \sum_{n=j}^{\infty} S^n(Q,E), \tag{4.36}$$

$$C_{\text{ms}} = (1+a_2)/(1+a_1) - 1, \tag{4.37}$$

$$N = N'(1+a_1)(1+\sigma_{\text{coh}}/\sigma_{\text{inc}}). \tag{4.38}$$

This C_{ms} value could be selected by judging the reduced phonon DOS through some conditions, although, in theory, the scattering thickness of the sample should give an good estimation. [16] The algorithm is implemented in the *getdos* software package. [73]

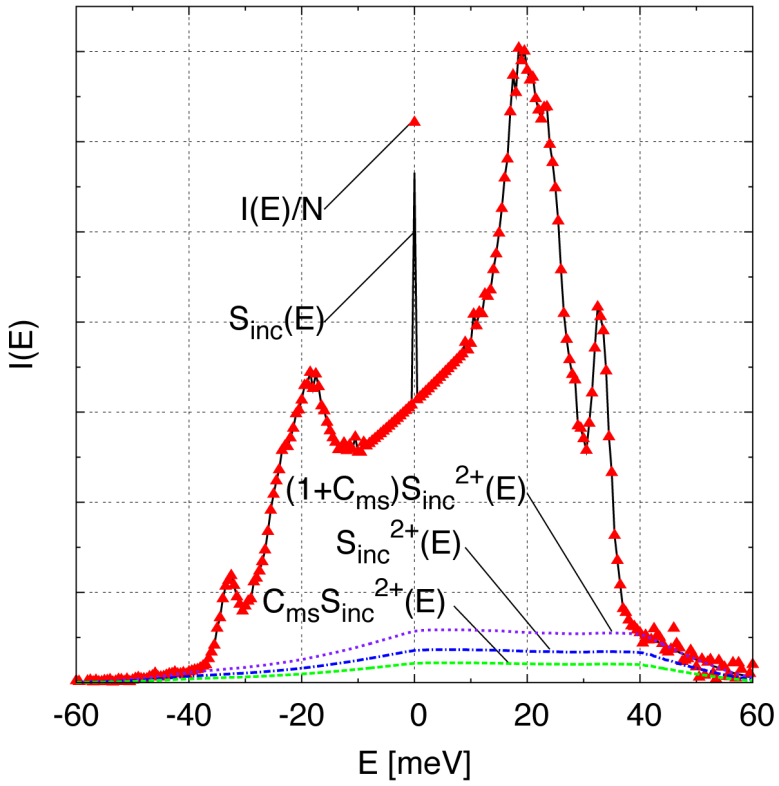

Figure 4.9: Best fit to multiphonon and multiple scattering for nickel at 300 K. From [16]

4.3.6 Other Considerations

Detailed balance determines the differences in the measured spectra between positive energy transfers (phonon creation) and negative energy transfers (phonon annihilation). The ratio of the cross section for the two scattering events will be proportional to the initial density of states

$$\frac{S(Q,-E)}{S(Q,E)} = \exp(-\frac{E}{k_B T}). \tag{4.39}$$

A complication in using Eq. 4.39 is that the data on the negative energy transfer side have lower energy resolution because neutrons gain energy in these processes, fly faster, and their energy is measured less accurately.

It is very important to understand how the energy resolution function for a time-of-flight chopper neutron spectrometer depends on incident energy and

energy transfer. It can be calculated with Monte Carlo instrument simulation using packages such as McVine and McStas. In Fig. 4.10, resolution functions for four incident energies—30, 80, 120, and 165 meV—are shown. The resolution function varies with energy transfer, but also with incident energy. Often an instrument performance is parameterized by the fraction $\Delta E/E_{\mathrm{i}}$, where the energy spread is ΔE at the elastic line, and E_{i} is the incident energy. For the Fermi chopper used for Fig. 4.10, $\Delta E/E_{\mathrm{i}} \sim 4.5\%$.

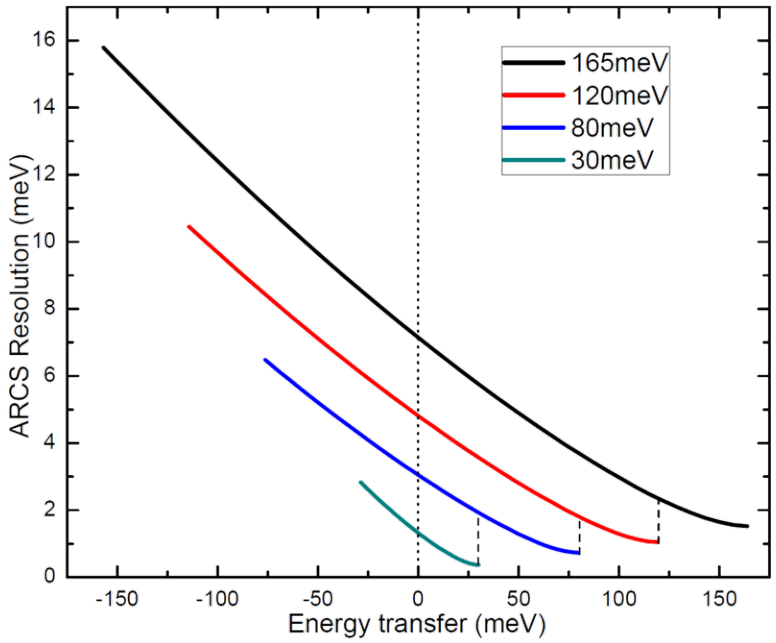

Figure 4.10: Resolution functions for ARCS at four incident energies, E_{i}, for a typical configuration

For study of samples made of multiple elements, neutron weighting is a problem. Because neutron cross sections are different for different isotopes, the modes corresponding to the large vibrational amplitude of some of the elements are overemphasized, while the others are underemphasized. In this sense, the measured phonon density of states should be called a “neutron-weighted phonon density of states”

$$g_{\mathrm{NW}}(E) \propto \sum_j g_j(E) \exp(-2W_j) \exp(2W) \frac{\sigma_j}{M_j}, \tag{4.40}$$

where $g_j(E)$, $\exp(-2W_j)$, $\exp(-2W)$, σ_j, and M_j are the partial phonon DOS, Debye-Waller factors for the jth species and overall lattice, total cross sections and atomic mass for for the jth specie. Usually the major contribution is from the last term σ_j/M_j, in which lighter atoms with larger scattering cross sections dominate.

Correcting for the neutron weighting to obtain the true phonon DOS requires knowledge of phonon partial DOS curves obtained by computation or other experimental technique. For example, in the case of Fe-based compounds, nuclear resonant inelastic x-ray scattering (NRIXS) could provide Fe partial DOS, and together with TOF neutron technique, the true phonon DOS can be obtained.

4.4 Triple-Axis Neutron Spectrometer

4.4.1 Concept and Setup

TOF is quite good at exploring large regions of the Q, E phase space, but at the price of resolution. On the other hand, the triple-axis neutron spectrometer, pioneered by Brockhouse, is the technique of choice for studying excitations in oriented single crystals at specific points in the reciprocal space. Before the development of the modern TOF instruments, which rely on the high peak intensity of spallation neutron sources, triple-axis techniques were used to optimize models of lattice dynamics, from which the phonon density of states could be calculated. This differs from the case for TOF instruments, which can measure the phonon DOS directly in favorable cases. Still, for studying the dispersion relations of phonon and magnons, or studying the properties of specific excitations, the triple-axis spectrometer is usually the best tool.

The technical details of the triple-axis spectrometer are explained in the book by Shirane, Shapiro, and Tranquada, [74] and are only briefly discussed here. In a typical triple-axis neutron spectrometer setup, as shown in Fig. 4.11, neutrons of a defined wavelength are selected by Bragg diffraction at angle $2\theta_M$ (first axis).

The neutrons scattered by the sample are selected at the angle $2\theta_S$ (second axis). The scattered neutrons are analyzed for final energy by the analyzer via further diffraction process by an angle $2\theta_A$ (third axis), and finally counted by the detector. The scattering vector **Q** and the energy transfer E are uniquely determined by the angles $2\theta_S$ and $2\theta_A$:

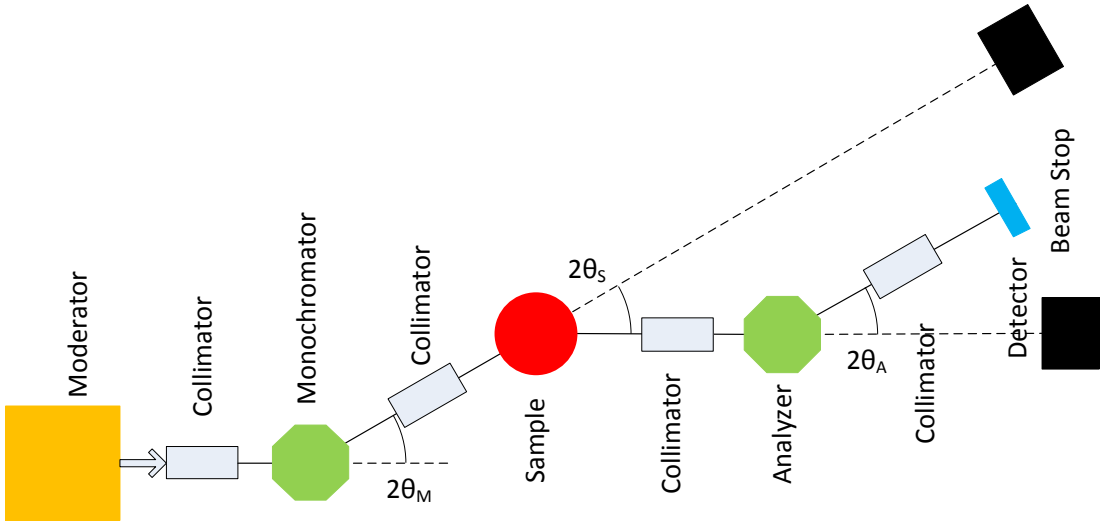

Figure 4.11: Schematic of a triple-axis spectrometer

$$\mathbf{Q} = \mathbf{Q}_i - \mathbf{Q}_f, \tag{4.41}$$

$$Q = \sqrt{Q_i^2 + Q_f^2 - 2Q_iQ_f\cos 2\theta_S}, \tag{4.42}$$

$$E = \frac{\hbar^2({Q_i}^2 - {Q_f}^2)}{2m}. \tag{4.43}$$

Usually triple-axis neutron spectrometers are operated in constant-**Q** or constant-E modes by scanning the other parameter under computer control.

A variety of triple-axis neutron spectrometers are designed with different applications in mind. Currently there are four triple-axis spectrometers (HB-1, HB-1A, HB-3, and CG-4C) at the High Flux Isotope Reactor (HFIR), ORNL, and three

at the NIST Center for Neutron Research (NCNR). They use either thermal or cold neutrons for measuring excitations in different energy ranges. Some of them were designed to work with spin-polarized neutrons, invaluable for studying magnetic dynamics. A schematic setup of HB-3 is shown in Fig. 4.12.

4.4.2 Resolution and Data Reduction

Perhaps the most important aspect of analyzing inelastic neutron scattering data measured using a triple-axis spectrometer is properly taking into account the experimental resolution. The problem is non-trivial. In general, to properly analyze experimental scans using a parameterized model cross section $S(\mathbf{Q}, E, \mathbf{p})$ ($\mathbf{p}$ is the polarization), one needs to calculate the resolution function at each data point for the spectrometer configuration and sample parameters, then numerically convolute the theoretical cross section with this resolution function, and fit the convoluted cross section to the data. [74] Understanding the resolution function is also crucial for experiment planning.

In the Cooper-Nathans approximation [75, 76], it is assumed that the beam divergences on each arm of the triple-axis spectrometer are determined by the Soller collimators and the mosaic spread of monochromator and analyzer crystals. The resolution matrix is

$$\tilde{M}^{-1} = BA(G + C^T F C)^{-1} A^T B^T, \tag{4.44}$$

where G is an 8×8 matrix defining the collimators, F is an 4×4 matrix defining the mosaic spread, and A, C, B are 6×8, 6×8, 4×6 matrices defining the angles and momenta.

In a more accurate approximation, the Popovici resolution matrix is influenced not only by Soller collimators, but also by the shapes and dimensions of the source, monochromator, sample, analyzer, and detector. These shapes are described by

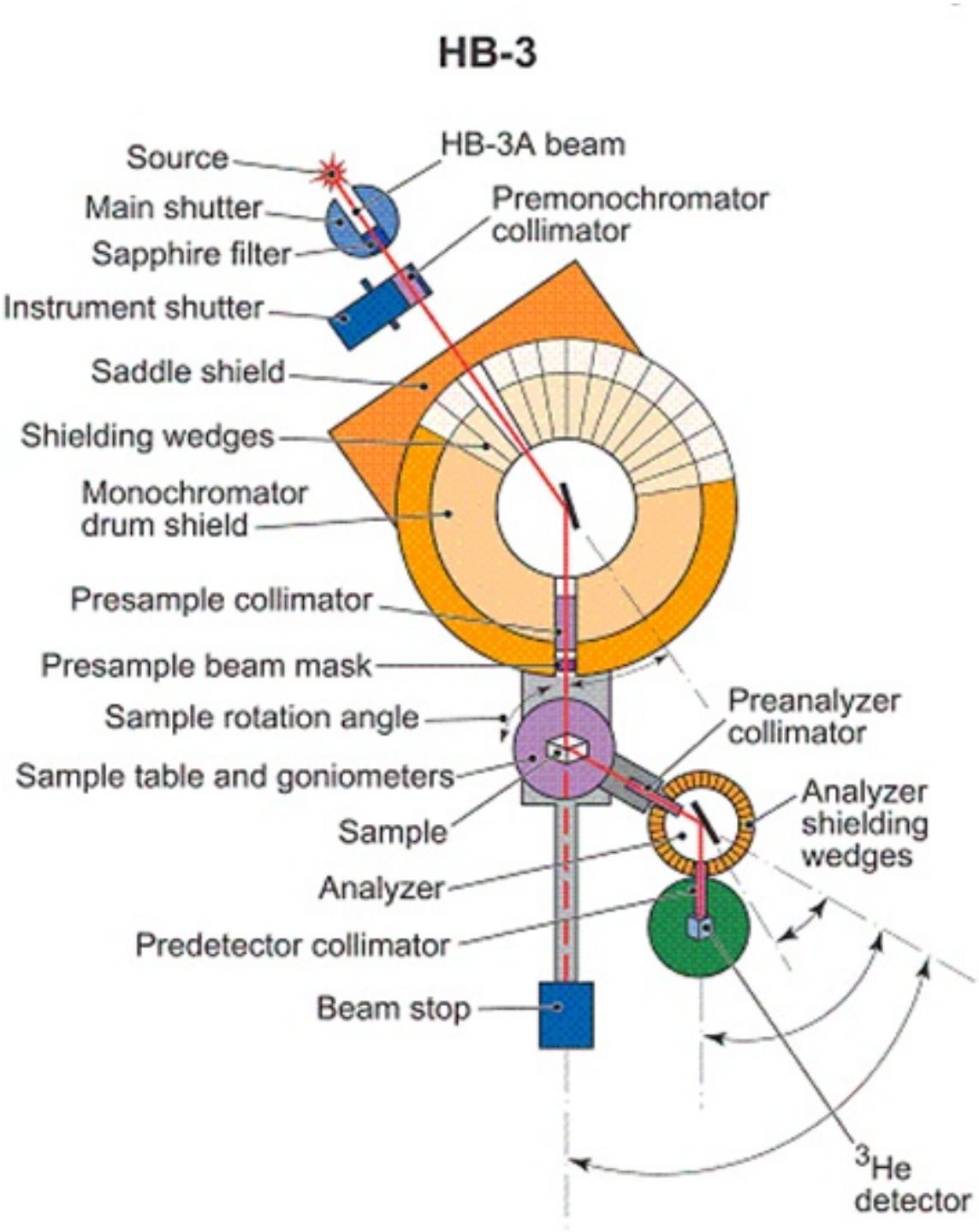

Figure 4.12: Schematic of HB-3 triple-axis spectrometer at HFIR

the 13×13 covariance matrix S^{-1}, and the resolution matrix is

$$\tilde{M}^{-1} = BA\left(G + D\left((S + T^T F T)D^T\right)^{-1}\right)^{-1} A^T B^T. \tag{4.45}$$

The measured intensity should be normalized. In the Popovici approximation, the normalization factors are

$$R_0 = \frac{Q_\mathrm{f}}{Q_\mathrm{i}} \frac{{Q_\mathrm{i}}^3 \cot\theta_M {Q_\mathrm{f}}^3 \cot\theta_A}{64 \sin\theta_M \sin\theta_A} \sqrt{\frac{\det(F)}{\det\left(G + D((S + T^T F T)D^T)^{-1}\right)}} \times \sqrt{\det(M)}, \tag{4.46}$$

when normalized to the source flux, and

$$R_\mathrm{mon} = \frac{1}{Q_\mathrm{i}} \frac{\pi {Q_\mathrm{i}}^3 \cot\theta_M}{2 \sin\theta_M} \sqrt{\frac{\det(f)}{\det\left(g + d((s + t^T f t)d^T)^{-1}\right)}}, \tag{4.47}$$

when normalized to monitor counts. Note that f, g, c, s, and t are defined differently. [74]

The de facto standard for calculating the resolution of triple-axis neutron spectrometers is the *Reslib* package [77], which has engines using both of the approximations mentioned above.

The calculated resolution function in the 4-dimensional phase space $(\mathbf{Q}, E)$ can be visualized in 3-dimensional (Q_i, Q_j, E) as ellipsoids. An example of the ellipsoids for four different energy transfers at one $\mathbf{Q}$-point is shown in Fig. 4.13, together with the phonon dispersion surfaces for Al. How these ellipsoids cut through dispersion surface as they move up and down in energy determines the resolution for the measurement.

By convoluting the 4-dimensional resolution function and the scattering cross section function (dispersion function), the triple-axis spectra can be calculated. This 4-dimensional convolution can be computationally expensive because a high sampling density is necessary for correct results. Usually a single-mode approximation and/or a Monte Carlo sampling can be used to save computing time. In the single-mode approximation, dimensions are reduced by assuming the

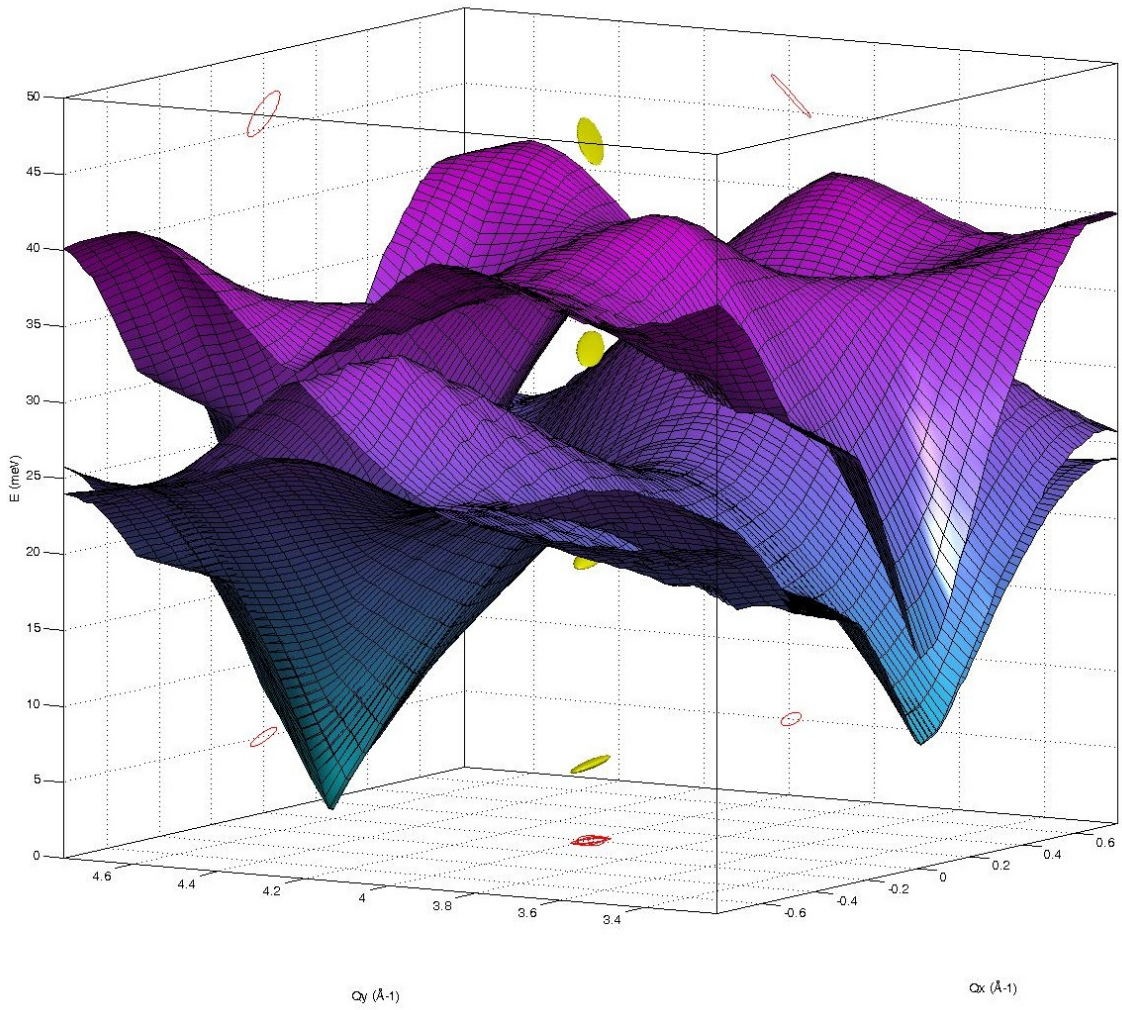

Figure 4.13: Resolution ellipsoids at (0,0,2.6) (for a typical setup) and the phonon dispersion surface of Al near the location

dispersion functions have Lorentzian broadening, and the convolution for those dimensions is done analytically.

Usually we have only the measured spectra, so to calculate the dispersion, parameterized scattering cross section functions are used to fit the experiment by convolution with the resolution function. These functions are then optimized iteratively for the solution.

4.4.3 Other Considerations

There are a few other considerations intrinsic to the triple-axis neutron spectrometer and they need to be noted throughout the planning and execution of the experiment. With many axes moving in the spectrometer, there are limitations on the possible combinations of angles, giving kinematic constraints for $\mathbf{Q}$ and E. This is commonly called “closing the triangle”.

It is a constant struggle to balance between resolution and intensity. Any improvement in resolution is paid for by a loss in count rate. A wise of choice of beam slits and collimator sizes usually involves a compromise between resolution and intensity, and this compromise varies with the phenomenon under study.

The axes of the resolution ellipsoids have different lengths, and the directions of these axes change with both $\mathbf{Q}$ and E. When the longer axis is parallel to the dispersion surface, the effective resolution function is sharper, and otherwise it is broader, resulting in the so-called focusing problem. Usually this can be solved by carefully planning the incident energy and energy gain or loss side of the inelastic measurement.

Although many $\mathbf{Q}$-points in reciprocal space may be equivalent in group theory, they do not give the same or similar triple-axis spectra due to different resolution functions, and, more importantly for phonons, the direction of the eigenvectors of the phonon modes. At certain high-symmetry directions, some phonon modes can become invisible to the neutrons. Such effects can be used to help differentiate between longitudinal and transverse modes, but this does increase the number of $\mathbf{Q}$-points to be measured.

Finally, spurious peaks can occur through a few different mechanisms, but they can usually also be avoided by the choice of incident energy.

4.5 Sample Environments

In neutron scattering, sample environments are not the most difficult or expensive part of the instruments, but they certainly have a large impact on the science that can be done and the quality of the results. Actually, our experience suggests that the sample environments are often the deciding factor for success or failure of an experiment.

It is common practice to design standardized sample environments that fit multiple instruments. However, different scattering methods often dictate different requirements. For example, the ILL furnaces have been the workhorses for neutron diffraction, for which they work very well up to 1800 K. They are almost automatic, fairly efficient, and quite reliable, but they have a huge background. This is not a problem for neutron diffraction, which usually works with intense elastic scatterings. Similarly, triple-axis spectrometers also have less strict requirements for the background because they work in single-channel mode and collimation into the analyzer crystal is very effective in rejecting background scatterings. For inelastic neutron scattering on TOF chopper spectrometers, the background from ILL furnaces is not acceptable, and there have been constant efforts to design and build better furnaces.

At ARCS, the low temperatures (5 K ~ ambient) and moderately high temperatures (ambient ~ 750 K) are covered by displex refrigerators and resistive "stick" furnaces. Their parts (mostly the thermal radiation shielding) in the neutron beam are either made of thin aluminum or well-shielded with BN (for furnaces) or Cd (for refrigerators), and their small contribution to the background can be easily corrected. When the aluminum parts, including the thermal radiation shielding in the "stick" furnace, are replaced by vanadium components, the operation temperature can reach 800 to 850 K. A recent revision of the MICAS furnace uses a configuration similar to the ILL furnace (see Fig. 4.14), but with more aggressive designs to reduce the amount of materials in the beam. It can reach 1500 K, and its background is still large but workable for most purposes.

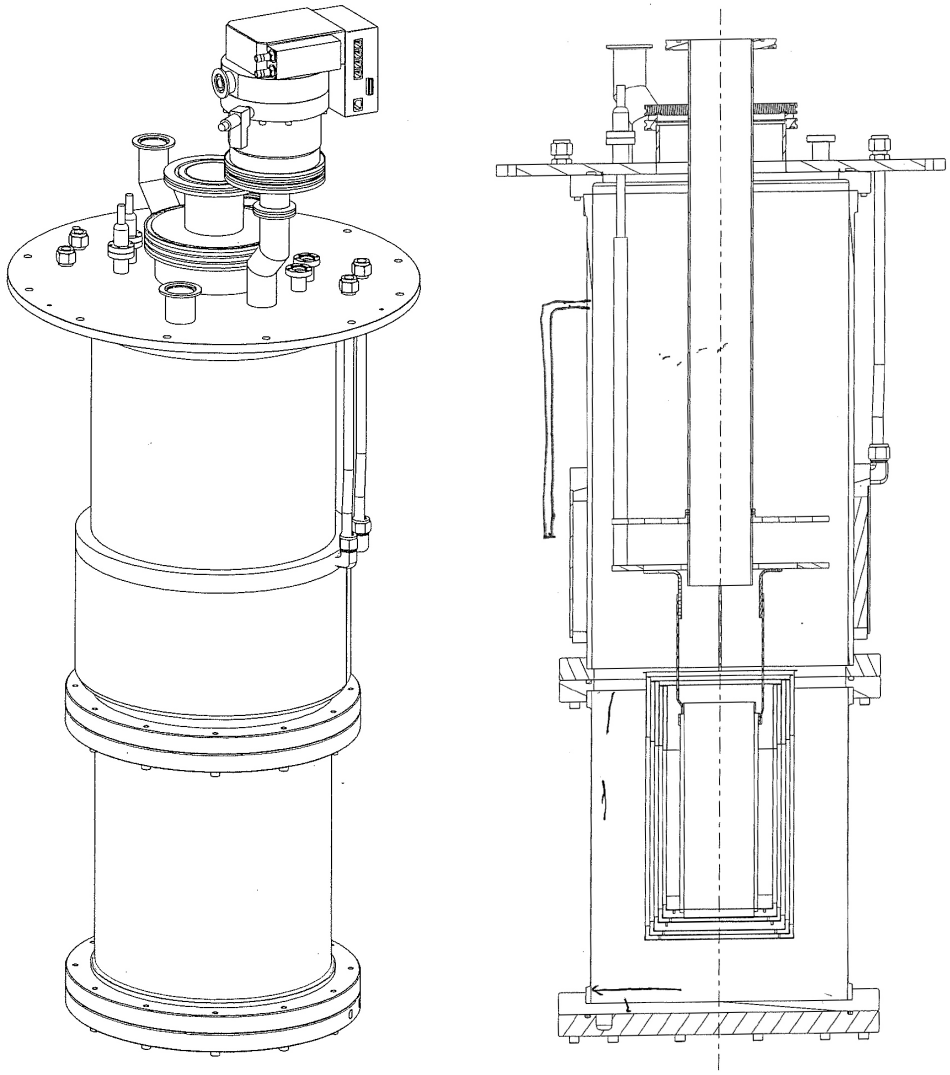

Figure 4.14: The MICAS furnace. The sample is enclosed at the lower part by a heating element and radiation shielding. Courtesy of Doug Abernathy, ORNL

While many metals or alloys can be shaped to plates with desired thickness, containers are necessary for other samples, especially powders. The container needs to maintain an even distribution of the sample across the beam, a good thermal contact with the sample, and a decent coverage of the neutron beam. Aluminum or vanadium sample cans with different diameters (an example is shown in Fig. 4.15) are useful for small amounts of samples or samples with large scattering cross sections. Inserts are available for some of the sizes and they are very helpful in keeping the powders in place rather than falling to the bottom of the cans. It is important to vent the can, otherwise it may expand at high temperatures under the internal pressure when the can material becomes softer.

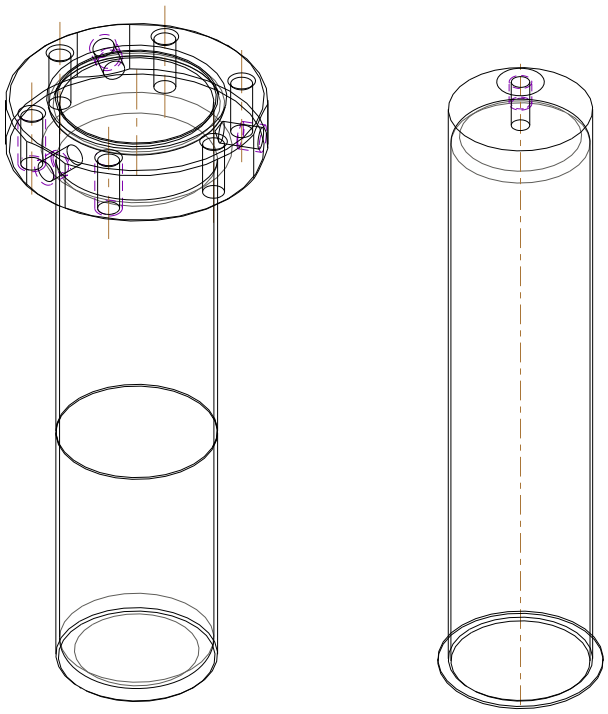

Figure 4.15: A sample can of 5/8 inch ID and its insert for a 1 mm gap. Courtesy of Doug Abernathy, ORNL

Sachets are another way to hold the samples. Aluminum, niobium, and vanadium are the common metals of choice for different temperatures. Sachets are effective in covering the whole neutron beam but the problem is keeping the sam-

ple evenly distributed. This may be possible by using multiple smaller, horizontal sachets sewn in parallel or making some rigid “bridges” that keep the shape of these sachets. One major drawback of sachets is the possibility of sample leakage, especially for very fine or nano powders. E-beam welding can provide an ideal seal, but it is expensive and time consuming. We designed a way to fold a single piece of foil into a sachet that is sealed on three sides (see Appendix C). The thicker folded parts are shielded by a BN frame. This design turns out to be very effective, as long as the thickness is kept even.

Chapter 5

Raman Spectroscopy

5.1 Introduction

Light can be scattered easily by particles much smaller than the the wavelength (λ) of the light. The majority of the scattering is elastic, also called Rayleigh scattering, in which the wavelength and energy of the scattered photons remain unchanged. The cross section of Rayleigh scattering goes as λ^{-4}, so the shorter wavelength photons are scattered much more strongly. This is the reason for the blue color of the blue sky and the yellow tone of the sun itself. [78]

Although the inelastic scattering of light was predicted by Adolf Smekal in 1921, Raman effects were first discovered in 1928 by Indian physicist Sir Chandrasekhara Venkata Raman, who was later awarded the Nobel Prize for Physics in 1930 for his work on the scattering of light. [79]

Unlike the process used in the IR spectroscopy, where photons are absorbed by materials and their energies are transferred to the material, Raman scattering is the inelastic scattering of a photon which creates transitions between vibrational, rotational, and translational states of materials, as illustrated in Fig. 5.5. This includes higher-order transitions, for example, multiphonon processes. The (photon) energy-loss process is called Stokes scattering and the energy-gain process anti-Stokes scattering. By subtracting the energies of the scattered photons from those of the incident photons, energy spectra are measured. The Raman spectra are symmetric on two sides of the Rayleigh light, although the Stokes scattering is usually stronger than its anti-Stokes counterpart, with the difference determined by the principle of detail balance.

Since its discovery, Raman spectroscopy has seen widespread usage in physics, chemistry, geology, and many other science and engineering fields. It has been used to study both organic and inorganic materials ranging from gases, vapors, and aerosols to solids and liquids. Its versatility makes it possible to perform *in situ* measurements under extreme environments, such as high temperature, low temperature, and/or high pressure. Raman spectroscopy can also be done remotely through optical fibers, and micro-Raman methods can analyze samples

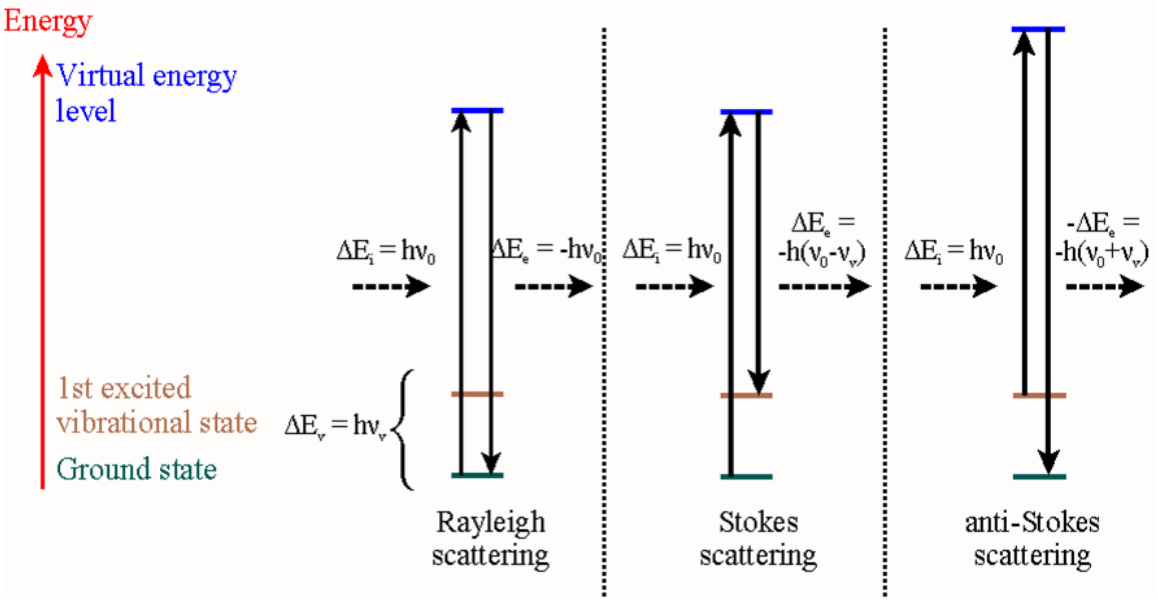

Figure 5.1: Principles of Raman scattering: elastic (Rayleigh) and inelastic (Stokes and anti-Stokes) scattering processes

of submicron sizes. For chemists and geologists, Raman spectroscopy is mostly used for material identification, including structure and phase analysis. For physicists and materials scientists, it is an excellent tool for studying excitations such as phonons and magnons in solids.

The success of Raman spectroscopy is largely the result of successive improvements in the techniques related to Raman instrumentation, especially the invention and minimization of the laser, which helps in measuring the weak scattering process (usually 10^{-7} of the incident beam). It is no surprise that a Raman spectrometer will be on the ExoMars Mars rover to help identify mineral phases, especially those produced by water processes. [80]

Many variations of Raman spectroscopy have been developed to (a) enhance the sensitivity (surface-enhanced Raman), (b) improve the spatial resolution (Raman microscopy), or (c) acquire very specific information (resonance Raman, angle-resolved Raman, hyper Raman). A stimulated or time-resolved excited-state Raman spectroscopy is also possible and can provide valuable information about the dynamics of the system. [81]

The theory and techniques of Raman spectroscopy have been well documented,

[79, 81–93] but the reader will find that most of the books emphasize Raman scattering from molecules. In this chapter, we will review the principles that are related to the study of phonons in crystals, and briefly discuss the techniques used for the current work.

5.2 Principles

5.2.1 Classical Model

A classical model is able to provide an intuitive view of the scattering process, although its limitations will be discussed later with the quantum model. In the classical view of light scattering, the oscillating electrical field generates an oscillating dipole in the material. This dipole, in turn, emits radiation. Treating the incident light as an electromagnetic radiation within the linear responsive range, the dipole moment (μ_j) of jth frequency component can be written as:

$$\mu_j(t) = \alpha E_{\text{in},j}(t), \tag{5.1}$$

in which α is the polarizability and $E_{\text{in,j}}$ is the corresponding frequency component of the driving electric field. For the following discussion, we will focus on one frequency component, so the subscript j will be omitted.

Consider an isotropically polarizable material, where μ is always parallel to, and depends only on, E_{in}. The scattered electric field at distance $r \gg \lambda$ can be calculated from Maxwell's equations as: [85, 86, 92]

$$E_{\text{out}}(t) = \frac{\pi}{\varepsilon_0}\left(\frac{\mu(t)}{r\lambda^2}\right)\sin\phi, \tag{5.2}$$

where Φ is the angle of scattering with respect to the dipole axis, λ is the scattered wavelength, and ε_0 is the vacuum permittivity. Note that the irradiance E is proportional to E^2, and the intensity is $I = Er^2$. The scattered intensity of a

polarized light then can be written as:

$$I(\phi) = \left(\frac{\pi}{\varepsilon_0}\right)^2 \left(\frac{\alpha^2}{\lambda^4}\right) \mathrm{E_{in}} \sin^2\phi. \tag{5.3}$$

This is similar to a dipole antenna, as shown in Fig. 5.2:

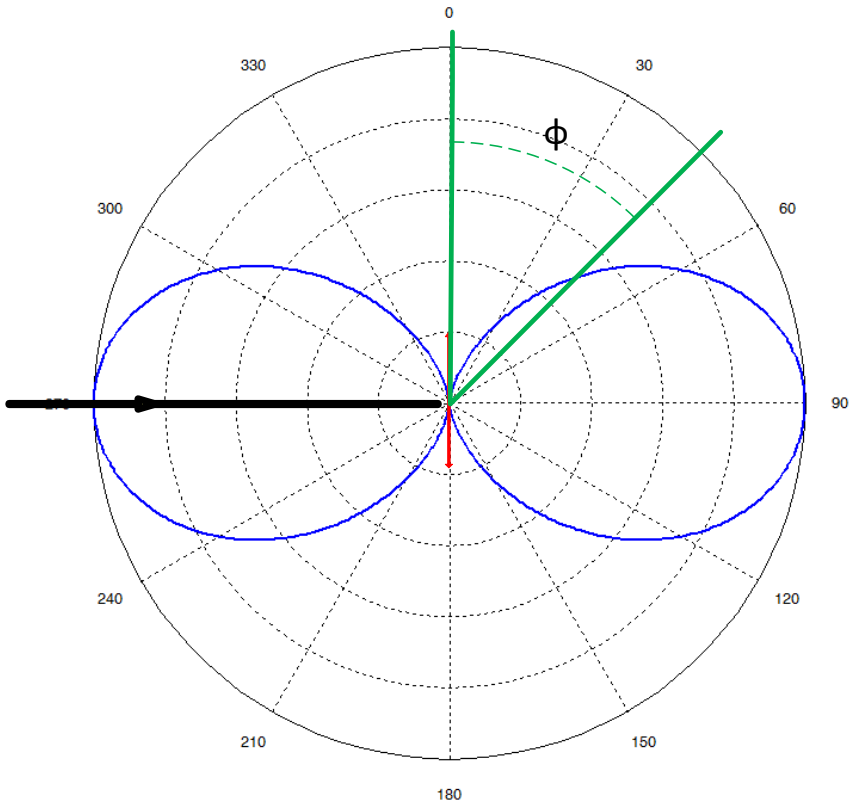

Figure 5.2: Scattered radiation of a polarized incident light

When the incident light is unpolarized, the scattering can be calculated by decomposing the two polarization components and calculating the intensity of scattering from each of them separately from Eq. 5.2:

$$I_{\parallel}(\theta) = \left(\frac{\pi}{\varepsilon_0}\right)^2 \left(\frac{\alpha^2}{2\lambda^4}\right) \mathrm{E_{in}} \cos^2\theta, \tag{5.4}$$

$$I_{\perp}(\theta) = \left(\frac{\pi}{\varepsilon_0}\right)^2 \left(\frac{\alpha^2}{2\lambda^4}\right) \mathrm{E_{in}}, \tag{5.5}$$

where θ is the scattering angle between the incident and scattered beams. They add up to the total scattering intensity in Fig .5.3:

$$I(\theta) = \left(\frac{\pi}{\varepsilon_0}\right)^2 \left(\frac{\alpha^2}{2\lambda^4}\right) \mathrm{E_{in}}(1 + \cos^2\theta). \tag{5.6}$$

This is the Rayleigh scattering and its negative fourth-order dependence on wavelength. Raman scattering is forbidden in isotropically polarized materials. Notice that even with an unpolarized light, the scattered light become polarized, and the polarization is angular dependent.

In an anisotropic material, the problem is more complicated. A more generalized version of Eq. 5.1 is:

$$\mu = \alpha \mathbf{E_{in}}, \tag{5.7}$$

where the polarizability tensor is defined as:

$$\alpha = \begin{bmatrix} \alpha_{xx} & \alpha_{xy} & \alpha_{xz} \\ \alpha_{yx} & \alpha_{yy} & \alpha_{yz} \\ \alpha_{zx} & \alpha_{zy} & \alpha_{zz} \end{bmatrix}. \tag{5.8}$$

The tensor is symmetric and can be illustrated by a polarizability ellipsoid. By rotating the coordinate axes, the tensor can be diagonalized as:

$$\alpha' = \begin{bmatrix} \alpha_1 & 0 & 0 \\ 0 & \alpha_2 & 0 \\ 0 & 0 & \alpha_3 \end{bmatrix}. \tag{5.9}$$

In this coordinate system (shown in Fig. 5.4), the incident light with polarization on only one axis will induce a dipole only on that axis. In the special case where $\alpha = \alpha_1 = \alpha_2 = \alpha_3$, the material has isotropic polarizability.

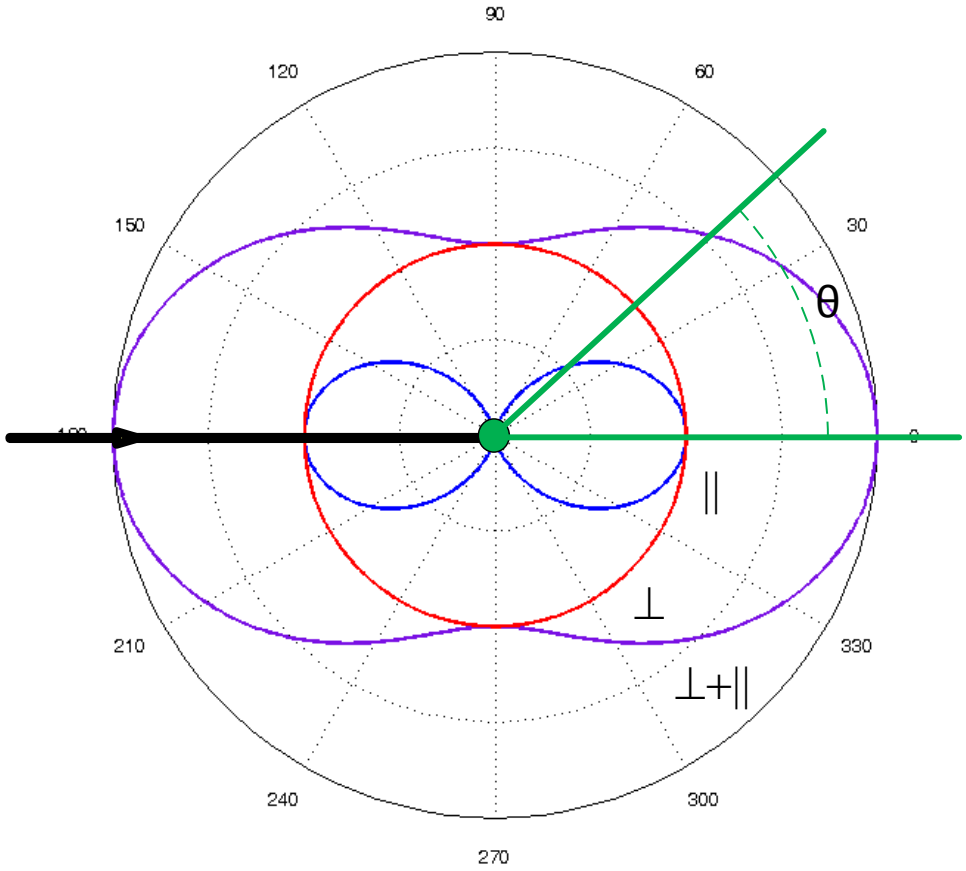

Figure 5.3: Scattered radiation of an unpolarized incident light

It is conventional to define the mean polarizability $\langle\alpha\rangle$ and anisotropy γ:

$$\langle\alpha\rangle = \frac{1}{3}(\alpha_1 + \alpha_2 + \alpha_3), \tag{5.10}$$

$$\gamma^2 = \frac{1}{2}[(\alpha_1 - \alpha_2)^2 + (\alpha_2 - \alpha_3)^2 + (\alpha_3 - \alpha_1)^2). \tag{5.11}$$

For gaseous or liquid materials, the orientations of the molecules are both random and evenly distributed. The average tensor $\bar{\alpha}$ can be conveniently represented by the two above values. [92]

Both vibrational and rotational motions in the material can give rise to a

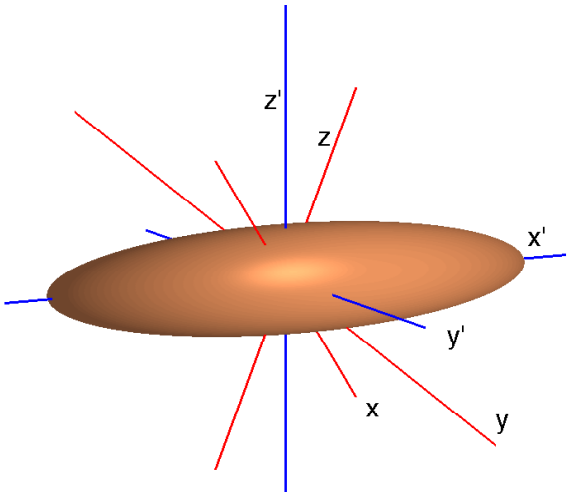

Figure 5.4: Coordinate systems for a polarizability ellipsoid

Raman effect, but for studying phonons in solid state materials, we consider only vibrational degrees of freedom. The thermal vibrations in materials can change the polarizability tensor. The time-dependent tensor element α_{ij} can be written by Taylor expansion about the atomic displacements $\Delta\mathbf{R}$ from the equilibrium positions (expressed in normal coordinates) as:

$$\alpha_{ij}(t) = \alpha_{ij} + \sum_{k=1}^{J} \left(\frac{\partial \alpha_{ij}}{\partial \Delta \mathbf{R}_k} \right)_{\Delta \mathbf{R}_k = 0} \Delta \mathbf{R}_k(t) + \frac{1}{2} \sum_{k=1}^{J} \left(\frac{\partial^2 \alpha_{ij}}{\partial^2 \Delta \mathbf{R}_k} \right)_{\Delta \mathbf{R}_k = 0} (\Delta \mathbf{R}_k(t))^2 + \dots , \tag{5.12}$$

where the sums are over J normal phonon modes. In the harmonic approximation:

$$\Delta \mathbf{R}_k(t) = \Delta {\mathbf{R}_k}^0 \cos 2\pi \nu_k t, \tag{5.13}$$

where $\Delta {\mathbf{R}_k}^0$ is the amplitude and ν_k is the vibrational frequency for the kth normal mode.

Making an approximation by assuming that $\Delta {\mathbf{R}_k}^0$ is small and ignoring the second- and higher-order terms, the induced dipole moment can be written as:

$$\mu(t) = \alpha \mathrm{E}_0 \cos 2\pi \nu_{in} t + \mathrm{E}_0 \cos 2\pi \nu_{in} t \sum_{k=1}^{J} \alpha'_k \cos 2\pi \nu_k t, \tag{5.14}$$

where

$$\alpha'_k = \left(\frac{\partial \alpha}{\partial \Delta \mathbf{R}_k}\right)_{\Delta \mathbf{R}_k = 0}. \tag{5.15}$$

Using the trigonometric relation: $\cos a \cos b = 1/2 \cos(a+b) + 1/2 \cos(a-b)$, we can easily see there are two additional frequencies for each the normal mode and $2J+1$ in total, including the Rayleigh term:

$$\mu(t) = \sum_{k=-J}^{J} \mu_k^0 \cos 2\pi \nu_k t, \tag{5.16}$$

where μ_k^0 is the maximum dipole moment for the kth frequency component and

$$\nu_{\pm j} = \nu_{\text{in}} \pm \nu_j. \tag{5.17}$$

This is the origin of energy gain or loss in Raman scattering, shown in Fig. 5.5. It is a tradition to use wavenumbers (cm^{-1}) as the unit for these frequencies in both Raman and IR spectroscopy.

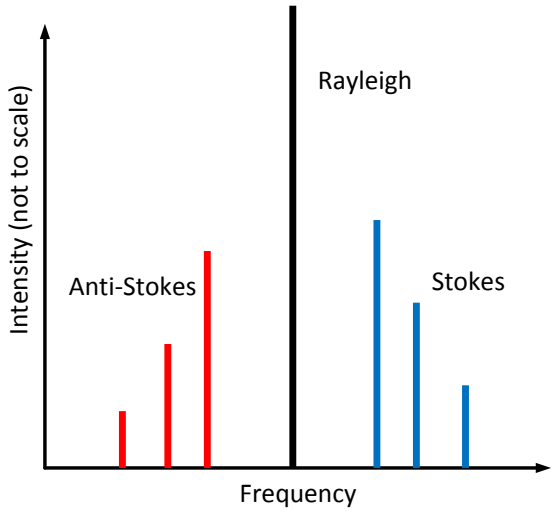

Figure 5.5: A typical Raman spectrum

One would expect the polarizability tensor to be much larger than its first

derivative, and thus the Rayleigh scattering is much stronger than the Raman scattering. Experiment confirms this prediction, and actually the Rayleigh scattering is about three orders of magnitude stronger. However another prediction about a slightly stronger anti-Stokes than Stokes scattering, due to shorter wavelengths, fails. The classical model cannot explain the stronger Stokes lines in experiments.

5.2.2 Quantum Mechanical Model

Treating the light scattering process in full quantum theory is possible, but quite complicated, because it involves describing both the incident radiation and the scattered radiation as quantum particles, while taking into account the relativistic effects. A less-rigorous but more convenient way is to use the perturbation theory and the time-dependent Schrödinger equation, treating the incident radiation as a perturbation to the eigenstates of a molecule. [85, 86, 92]

Assuming that the perturbation generates a time-dependent virtual state, which does not lie close to any of the stationary states, and the scatterer is in one stationary state $|m\rangle$, the eigenvalues of the polarizability tensor of this state can be written as:

$$\alpha_i^m = \frac{2}{\hbar} \sum_r \frac{\nu_{rm} (M_{rm})_i^2}{\nu_{rm}^2 - \nu_{\text{in}}^2}, \tag{5.18}$$

where the summation is over all the unperturbed states $|r\rangle$ and i is the axis index. M_{rm} is the transition dipole moment for $|m\rangle \to |r\rangle$, and ν_{rm} is the related frequency. Similarly, the maximum dipole moment for transition $|m\rangle \to |n\rangle$ can also be calculated from perturbation theory as:

$$\mu^0 = -\frac{1}{2\hbar} \sum_r \left(\frac{E M_{mr} M_{rn}}{\nu_{nr} - \nu_{in}} - \frac{E M_{rn} M_{mr}}{\nu_{mr} + \nu_{in}} \right) \tag{5.19}$$

for anti-Stokes scatterings and

$$\mu^0 = -\frac{1}{2\hbar} \sum_r \left(\frac{E M_{mr} M_{rn}}{\nu_{nr} + \nu_{in}} + \frac{E M_{rn} M_{mr}}{\nu_{mr} - \nu_{in}} \right) \tag{5.20}$$

for Stokes scatterings. These are the quantum equivalent to the results from the classical model. Note that the virtual state cannot be very close to any other stationary states for the denominator to be nonzero.

An important result from the quantum theory corrects the detailed balance between Stokes and anti-Stokes scatterings. The Raman scattering of a photon of the scatterer results from a transition between two different quantum states and because the vibrational, rotational, or translational energies are quantized, the energy loss or gain is carried away by the scattered photon, whose frequency shifts. At finite temperatures, vibrational phonon states are always better occupied at lower energy than higher energy, following the Bose-Einstein distribution. It is easy to show that at ambient temperature most of the phonons are packed in the ground state and even the first excited state is sparsely populated. As a result, the probability of having a Stokes transition is higher than of having an anti-Stokes one.

Combining the classical and quantum results, it is possible to calculate the Raman scattering in certain experiment configurations. For example, for a setup of 90° detection angle and linearly-polarized incident light, the intensity of the Stokes scattering from a scatterer in the ground state can be written as:

$$I_r^p = \left(\frac{h}{360{\varepsilon_0}^2\mu_r\nu_k}\right)\left(1-\exp\left(-\frac{h\nu_k}{k_\mathrm{B}T}\right)\right)\left(\frac{45\langle\alpha_k'\rangle^2+7\langle\gamma_k'\rangle^2}{\lambda_k^4}\right)\mathrm{E_{in}}, \tag{5.21}$$

where μ_r is the effective mass for the rth normal mode. The results for different configurations will be different, but some of the qualitative results are universal. (a) The intensity has a strong dependence on the vibrational frequency as λ_k^4, similar to the Rayleigh process. (b) The lighter the effective mass ν_k, the stronger the Raman scattering. (c) The Raman intensity is proportional to a linear combination of the squares of the first derivatives of the mean polarizability $\langle\alpha_k'\rangle$ and the anisotropy $\langle\gamma_k'\rangle$. That is, the stronger the changes in the polarizability and its isotropy, the stronger the Raman scattering.

5.2.3 Selection Rules

The derivation of the selection rules of Raman scattering, and the methods to determine whether a certain vibration mode is Raman active, needs a rigorous analysis using group theory and is beyond the scope this work. [85, 86] However, the basic idea of the selection rules is simple and is described here.

When discussing the selection rules, Raman and IR spectroscopy are usually compared because both methods are dealing with vibrations in materials. With molecules, it is straightforward to calculate the number of the vibrational degrees of freedom. For a molecule with N atoms, there are $3N$ degrees of freedom in total, 3 of which are translational. If the molecule is linear, there are 2 rotational degrees of freedom; otherwise there are 3. So a molecule will have $3N - 5$ or $3N - 6$ normal modes depending on whether it is linear or not.

For a periodic system such as a lattice, where the vibrations have dispersion and depend on momentum Q, the problem is different. Because the momentum transfer allowed by the scattering of photons in the visible range is small, only scattering from the modes that are very close to the Brillouin zone center are allowed. The number of normal modes at the zone center is $3N$, and N here is the number of atoms in one unit cell. However, it is possible that some of the normal modes may not allow Raman scattering due to symmetry reasons, or two vibrational modes may be degenerate with the same energy. As a result, the observed Raman spectra may have fewer peaks than the number of normal modes.

The selection rules for Raman and IR are: **A vibration is IR active if the dipole moment is changed during the vibration, and is Raman active if the polarizability is changed during the vibration**.

To check if a normal mode is IR active, one inspects the motions of atoms in the normal mode to see if they change the dipole moment. For example, the vibration of a homopolar diatomic molecule is not IR active, whereas that of a heteropolar diatomic molecule is IR active.

To check if a normal mode is Raman active, one needs to find out if the polarizability tensor α is changed. One useful method is to visualize the polarizability ellipsoid and find out if its size, shape, or orientation change during the normal vibration. This turns out to be quite straightforward for small molecules and simple crystals. A more general method is determining the symmetry class of the normal vibration and checking if it falls into one of the symmetry classes of the six unique components of α. [82, 94, 95]

While the Raman effect is a scattering process, IR spectroscopy involves an absorption process. Because of their different mechanism, the cross sections of Raman and IR processes are usually quite different. One vibrational normal mode can be Raman active only, IR active only, both Raman and IR active, or nonactive for both processes. For the special case when there is a center of symmetry for the molecule or unit cell, the Raman and IR processes are mutually exclusive: each vibrational normal mode has be to Raman or IR active, but not both. To determine if a certain normal mode is Raman active, it is helpful to measure the depolarization ratio of Rayleigh scattering and compare this ratio to theory. [92]

5.2.4 Enhanced Raman

One intrinsic experimental obstacle of Raman spectroscopy is its small cross section and thus its low observed intensity, as detailed in 5.2.1. In the quantum mechanical model, this can be explained by the small cross section of exciting the material into a virtual state. The typical total cross sections of common photon processes are listed in Table 5.1. As a comparison, the Raman process typically has a scattering cross section that is 9 orders of magnitude lower than the IR process, and is therefore difficult to detect. The interference from Rayleigh and fluorescence processes, both of which are much stronger, adds to the difficulty. Fortunately, there are a few techniques which can increase the Raman scattering cross sections, and we will discuss them briefly.

When we used quantum perturbation theory on Raman process in Section

Table 5.1: Typical cross sections of common photon proceeses

Process	Cross section (σ/barn)
UV Absorption	10^{6}
IR Absorption	10^{4}
Fluorescence	10^{5}
Rayleigh	10^{-2}
Raman	10^{-5}

5.2.2, it was assumed that the virtual state is sufficiently far away in energy from any of the stationary states. However, if we choose an incident light with an energy that matches an electronic transition in the material, this electronic state will strongly contribute to the virtual state and enhance the probability and cross section of Raman scattering. This is called the resonance Raman effect, and can increase the Raman scattering cross section by as much as 6 orders of magnitude for those vibrational normal modes coupled to the electronic excited state. This coupling actually will help in the spectrum interpretation and will not change the selection rules. A possible drawback may be the increase in fluorescence, but this can be (partially) solved by temporal discrimination and environmental quenching. A preresonance Raman spectroscopy using an incident light with slightly lower frequency may able to enhance the Raman scattering by one or two orders of magnitude without significant increase in the intensity of fluorescence.

Raman scattering can also be enhanced by surface effects. This phenomenon is useful for studies of molecules and less so for studies of phonons in solid. Surface-enhanced Raman scattering was first reported by Fleishmann et al. in 1974 for pyridine molecules adsorbed on a roughened sliver surface. The surface effects can enhance the Raman scattering cross section up to 6 orders of magnitude compared to the free molecules in gas phase. There are at least two major types of mechanism for the surface enhancement. The one attributed to the electromagnetic effects associated with the large local field caused by electromagnetic resonance near the metal surface is well understood. Other aspects, including the contribution

of chemical effects from the chemical interactions between the molecules and the metal surface, are less well understood.

5.3 Experimental Techniques

5.3.1 Basic Setup

In the previous section, we discussed the concepts and cross section of Raman scattering. Experimentally, many techniques are necessary to maximize the signal-to-noise ratio and they are the topics of this section. Two common types of Raman spectroscopy are dispersive (grating-spectrograph-based) and interference-based Fourier-transform (FT) Raman spectroscopy, but dispersive spectroscopy is the simplest and most general technique. Only incoherent Raman scattering will be discussed here.

A basic dispersive Raman system setup is illustrated in Fig. 5.6, where the light from a laser is Raman-scattered by the sample and then filtered, collected, and characterized by frequency to produce the Raman spectra. The choice of each component and their detailed parameters depends on the applications and often need to be compromised.

5.3.1.1 Lasers

The choice of lasers for Raman spectroscopy is usually determined by the sensitivity and fluorescent reduction. Usually visible light provides good sensitivity with the convenience of the easier alignment without IR detection cards. However, some samples will fluorescent violently at these wavelengths, so near-IR wavelengths, which induce much less fluorescence, may be required. Lasers with wavelengths longer than 1000 nm are used almost exclusively for FT Raman spectrometry. The limitation is comes from the silicon-based CCD detector (even when back-thinned for better red response), which has a sensitivity range from about 400 to 1000 nm.

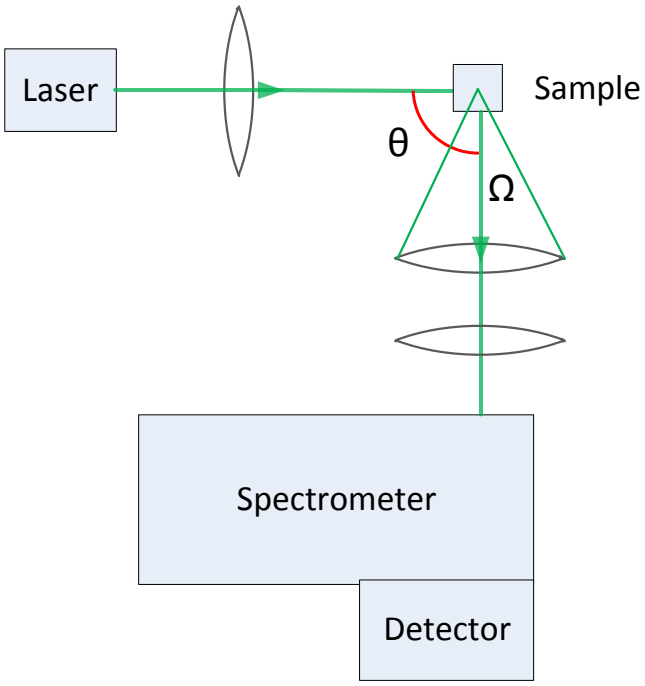

Figure 5.6: A schematic Raman system using 90° geometry

Many types of lasers are suitable for Raman systems. Some of the most widely used are gas lasers such as Ar^+ and Kr^+ ion lasers, which provide a set of high intensity lines (e.g., 457, 488, 514.5, and 406, 647, 752 nm, respectively) up to 2000 mW (combined) at reasonable costs. They are not efficient and usually require big power supplies and water cooling. A cheap alternative is a He-Ne laser (632.8 nm), which has relatively low power up to 50 mW.

Laser diodes (up to 500 mW, 650–800 nm) are becoming popular, owing to their compact design and low cost. There are some fundamental drawbacks though: (a) only a single-mode diode will work because of its broad gain curve; (b) the temperature of the diodes must be regulated to eliminate mode hopping; (c) the long-term wavelength stability is not easy to achieve; (d) optical feedbacks, which may cause frequency instability, must be minimized; (e) a good bandpass filter is necessary due to the spontaneous emission tails; and (f) an optical design that

takes into account beam divergence is necessary. Even with these drawbacks, diode laser systems have been quite successful. Some of the problems, such as stability, can also be alleviated by using an external cavity with the diodes.

All the lasers mentioned above are continuous (CW) ones. For non-dynamics studies, there is no advantage to using pulsed lasers, which cause sample damage or nonlinear effects. But some lasers, such as Nd:YAG lasers are able to produce high-frequency (MHz) low-peak power pulses, which could be considered as quasi-continuous. The neodymium ions in a YAG laser are pumped by flashtube to a short-lived excited-state, which quickly decays to to a relatively long-lived state. The decay from this state will produce the well-known 1064 nm laser (shown in Fig. 5.7. The output from a Nd:YAG laser can also be frequency doubled through nonlinear process to produce a 532 nm laser. The Nd:YAG lasers can also operate in the so called "Q-switched mode", in which they can produce intense (250 MW) 10–25 nanosecond pulses. Although not useful for normal dispersive Raman spectroscopy, the pulsed lasers can be quite useful for time-resolved dynamics studies, as discussed later. Dye lasers pumped by YAG lasers can provide a wide tunable range, and this is also important to dynamics studies. This is the one of the laser systems that was used for the Raman studies in this work.

The Ti:sapphire (650–1100 nm) CW laser is probably the most versatile laser for use with Raman systems, due to its tunability, and it can have an output up to 2000 mW. It has a quasi-continuum background that needs to be filtered. It is probably the laser of choice when cost is not considered. Ultrafast Ti:sapphire lasers in femtosecond or picosecond pulsed modes are also used for time-resolved dynamics studies.

Last, but not least, the diode-pumped solid-state (DPSS) laser is a recent entry to Raman spectroscopy. It usually uses Nd:YAG crystal pumped by diodes and can produce up to 15 W at 532 nm. DPSS lasers generally have a higher beam quality and can reach very high powers while maintaining a relatively good beam quality in single mode. As a drawback, DPSS lasers are also more sensitive to temperature and can only operate optimally within a small range, so an environment control

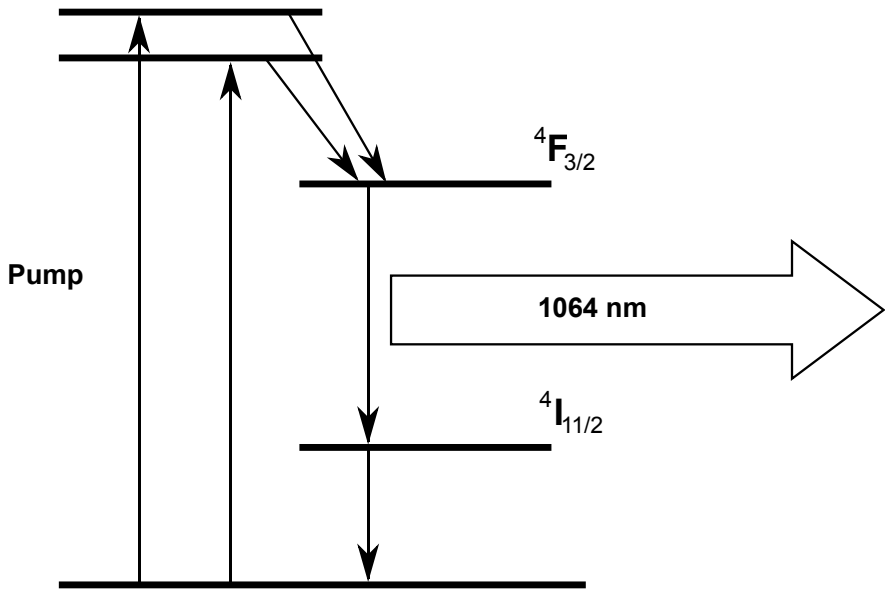

Figure 5.7: A schematic energy levels for Nd ions in a Nd:YAG laser

system is necessary. Some DPSS lasers only cost as much as diode lasers and significantly less than other lasers with the same output performance and quality. High quality DPSS lasers at $1–2K are available through many manufactures. One additional benefit of DPSS lasers pumped by Nd:YAG is that they can share the same set of notch or edge filters as the Nd:YAG laser. A DPSS laser of this type is also used for the the Raman studies in this work.

5.3.1.2 Spectrometers and Filters

To separate the frequency components of the scattered light, spectrometer(s) or a combination of spectrometer(s) and filter(s) are used. The first consideration of a spectrometer for Raman scattering is the low stray light. Because the intensity of the laser can be very strong and a significant percentage of the light is scattered elastically, the spectrometers and filters must be very effective at rejecting the laser line, otherwise the background from stray light will overwhelm the Raman signal. Secondly, to maximize the signal, a low f number, and thus larger light collection solid angle, is preferred. Thirdly, the grating line density must be chosen

depending on the detector system and the wavelength range of the application. There is always a balance between spectral coverage and spectral resolution. Many modern spectrometers have multiple gratings mounted on a turret, which can precisely change gratings remotely.

Double monochromators were standard in past. They are very effective at rejecting the stray light because the two monochromators are in series. They do suffer from some drawbacks, including a high f number, a narrow focal plane, and a very high dispersion, which is good for photomultiplier tubes (PMT), but not very useful for array detectors. Triple monochromators solve the problem of high dispersion by using a pair of the three monochromators in a subtractive configuration as a bandpass filter. They are similar to double monochromators in high stray light rejection (good) and a high f number (bad). But with so many gratings and mirrors, they suffer significantly in the signal intensity.

Use of single spectrometer is becoming more popular because of advances in filter making and spectrometer design. Single spectrometers have the obvious advantage of high throughput and low f number, but the stray light is usually a big challenge. Modern holographic notch filters or edge filters (Semrock Ultrasteep is one type of filter used for this work) are able to achieve optical density (OD) > 6 rejection at laser lines and the transition can be less than 90 cm^{-1}. The actual performance of the filters depends on the choice of wavelength and it can become quite expensive (at over one thousand dollars a piece) if it is necessary to work at several different wavelengths. There are always variations of the filter transmission near the transition edges and they need to be corrected, especially for broad and slow-varying signals very close to the edge. Some spectrometers are specially designed for Raman spectroscopy to address the conflicting challenges of low f numbers, low stray light, and flat focal plane. In an imaging spectrometer, the aberration is corrected by nonspherical mirrors or special grating designs. In a holographic spectrometer, diffraction gratings are made by the same technique as holographic filters, which allows more radical designs.

5.3.1.3 Detectors

Photomultiplier tubes (PMT) and intensified photodiode arrays (IPDA) were standard equipment for Raman spectroscopy applications, but charge-coupled device (CCD) detectors are quickly replacing them everywhere except in special cases.

A PMT is usually much less expensive, and has the advantage of a wide operation range at the UV end, but it can operate only in a single-channel (frequency) mode. An IPDA has the same advantage for UV operation and is easily gated down to 5 ns, which can effectively reject most fluorescence, which is a slow process compared to Raman scattering.

Nowadays CCDs are the *de facto* standard for Raman detectors. They have high yield, two-dimension capacity, and very low dark current. (They can be quite expensive, however.) To reduce the dark current, they need to operate at low temperature (e.g., < 70°C). This was previously achieved by liquid nitrogen cooling, but lately it has become possible to use thermoelectric devices to achieve similar performance. This is the detector that was used for this work. New coatings and designs help extend the effective range well into the IR and UV. CCDs can also be gated for time-resolved- or fluorescence-related applications. The signals from 2D CCD detectors are usually binned along one dimension for Raman spectra. When taking long exposures, the spectra are collected either through hardware binning or software binning. The first has limitations on the maximum intensity but generates less readout error, while the latter gives more error and is much slower.

5.3.2 Signal-to-Noise Ratio

5.3.2.1 Signal

As we mentioned before, the most important consideration of a Raman system is its signal-to-noise ratio (S/N). For a dispersive Raman system, it can be separated into two questions: (1) How much light is scattered? (2) How much of the scattered

light is collected and detected?

The radiance of scattered light can be written as:

$$L = P\left(\frac{\mathrm{d}\sigma}{\mathrm{d}\Omega}\right)DK, \tag{5.22}$$

where P is the laser power density, $\mathrm{d}\sigma/\mathrm{d}\Omega$ is the scattering cross section, D is the number density of molecules, and K is a geometric factor. K is used to describe the relation between scattering volume and the scattering area. K is 1 for a surface scatterer when D is the 2D density, and $r/2$ for 90° geometry (discussed later), where r is the beam radius. For the 180° geometry and a liquid sample, K is the shorter of the spectrometer depth of field or the sample path length. P is usually chosen to be the maximum allowed by the sample damage threshold.

The Raman signal from the detected scattered light is:

$$S = LA\Omega TQt, \tag{5.23}$$

where A is the area of sample monitored, Ω is the collection angle (shown in Fig. 5.6), T is the spectrometer and optics transmission, Q is the quantum efficiency of the detector per photon, and t is the measurement time.

Considering a multichannel detector system such as a CCD with N channels, the Raman signal can be written as:

$$S = \left[P\left(\frac{\mathrm{d}\sigma}{\mathrm{d}\Omega}\right)DK\right]\left[A\Omega TQNt\right], \tag{5.24}$$

where the left part is how much light is scattered and the right part determines the collection and detection efficiency. It should be noted that we made quite a few approximations here by assuming that the scattering is homogenous throughout the effective sample area, the power density is uniform across the beam, the sample is not absorbing, and spectrometer efficiency does not depend on angle, the cross section is isotropic, and the scattering light overfills the slit and collection angle. A modern single-pass spectrometer with a CCD detector can achieve an

$A\Omega TQN$ value about 4 orders of magnitude larger than the first-generation double spectrometers coupled with a PMT, an enormous improvement.

5.3.2.2 Noise

Modern CCD detectors can reduce the dark current by 4 orders of magnitude compared to PMTs. Considering all the noise sources, the total noise can be written as:

$$N = (S + S_B + \phi t + \sigma_R^2)^{\frac{1}{2}}, \tag{5.25}$$

where S_B is the background signal, ϕ is the dark current, and σ_R is the readout noise, which is independent of measurement time.

Assuming the sample has very low background and there is no readout noise, the signal-to-noise ratio is:

$$S/N = \frac{S}{\sqrt{S + \phi t}}. \tag{5.26}$$

When the dark current is very low compared to the signal, the S/N reaches the detector noise limit:

$$S/N = S^{\frac{1}{2}}. \tag{5.27}$$

For a high throughput single-pass spectrometer with a CCD detector system, the large number of channels (1000s) and the reduced dark current can significantly increase the S/N ratio by up to 3 orders of magnitude.

5.3.3 Geometry

There are quite a few common geometries for collecting Raman scattering. The main considerations when deciding on the geometry are the following: (1) Increasing the $A\Omega$ product by overfilling the slit and collection angles, (2) balancing the sample volume and laser power intensity, and (3) the ability to obtain polarization information when applicable.

The 90° collection geometry ($\theta = 90°$) is one of the most common (see Fig. 5.6). It can increase the collection angle at the sample while decreasing the effective

area, but that in turn requires a tighter focus of the laser beam and is also more difficult to align. This is the geometry used for this work, but instead of using a single lens to focus the laser beam onto the sample, as in Fig. 5.6, two cylindrical lenses are used in series to match the illuminated area to the aperture of the spectrometer. One of the benefits is a reduced power intensity, thus less sample damage.

The 180° collection geometry, also called backscattering geometry, is shown in Fig. 5.8. It is possible to overlap the axes of the laser and collection optics. It greatly simplifies the alignment and also makes it possible to use aspheric lenses with very low f numbers and short focal lengths. This is also the common geometry for a microscopic Raman spectrometer.

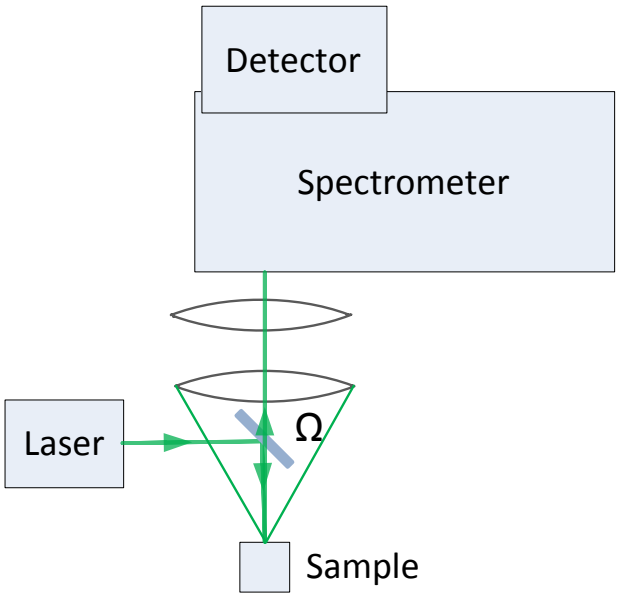

Figure 5.8: A schematic of the Raman system using 180° geometry

Other than the Raman systems using traditional optics, designs using optical fibers also have some advantages, mostly from the flexibility of the geometry setup and remote measurement ability. The drawback, however, is the background

Raman signal from the materials of the fibres (mostly silica), which can be partially overcome by using filters.

5.3.4 Calibration

Raman spectroscopy, like any other spectroscopy technique, requires careful calibration for accuracy. It is well known that the agreements between literature values can be poor, and the differences are often several wavenumbers, which corresponds to a couple of Å near a 500 nm wavelength.

To calibrate Raman spectrometers, the common approach is to use standard spectra lights, such as Ar, Kr, or He-Ne. They offer spectral lines throughout the wavelength range used by Raman scattering. The spectra from these standard lights can be used to fit the polynomial that gives the relation between pixel number and the wavelength. For 2D detectors such as CCDs, there are many degrees of freedom for the alignment, such as the tilting angle of the detector surface. The manufacturer of the spectrometer usually provides the procedure to measure and calculate these parameters, which are later used in the fitting algorithm. It should be noted that the 2D detectors must be carefully aligned to the direction of the spectral line. This can be a tedious process involving trial and error by rotating the detector while measuring a peak spectrum. It is advisable to redo the calibration every time when the operating wavelength or grating of the spectrometer are changed, because of the offsets introduced by stepper motors.

It is also possible to use Raman shift standards for calibration. The advantage is that the laser wavelength need not be known accurately. Because there are usually fewer spectral lines and less intensity, this procedure can be more difficult in practice.

Without a convenient standard intensity like IR spectroscopy, accurate absolute intensities for Raman scattering are almost impossible. Raman spectrometry is not good as a quantitative method, and even measurements of relative intensities can be difficult owing to distortions introduced by the optics and spectrometers. The

reproducibility of the measurement is very difficult, and depends on the detailed alignment of the optics. The most common approach for intensity calibration is to use a standard white-light source with a known output in the wavelength range of interest.

5.3.5 Sample Environments

Sample environments are important parts of a Raman system for studies of the temperature- or pressure-induced effects. Unlike the environments for neutron spectroscopy, an optical window is often necessary for the incident and scattered beams. This creates multiple difficulties, including the background from the window material and the ineffectiveness of heat shielding. Quartz glass is usually the material of choice for the optical window and sample holder, due to its relatively low background, high thermal conductivity, good thermal stability, and high mechanical strength.

The simplest method for high-temperature measurements uses a hot plate. It may even be used in the air without a window for air-inert samples, but due to its open design, ours works only as high as 300 K above ambient temperature.

For most of the measurements at elevated temperatures in this work, the samples were either loaded in a quartz optical cell or pressed into a pellet (under about 50 MPa pressure). The quartz cell or the pellet is then mounted inside a large quartz tube by tethering it to two ceramic rods using niobium foil. Sample heating was provided by three electrical resistive heating elements, which are also supported by ceramic rods. These rods are held in place by stainless steel flanges, which fit tightly inside the quartz tube, as shown in Fig. 5.9. As heat shielding, several pieces of stainless steel plate shaped similar to the flanges are placed between the parts of the tube that have heating elements and the flanges. Additionally, several layers of niobium and aluminum foil cover the interior and exterior of the quartz tube, respectively, as radiation shielding. The quartz tube is sealed by two Swagelok fittings with high-temperature o-rings and the whole

system is evacuated by a turbomolecular pump to a pressure below 10^{-6} Pa. A programmable temperature controller was used to drive a 1 kW DC power supply through a solid state relay. Uniformity of sample temperature was confirmed by placing multiple ultra-fine thermocouples at different positions inside the quartz sample cell or on the sample pellet.

Figure 5.9: The structure of a Raman furnace, including ceramic rods, stainless flanges, and quartz tube

Low-temperature measurements are possible by mounting samples on cold fingers cooled by either displex refrigerators or liquid nitrogen or helium. The base temperature is usually limited by radiation heating through the optical window from the environment. Our configuration using liquid nitrogen can reach about 90 K.

In high-pressure Raman spectroscopy, diamond anvil cells (DAC) and micro Raman systems are used together. A long-distance objective lens is necessary due to the large size of the cell. The DAC is quite similar to those used for synchrotron experiments, but the diamonds need to have good optical quality because impurities may cause an overwhelming amount of fluorescence.

5.4 Data Analysis

Compared to neutron scattering, analyzing Raman spectra is more straightforward, although it does have some of its own tricks. Spectra from 2D detectors such as CCDs are firstly binned into one dimension, but it is always a good idea to check the 2D spectra for possible alignment issues. If multiple spectra were collected during the same measurement series, they are combined. CCDs are sensitive to high-energy particles from cosmic rays or background radiation, so there are always sporadic peaks. It is easy to determine them by comparing spectra from the same measurements, and they must be removed carefully before processing.

The backgrounds then need to be removed. For spectra with small wavelength ranges, linear functions are usually sufficient, but otherwise the background is more complex and should be fitted with polynomials and then removed. The curvature of the background could come from stray light, black-body radiation, the dependency of scattering efficiency (ν^{-4}), detector efficiency, and many other factors.

After background substraction, the spectra are fitted by multiple-peak fitting routines using Gaussian or Lorentzian functions. For a structural study, only the peak centers are of interest, but the linewidths are just as important for studies of phonon lifetime.

5.5 Time-Resolved Raman Spectroscopy

The development of nanosecond, picosecond, and femtosecond lasers have made it possible to use time-resolved spectroscopies for characterizing the dynamics of chemical and biological systems. Detailed explanations of the principles are clearly beyond the scope of this work, so only some concepts are presented here.

Time-resolved Raman (TRR) spectroscopy can be divided roughly into two different categories: transient resonance Raman spectroscopy and the more general time-resolved Raman spectroscopy. The former involves only one laser

pulse and studies the process within the time scale of the pulse length, while the later uses two pulses and the “ump-probe” method. These two pulses are split from a single laser output and spatially delayed to arrive at the sample at different times. However, this allows at most tens of nanoseconds in delay time. For longer time delays, two sets of electronically synchronized lasers are necessary. Our system is designed to work in both modes.

To be able to gate the Raman spectra for time-dependent measurement, a few different techniques are possible. For laser pulses at picosecond scales or shorter, it is possible to optically gate the signal using a Kerr gate, which utilizes the Kerr effect to turn the media into a waveplate. It is also possible to use an electronically synchronized Pockels cell for gating, as shown in Fig. 5.10 for our setup in single laser mode. Gating at the detectors is another approach, and benefits from advances in detector techniques. Beside studying dynamics, time-resolved techniques can also help in the fluorescence suppression in conventional Raman spectroscopy.

5.6 Other Raman Techniques

There is a quite large family of spectroscopy techniques using Raman effects. Each of them has unique advantages and also some drawbacks. Here is a brief summary of the concepts.

Second-order Raman scattering is much weaker (1/100) than its first-order counterpart, but it is not governed by the same selection rules so it is able to measure the whole Brillouin zone. Second-order Raman spectroscopy can be reasonably approximated by a phonon DOS with the frequency axis multiplied by two. Its shape may be quite similar to a 2-phonon DOS in many cases.

Fourier-transform (FT) Raman uses a near-IR laser and the collection of the scattered light is performed using Michelson interferometers and Fourier-transform processors. The spectra usually have modest quality and limited range, but the method can be made suitable for routine analysis. Hadamard-transform spec-

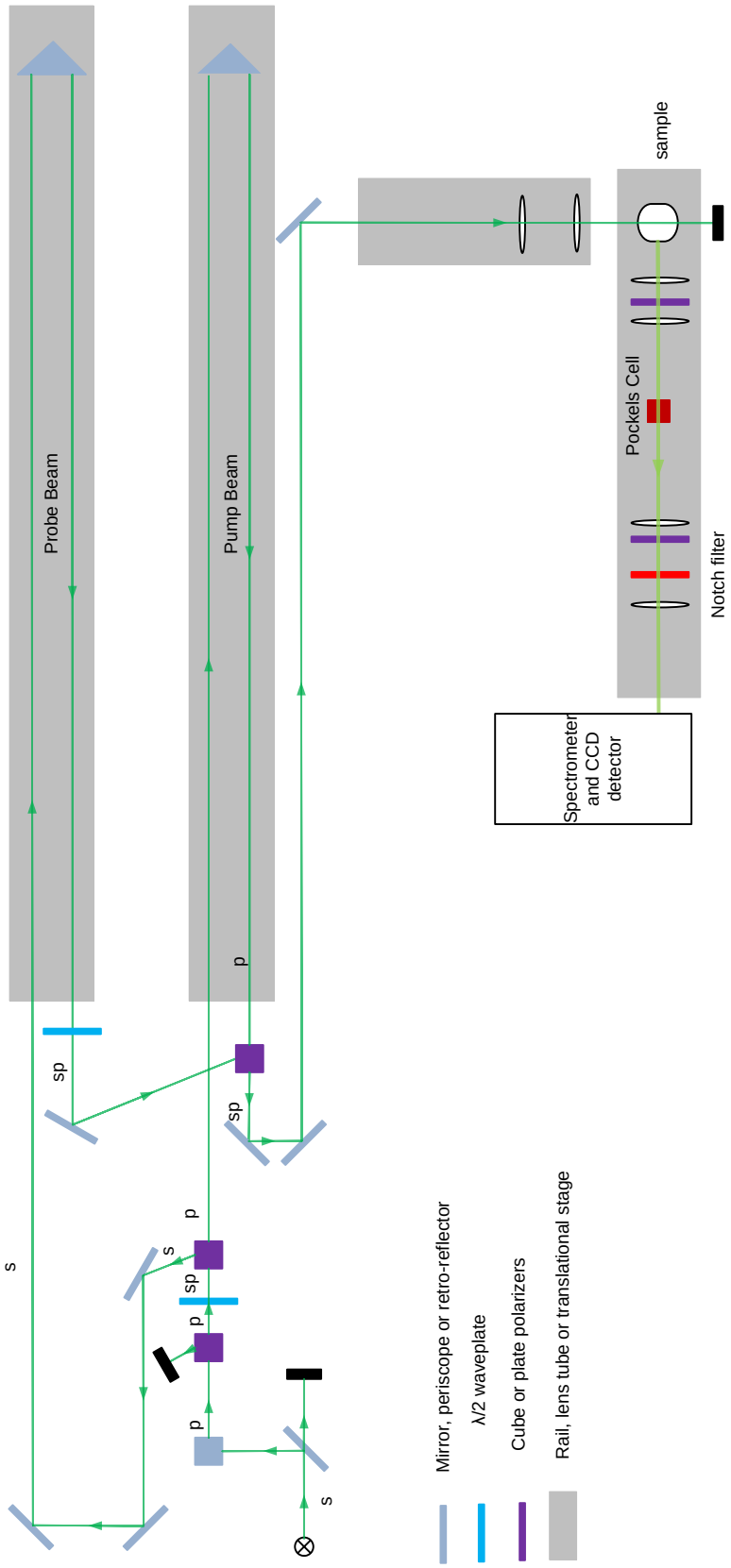

Figure 5.10: A schematic of the time-resolved Raman system using optical delay lines and Pockels cell in a single laser configuration

troscopy is a third alternative to dispersive and FT Raman. It has some of the desired features of both.

Micro-Raman spectroscopy uses the backscattering geometry mentioned above, and can study a small sample volume thanks to its use of a microscope objective lens. It is quite useful for polarization studies on small single crystals and samples under high pressure in diamond anvil cells.

Coherent Raman spectroscopy goes beyond the linear response approximation with stronger amplitude. Among many coherent Raman techniques, two are most popular: coherent anti-Stokes Raman spectroscopy (CARS) and stimulated Raman spectroscopy (SRS).

5.7 Other Considerations

During the Raman scattering process, incident photons interact with the dipole moments in the material through polarizability. It is very important to note that, in general, molecule sizes are negligible compared to the photon wavelength. As a result, the molecules are treated as a whole, and the polarizability is in terms of the molecule instead of the underlying bonds. [96] However, this approximation is not always valid, and the scattering process is much more complicated if the local polarizability is taken into account.

Part IV

Ionic Compounds

Chapter 6

Hafnium(IV) Oxide (Hafnia, HfO_2)

Raman spectra of monoclinic hafnium(IV) oxide (HfO_2) were measured at temperatures up to 1100 K. Raman peak shifts and broadenings are reported. Phonon dynamics calculations were performed with the shell model to obtain the total and partial phonon density of states (DOS), and to identify the individual motions of hafnium and oxygen atoms in the Raman modes. Correlating these motions to the thermal peak shifts and broadenings, it was found that modes involving changes in oxygen-oxygen bond length were the most anharmonic. The hafnium-dominated modes were more harmonic, and showed relatively less broadening with temperature. Comparatively, the oxygen-dominated modes were more influenced by the cubic term in the interatomic potential than the hafnium-dominated modes. An approximately quadratic correlation was found between phonon-line broadening and softening.

6.1 Introduction

Hafnium(IV) oxide (HfO_2), also known as hafnia, is one of the most common and stable compounds of hafnium. Hafnium-based oxides are leading candidates to replace silicon oxide as gate insulators in field-effect transistors, largely because the high dielectric constant of hafnia allows greater miniaturization of microelectronic components without increased leakage current. [97, 98] Owing to its chemical stability, physical hardness, high refractive index, and high threshold for laser damage, hafnia has been widely used in coatings on optical components for laser applications in the near-UV-to-IR spectral regions. Hafnia is also an important material for applications at high temperatures, owing to its high bulk modulus and high melting temperature. [99]

Hafnia, like zirconia (ZrO_2), is monoclinic ($P2_1c$) at ambient pressure and temperature (see Fig. 6.1). Both hafnia and zirconia transform to a tetragonal phase ($P4_2nmc$) at approximately 2000 K [100, 101], and to a cubic phase ($Fm3m$) at higher temperatures and pressures. [100] Many other similarities between hafnia and zirconia are sometimes attributed to the lanthanide contraction [101],

and these include a nearly one-to-one correspondence of their Raman spectra. [101, 102] The room-temperature monoclinic crystal structure of hafnia has four formula units (i.e., 12 atoms) per unit cell, and hence 36 normal modes at the Γ point. The group theoretical analysis of mode symmetry by Anastassakis et al., [103] predicts 18 Raman active modes (A_g and B_g), 15 infrared active modes, and 3 acoustic modes. The Raman-active and infrared-active modes of hafnia prove mutually exclusive (a mode can be Raman-active only or IR-active only). Prior experimental and theoretical Raman spectroscopy analysis of hafnia has been hindered by the complexity of the vibrational symmetry. Anastassakis et al. [103] were able to identify 17 modes of vibration, but assignment of the peaks proved difficult, especially for modes at higher energies. Other studies have focused on the phase transition under pressure [104, 105], while first-principles calculations were performed to obtain a better understanding of the vibration modes. [106, 107] To date the assignment of Raman peaks of hafnia has not been fully convincing.

The focus of the present work is on the non-harmonic vibrational dynamics of hafnia. High-temperature vibrational studies of metal oxides are relatively rare. Several metal oxides, such as beryllia (BeO) and lithia (Li_2O), have been shown to exhibit anharmonic behavior at elevated temperatures, primarily due to a change of phonon lifetime resulting from phonon-phonon interactions. [108] Although there has been no previous reports of phonon anharmonicity in hafnia, its unusually high specific heat at temperatures above 800 K [109], which is well below the temperature of any phase transition, suggests interesting anharmonic behavior. Similar behavior has been reported in a thermodynamic assessment of zirconia. [110]

A contribution to the heat capacity at constant pressure is expected as a crystal expands against its bulk modulus. “Quasiharmonic” shifts of phonon frequencies arise because these frequencies are reduced in an expanded crystal, thus yielding a larger vibrational entropy that favors some thermal expansion. The reported increase in heat capacity [109] of around $2 - 3 \times 10^{-2}$ [J/(mol K)]/K is much larger

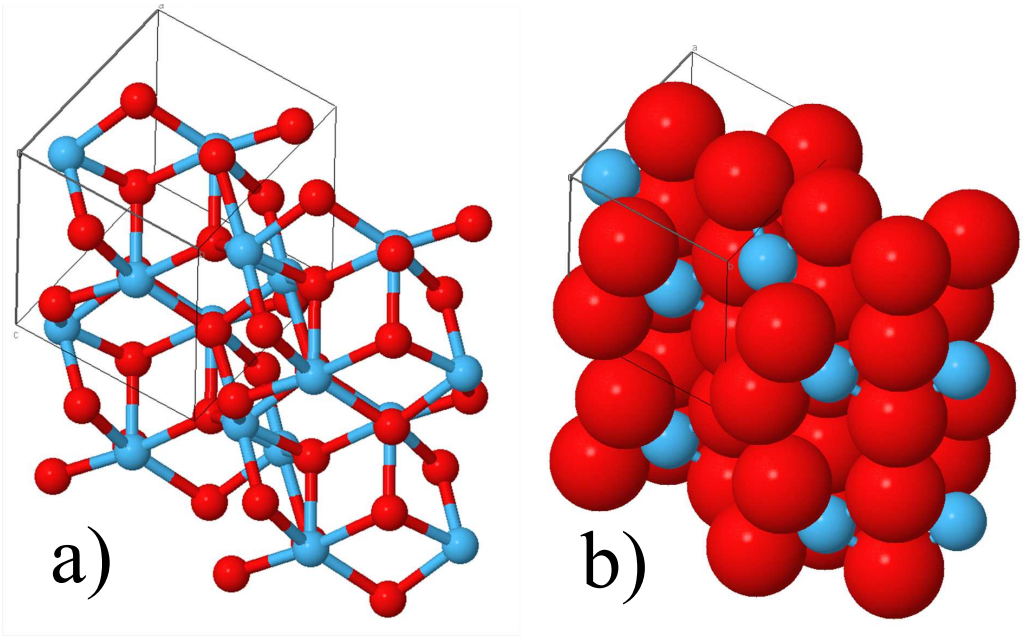

Figure 6.1: Two views of the crystal structure of monoclinic hafnia. Red and blue spheres denote oxygen and hafnium atoms, respectively. a: skeletal; b: space-filled model, scaled for ionic radii. Note that the majority of the volume is composed of oxygen, while hafnium fits loosely between oxygen planes. (Zirconia has the same structure with a small difference in lattice parameters.)

than expected from this quasiharmonic phonon mechanism, however. Anharmonic effects from phonon-phonon interactions are therefore of interest. Inelastic neutron scattering studies of hafnia are impractical, owing to the large neutron absorption cross section of hafnium. [111] Previous temperature-dependent Raman spectroscopy studies of hafnia were limited to 800 K , [105] and were performed with relatively low resolution. Besides the phonon frequency shift information that is typically used to understand vibrational thermodynamics, line broadening information from high-resolution measurements allows an assessment of how anharmonic effects originate from the third- or fourth-order terms of the interatomic potential. In the present work on hafnia, we report measurements of Raman line positions and shapes to temperatures of 1100 K, characterize the types of modes that are most anharmonic, and correlate anharmonic effects to the vibrational displacements of individual atoms in the unit cell.

6.2 Experiment

Samples were prepared from commercial hafnia powder[1] having a grain size around 40 μm. Two methods of preparation were used: 1) Hafnia powder was loosely packed inside a quartz cell, or 2) the powder was compressed into pellets at ambient temperature and under a pressure of 30 MPa. Both samples were characterized by X-ray diffractometry and both types exhibited a pure monoclinic phase (with phase fraction of at least 99%). It was found that samples prepared as pellets gave spectra identical to those prepared as a loose powder.

Many details of the experiment can be found in Chapter 5. The samples were mounted in a quartz optical cell of 1 mm thickness, evacuated by a turbomolecular pump to a pressure below 10^{-8} Pa. Sample heating was provided by electrical-resistance heating elements in the vacuum space. The furnace was composed of ceramic rods for insulation, stainless steel flanges as structure support, several layers of niobium foil as heat shields, stainless steel plates, and aluminum foil covering the interior and exterior of the quartz tube as radiation shielding. A temperature controller was used to drive a 1 kW DC power supply through a solid state relay. Uniformity of sample temperature was confirmed by placing multiple ultra-fine thermocouples at different positions inside the quartz sample cell.

The excitation source for the Raman spectrometer was the 532 nm line of a Nd:YAG laser[2] at power levels of 200 mW or lower. A high-efficiency edge filter[3] ($OD = 6$) was used to block the laser line. A single-pass spectrometer[4] was used for the spectral imaging on a 2D CCD camera with thermoelectric cooling[5]. Raman spectra were acquired at temperatures from 300 K to 1100 K in increments of approximately 25 K, with a temperature resolution of ± 1 K. Spectra at the higher temperatures had a sloping background from black-body radiation that was subtracted before fitting. Measurements at 300 K, repeated after the heating

[1] Alfa Aesar, Ward Hill, MA 01835
[2] Quanta-Ray Lab Series
[3] Semrock Stopline E-grade single-notch filter
[4] Princeton Instruments Acton Series 500 mm
[5] Princeton Instruments PIXIS 400B

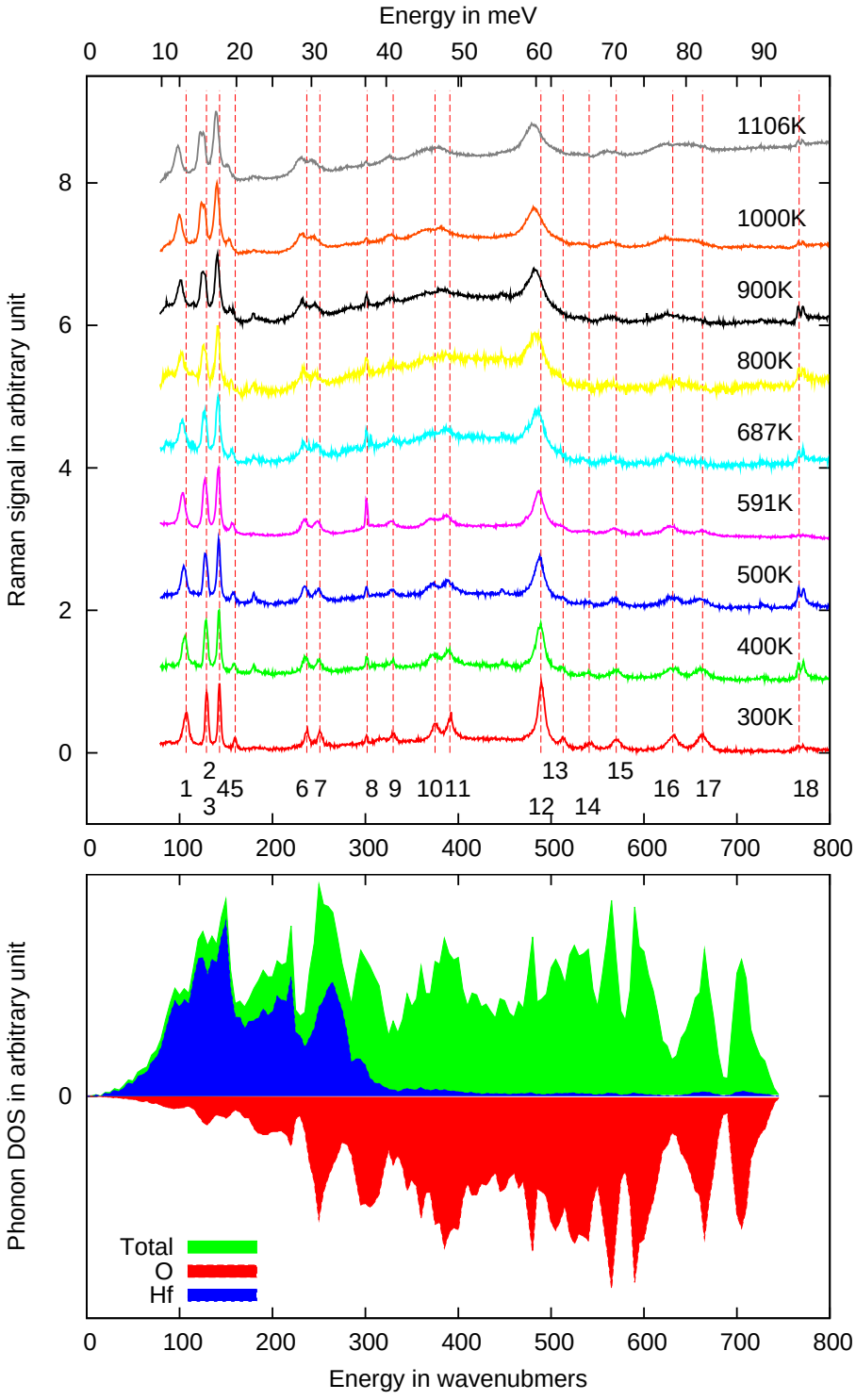

Figure 6.2: (Upper) Raman spectra of hafnia at temperatures from 300 to 1106 K, with laser power at 200 mW, exposure time of 30 seconds, and at least 10 accumulations of the spectra. Peaks are numbered for reference. The features between peaks 5 and 6 are artifacts.
(Lower) Partial and total phonon density of states of hafnia at room temperature, calculated using GULP. Hafnium contributes much more strongly to the lower-energy modes, while oxygen contributes to the higher-energy modes.

sequence, confirmed that the samples underwent no changes that affected their Raman spectra.

6.3 Results

The Raman spectrum at room temperature and ambient pressure appears to consist of 17 peaks, but the second peak consists of two overlapping modes (labeled 2 and 3 in Fig. 6.2). Spectra measured at temperatures above 600 K show the separation of a shoulder from the second peak, evidence of a two-peak structure. At higher temperatures, several of the weaker modes either could not be resolved from the background or their position could not be determined reliably. Nevertheless, several strong peaks remained distinct to the highest temperature attained. The spectra acquired at all 33 temperatures (many not shown in Fig. 6.2) were used to obtain the effects of temperature on line position and linewidth. A curved background, believed intrinsic to each sample, was first subtracted from each spectrum. Each measured spectrum was then fit with multiple Lorentzian functions to extract the centroid and the full-width at half-maximum (FWHM) for each peak. The linewidth of the spectrometer resolution was negligible when compared to the error in the fitted linewidth.

The results, presented in Figs. 6.3 and 6.4, show that with increasing temperature, the Raman peaks generally shift to lower frequencies, and generally broaden in width. (Owing to the larger uncertainty for the linewidths of weak peaks, results from only the stronger peaks are presented in Fig. 6.4.) There are substantial differences in the amount of shift and amount of broadening for the different Raman peaks, with some peaks showing minimal effects of temperature. Interpreting the different non-harmonic behaviors of the different Raman peaks requires a detailed understanding of the atom motions in the different Raman modes.

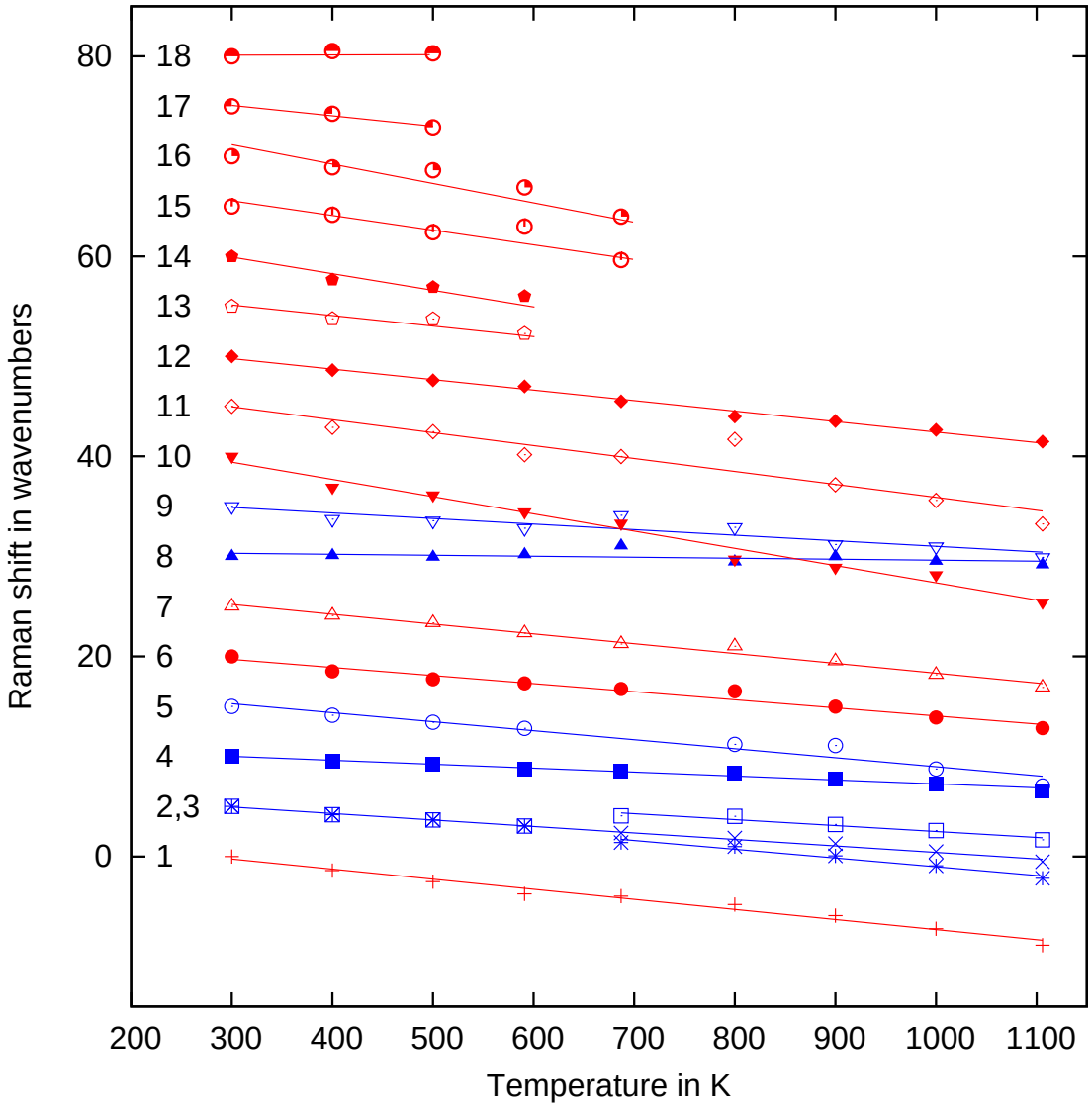

Figure 6.3: Temperature-dependent Raman mode softening in hafnia. At 300 K, modes are evenly spaced in the figure to facilitate comparison of thermal shifts. Blue and red represent metal- and oxygen-dominated modes, respectively. Lines are linear fits to the data points. Note that 2nd and 3rd modes are decoupled above 700 K, where the line between the 2nd and 3rd modes represents an average peak position. Most error bars are negligibly small. Peaks from the 13th to 18th were not sufficiently distinct to allow fitting at high temperature.

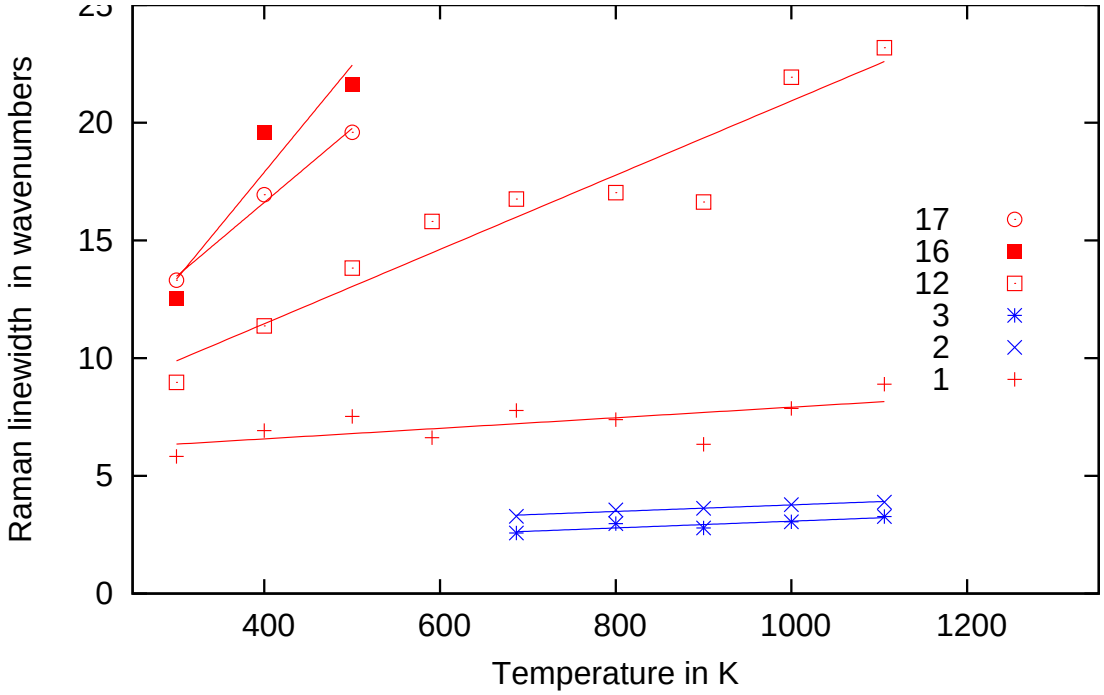

Figure 6.4: Temperature-dependent peak broadening in hafnia. Blue and red represent metal- and oxygen-dominated modes, respectively. Lines are linear fits to the data.

6.4 Calculations

To assign vibration modes to spectral peaks, Raman mode frequency calculations were performed with the GULP package, [59] using the force-field constants from Lewis, [112] and the Buckingham two-body shell model potential. Results are listed in Table 6.1. Good agreement was found between the calculations and Raman spectroscopic data from the present and previous experiments, and reasonable agreement with previous ab initio calculations, especially with the GGA method.

Calculations of the phonon density of states (DOS) were also performed with the GULP software package by sampling over points in k-space. The resulting total and partial DOS are shown in Fig. 6.2. Many of the phonon branches had low dispersion, giving a number of sharp peaks in the DOS. The maximum phonon energy was about 90 meV. Calculations with GULP of the heat capacity at constant volume gave results as expected for harmonic oscillators, approaching 25 J/(mol K) at temperatures above 1000 K. The eigenvectors of phonons at the Γ point

Table 6.1: Raman mode frequencies, fractional atomic contribution for each mode, and mode Grüneisen parameters of hafnia

Mode	Exp	GULP	Lit-1[1]	Lit-2[2]	Lit-3[3]	Hf%	O%	γ_j[4]	γ_k[5]
1	106.8	120.9	128	125	113	0.30	0.70	4.83	10.6
2	129.1	162.5	142	132	133	0.95	0.05	3.45	2.7
3	129.1	172.8	131	120	133	0.74	0.26	2.35	2.7
4	142.9	181.0	152	171	149	0.99	0.01	1.40	2.2
5	159.6	185.8	175	152	164	0.99	0.01	2.89	1.8
6	236.8	228.2	250	223	242	0.05	0.95	1.75	0.4
7	251.3	268.4	261	248	256	0.03	0.97	2.00	0.8
8	301.5	291.8	326	339	323	0.97	0.03	0.17	-
9	329.9	308.3	380	318	336	0.81	0.19	0.86	1.5
10	375.0	341.2	423	382	382	0.10	0.90	2.35	1.8
11	391.1	357.2	424	385	398	0.13	0.87	1.69	1.8
12	489.3	448.1	514	440	498	0.00	1.00	1.10	-0.4
13	513.3	518.0	533	466	520	0.01	0.99	1.05	-0.4
14	541.3	537.0	570	529	551	0.02	0.98	1.58	1.5
15	570.3	552.9	608	557	577	0.01	0.99	1.32	1.2
16	631.1	628.8	667	627	640	0.00	1.00	1.57	1.5
17	662.5	662.0	738	640	672	0.02	0.98	0.81	0.9
18	769.8	727.1	821	716	773	0.01	0.99	-0.016	-

[1]LDA calculation by Zhao and Vanderbilt [106]
[2]GGA calculation by Zhao and Vanderbilt [106]
[3]Experimental measurement by Arashi [113]
[4]Calculated from present experimental data
[5]Room-temperature pressure data by Jayaraman et al. [104]

were used to estimate the participation of Hf or O in each Raman-active mode, with results listed in Table 6.1. Consistent with Fig. 6.2, the heavier metal atoms dominate the low-energy modes, whereas the lighter oxygen atoms have most of the energy of the high-energy modes. Most of the Raman modes are either metal dominated (2, 4, 5, and 8), or oxygen dominated (6, 7, 10, and 12–18). The few mixed modes (1, 3, 9, and 11) are still heavily biased. This approximate separation of modes into Hf-modes and O-modes is consistent with the large difference in mass of oxygen and hafnium atoms.

6.5 Discussion

The quasiharmonic softening of a normal mode is related to thermal expansion

$$\omega_j(T) = \omega_j(0) \exp\left(-\gamma_j \int_0^T \beta(T)\, \mathrm{d}T \right) , \tag{6.1}$$

where $\omega_j(T)$ is a temperature-dependent vibrational frequency, β is the volume thermal expansivity, and γ_j is the mode Grüneisen parameter, which relates the fractional change in vibrational frequency to the fractional change in volume

$$\frac{\Delta\omega_j}{\omega_j} = -\gamma_j \frac{\Delta V}{V} . \tag{6.2}$$

The thermodynamic Grüneisen parameter, γ, for a quasiharmonic solid is

$$\gamma = \frac{\beta B V}{C_V} , \tag{6.3}$$

where B is bulk modulus and and C_V is the specific heat at constant volume. This γ is an average of all mode Grüneisen parameters $\{\gamma_j\}$, weighted by the modal Einstein specific heats C_j

$$\gamma = \frac{\sum_j \gamma_j C_j}{\sum_j C_j} . \tag{6.4}$$

From Table 6.1, however, we see that an average Grüneisen parameter misses the rich variation of the mode Grüneisen parameters. Such a wide variation of mode Grüneisen parameters might be expected from the highly anisotropic thermal expansion of hafnia. From 300 K to 500 K, its linear thermal expansion is 0.23%, 0.15%, and 0.0% for the c, a, and b axes, respectively. At higher temperatures, the a and c axes still expand much faster than the b axis. [114]

The remainder of this chapter focuses on the non-harmonicity of individual modes. Figure 6.3 and Table 6.1 show that temperature-dependent frequency shifts do not depend on the energy of each normal mode, as might be expected if all γ_j of Eq. 6.2 were similar. There is, instead, a tendency of the mode Grüneisen parameters to decrease with mode frequency, related to the atom displacements in each mode. We divide the normal modes into two groups: oxygen-dominated modes and metal-dominated modes. From Fig. 6.3 it is apparent that the oxygen modes undergo more thermal softening than the metal modes. An especially interesting comparison is the softening of the number 2 and 3 modes. At 700 K the two modes are resolved, and the absolute mode spacing increases at higher temperatures. The number 2 mode is composed of 95% oxygen, whereas the number 3 mode is 75% oxygen.

The temperature dependence of the Raman peak widths provide further information about anharmonicity. [115, 116] The observed Lorentzian peak shapes are consistent with the expected energy broadening from shortened phonon lifetimes. In Fig. 6.4, a plot of the absolute broadening of normal modes demonstrates that the oxygen modes (with reasonable resolution across the measured range of temperatures) broaden faster than the metal modes, qualitatively consistent with the trend found for mode softening. (Note that in calculation of the linewidth, the number 2 and 3 peaks must be treated independently—as the two peaks begin to soften at different rates, fitting both peaks with a single Lorentzian function would result in widening, even if the individual peak widths remain unchanged.)

A useful perspective on the hafnia structure (Fig. 6.1) is that oxygen anions make up the structural framework of the crystal, and the hafnium ions are located

in the gaps between the oxygen ions. A more detailed view shows that the structure of hafnia contains layers of oxygen anions, with the remaining oxygen and hafnium ions inserted loosely between these layers. The oxygen layers lie approximately in the plane of the *b* and *c* axes, with the *b* direction closer packed than the *c* direction. Figure 6.1 depicts the ionic radius of oxygen (1.40 Å) as almost twice as big as that of hafnium (0.78 Å). Based on structure data from x-ray diffractometry, [117] the oxygen-oxygen bonds have lengths of 2.51 or 2.64 Å, and hafnium-oxygen bonds have lengths of 1.98, 2.22, 2.17, 2.23, and 2.26 Å. As the lattice expands with temperature, the largest changes in atomic overlap occur for oxygen anions. Changes in this overlap are expected to affect the vibrational frequencies, especially those for oxygen modes.

The analysis of individual normal modes, including the four shown in Fig. 6.5, offers more detailed information on the origin of non-harmonic behavior. The number 4 mode, representative of a hafnium-dominated mode, has hafnium cations moving into the cavity between three adjacent oxygen anions, in nearly parallel motion. The large size of the anions allow the cavity to impose few restrictions on the cations moving into it. Mode 4 is one of the most harmonic of all the Raman modes. For a comparison, mode number 3 also is a metal-dominated mode where the metal cations move into cavities between the oxygen anions; however, half the oxygen anions in mode 3 are also moving, and they are moving in different planes with respect to each other. The larger contribution from oxygen to mode number 3 (the partial DOS for mode 3 is 26% O, 74% Hf) makes it less harmonic than mode number 4 (the partial DOS is 99% Hf).

The behavior of oxygen-dominated modes is substantially different from that of the hafnium-dominated modes just considered. In mode number 6, half of the anions (the outer oxygen planes) are stationary, while the remaining anions (the inner oxygen plane) are moving parallel to the *c* axis—the non-stationary oxygen anions simply move into the space left by preceding ones. The result is that the oxygen-oxygen bond is largely unchanged during vibration. This mode is one of the most harmonic of all the oxygen-dominated modes. Mode number

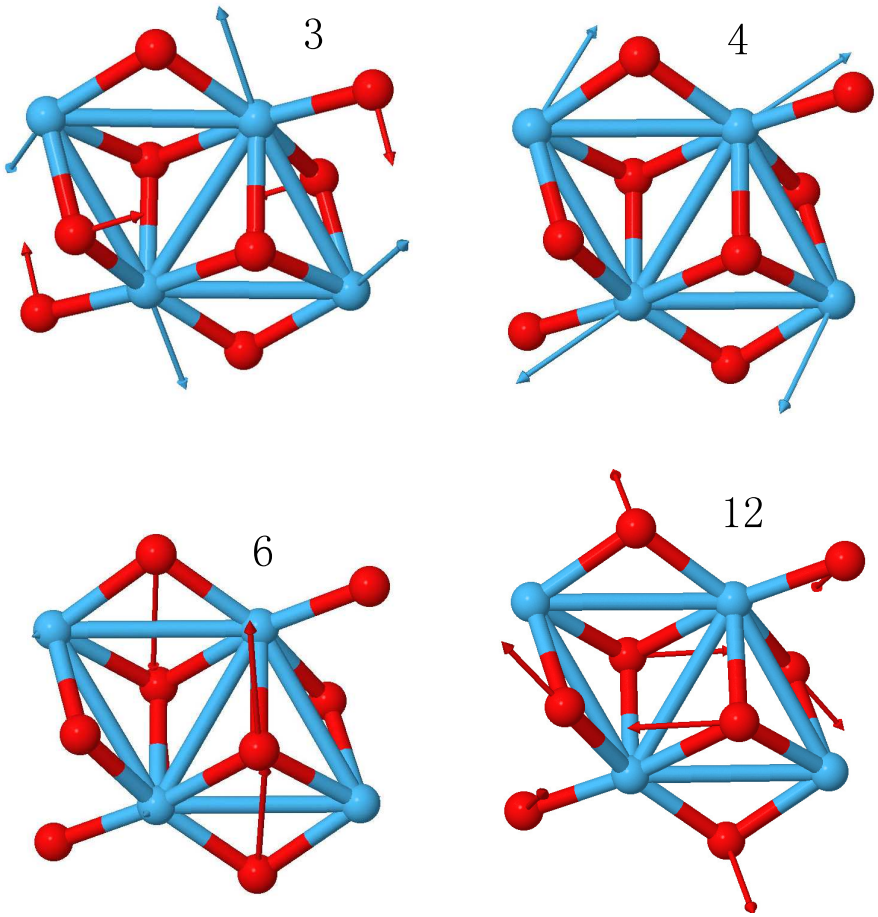

Figure 6.5: Representative Raman active normal modes in one hafnia or zirconia unit cell. Number 3 and 4 modes are hafnium(or zirconium) dominated. Number 6 and 12 are oxygen dominated. These modes were well resolved through the whole range of temperatures. Lengths of arrows are proportional to the contribution of vibration from each atom.

12 is less harmonic. It involves relatively large changes in oxygen-oxygen bond lengths, and the bending of oxygen-oxygen bonds. These four modes were chosen for their relatively simple pattern of vibration. Other normal modes not shown in Fig. 6.5 provide similar correlations between oxygen-oxygen bond distortions and non-harmonic behavior. We find that the oxygen-dominated modes in hafnia are less harmonic than the metal-dominated modes. Furthermore, the modes involving a change in oxygen-oxygen bonding exhibit the most non-harmonic behavior.

Figure 6.6 shows a parametric relationship between the the peak broadening and the peak softening. A boundary exists between oxygen modes and metal modes, and all modes with non-negligible contributions from both elements fall close to the boundary. The larger non-harmonic effects are found for oxygen-dominated modes.

Phonon frequency shifts and broadenings have been analyzed by treating phonon-phonon interactions with perturbation theory [30]. The analysis of Raman spectra is practical with the Klemens model [118], which considers how one optical phonon decays into two acoustical phonons. Analysis of this three-phonon process for decay of an optical phonon at the Γ-point is simplified because the two acoustic phonons must be of opposite wavevectors, and matched in energy if they are on the same branch. (Equilibrium phonon populations are also assumed.) This approach has been extended to four-phonon processes [119], but these simplifications are now less appropriate for describing the full physical picture. They do show that the temperature dependence becomes more complex [119], and the temperature-dependent phonon linewidth broadening Γ_j of mode j can be expected as

$$\Gamma_j(T) = \Gamma_j(0) + A_j\left[1 + \frac{2}{e^{\hbar\omega_j(0)/2k_BT}-1}\right] + B_j\left[1 + \frac{3}{e^{\hbar\omega_j(0)/3k_BT}-1} + \frac{3}{\left(e^{\hbar\omega_j(0)/3k_BT}-1\right)^2}\right] \tag{6.5}$$

where $\Gamma_j(0)$ is a constant; A and B are parameters for three-phonon and four-phonon processes, respectively. At ambient or higher temperatures, the contribu-

tions from the two terms vary as T and T^2, respectively. In the experimental data of Fig. 6.4, linewidth broadenings of the hafnia spectra are found to be linear with temperature, so there is little contribution from the four-phonon process of Eq. 6.5 ($B = 0$). For different modes, the parameter A ranged from 0.02 to 0.77 cm^{-1}.

An analogous expression to Eq. 6.5 for the frequency shift at elevated temperature has been proposed [119], but from experimental data at elevated temperature it is not practical to separate the anharmonic frequency shift from the shift from quasiharmonic lattice dilation. Fortunately, pressure-induced shifts of Raman peaks were reported by Jayaraman et al. [104], and these can be used to identify the quasiharmonic contribution. Their results are listed as Grüneisen parameters in Table 6.1. By comparing the pressure Grüneisen parameters to the thermal Grüneisen parameters, we find general agreement for all modes dominated by hafnium motions. On the other hand, there are major discrepancies for at least half of the oxygen modes, and some have opposite signs. The deviation of our elevated temperature results from those of prior high-pressure work again suggests that the oxygen-dominated modes are more anharmonic than the metal modes. Another result from perturbation theory is that the leading term for phonon broadening is the cubic term, whereas the peak shift originates from the quartic term in first order, and the cubic term in second order. [32] With temperature, the metal-dominated modes shift in frequency with comparatively little broadening. This could be primarily quasiharmonic behavior consistent with the high-pressure results. In contrast, for the oxygen-dominated modes, which show more broadening, the non-harmonic effects likely originate from the cubic term in the interatomic potential, consistent with the linearity with T of the shifts and broadenings over the range of temperature in this study.

Nevertheless, the non-harmonic effects in hafnia at temperatures to 1100 K are relatively small, and hafnia is generally quasiharmonic. The non-harmonic contribution is estimated to be about only 2×10^{-3} [J/(mol K)]/K, which is not large enough to explain the anomalously large slope of the heat capacity vs. temperature curve for hafnia at these temperatures. [109] Perhaps degrees of

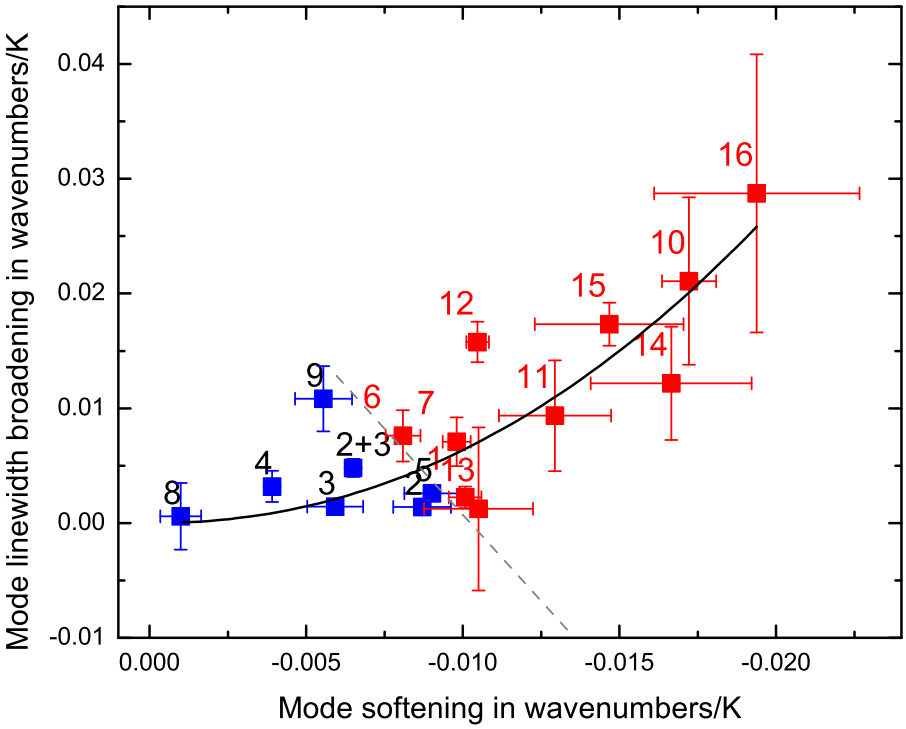

Figure 6.6: Broadening vs. softening of Raman modes. Blue and red squares are metal and oxygen modes, respectively. The dashed line is the boundary separating metal-dominated modes and oxygen-dominated modes. The solid line is a fitting to the points, showing that the relation between absolute linewidth broadening and absolute peak softening is of power 2.1, close to quadratic.

freedom other than phonons account for the excess heat capacity above 800 K, or perhaps the heat capacity results need to be checked.

6.6 Conclusion

Raman spectra were measured on monoclinic hafnia at elevated temperatures up to 1100 K. The peaks in the spectra were assigned to vibrational modes obtained by shell-model calculations, which provided the individual atom polarizations in each mode. The thermal softening and broadening of the Raman peaks were obtained from the measured spectra, and correlated to the individual atom dis-

placements in each mode. The oxygen-dominated modes were found to be more anharmonic than the hafnium-dominated modes. The least harmonic modes were found to involve the largest distortions of oxygen-oxygen bond distances (as opposed to oxygen-hafnium or hafnium-hafnium). Hafnium-dominated modes showed relatively little peak broadening for the peak shift, consistent with an approximately quasiharmonic behavior, having thermal Grüneisen parameters that were more consistent with previous high-pressure results than those for oxygen-dominated modes. The oxygen-dominated modes showed more peak broadening with peak shift, indicating a relatively large role for the first-order cubic term in the anharmonic behavior. Very little contribution from four-phonon processes is found through fitting perturbation theory results. Peak shifts and peak broadening, two strong indicators of the non-harmonicity of Raman modes, were quadratically correlated within the measured range of temperatures. The non-harmonic peak shifts in this temperature range are not large enough to account for the large previously reported heat capacity of hafnia above 800 K.

Chapter 7

Zirconium(IV) Oxide (Zirconia, ZrO_2)

Raman spectra of monoclinic zirconia (ZrO_2) were measured at temperatures up to 950 K. Temperature-dependent Raman peak shifts and broadenings were reported and compared to the results on hafnia (HfO_2). Lattice dynamics calculations were performed with both shell model and density functional theory methods to obtain Raman frequencies and the total and partial phonon density of states (DOS). These calculations were also used to identify the individual motions of metal and oxygen atoms in the different Raman modes. By correlating these motions to the thermal peak shifts and broadenings, it was confirmed that modes involving changes in oxygen-oxygen bond length were the most anharmonic, similar to the case of hafnia. The metal-dominated modes were found to be more quasiharmonic, and thus showed less broadening with temperature. Mass effects were evident by comparing the mode softening and shifting between zirconia and hafnia.

7.1 Introduction

Zirconium oxide (ZrO_2), also known as zirconia or baddeleyite, and hafnium oxide (hafnia, HfO_2), are structural twins. They are two of the most studied ceramic materials. They share many properties and applications. Oxides based on zirconium and hafnium are leading candidates to replace silicon oxide as gate insulators in field-effect transistors, largely because their high dielectric constant allows greater miniaturization of nanoelectronic components without increased leakage current. [97, 98] Their chemical stability and physical hardness also make them useful as optical coatings. Both zirconia and hafnia are important materials for service at high temperatures, owing to their high bulk moduli and high melting temperatures. [99]

Both zirconia and hafnia are monoclinic ($P2_1c$) at ambient pressure and temperature, while transforming to a tetragonal phase ($P4_2nmc$) at approximately 2000 K [100, 101], and to a cubic phase ($Fm3m$) at higher temperatures and pressures. [100] Other similarities between hafnia and zirconia, such as ionic

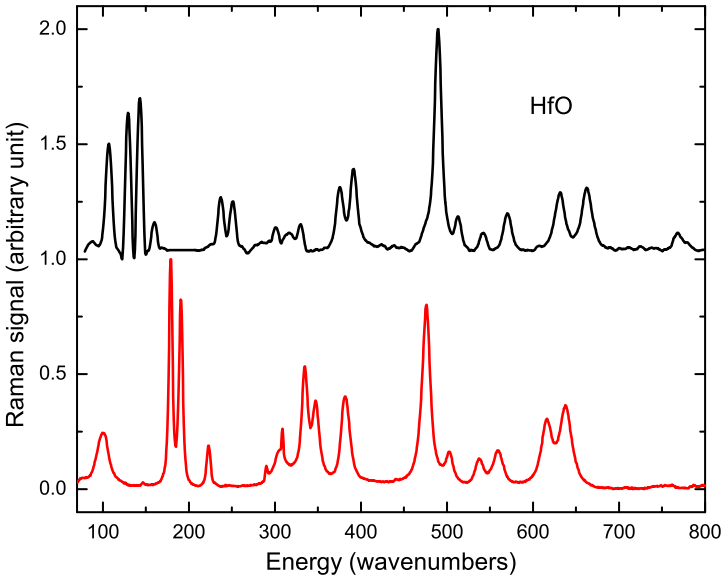

Figure 7.1: A comparison of the Raman spectra of hafnia and zirconia. Most modes are easily matched with one-to-one correlation.

radii, chemical properties, and a nearly one-to-one correspondence (Fig. 7.1) of their Raman spectra [101, 102], are sometimes attributed to the lanthanide contraction. [101] These two oxides have room-temperature monoclinic crystal structures with four formula units (i.e., 12 atoms) per unit cell, and hence 36 normal modes at the Γ point. The group theoretical analysis of mode symmetry, performed by Anastassakis et al. [103] predicts 18 Raman active modes (A_g and B_g), 15 infrared active modes, and 3 acoustic modes. The Raman active and infrared active modes of zirconia and hafnia are mutually exclusive (a mode can be Raman active only or IR active only). Prior experimental and theoretical Raman spectroscopy analysis of the two oxides have been hindered by the complexity in the vibrational symmetry of these compounds, especially for the modes at higher energies. [100] First-principles calculations have been performed to obtain a better understanding of these vibrational modes. [106, 107] Other studies have focused on phase transitions under pressure [104, 105, 120].

While the anharmonic behavior in hafnia and zirconia are not well understood,

these two oxides have a high specific heat per atom at temperatures well below the point of any phase transition [121] [109], suggesting that these materials should have interesting anharmonic behavior. In metal oxides, a contribution to the heat capacity at constant pressure is expected as the crystal expands against its bulk modulus. “Quasiharmonic" shifts of phonon frequencies may arise because phonon frequencies are reduced in an expanded crystal, thus yielding an increased vibrational entropy.

Studies of non-harmonic effects are important for understanding the thermodynamic stability and the thermal transport properties at elevated temperature. Aside from the phonon frequency shift information that is typically used to understand vibrational thermodynamics, phonon energy broadening measured with high resolution allows an assessment of how anharmonic effects originate from the third- or fourth-order terms of the interatomic potential. Unfortunately, prior Raman spectroscopy studies on zirconia have been limited in temperature, and have been performed with relatively low resolution. Further, inelastic neutron scattering studies of zirconia are also few and incomplete. [122]

In the previous chapter on the phonon dynamics of hafnia, as measured by Raman spectroscopy, we reported measurements of Raman line positions and shapes to temperatures of 1100 K, characterized the types of modes that are most anharmonic, and correlated anharmonic effects to the vibrational displacements of individual atoms in the unit cell. [123] It was found that although anharmonicity in hafnia is relatively small on average, it is quite large from the perspective of the individual mode. Similar behavior had been reported in an earlier thermodynamic assessment of zirconia. [110] The present work reports temperature-dependent Raman spectrometry on monoclinic zirconia. A comparison of zirconia and hafnia aids in interpreting the phonon dynamics in these two systems.

7.2 Experiment

The Raman measurements utilized commercial zirconia powder (Alfa Aesar) with a grain size of around 100 microns, tightly packed inside a spectrum-grade quartz cell. Additionally, pellets compressed from powders under a pressure of 30 MPa were also used, and gave spectra identical to the packed powder. Samples were characterized by X-ray diffractometry and were found to have a monoclinic phase with a phase fraction of at least 99.9%. Temperature-dependent Raman measurements were performed using the same electrical resistance furnace as for the hafnia study. [123]

The excitation source for the Raman spectrometer was the 532 nm line of a Nd:YAG laser (Quanta-Ray Lab Series) set at power levels of 200 mW or lower to minimize sample damage. A high-efficiency edge filter (Semrock Stopline E-grade single-notch filter, OD = 6) was used to block the laser line, and a single-pass spectrometer (PI Acton Series 500 mm) was used for the spectral imaging on a thermoelectrically cooled 2D CCD camera (Princeton Instruments PIXIS 400B). Raman spectra were acquired at temperatures from 295 K to 950 K, in increments of approximately 50 K. Further measurements were taken as the samples cooled to ambient temperature, confirming sample integrity against changes due to heating, such as the loss of oxygen.

7.3 Results

Fourteen of the eighteen Raman-active normal modes could be easily identified in the Raman spectrum measured at ambient temperature and pressure. These modes are labeled in Fig. 7.2, and vertical lines are aligned to the peak centers at 295 K. Previous studies suggest that modes 2 and 3 are likely overlapped, as was found for hafnia. [104] Experimental results and peak assignments to date have been inconsistent in regard to the missing modes.

With our improved furnace and optical system design, even at the highest

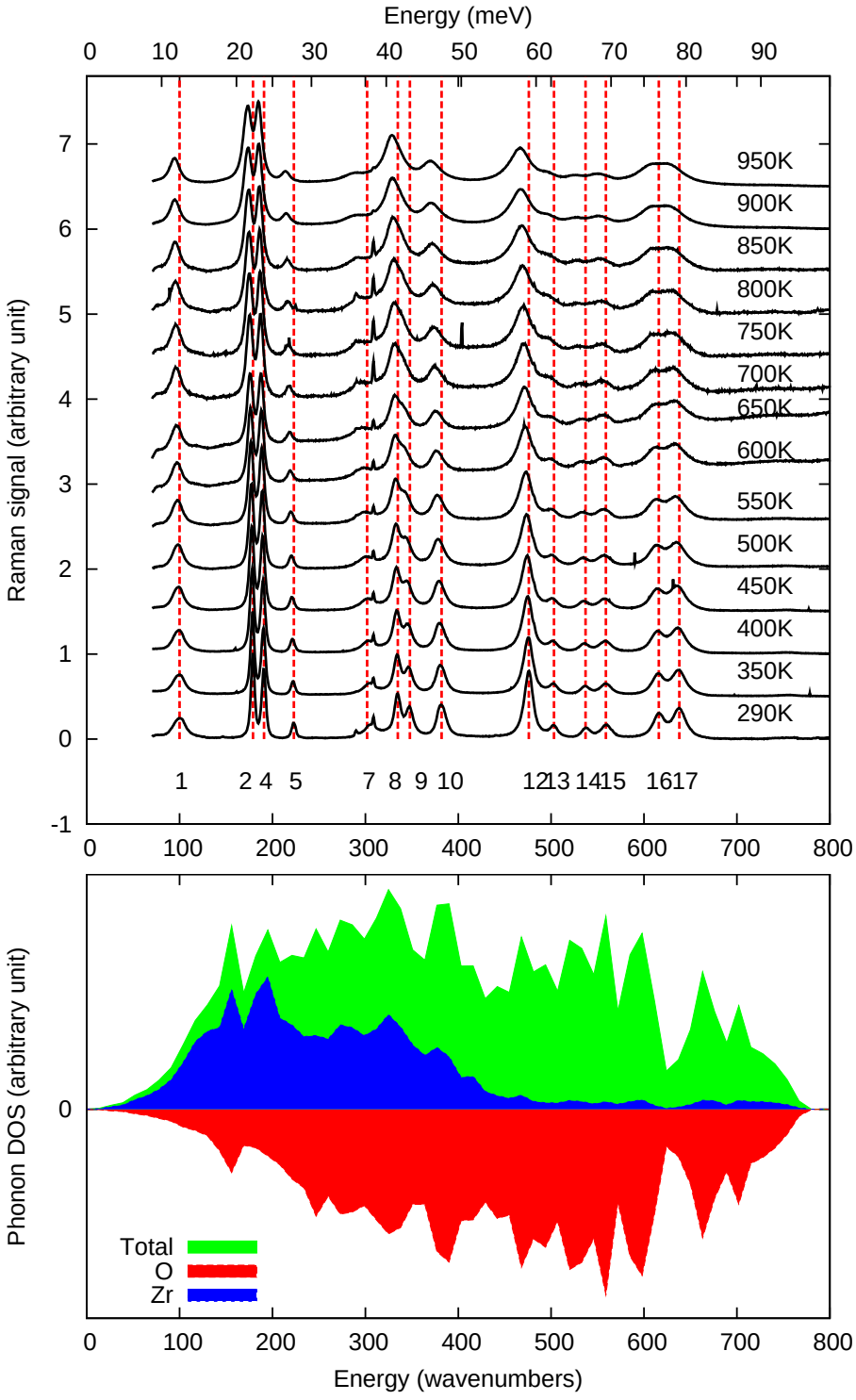

Figure 7.2: (Upper) Raman spectra of monoclinic zirconia at temperatures from 295 to 950 K, with laser power at 50 mW, exposure time of 60 seconds, and at least 20 accumulations of the spectra. Peaks are numbered as proposed assignments. The sharp features near peak 7 are artifacts. (Lower) Partial and total phonon density of states of zirconia at room temperature, calculated using the lattice dynamics feature in GULP.

temperatures, all 14 modes could be easily resolved. All of the acquired spectra were used to obtain the effects of temperature on line position and linewidth. The background from thermal radiation, and a slightly nonlinear background believed to be intrinsic to the sample, were first subtracted from each spectrum. Each measured spectrum was then fit with multiple Lorentzian functions to extract the centroid and the full-width at half-maximum (FWHM) for each peak. The linewidth of the spectrometer resolution was negligible compared to the resolution of the fitted linewidth.

The results, presented in Figs. 7.3 and 7.4, show that, with increasing temperature, the Raman peaks generally shift to lower frequencies, and generally broaden in linewidth. Similar to our previous results on hafnia [123], there are substantial differences in the amount of peak shifting and peak broadening for the different Raman modes. The differences in atomic motions for each Raman mode will be used to interpret the different non-harmonic behaviors of each mode.

7.4 Calculations

Results from Raman-mode frequency calculations performed with GULP [59] were used to assign vibrational modes to Raman spectral peaks. We used the Buckingham two-body shell model

$$U = A\exp(-\frac{r}{\rho}) - \frac{c}{r^6}, \tag{7.1}$$

in which A, ρ, and c are constants from Lewis [112] for the zirconium-oxygen and oxygen-oxygen potentials, and used a harmonic spring for the oxygen shell-core potential. First principles DFT calculations using Quantum Espresso (QE) [56] also produced similar results. All results are listed in Table 7.1. Good agreement was found between our calculations and the Raman spectroscopic data from the present and previous experiments. [100, 105] There is also reasonable agreement with previous lattice dynamical calculations of Quintard et al. [100] Using atomic

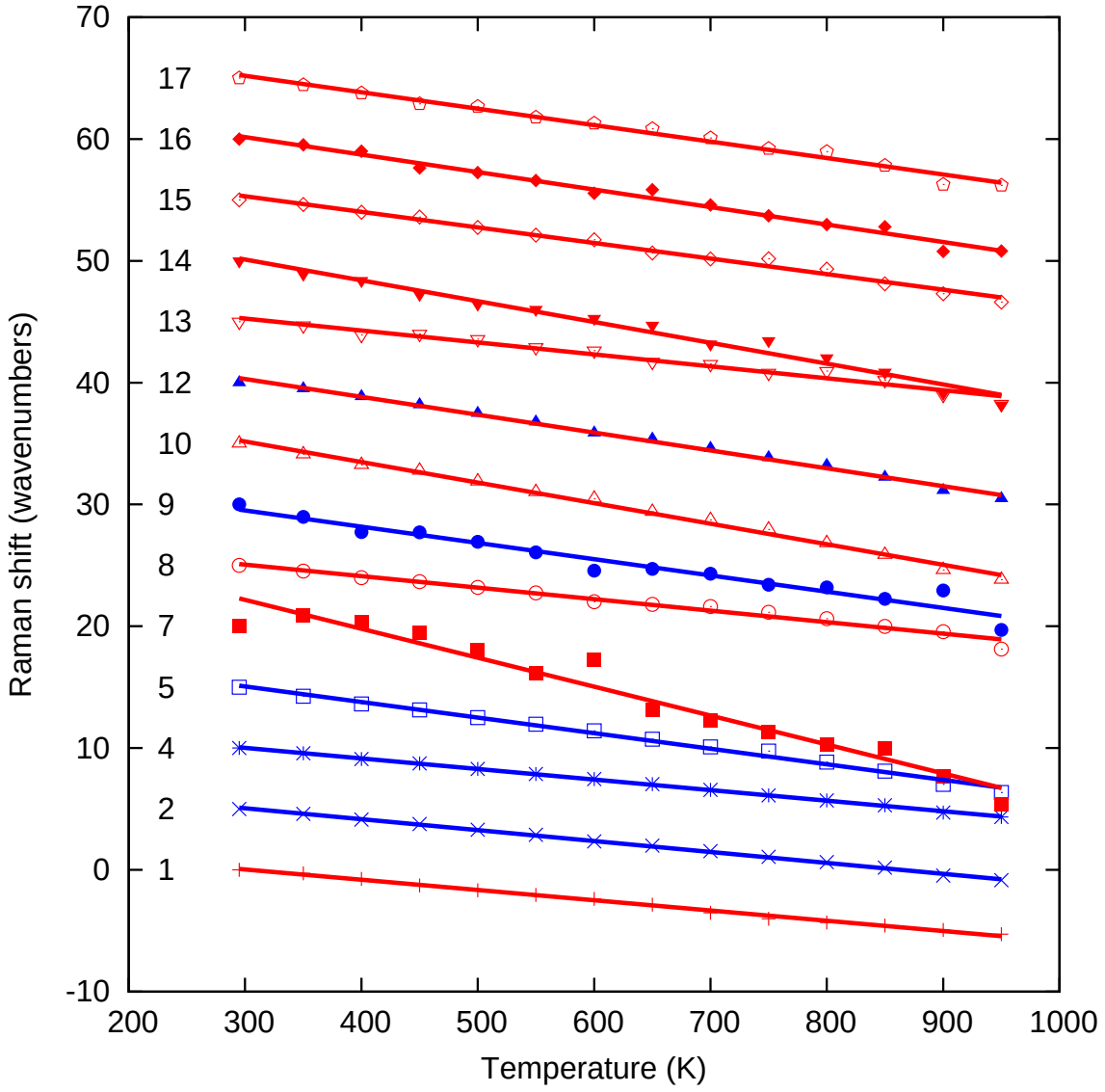

Figure 7.3: Temperature-dependent Raman mode softening in zirconia. In the figure, all modes are evenly spaced at 295 K, to facilitate comparison of resulting thermal shift. Blue (darker) and red (lighter) lines represent metal-dominated and oxygen-dominated modes, respectively, and are linear fits to the data. Notably, mode number 7 had a faint signal, and thus the data quality is lower.

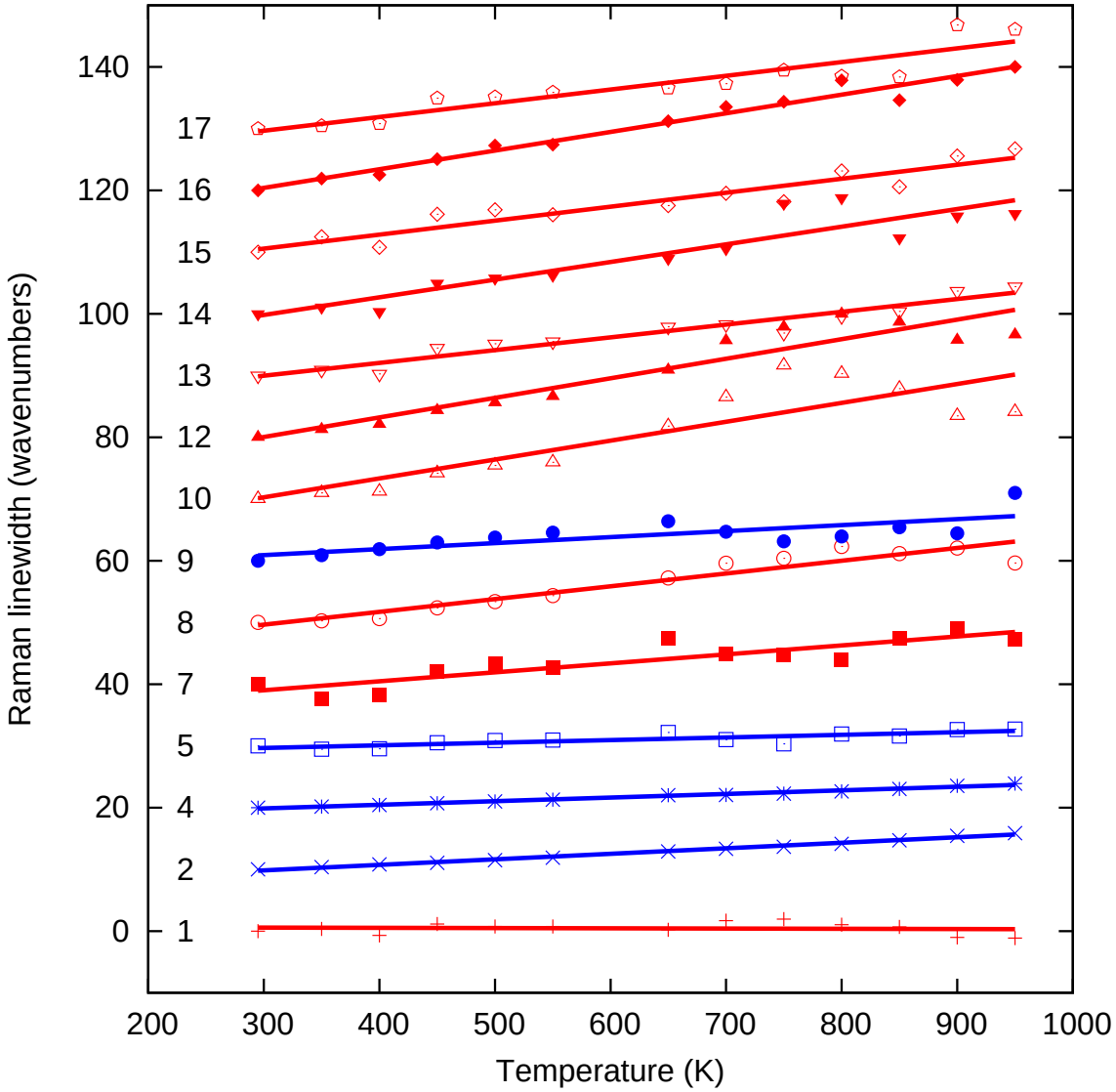

Figure 7.4: Temperature-dependent peak broadening in zirconia. Blue (darker) and red (lighter) lines represent metal-dominated and oxygen-dominated modes, respectively, and are linear fits to the data.

Table 7.1: Raman mode frequencies, fractional atomic participation of each mode, and mode Grüneisen parameters of zirconia

Mode	Exp	GULP[1]	QE[2]	Lt1[3]	Lt2[4]	Zr%	O%	γ_j[5]	γ_k[6]	γ_l[7]
1	100	137	108	102	97	0.10	0.90	3.2	13.4	1.6
2	179	213	159	179	177	0.89	0.11	1.9	2.3	2.0
3	-	228	164	179	-	0.89	0.11	-	-	-
4	190	245	175	190	190	0.98	0.02	1.7	2.9	-
5	223	254	213	224	222	0.94	0.06	2.2	1.1	1.2
6	-	254	288	270	-	0.06	0.94	-	-	-
7	306	342	311	305	306	0.05	0.95	3.0	4.2	0.8
8	335	346	317	334	335	0.05	0.95	1.1	-0.1	0.9
9	348	417	324	348	347	0.82	0.18	1.5	2.8	-
10	382	429	366	381	383	0.03	0.97	1.7	-0.1	-
11	-	430	366	385	383	0.81	0.19	-	2.0	-
12	476	509	447	476	477	0.14	0.86	1.2	-0.5	1.1
13	503	538	477	505	503	0.01	0.99	0.7	-0.4	0.5
14	538	549	516	536	538	0.14	0.86	1.2	1.6	-
15	559	616	522	556	558	0.01	0.99	0.9	1.4	0.3
16	616	622	578	616	615	0.01	0.99	0.9	2.1	-
17	638	662	600	637	638	0.04	0.96	0.8	0.9	0.6
18	-	766	724	756	-	0.02	0.98	-	-	-

[1]Classical lattice dynamics calculation [2]PBE calculation
[3]Experimental measurement by Quintard [100]
[4]Experimental measurement by Kourouklis [105]
[5]Calculated from present experimental data
[6]Room-temperature pressure data by Kourouklis, et al. [105]
[7]Calculated from MD

motions calculated by lattice dynamics, a comparison of results for zirconia and hafnia spectra showed the Raman peaks have the same ordering in energy, and similar relative intensities. The measured pattern of the peaks, especially their relative intensities, were in good agreement with the calculations.

Calculations of the phonon density of states (DOS) were also performed with GULP [59] using the same shell model and potentials that were used for the Raman calculations. The resulting total and partial DOS are shown in Fig. 7.2. It was found that many of the phonon branches had low dispersion, thus yielding a number of sharp peaks in the DOS. The maximum phonon energy was determined

to be about 700 wavenumbers, quite similar to that of hafnia. The square of the eigenvectors of phonons at the Γ point gave the participation of Zr and O in each Raman-active mode, with the results listed in Table 7.1. As can be seen in Fig. 7.2, the heavier metal-dominated modes bunch together on the low-energy end of the DOS at around 200 wavenumbers, and also around 400 wavenumbers. The lighter oxygen atoms tend to dominate the high-energy modes, and also contribute to some of the low-energy modes. There are relatively few mixed modes—the Raman modes are either strongly metal dominated or strongly oxygen dominated. This approximate separation into Zr modes and O modes is expected from the large difference in the mass of oxygen and zirconium atoms. The present results are similar to those found for hafnia, [123] but zirconia shows more mixing in the modes because zirconium atoms are only about half the mass of hafnium atoms.

Molecular dynamics calculations were performed with GULP at temperatures from 300 to 1000 K. The same two-body potential model and force-field constants were used as in the lattice dynamics frequency calculations. Velocity correlation functions were generated from equilibrium atomic trajectories, and these functions were used to calculate the temperature-dependent phonon DOS, as shown in Fig. 7.5. Owing to the relatively flat phonon dispersions of the system, the sharp features in the spectrum can be largely associated with particular optical phonon modes. The thermal mode softening agrees qualitatively with the Raman results, as shown by the calculated Grüneisen parameters in Table 7.1.

7.5 Discussion

The quasiharmonic softening of a normal mode is related to thermal expansion as

$$\omega_j(T) = \omega_j(0) \exp\left(-\gamma_j \int_0^T \beta(T)\, \mathrm{d}T \right) , \tag{7.2}$$

where $\omega_j(T)$ is the jth temperature-dependent vibrational frequency, β is the volume thermal expansivity, and γ_j is the mode Grüneisen parameter. The

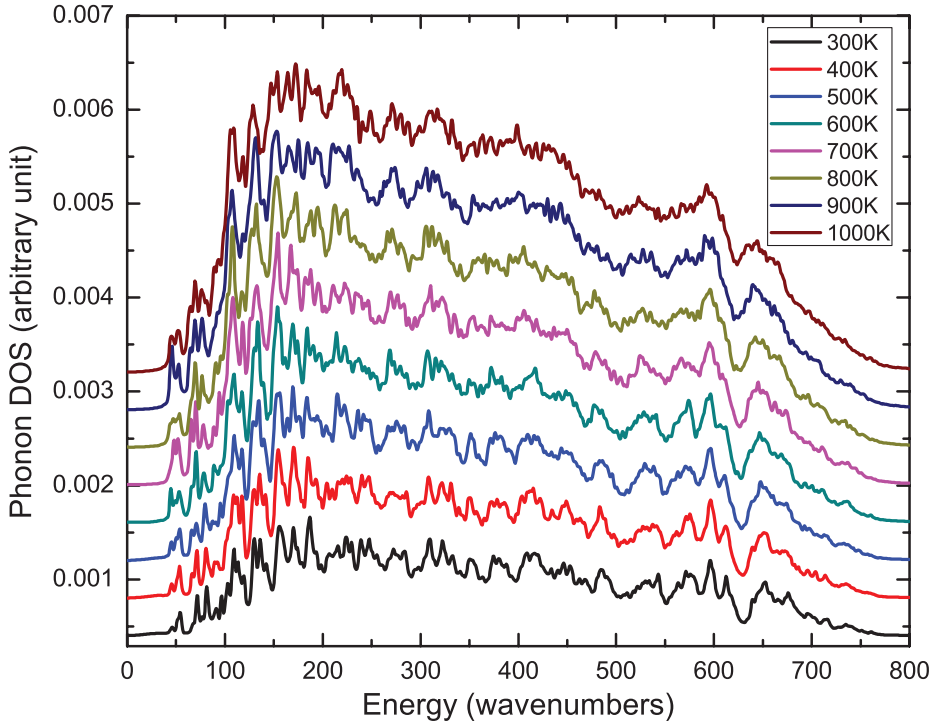

Figure 7.5: Phonon DOS calculated by molecular dynamics for zirconia at different temperatures using GULP. Note the phonon softening at elevated temperatures.

fractional change in vibrational frequency is related to the fractional change in volume by

$$\frac{\Delta\omega_j}{\omega_j} = -\gamma_j \frac{\Delta V}{V} \,. \tag{7.3}$$

The thermodynamic Grüneisen parameter, γ, for a quasiharmonic solid is

$$\gamma = \frac{\beta B V}{C_V} \,, \tag{7.4}$$

where B is bulk modulus, and C_V is the specific heat at constant volume. This γ is an average of all mode Grüneisen parameters $\{\gamma_j\}$, weighted by the modal specific heats C_j

$$\gamma = \frac{\sum_j \gamma_j C_j}{\sum_j C_j} \,. \tag{7.5}$$

From Table 7.1, however, we see that in zirconia an average Grüneisen parameter misses the rich variation of the mode Grüneisen parameters. Although zirconia is

slightly more anisotropic than hafnia, such a wide variation of mode Grüneisen parameters might be expected from the highly anisotropic thermal expansion of either oxide. In both zirconia and hafnia, at all temperatures, the a and c axes expand much faster than the b axis. [114] Figure 7.3 and Table 7.1 show that temperature-dependent frequency shifts do not depend on the energy of each normal mode, as might be expected if all γ_j in Eq. 7.3 were similar. There is, instead, a tendency of the mode Grüneisen parameters to decrease with mode frequency, as in hafnia. [123] From Fig. 7.3 it is apparent that some oxygen modes undergo more thermal softening than the metal modes.

The temperature dependence of the Raman peak widths provide further information about anharmonicity. [115, 116] The observed Lorentzian peak shapes are consistent with the expected energy broadening from shortened phonon lifetimes. In Fig. 7.4, a plot of the absolute broadening of normal modes demonstrates that the oxygen modes (with reasonable resolution across the measured range of temperatures) broaden faster than the metal modes, qualitatively consistent with the trend found for mode softening.

To better understand the phonon dynamics, the parameters of the GULP shell model were subjected to an optimization study against the experimental data. The eight experimental Raman peaks with the best resolution were chosen, and their centroid frequencies were chosen as the target for the optimization. The force-field parameters in the GULP model were fit to the target frequencies using a genetic algorithm implemented in the Mystic software package. [124, 125] The optimized force-field parameters were found to generate Raman frequencies very close to frequencies calculated using the parameters from Lewis. [112] Using parameter sensitivity tools available in Mystic, the impact of each force field parameter on the phonon energy was assessed. [125–127]

The McDiarmid diameter of a function D(f,E) for a real function f over a set E is defined by: [126]

$$D(f,E) = \left(\sum_{i=1}^{n} \mathrm{osc}_i^2 (f,E) \right)^{1/2} \tag{7.6}$$

where:

$$\mathrm{osc}_i(f,E) = \sup\{|f(x) - f(y)| : x, y \epsilon E, x_j = y_j \text{ for } j \neq i\}. \qquad (7.7)$$

The McDiarmid diameter provides a rigorous but very conservative upper bound on the impact of a parameter on a given model. The relative contribution from each force-field parameter to the McDiarmid diameter for the GULP model was calculated for the region of parameter space defined by the Lewis constants ±30%. Different parameter spaces were also tested with similar results. The $-r^{-6}$ terms in Eq. 7.1 proved far less sensitive in the fit, thus a larger range was used for these parameters. The phonon energy was two orders of magnitude more sensitive to the constants involving oxygen-zirconium interactions than the oxygen-oxygen force constants, but the sensitivities to the A, ρ, and c parameters of Eq. 7.1 were comparable. These results indicate that the lattice forces are much more sensitive to Coulomb interactions between ions of opposite charges.

A useful perspective on the structure of zirconia is that oxygen anions make up the structural framework of the crystal, and the zirconium cations are located in the gaps between the oxygen ions (Fig. 6.1). A more detailed view shows that the structure of zirconia contains layers of oxygen anions, with the remaining oxygen and zirconium ions inserted loosely between these layers. The oxygen layers lie approximately in the plane of the b and c axes, with the b direction closer packed than the c direction. Figure 6.1 depicts the ionic radius of oxygen (1.40 Å) as almost twice that of zirconium (0.72 Å), which is slightly smaller than that of hafnium (0.78 Å). As the lattice expands with temperature, the a and c axes expand much faster than the b axis, and thus the largest changes in atomic overlap occur for oxygen anions. Changes in this overlap are expected to affect the vibrational frequencies, especially for oxygen modes.

The analysis of individual normal modes, including the two shown in Fig. 6.5, offers more detailed information on the origin of the non-harmonic behavior exhibited by zirconia. The number 4 mode, representative of a metal-dominated

mode, has zirconium cations moving into the cavity between three adjacent oxygen anions, in nearly parallel motion. The large size of the cavity results in few restrictions on the cations, and as a result mode 4 is one of the most harmonic of all the Raman modes.

Comparatively, mode number 12 is one of the least harmonic modes. This mode involves relatively large changes in oxygen-oxygen bond lengths, and the bending of oxygen-oxygen bonds. Several other modes that exhibit strong non-harmonic behavior have a similar correlation to oxygen-oxygen bond distortion. We find that in zirconia the oxygen-dominated modes are less harmonic than the metal-dominated modes. Furthermore, the modes involving a change in oxygen-oxygen bending exhibit the most non-harmonic behavior.

Figure 7.6 presents the parametric relationship between the the peak broadening and the peak softening rates in zirconia, determined by fitting temperature-dependent broadening and softening data with linear functions. In contrast, a plot of previous results on hafnia [123] reveals a clear boundary between oxygen modes and metal modes. Since zirconium is much lighter than hafnium (atomic mass of 91 compared to 178 for hafnium) the distinction between oxygen and metal modes is less significant, even though the oxygen-dominated modes in zirconium are more non-harmonic, with the exception of mode number 1. Another interesting comparison is that there are a few modes in hafnia that demonstrate negligible softening, while in zirconia no such modes exist.

Phonon frequency shifts and broadenings have been analyzed by treating phonon-phonon interactions by perturbation theory [30, 128]. The analysis of Raman spectra is performed using the Klemens model [118], which considers how one optical phonon decays into two acoustical phonons. Analysis of this three-phonon process for the decay of an optical phonon at the Γ-point is simplified because the two acoustical phonons must be of opposite wavevectors and matched in energy if they are on the same branch. This approach has been extended to four-phonon processes [119], however these simplifications then become less appropriate for describing the full physical picture. In this case, the temperature

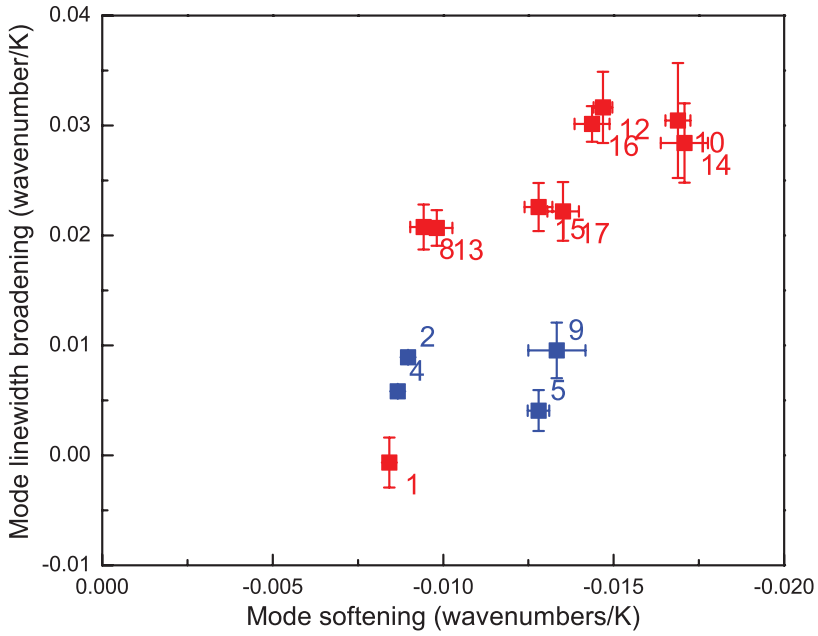

Figure 7.6: Broadening vs. softening of Raman modes in zirconia. Blue (darker) and red (lighter) squares are metal and oxygen modes, respectively. The scale is chosen for easy comparison with hafnia results. [123] Note the absence of modes with little softening.

dependence becomes more complex [119], as the temperature-dependent phonon linewidth broadening Γ_j of mode j can be expressed by

$$\Gamma_j(T) = \Gamma_j(0) + A_j\left[1 + \frac{2}{e^{\hbar\omega_j(0)/2k_BT}-1}\right] + B_j\left[1 + \frac{3}{e^{\hbar\omega_j(0)/3k_BT}-1} + \frac{3}{\left(e^{\hbar\omega_j(0)/3k_BT}-1\right)^2}\right] \tag{7.8}$$

where $\Gamma_j(0)$ is a constant. Here, A and B are parameters for the three-phonon and four-phonon processes, respectively. At ambient or higher temperatures, the contributions from the two terms vary as T and T^2, respectively. In the experimental data of Fig. 7.4, the linewidth broadenings of the zirconia spectra are found to be linear with temperature, so there is little contribution from the four-phonon process of Eq. 7.8 ($B = 0$). For different modes, we found that parameter A ranges from -0.02 to $+0.67\,\mathrm{cm}^{-1}$. Phonon lifetime broadening can also be calculated using the two-phonon density of states at the Γ point, assuming that the three-phonon scattering is the dominant process and the kinematical constraints are dominant.

An analogous expression to Eq. 7.8 for the frequency shift at elevated temperature has been proposed [119], however experimental data at elevated temperature suggests it is not practical to separate the anharmonic frequency shift from quasiharmonic lattice dilation. Fortunately, pressure-induced shifts in Raman spectra have been reported by Kourouklis et al. [105], and these can be used to identify the quasiharmonic contribution. Their results are listed as Grüneisen parameters in Table 7.1. By comparing the pressure Grüneisen parameters to the thermal Grüneisen parameters, we find general agreement for all modes in zirconia dominated by metal ion motions. On the other hand, there are major discrepancies for at least half of the oxygen modes. The deviation of our elevated-temperature results from those of prior high-pressure work again suggests that the oxygen-dominated modes are more anharmonic than the metal modes.

Another result from perturbation theory is that the leading term for phonon broadening is the cubic term, whereas the peak shift originates from the quartic term in first order, and the cubic term in second order. [32] With temperature, the metal-dominated modes shift in frequency with comparatively little broadening. This could be primarily quasiharmonic behavior, consistent with the high-pressure results. In contrast, the oxygen-dominated modes tend to show more broadening. The linearity of the broadening with temperature and the inconsistency with the pressure Grüneisen parameters suggest that these effects originate from the cubic term in the interatomic potential. From a macroscopic view, the non-harmonic effects in zirconia at temperatures up to 950 K are small, and it seems that zirconia can be considered generally quasiharmonic. However, the opinion will miss the rich information about individual phonon modes, which have large effect on phonon behaviors with opposite signs.

7.6 Conclusion

Raman spectra were measured on monoclinic ZrO_2 at temperatures up to 950 K. The peaks in the spectra were assigned to vibrational modes obtained by shell-

model calculations, and compared with the corresponding modes in hafnia. The thermal softening and broadening of the Raman peaks were obtained from the measured spectra, and then were correlated to the individual atomic displacements in each mode. Metal-dominated modes showed relatively little peak broadening for the peak shift, consistent with an approximately quasiharmonic behavior, and had thermal Grüneisen parameters that were more consistent with previous high-pressure results than those for oxygen-dominated modes. The oxygen-dominated modes showed more peak broadening with peak shift, indicating a larger role for the first-order cubic term in the anharmonic behavior. The rich details about the thermodynamics of individual phonon mode in zirconia and hafnia are astonishing: some phonon modes are found to be highly anharmonic, while some others are mostly quasiharmonic. These are completely missed by models that use one single macroscopic Grüneisen parameter. Very little contribution from four-phonon processes is found by fitting to perturbation theory results. The differences between zirconia and hafnia are generally consistent with the mass effects.

Chapter 8

Phonon Anharmonicity and Negative Thermal Expansion in Scandium Fluoride (ScF_3)

Cubic scandium tri-fluoride (ScF_3) has a large negative thermal expansion over a wide range of temperature. Inelastic neutron scattering experiments were performed to study the temperature dependence of the lattice dynamics of ScF_3 from 7 to 750 K. The measured phonon densities of states (DOS) show a large anharmonic contribution with a thermal stiffening of modes around 25 meV. Phonon calculations with first-principles methods identified the individual modes in the DOS, and frozen phonon calculations showed that some of the modes with motions of F atoms transverse to their bond direction behave as quantum quartic oscillators. The quartic potential originates from harmonic interatomic forces in the DO_9 structure of ScF_3, and accounts for phonon stiffening with temperature and a significant part of the negative thermal expansion. The vibrational entropy contribution from these soft phonon modes helps to stabilize the cubic phase over a wide range of temperature.

8.1 Introduction

Nearly all materials expand when heated, so exceptions are interesting. It is well known that phase transitions can cause a reduction in volume with temperature, for example. Negative thermal expansion (NTE) of a pure phase has attracted much attention over the past twenty years, driven both by curiosity, and by opportunities to design materials with special thermal properties. For materials like face-centered cubic plutonium and Invar alloys, NTE involves electronic or magnetic excitations. Other types of NTE are structure-induced, originating from atom arrangements in the crystal [129]. Several mechanisms of NTE have been proposed, such as deformations of polyhedra, one or two-dimensional NTE caused by normal thermal expansion of anisotropic bonds, NTE induced by interstitial cations, and NTE associated with transverse motions of linkage atoms (as in Fig. 8.1) [130]. Often NTE is anisotropic, and it usually occurs only in a small range of temperature [131]. Zirconium tungstate (ZrW_2O_8) is a notable exception [132–137]. The NTE in ZrW_2O_8 is associated with under-constrained

atom sites in the crystal structure [138]. Although some of the behavior can be understood with a “quasiharmonic” model (a harmonic model with interatomic forces adapted to the bond lengths at a given temperature), anharmonic effects are expected, but the full connection between anharmonic lattice dynamics and NTE is obscured by the complexity of the structure [138]. Simplified 2-D models like a rigid square [139,140], and a 3-atom Bravais lattice [138] have been used to explain the “soft-phonon" NTE mechanism, but accurate lattice dynamics for materials such as ZrW_2O_8 are not easy to obtain from geometrical models. Metal-organic framework (MOF) materials with linkage such as benzene [141] or –CN– [142] can have even larger NTE, although they may not be suitable for high temperature applications.

Very recently, a surprisingly large and isotropic negative thermal expansion was discovered in cubic scandium tri-fluoride (ScF_3) by Greve et al. [143] It occurs over a wide range of temperature from 10 to about 1100 K, and exceeds -1.0×10^{-5} K^{-1}. ScF_3 is commonly used in producing metallic scandium but it also has been used in phosphors, light amplifiers, catalysts, and glass modifiers. ScF_3 has several polymorphs, including cubic, rhombohedral, and orthorhombic structures. This suggests that structural changes involve quite small differences in free energy [144]. It is also known that the phase diagram of ScF_3 is very sensitive to structural defects and impurities [145]. Under ambient conditions, ScF_3 has the DO_9 crystal structure of α-ReO_3, a perovskite structure with one vacant cation site, shown in Fig. 8.1, and is stable from 10 K to over 1600 K. The wide temperature range of the NTE, up to about 1100 K (about half its melting temperature), does not involve a phase transition. Although α-ReO_3 itself shows modest negative thermal expansion below 300 K [146,147], the NTE of ScF_3 is an order of magnitude larger. Only a small amount of work has been performed on the lattice dynamics of ScF_3 [144], although materials with similar structure have been studied [148]. ScF_3 has no Raman-active modes under ambient pressures owing to its cubic symmetry. Under pressure, however, its Raman spectra showed some interesting results. [144]. With external pressure, the octahedra in the structure begin to bend

and twist with respect to each other, and cubic ScF_3 transforms to a rhombohedral phase at 0.6 GPa and then to another structure at about 3 GPa. Perhaps the most interesting behavior is found at 0.6 GPa, with the rhombohedral symmetry leading to Raman active modes. With increasing pressure, the mode at about 480 cm^{-1} softens, while two other lower energy modes stiffen enormously.

From chemical intuition, and from our electronic structure calculations, cubic ScF_3 is an insulator with a wide band gap, so electronic excitations do not play a role in the NTE. Changes in the Sc-F bond distances cannot be ruled out, however, as the negative thermal expansion is so big and strongly temperature dependent while the Sc-F "bonds" are not expected to be unusually strong. The simplicity of the ScF_3 crystal structure makes it an ideal case for experimental and theoretical study on a material with isotropic NTE over a wide range of temperature. Here we report results from inelastic neutron scattering measurements of the lattice dynamics of ScF_3 from 7 to 750 K. First principles lattice dynamics, molecular dynamics, and frozen phonon calculations were performed to assess the relationship between NTE and phonon anharmonicity. For some normal modes, the F atoms move in a potential with a dominant quartic term in their two under-constrained dimensions. The quartic term is a geometrical consequence of the DO_9 structure, even with harmonic interatomic forces. It accounts for the thermal stiffening of the low-energy modes of F atoms and for a reduction of lattice parameter with an increase in temperature. The simplicity of the DO_9 structure of cubic ScF_3 allows a detailed analysis of the lattice dynamics, elucidating the connection between NTE and phonon anharmonicity.

8.2 Experiments

Inelastic neutron scattering measurements were performed with the time-of-flight Fermi chopper spectrometer ARCS at the Spallation Neutron Source. Powdered ScF_3 is known to absorb water from the atmosphere, but the vacuum and high temperature in the furnace helped to keep the sample anhydrous during the

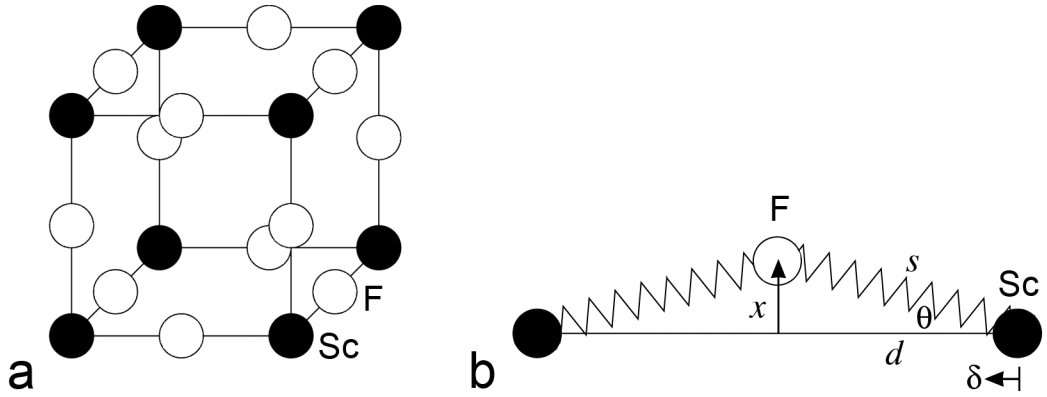

Figure 8.1: (a) DO_9 structure of ScF_3 (b) Geometry and variables for the mechanical model of Sc-F bonds

measurements. Coarse powders of cubic ScF_3 crystals of 99.99% purity were ground to powders with particle sizes less than 0.1 mm and loaded into annular aluminum containers with outer diameters of 30.0 mm and heights of 64.0 mm. An aluminum insert was used to hold the powder in place and the effective sample thickness was 2.0 mm, giving a ratio of multiply to singly scattered neutrons of approximately 5%. For best resolution of the spectrum throughout the energy range, four incident neutron energies were used, 30.0, 79.5, 118.7, and 163.0 meV. Each measurement included approximately 2×10^6 neutron counts. For temperatures of 7, 100, 200, and 300 K, the sample was mounted in a closed-cycle helium refrigerator. An electrical resistance furnace designed for vacuum service was used for temperatures of 320, 450, 600, and 750 K. By monitoring with several thermocouples, we found the temperature be accurate to within 5 K over the bulk of the sample. Backgrounds with empty sample cans were measured at each temperature. Scandium is challenging for neutron scattering because of its absorption cross section of about 27.5 barn. However, the high flux of ARCS makes the experiment possible within reasonable time. The details of the experiment were described in Chapter 4

Data reduction and phonon DOS generation were performed with the standard software package for ARCS as described previously in references [70, 149] and in Chapter 4. The data were corrected for detector efficiency using scattering

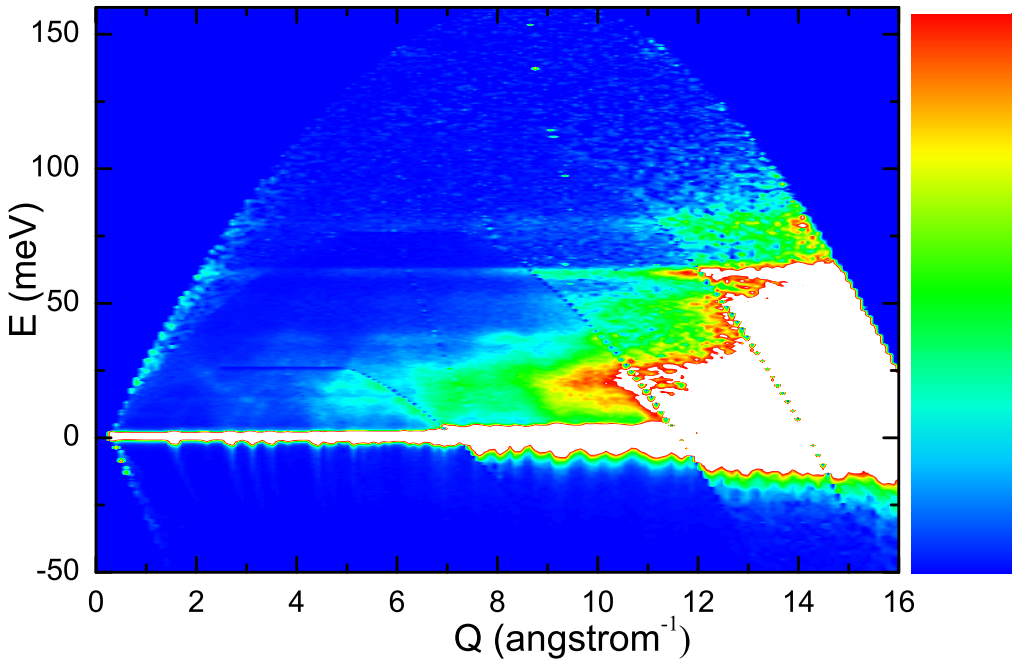

Figure 8.2: Four-energy-overlaped $S(Q,E)$ of ScF_3 at 7 K. The arcs of lines through the data are kinematical limits of 4 incident energies and coherent scattering. The color scale on the right is linear.

data from vanadium, backgrounds were subtracted, and the intensities were converted to $S(Q,E)$, where $\hbar Q$ is the momentum transfer to the sample. The combined $S(Q,E)$ results at 7 K after background subtraction are shown in Fig. 8.2. The data were corrected for multiphonon scattering in the incoherent approximation, and approximately corrected for the small amount of multiple scattering. The neutron-weighted phonon density of states (DOS) curves for three incident energies are shown in Fig. 8.3a. Differences among the phonon DOS curves are expected from differences in instrument resolution, which improves for lower incident neutron energies. Good agreement is seen for the DOS curves measured in the refrigerator and furnace at 300 K and 320 K, showing the success of the background subtraction. Neutron diffraction patterns were obtained from the elastic scattering and used to verify the structure and lattice parameters.

All major features in the DOS broaden with temperature, indicating a decrease in phonon lifetime. Phonon modes shift with temperature, but the shifts are complicated. To quantify thermal shifts, Gaussian functions were fitted to the

five features in the phonon DOS, and Fig. 8.3b presents the shifts (ΔE) of the peak centers. The high-energy features 4 and 5 soften normally with temperature, but the low-energy feature 2 stiffens anomalously. Feature 3 may also stiffen, and feature 1 changes little with temperature. The shifts obtained from different incident energies agree reasonably well. Some of the features correspond to more than one phonon branch, so while the fitted shifts give a good indication of the trend of the phonon energy changes, they usually do not pinpoint a specific mode.

8.3 Calculations

First-principles calculations were performed with the local density approximation to the density functional theory, implemented in the VASP package [54]. Projector-augmented wave (PAW) [150] pseudopotentials and a plane-wave basis set with energy cutoff of 450 eV were used in all calculations. Within the quasiharmonic approximation (QHA), the free energy is

$$F(T,V) = E_s(V) + \int g(\omega)\left(\frac{\hbar\omega}{2} + k_B T \ln(1-e^{-\frac{\hbar\omega}{k_B T}})\right)\mathrm{d}\omega \tag{8.1}$$

where the static energy, E_s, is the total energy of the crystal when all the atoms are fixed at their equilibrium positions, ω is the (angular) phonon frequency, and $g(\omega)$ is the phonon DOS for the lattice parameter, a, that minimizes $F(T,V(a))$. Here E_s was calculated self-consistently using a 4-atom primitive cell and a $12\times12\times12$ k-point grid, and phonon energies were calculated using the direct supercell method with a 108-atom supercell and a $2\times2\times2$ k-point grid. The LO-TO correction for the optical phonons was included based on the inter-plane force-constant model [151]. Given the phonon energies and static energy calculated at different volumes, Helmholtz free energy as a function of volume and temperature ($F(T,V)$) was then obtained within the quasiharmonic approximation. Statistical thermodynamic relationships were then used to deduce the coefficient of thermal expansion and Grüneisen parameter, allowing thermodynamic properties to be

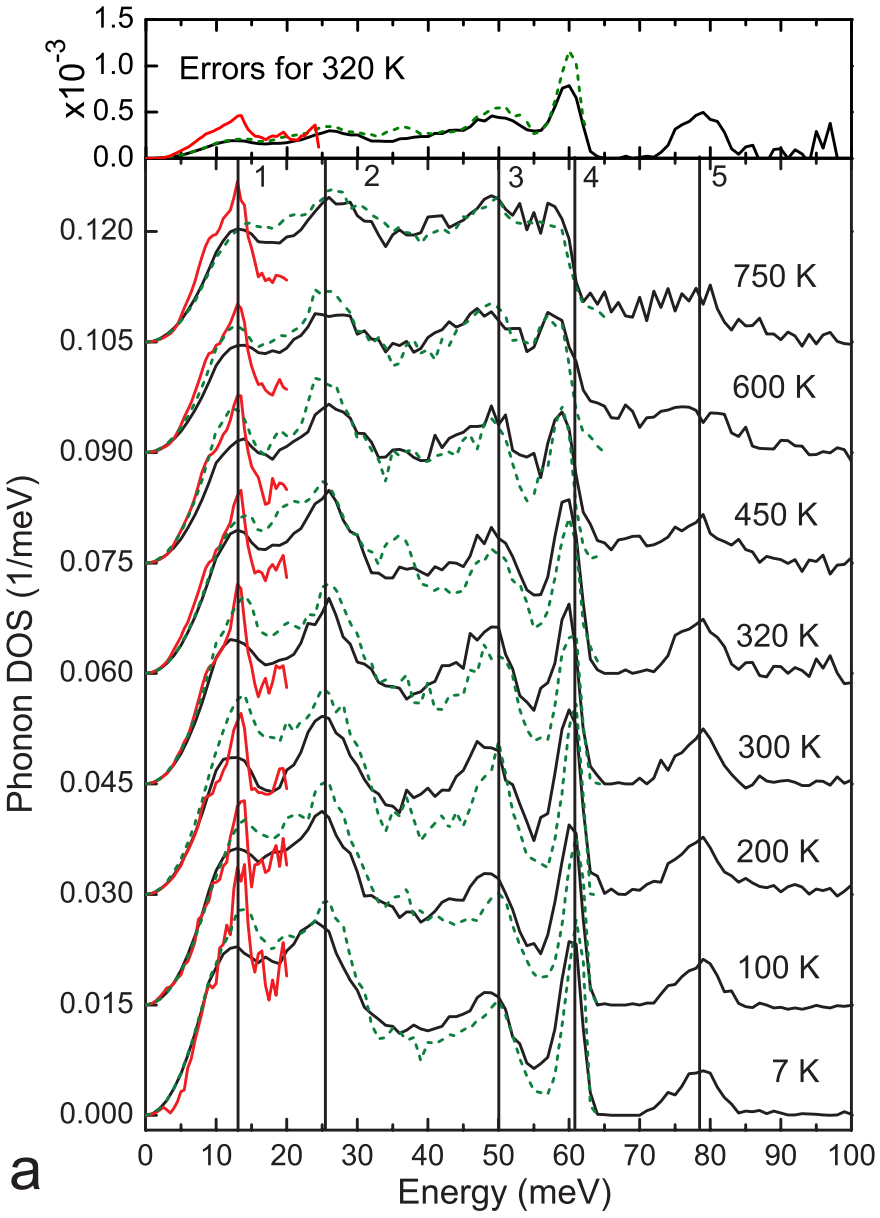
Errors for 320 K
x10^-3
1.5
1.0
0.5
0.0
1
2
3
4
5
750 K
600 K
450 K
320 K
300 K
200 K
100 K
7 K
Phonon DOS (1/meV)
0.120
0.105
0.090
0.075
0.060
0.045
0.030
0.015
0.000
0
10
20
30
40
50
60
70
80
90
100
Energy (meV)
a

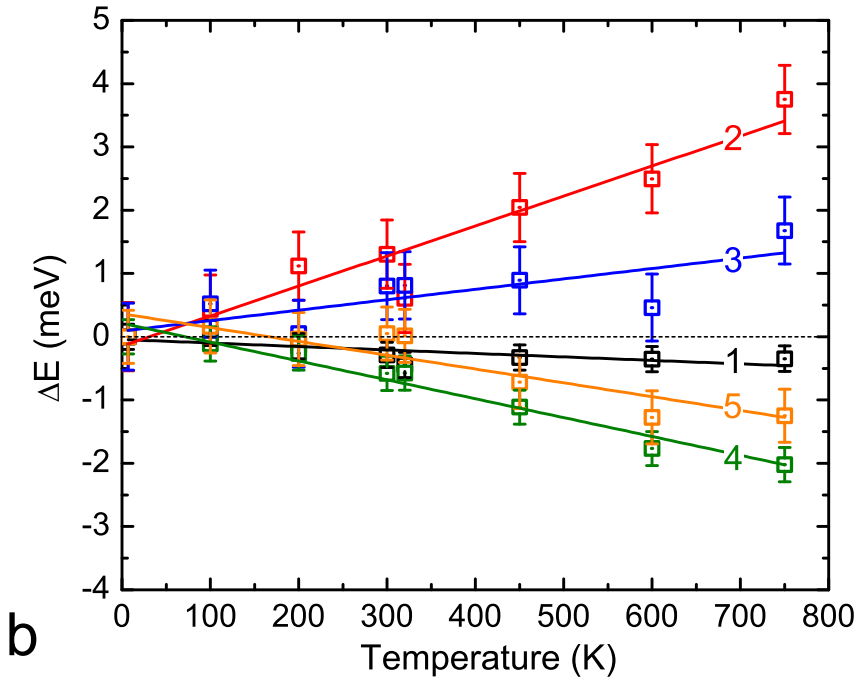

Figure 8.3: (a) Neutron-weighted ScF_3 phonon DOS from incident energies of 118.7 meV (black), 79.5 meV (green, dashed), and 30.0 meV (red), scaled to conserve spectral areas and offset for clarity. Five vertical lines are aligned to peak centers at 7 K, and labeled by numbers. Errors at top are from counting statistics, and similar at all temperatures. (b) Shifts of phonon peak centers relative to 7 K data. The solid lines are linear fits. For each point, the spectrum with the best resolution was used. Error bars are mean differences between the spectra of different incident energies at all temperatures.

obtained from statistical thermodynamic relationships. For example, the thermal equation of state $P(T,V)$ can be deduced via

$$P(T,V) = -\frac{\partial F(T,V)}{\partial V}\bigg|_T, \tag{8.2}$$

from which the V(T,P) relationship was obtained by interpolation, and the thermal expansion coefficient was deduced from

$$\alpha = \frac{1}{V}\frac{\partial V}{\partial T}\bigg|_P. \tag{8.3}$$

To study anharmonic effects with VASP, we performed ab initio Born-Oppenheimer molecular dynamics (MD) calculations at 7, 100, 200, 300, 450, 600, and 750 K, and we also performed frozen phonon calculations. The MD simulations used a 108-atom supercell, and temperature was controlled by Nosé thermostats. For each temperature, the system was first equilibrated and then simulated for 5 ps with a time step of 5 fs. The QHA and MD simulations were used to identify modes corresponding to experimental spectral features having anomalous temperature dependencies. The vibrational potentials of these modes were obtained through frozen phonon calculations on the minimum supercell determined by symmetry.

8.4 Results

Figure 8.4 shows phonon properties calculated from first principles within the harmonic approximation. The agreement between the experimental and calculated phonon DOS curves is good after accounting for instrumental broadening and neutron weighting (neutrons are scattered about twice as efficiently from motions of Sc atoms as from F atoms). All major features in the experimental phonon DOS can be assigned to specific groups of phonon modes. According to phonon dispersion in Fig. 8.4a, high-energy fluorine modes have relatively flat branches and the change of the DOS can accurately represent the change in these modes.

The first Brillouin zone and its high symmetry points are shown in Fig. 8.5. Lower energy modes have more complex dispersions and result in broader peaks in phonon DOS. Judging from the mass difference between fluorine and scandium atoms, the fluorine-dominated phonon modes should be relatively separated from the scandium modes and this is mostly true. Naturally, one expects the lighter atoms like fluorine to dominate the high-energy modes while heavier atoms like scandium dominate the lower-energy modes. However, the motions of F atoms dominate both the higher- and lower-energy parts of the DOS, and the majority of Sc-dominated modes are between 40 and 60 meV. This can be explained if the low-energy "rigid unit modes", where ScF_6 octahedra pivot about corner-shared F atoms, have much larger effective mass than individual atoms.

As thermal expansion is closely related to Grüneisen parameters, we show in Fig. 8.4c the mode Grüneisen parameters. Some phonon modes have negative Grüneisen constants, such as the low-energy modes at R and M with anomalous Grüneisen constants of –371 and –84. It is likely these are the softest modes that might contribute to the negative thermal expansion. In what follows we show that these modes have quartic potentials, so these Grüneisen constants are not meaningful and the QHA is not reliable. Figure 8.14 shows the thermal expansion calculated with the QHA equation of state from Eq. 8.1, compared with recent measurements. [143] Some difference at the highest temperatures could be caused by the creation of defects. For low temperatures, the QHA underestimates the NTE.

The ScF_6 octahedra are more flexible than their oxide counterparts—our MD simulations showed that the F atoms in an octahedron executed largely independent and uncorrelated motions, as shown in the attached animation, and by the pair, radial, and angular distribution functions. The pair distribution functions (PDF) (Fig. 8.6) and radial distribution functions (RDF) (Fig. 8.7) calculated by first-principles MD show a large broadening of the second peak (nearest F-F distance) compared to the first peak (nearest Sc-F distance) at higher temperatures. The calculated RDFs agree surprisingly well with the results from X-ray diffrac-

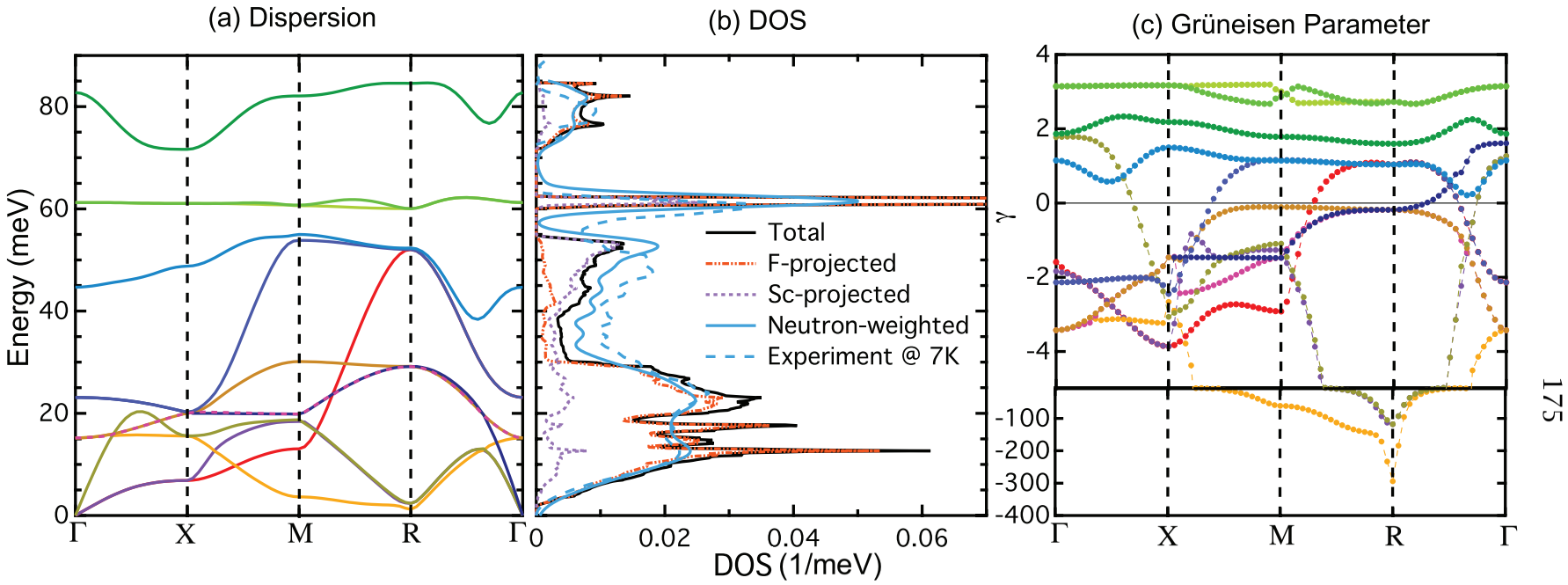

Figure 8.4: (a) Calculated phonon dispersions along high-symmetry directions of ScF_3 at 0 K. X = $(1,0,0)\pi/a$; M = $(1,1,0)\pi/a$; R = $(1,1,1)\pi/a$. (b) Total and partial phonon DOS curves at 0 K from first-principles calculation, neutron-weighted phonon DOS with instrument broadening at 120 meV added, and experimental neutron-weighted phonon DOS at 7 K. (c) Grüneisen parameters (γ) calculated with the QHA for modes along high-symmetry directions. Colors correspond to the phonon dispersions in a.

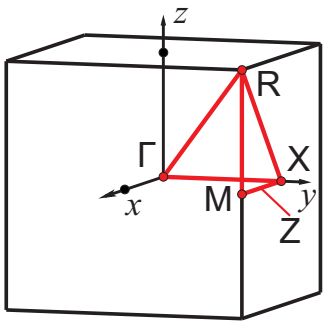

Figure 8.5: The first Brillouin zone of ScF_3 and its high-symmetry points

tion experiments using synchrotron sources. Similarly, the angular distribution function for the F-Sc-F bond angle at 300 K (Fig. 8.8) shows a broad distribution with a FHWM of 10 degrees. Both of these results are consistent with uncorrelated motions of fluorine atoms. This is also evident in the animation, in which relative motions of two nearby F atoms undergo frequent changes in phase and frequency. The structural geometry of the DO_9 structure offers little constraint on the transverse modes of F atom motion, also suggested by the first-principle MD calculations.

Figure 8.9 shows the plane-projected atomic trajectories of Sc and F atoms at 300 K. Fluorine atoms execute large excursions in the two directions transverse to the Sc-F bond. The distributions of atom centers, projected onto one axis and binned into a histogram, were satisfactorily fit to Gaussian functions. The full-width-half-maxima (FWHM) were 0.124 Å for Sc (isotropic) and 0.124 Å for F along the z-axis (longitudinal), and 0.270 Å for F along the x- and y-axes (transverse). This anisotropy of F-atom motions decreases with temperature, but the average transverse amplitude of the F-atom motion is more than 10% of the Sc-F bond length at 300 K.

Although the large-amplitude F atom displacements occur largely independently, the rocking modes of ScF_6 octahedra are useful for analyzing the dynamics of a periodic structure. We performed frozen phonon calculations for the five

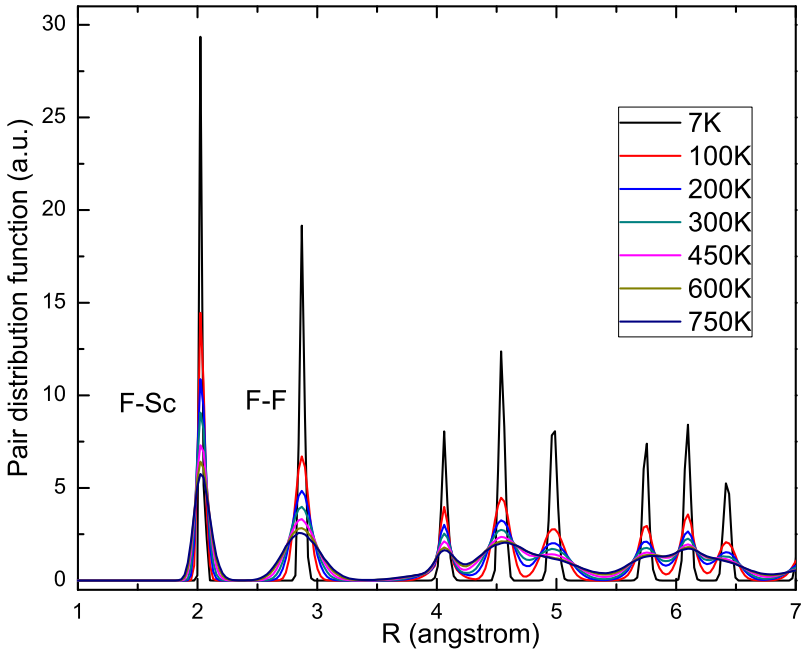

Figure 8.6: Pair distribution functions from first-principle MD calculations at various temperatures

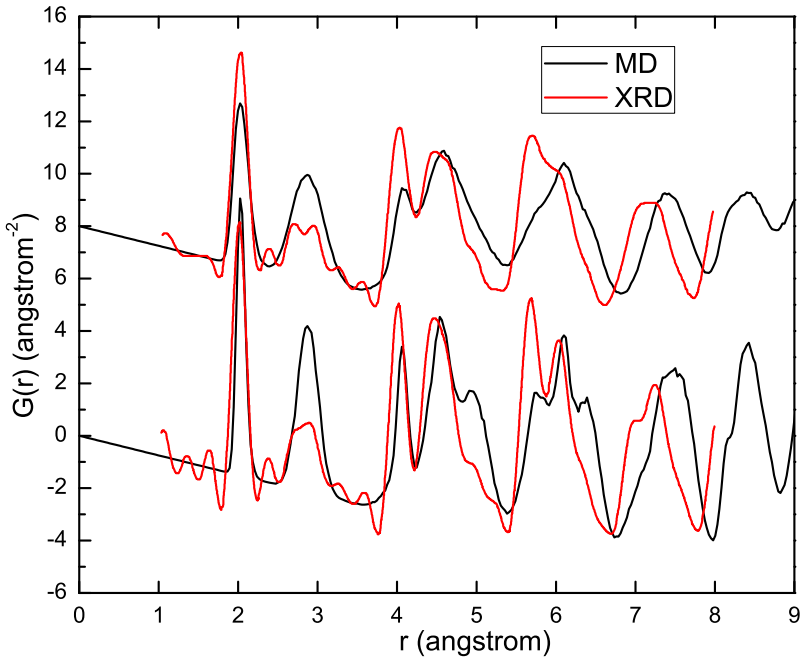

Figure 8.7: Radial distribution functions from first-principle MD calculations compared to the results from X-ray diffraction by Wilkinson et al. Lower: 300 K; Upper: 750 K

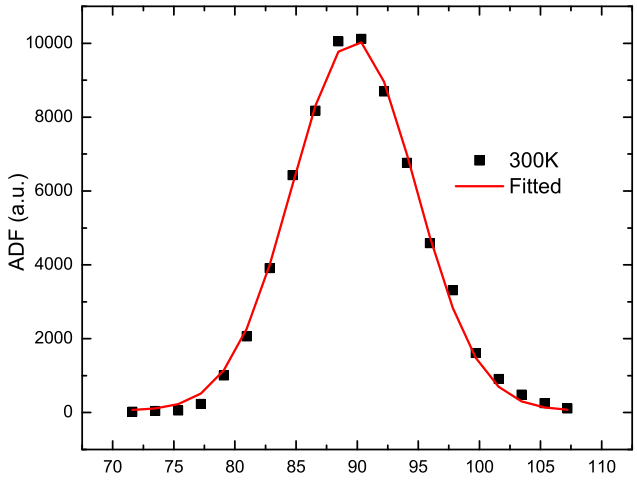

Figure 8.8: The angular distribution function for F-Sc-F angle at 300 K from first-principle MD and its Gaussian fit

modes R1, R3, R4-, R5, and R4+ at the R point with energy decreasing in that order, as shown in Fig. 8.11. Modes R1 and R3 can be easily classified as “breathing" modes, which involve the change of bond lengths inside octahedra without a change of bond angles. For mode R4-, the scandium atoms are displaced while fluorine atoms are fixed. Mode R5 only involves the change of F-Sc-F angles inside the octahedra. Most of these modes were fit well to a quadratic potential within the range of atomic displacements predicted by the MD calculations, but the R4+ mode (the mode of lowest energy calculated with the harmonic approximation), depicted in detail in Fig. 8.12, was found to have a nearly pure quartic potential. The R4+ mode, with its quartic potential, is not expected to be modeled well with a harmonic potential, especially when the amplitudes of displacement are large. If the NTE depends on the dynamics of this mode, it is not surprising that the quasiharmonic approximation would fail to account quantitatively for the thermal expansion. Many other NTE crystals are associated with anharmonicity, but the relationship has been unclear. Nevertheless, considering the large excursion of F atoms, anharmonicity seems to be important.

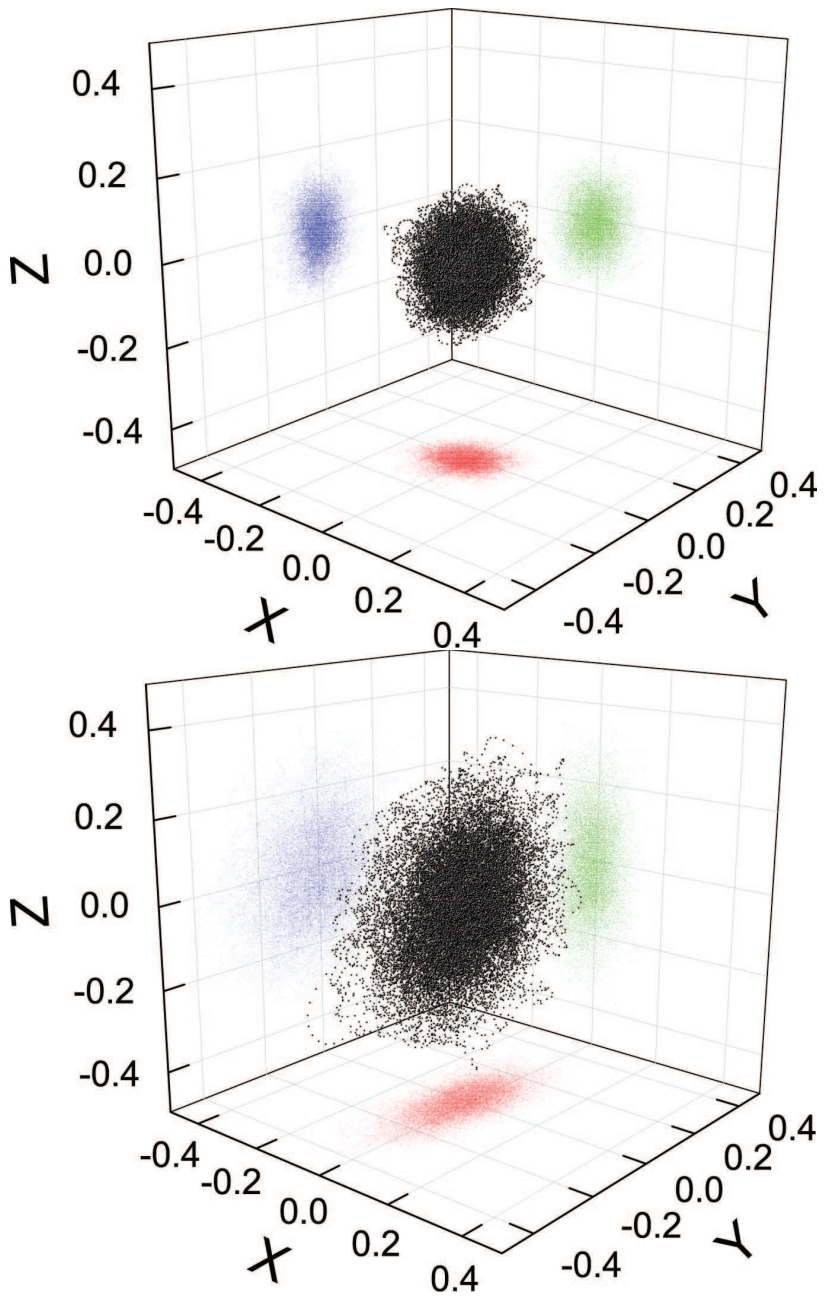

Figure 8.9: First principles MD trajectories and their projections onto x-y, y-z, and x-z planes for Sc (top) and F (bottom) at 300 K. Distances are in Å. The direction of Sc-F bond is $\hat{x}$.

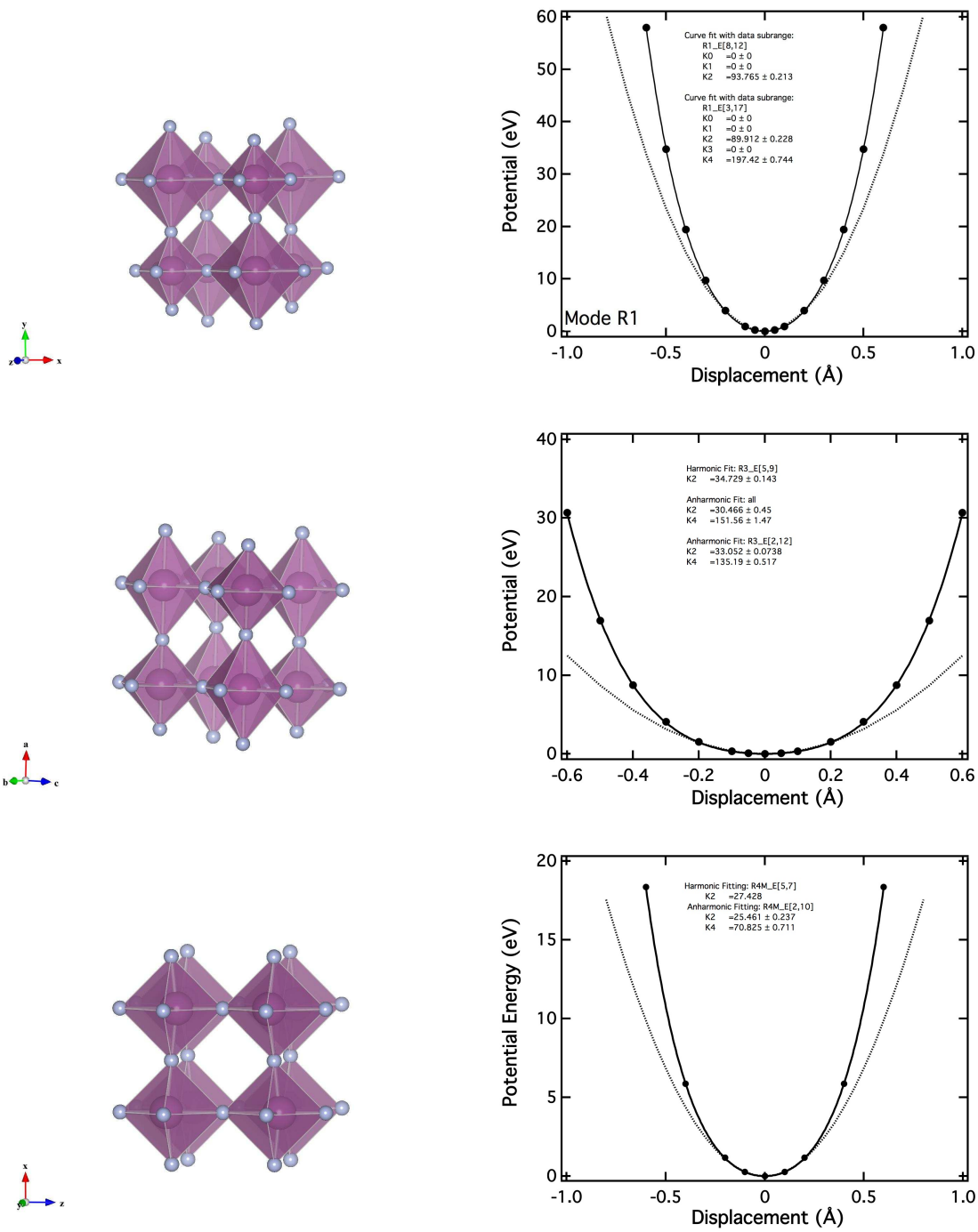
Curve fit with data subrange:
R1_E[8,12]
K0 =0 ± 0
K1 =0 ± 0
K2 =93.765 ± 0.213
Curve fit with data subrange:
R1_E[3,17]
K0 =0 ± 0
K1 =0 ± 0
K2 =89.912 ± 0.228
K3 =0 ± 0
K4 =197.42 ± 0.744
Mode R1
Potential (eV)
Displacement (Å)
Harmonic Fit: R3_E[5,9]
K2 =34.729 ± 0.143
Anharmonic Fit: all
K2 =30.466 ± 0.45
K4 =151.56 ± 1.47
Anharmonic Fit: R3_E[2,12]
K2 =33.052 ± 0.0738
K4 =135.19 ± 0.517
Potential (eV)
Displacement (Å)
Harmonic Fitting: R4M_E[5,7]
K2 =27.428
Anharmonic Fitting: R4M_E[2,10]
K2 =25.461 ± 0.237
K4 =70.825 ± 0.711
Potential Energy (eV)
Displacement (Å)

Figure 8.10

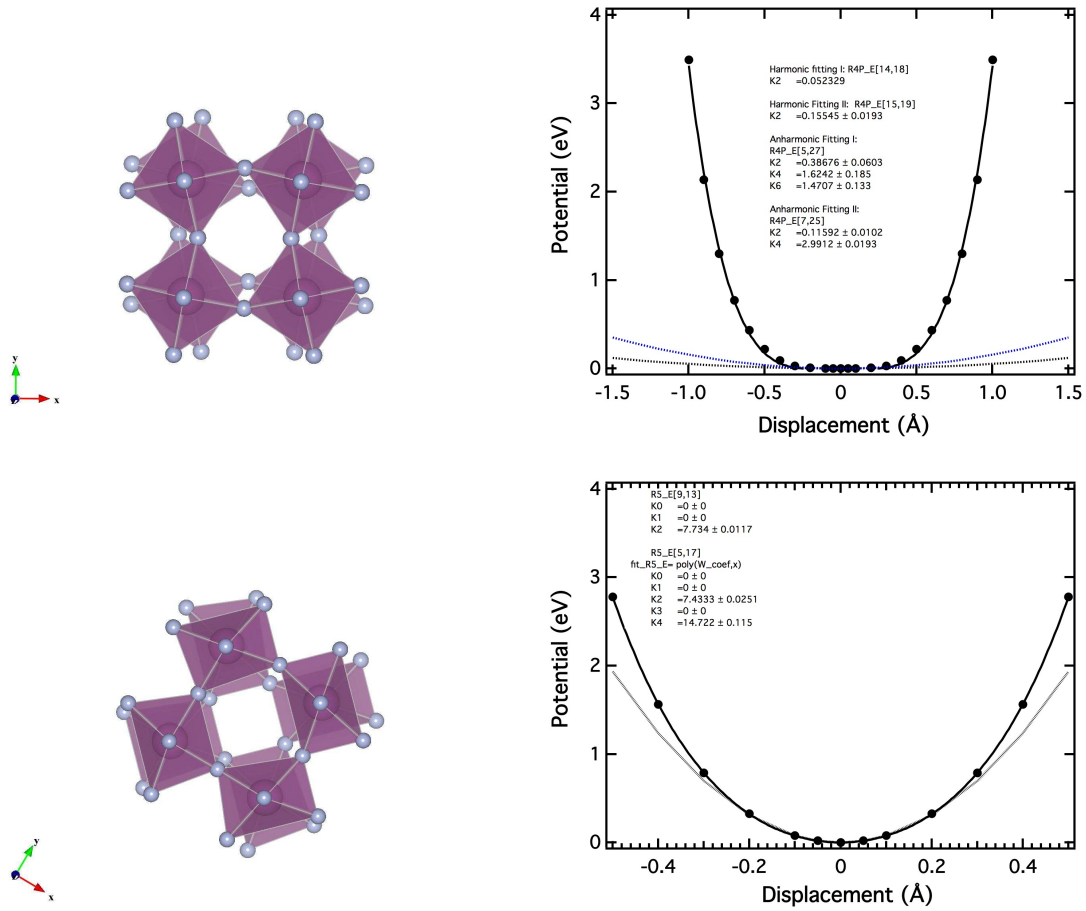

Figure 8.11: Phonon modes in ScF_3 at R-point (in the order of R1, R3, R4-, R4+, and R5) and their frozen phonon potentials and quadratic (harmonic) fits to the frozen phonon potentials. The ranges of the quadratic fits vary, but are comparable.

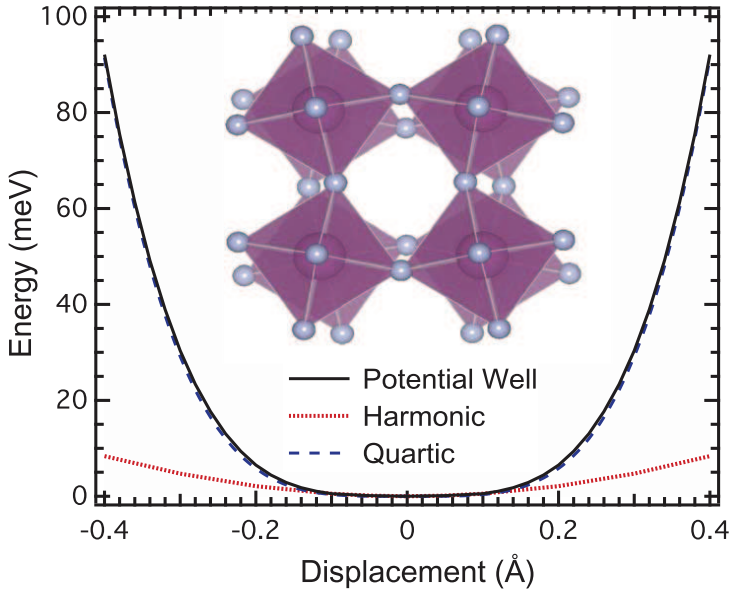

Figure 8.12: Phonon mode R4+, its frozen phonon potential, quadratic (harmonic) and quartic fit to the frozen phonon potential. The range of the quadratic fit is from -0.1 to 0.1 Å for transverse displacements of F atoms.

The Grüneisen parameter for the ith mode, γ_i, is

$$\gamma_i = -\frac{V}{\omega_i}\frac{\partial \omega_i}{\partial V} = -\frac{V}{\omega_i}\frac{\partial \omega_i}{\partial T}\frac{\partial T}{\partial V} = -\frac{V}{\omega_i}\frac{\partial \omega_i}{\partial T}\frac{1}{\alpha}, \tag{8.4}$$

in which α is the volume expansion coefficient, V is the volume, and ω_i is the frequency of the ith mode. Since $\alpha < 0$ in this system, Grüneisen parameters should also be negative in their frequency dependence on temperature, $\partial\omega_i/\partial T$, but experimental results suggest differently. The calculations also predict a lattice parameter 1% larger than the room-temperature experimental value, at least part of which could be explained by NTE in the ground state.

The failure of the QHA is a good indicator that the dynamics and anharmonicity, more than of the static lattice structure, play an important role. Two effects could account for the “potential-induced" anharmonicity: one is an implicit effect due to the change in volume with temperature or pressure, and the other one is an explicit effect from the increase in vibration amplitude with temperature [152]. QHA calculations were performed at zero temperature, and they usually only

account for the implicit contribution and totally ignore the explicit one. The QHA results do predict the NTE, shown in Fig. 8.4c. The explicit contribution of anharmonicity accounts for the reversed results in Grüneisen parameters and difference in the calculated NTE. Another interesting observation is that low-energy fluorine modes are very sensitive to the lattice parameters, and small deviations from the optimized geometry result in large changes in phonon energies and sometimes create imaginary modes. Such results usually suggest that the phase transition is imminent, but that is obviously not the case for the system here. (The system only becomes unstable under pressure.)

The simplest explanation of normal thermal expansion uses an interatomic potential that is skewed towards larger interatomic separations. Expanding the crystal has a cost in elastic energy, but this is offset at finite temperature because a larger phonon entropy is obtained by lower frequency vibrations. It is tempting to associate the negative thermal expansion of ScF_3 with the opposite skewness of the interatomic potential, which could be consistent with the thermal stiffening of the low-frequency modes. In its simple form this explanation is misleading because the large-amplitude displacements are perpendicular to the bond direction. Furthermore, skewness is not a property of a quartic potential. Temperature changes produce (1) changes of volume, an implicit anharmonic effect, and (2) increased vibrational amplitudes, an explicit anharmonic effect. The anomalous temperature dependence of the phonon energy can be caused by both. We examined the implicit anharmonic effect through the quasiharmonic lattice dynamics simulations and the explicit effect through a combination of molecular dynamics simulation and frozen phonon calculations. The explicit anharmonic effect can be either the results of changes in bond length because of anharmonic interatomic potentials, or it could be “structure-induced", as discussed next.

8.5 Structural Model

The simple mechanical model of Fig. 8.1b, depicting the transverse motions of the F atoms, helps to show the important relationship between phonon anharmonicity and NTE. We first use the model to understand the phonon partial DOS curves of F atoms in Fig. 8.4b, which show approximately two bands of vibrations at 0 ~ 30 and 60 ~ 90 meV in the transverse (vertical) and longitudinal (horizontal) directions of Fig. 8.1b, respectively. First consider the two Sc atoms in Fig. 8.1b to be positioned in equilibrium so there are no net forces on them when the F atom is at rest in mid-position ($x = 0$), as expected for a classical crystal with lattice parameter $2d$ at $T = 0$. For simplicity, first consider the Sc atoms rigidly positioned, as if they had infinite mass. What is particularly interesting about the vertical motion of the F atom in Fig. 8.1b is that it moves as a pure quartic oscillator. The transverse restoring force on the F atom depends on the elongation of the springs, s, which goes as $1-\cos\theta$ times the resolved transverse force, giving a transverse restoring force going as x^3.

$$F_{\mathrm{v}} = k\frac{x^3}{d^2} \tag{8.5}$$

The total potential for the transverse displacement of the F atom with two springs is

$$U_{\mathrm{t}} = \frac{k}{4}\frac{x^4}{d^2}, \tag{8.6}$$

consistent with the quartic potential of the R4+ mode and also the failure of QHA, because the mode can not be approximated by harmonic potentials, even with small amplitude at very low temperatures.

We cannot expect a harmonic theory to calculate accurately the energies of a quantized quartic oscillator, even when the quartic behavior is a geometrical consequence of harmonic interatomic forces. The phonon energies and the unusual Grüneisen constants for the quartic modes in Fig. 8.3c are therefore

not expected to be reliable. The force constant k was obtained from the frozen phonon calculations by fitting the transverse fluorine mode to a quartic function, and also by fitting the longitudinal fluorine mode to a quadratic function. The results, 901 and 744 N/m, respectively, are close. For these force constants the harmonic longitudinal vibrations of F atoms were 111 or 91.7 meV, reasonably close to the actual frequencies of these modes in the DOS.

From a numerical analysis of the quartic quantum oscillator [153], the k = 901 N/m gives energies of 7.4, 26.4, 51.9, 81.0, and 113 meV for levels 0, 1, 2, 3, and 4, as shown in Fig. 8.13. The transition to the first excited state requires 19.0 meV, which is in good agreement with peak 2 in the phonon DOS. The spread between these levels increases with temperature, so excitations to higher levels absorb increasingly more energy from the neutron, and peak 2 in Fig. 8.3 stiffens with temperature. This temperature dependence was calculated by assigning Boltzmann factors to the different oscillator levels, giving a shift of 7 meV over 750 K. This is about three times larger than the shift of peak 2, but peak 2 contains contributions from other phonon branches that are more harmonic. The flatness near the bottom of the quartic potential and the relatively larger zero-level energy cause large zero point displacements of F atoms. As a result, there is substantial fluorine vibrations at zero temperature, which may be the explanation of non-vanishing NTE even at 0.3 K. The anharmonicity is primarily a consequence of the structure which also leads to NTE. Similarly, the NTE has contribution from both implicit and explicit effects.

The frequency of a quartic oscillator depends on its amplitude. We obtain the period from integration of the inverse velocity around a full cycle

$$\tau = \oint \sqrt{\frac{2m\,d^2}{k(x_{\max}^4 - x^4)}}\,\mathrm{d}x \frac{1}{\tau} = 4 \int_0^{+x_{\max}} \sqrt{\frac{2m\,d^2}{k(x_{\max}^4 - x^4)}}\,\mathrm{d}x \tag{8.7}$$

Using the force constant k = 901 N/m from the fit to the frozen phonon calculation (Fig. 8.12), and a maximum displacement $x_{\max}$ = 0.2 Å from MD simulations at 300 K, we find a frequency (τ^{-1}) of 1.1 THz. Note that there is no simple relation

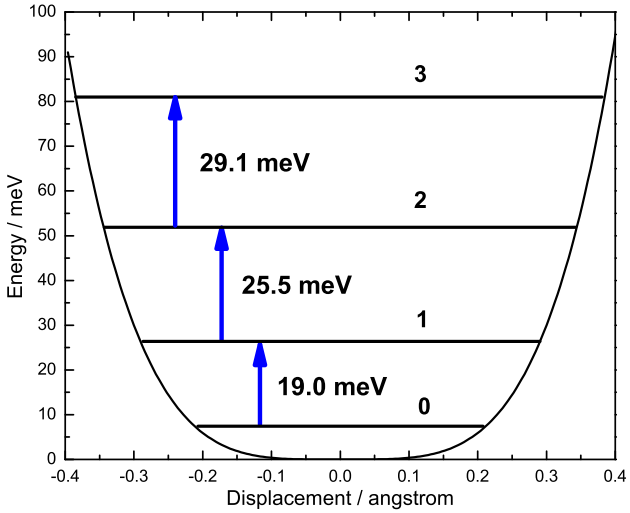

Figure 8.13: Energy levels of the quartic phonon mode R4+ and its frozen phonon potential

between vibrational frequency and energy levels similar to that for a harmonic oscillator. As a comparison, for the same force constant, the harmonic vibrational frequency of the F atom in the horizontal direction, towards and against the Sc atoms, is 27 THz (111 meV).

Next we allow for displacements of the Sc atoms and NTE. When the F atom is displaced transversely, the springs tend to pull the two Sc atoms together. The average displacements $\bar{x}_i$ of the F atoms at each energy level i were calculated numerically using quantum quartic wavefunctions. The average displacement $\bar{x}$ at temperature was then calculated by weighting $\{\bar{x}_i\}$ with level populations from Boltzmann distributions. Assuming the Sc-F bond length changes little with temperature, it is possible to calculate the thermal contraction of lattice parameters. The result in Fig. 8.14 shows many features of the experimental result of Greve [143], giving better agreement than the QHA. It should be noted that this approach takes into account only two-thirds of the fluorine modes.

The phonon modes at the M point are similar to those at the R point, differing only in the relative phase of the neighboring ScF_6 octahedra shown in Fig. 8.12.

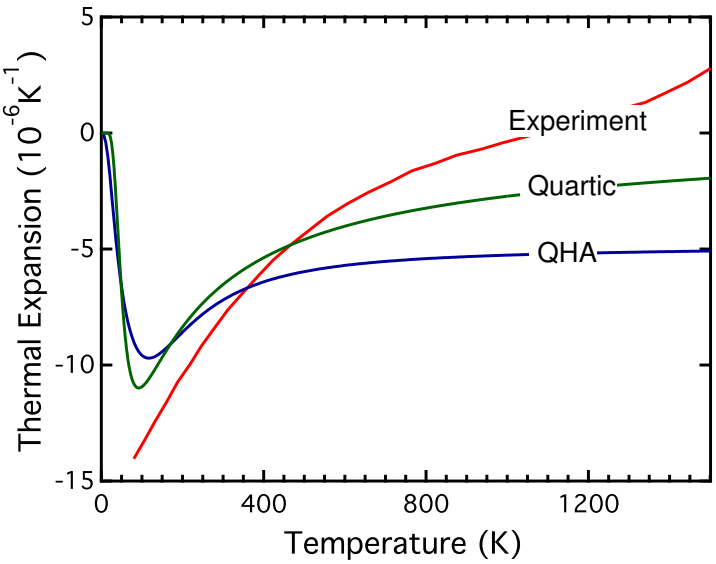

Figure 8.14: Experimental [143] and calculated linear thermal expansion coefficients using quasiharmonic approximation and quartic model

Most of the results for phonons at the R point therefore pertain to phonons at the M point as well.

Our frozen phonon calculations of modes with shape distortions of the octahedral ScF_6 units, but with fixed Sc-Fe first-nearest neighbor (1nn) distances, gave soft quadratic potentials, consistent with the Gaussian spread of F-atom displacements. The rocking of undistorted ScF_6 units about F-atom pivot points ("rigid unit modes") occurs without distortion of F-F 2nn distances, but these modes exist only on lines in the Brillouin zone along the M-R directions (the edges and corners of the cubic unit cell in reciprocal space). Nevertheless, with weak quadratic components, there are cylindrical volumes around these lines where the quartic potential dominates over the quadratic at modest temperatures. A full frozen phonon calculation for each mode in the Brillouin zone is not practical, but because these quartic modes caused the quasiharmonic calculations to predict very large and negative Grüneisen parameters, it is possible to map where this occurred in the Brillouin zone. We obtained a volume in the Brillouin zone by setting an isosurface where the QHA Grüneisen parameters (γ) were more negative than –5 (Fig. 8.15). The phonon modes inside the tubes of spheroids are the

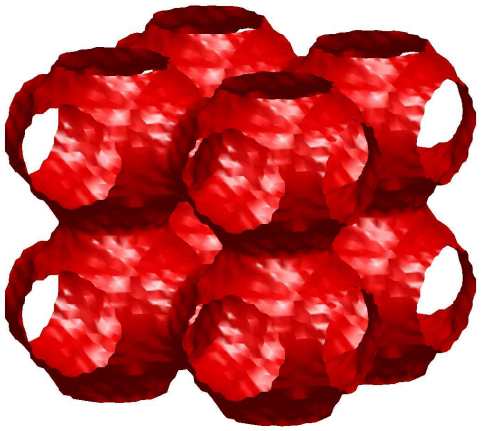

Figure 8.15: Isosurface of Grüneisen parameter $\gamma = -5$ for phonon dispersion branch 4+. The Γ point is at the center of the plot and R points are at centers of the spheroids. Centers of neighboring spheroids are connected along M-R directions.

ones that have substantial quartic terms in their potentials and contribute most to the NTE. For example, the frozen phonon calculation for Z point (Fig. 8.5), which is the midpoint between the M point (purely quartic mode potential) and the X point (purely quadratic mode potential), is shown in Fig. 8.16. The frozen phonon potential at the Z point has a substantial quartic term. For the R4+ modes centered around M-R, approximately two thirds of the Brillouin zone is within this anharmonic boundary, so there are a substantial number of modes with quartic behavior in ScF_3. The negative thermal expansion of ScF_3 should be a weighted combination of effects such as shown for the curves labeled QHA and quartic in Fig. 8.14.

Although cubic ScF_3 transforms to a rhombohedral phase at a pressure of 0.6 GPa and then to another structure at about 3 GPa [144], the cubic DO_9 structure is robust over a wide range of temperature at ambient pressure. The phase stability could be explained by the large vibrational entropy from the large-amplitude fluorine motions responsible for NTE. A full analysis requires information on the

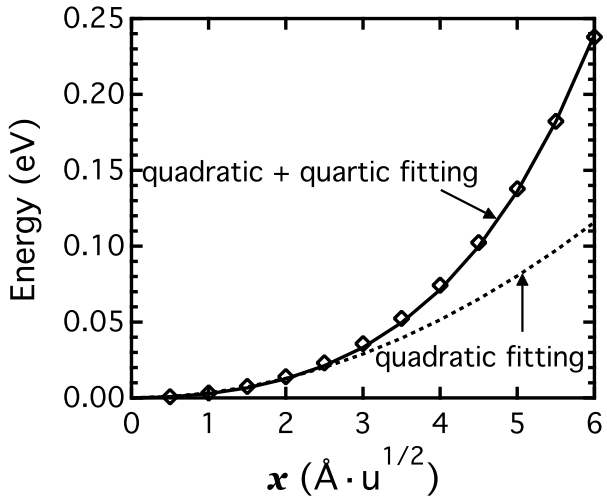

Figure 8.16: The frozen phonon potential of mode R4+ at Z point and its quadratic and quadratic + quartic fit. x is the normal mode coordinate. u is the atomic mass unit. For this mode, F atoms vibrate at different magnitudes and the largest displacement is 0.15 Å for x = 1.0 Å·u$^{1/2}$.

lattice dynamics of the competing phases, of course.

8.6 Conclusion

In summary, phonon DOS cures of ScF_3 with the cubic DO_9 structure were obtained from inelastic neutron scattering experiments, and from first-principles density functional theory calculations. The overall agreement between experiment and computation was good, allowing the identification of the atom motions in different parts of the phonon DOS. The geometry of the DO_9 structure offers transverse modes of F atom motion that are poorly constrained. These modes were found by frozen phonon calculation to be nearly pure quartic oscillators. Their dynamics are partly included in a quasiharmonic calculation of thermal expansion, which predicts the negative thermal expansion (NTE) semi-quantitatively. We understand the NTE of cubic ScF_3 as originating from these large transverse displacements of F atoms. Although the F atoms are confined to Sc neighbors by harmonic forces, by geometry the transverse modes are quartic oscillators that stiffen with

increased thermal vibrational amplitude. Meanwhile, the increased longitudinal forces on the Sc atoms pull them together, causing NTE, and the increased length of the Sc-F bonds cause longitudinal vibrations to soften with temperature.

Part V

Metals

Chapter 9

Aluminum

The thermal phonon broadening in aluminum was studied by theoretical and experimental methods. The majority of the theoretical work in this chapter was performed by Xiaoli Tang. Using second-order perturbation theory, phonon linewidths from the third-order anharmonicity were calculated from first-principles density functional theory (DFT) with the supercell finite-displacement method. The importance of all three-phonon processes were assessed, and individual phonon broadenings are presented. The good agreement between calculations and prior measurements of phonon linewidths at 300 K and new measurements of the phonon density of states to 750 K indicates that the third-order phonon-phonon interactions calculated from DFT can account for the lifetime broadenings of phonons in aluminum to at least 80% of its melting temperature.

9.1 Introduction

The shortening of phonon lifetimes owing to phonon-phonon interactions is a measure of lattice anharmonicity [10]. It is also closely related to nonequilibrium excitations of phonons and their evolution towards the ground state [154]. The method for calculating phonon lifetimes by perturbation theory has been known for some time [30], but quantitative evaluations require accurate energies and polarizations for all phonons, and accurate anharmonic force constants. Third-order anharmonic force constants are typically obtained from simple models consistent with empirical anharmonic elastic constants or thermal expansion [155,156]. First principles calculations of phonon linewidths have been performed with frozen phonon methods [157], which also allow a relatively easy calculation of phonon energy shifts [158,159]. More recent work on phonon lifetime broadening has been based on density functional perturbation theory (DFPT) [160]. This approach is often used for optical phonons [161–163], but only a few first-principles calculations have been performed for phonons outside the center of the Brillouin zone (BZ) [164,165]. Recently, Tang and Dong [128,166] extended the direct super-cell finite-displacement (SCFD) method to calculate the third-order anharmonicity

tensor. While DFPT and frozen phonon methods are efficient for studying the anharmonicity of a particular phonon, the SCFD method gives a direct evaluation of force constants, and is more efficient for assessments of all phonons in the BZ. Nevertheless, although ab-initio methods can often calculate harmonic phonon dynamics with reasonable accuracy, including the anharmonicity is a greater risk, and it is even less clear if three-phonon processes are sufficient to account for phonon lifetime broadenings at elevated temperatures.

Aluminum, a simple metal well-suited for plane wave density functional theory calculations, is a good test case for calculations of anharmonic effects. Phonon dispersions and linewidths in aluminum were measured by neutron spectrometry [167] at 80 K and 300 K, and a few modes were studied at 800 K [168]. The phonon density of states (DOS) was measured at temperatures to 775 K, showing a surprisingly large broadening [149] but small energy shifts that seemed consistent with conventional quasiharmonic behavior from thermal expansion. Some theoretical studies [33,169,170] assessed the phonon broadening using model potentials. Effects on phonons from the electron-phonon interaction were calculated within DFPT [171], but at high temperatures the phonon-phonon interactions are more important in aluminum [172,173].

Here we report results from an ab-initio study of the effects of three-phonon processes on the lifetimes of all phonons in aluminum. We find excellent agreement with experimental results on linewidths from triple-axis neutron scattering measurements along high-symmetry directions [167]. We also performed new measurements on the phonon DOS of aluminum at higher temperatures, and the broadening of the neutron spectra are accounted for by the ab-initio calculations. This demonstrates, first, that ab-initio methods are capable of predicting anharmonic effects, and second, that the anharmonic interactions in aluminum are dominated by third-order phonon-phonon scattering processes to at least 80% of the melting temperature. The dominant phonon-phonon scattering processes can then be identified, and detailed variations of phonon linewidths with wavevector $\vec{q}$ and temperature are reported.

9.2 Methods

9.2.1 Lattice-Dynamical Calculations

The phonon-phonon interaction is treated within second-order perturbation theory. When only three-phonon scattering processes are considered, the basic scattering processes are the annihilation of one phonon with the creation of two other phonons (down-conversion), and the annihilation of two phonons with the creation of one phonon (up-conversion). Simultaneous annihilations or creations of three phonons are excluded because they violate energy conservation. The phonon linewidth contributed from the leading third-order anharmonicity is [30, 31]:

$$\begin{aligned} 2\Gamma(\vec{q},j) = \frac{\pi\hbar}{8N}\sum_{\vec{q}_1 j_1,\vec{q}_2 j_2}\Delta(\vec{q}+\vec{q}_1+\vec{q}_2)\times\frac{|\Phi(\vec{q}j;\,\vec{q}_1 j_1;\,\vec{q}_2 j_2)|^2}{\omega(\vec{q}_1 j_1)\,\omega(\vec{q}_2 j_2)\,\omega(\vec{q}j)} \\ \times\left[(n_1+n_2+1)\,\delta(\omega-\omega_1-\omega_2)\right. \\ \left.+\,2(n_1-n_2)\,\delta(\omega+\omega_1-\omega_2)\right] \end{aligned} \tag{9.1}$$

where N is the number of unit cells, n is the Planck distribution function, ω_i is the phonon energy with wavevector $\vec{q}_i$ and branch index j_i, and Φ is the Fourier transform of the third-order lattice anharmonic tensor. The first term in the brace corresponds to a down-conversion process where the initial phonon of frequency ω decays into two lower-energy phonons of ω_1 and ω_2. The second term corresponds to a up-conversion process where an initial phonon of ω is scattered by a thermal phonon ω_1 into a phonon of higher energy (ω_2). The Δ and δ functions ensure the conservation of crystal momentum and energy, respectively. The sums extend over the first BZ. Full calculations of phonon widths therefore require knowledge of harmonic lattice dynamics and all applicable third-order anharmonicities. Harmonic lattice dynamics gives information of all one-phonon states that are characterized by energies and polarization vectors, while the anharmonic lattice tensor couples the one-phonon states and causes transitions between them.

The VASP software package [54] was used to calculate total energies and forces with Blöchl's projector-augmented wave pseudopotential [150] and planewave basis set within the local density approximation to density functional theory (DFT). The equilibrium structure was first determined by fitting energy-volume relationship to the third-order Birch-Murnaghan equation of state. The computed equilibrium lattice constants were approximately 1% less than the experimental values [174]. A Methfessel-Paxton smearing of 0.8 eV and a plane wave energy cutoff of 380 eV gave well-converged total energies. Both harmonic and anharmonic lattice dynamical properties were then obtained with a supercell finite-displacement method [166,175]. Independent force constants for a 108-atom periodic supercell were identified by the crystal symmetry, and the irreducible distorted supercell configurations for the force calculations were determined. Both harmonic and third-order anharmonic tensors were constructed based on the atomic forces that were computed for all these irreducible, distorted, 108-atom supercell configurations within DFT using a $\vec{k}$-point sampling grid of $2 \times 2 \times 2$. Phonon linewidths were finally calculated based on Eq. 9.1. A $24 \times 24 \times 24$ $\vec{q}$-point grid was found to give well-converged results, and an additional $32 \times 32 \times 32$ interpolation within the prism around each $\vec{q}$-point was used to more accurately account for energy conservation.

9.2.2 Inelastic Neutron-Scattering Experiments

Aluminum metal of 99.99% purity was formed as cylinders with outer diameter of 1.7 cm and total wall thickness of 0.06 cm, giving a ratio of multiply- to singly-scattered neutrons of only 2%. Inelastic neutron scattering measurements were performed with a time-of-flight Fermi chopper spectrometer, ARCS, at the Spallation Neutron Source at Oak Ridge National Laboratory. The incident neutron energy was 79.5 meV, and each measurement included a total of approximately 1.4×10^6 counts. For temperatures of 7, 100, 200, and 300 K, the sample was mounted in a closed-cycle helium refrigerator. For temperatures of 300, 450, 600,

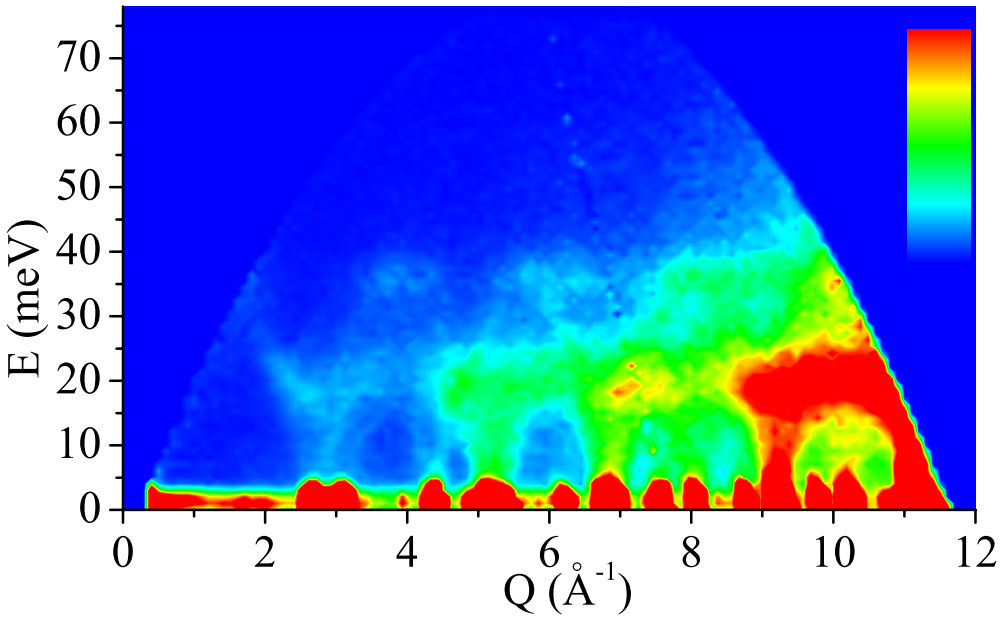

Figure 9.1: Neutron scattering $S(Q,E)$ from aluminum at 300 K. The vertical axis of the color scale is linear in intensity.

and 750 K, the sample was mounted in a low-background, electrical-resistance furnace designed for vacuum operation. Data reduction was performed with the standard software package for the ARCS instrument, as described previously. [70] The $S(Q,E)$ for 300 K is shown in Fig. 9.1. The Q ranged from 0 to 14 Å^{-1}, with a bin width of 0.1 Å^{-1}, and E ranged from –78.0 to 78.0 meV, with a bin width of 1.0 meV. The elastic peak was removed below 8.0 meV and replaced by a function of energy determined from the inelastic scattering just past the elastic peak [149]. The phonon DOS curves were obtained after corrections for multiphonon and multiple scattering, as described previously [149]. The averaging over all Q for a given E will eliminate effects of coherent interference between single- and two-phonon scattering. Compared to previous measurements on aluminum [149], the increased neutron flux of ARCS made it possible to use thinner samples, which greatly suppressed multiple scattering while achieving better statistics and energy resolution.

9.3 Results and Discussion

Figures 9.2a shows the calculated phonon energies along high-symmetry directions with the phonon DOS at right. Figure 9.2b shows the corresponding phonon linewidths of these high-symmetry modes. Both phonon energies and linewidths are compared with results from triple-axis neutron scattering measurements [167]. The $\vec{q}$-space distribution of phonon linewidths is seen more clearly on four high-symmetry planes in Figs. 9.3a, 9.3b, and 9.3c. The longitudinal acoustic (LA) phonons are generally much broader than the transverse acoustic (TA) phonons, and the breadths of the LA phonons vary more strongly with wavevector. The greatest broadening is for LA phonons near square surfaces centered at X, and near hexagonal surfaces centered at L.

The scattering kinematics are given by the two-phonon DOS functions D_1 and D_2, which are the BZ sums of second and first products of the δ and Δ functions in Eq. 9.1 [176]:

$$D_1(i,q) = \frac{1}{N} \sum_{\vec{q}_1,\vec{q}_2,j_1,j_2} \Delta(\vec{q} - \vec{q}_1 - \vec{q}_2)\, \delta(\omega - \omega_1 - \omega_2), \tag{9.2}$$

$$D_2(i,q) = \frac{1}{N} \sum_{\vec{q}_1,\vec{q}_2,j_1,j_2} \Delta(\vec{q} + \vec{q}_1 - \vec{q}_2)\, \delta(\omega + \omega_1 - \omega_2), \tag{9.3}$$

where D_1 and D_2 correspond to the down-conversion and up-conversion scattering processes, respectively. Figure 9.4 shows D_1 and D_2 along high-symmetry directions. While TA phonons are mostly scattered by up-conversion processes, LA phonons, especially short-wavelength ones, are mostly scattered by down-conversions. The dominant decay channels for LA phonons are LA↔TA+TA ($\backsim$ 85%) and LA↔LA+TA ($\backsim$ 15%). Fewer down-conversion channels become available towards the zone center, and up-conversion channels start to open for LA phonons at $\vec{q}$-vectors where their energies are lower than some TA phonons. The scattering channels change from LA↔LA–TA dominance to LA↔TA–TA dominance when the $\vec{q}$-vector approaches the zone center. Owing to the symmetry of the scattering channels, the dominant scattering channels for transverse phonons

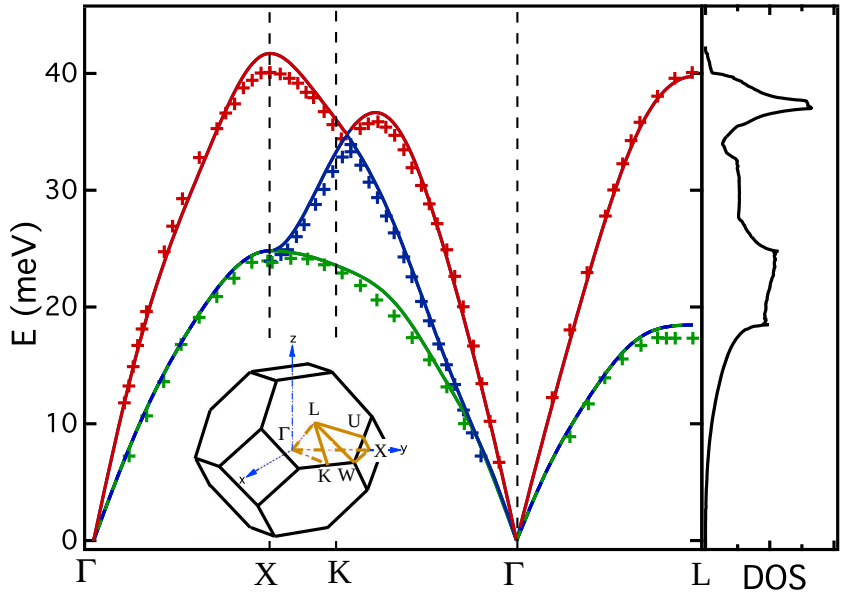

(a) Phonon dispersion

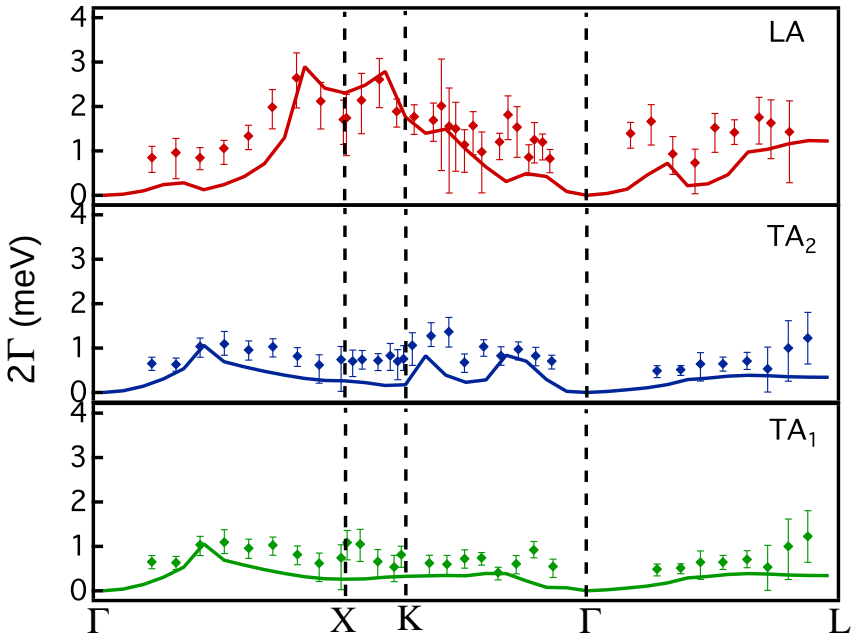

(b) Phonon linewidth

Figure 9.2: Calculated phonon dispersion at 0 K with DOS shown at right (a) and correspondent linewidth at 300 K (b) (solid lines), in comparison with neutron spectroscopy measurement from Ref. [167] (symbols)

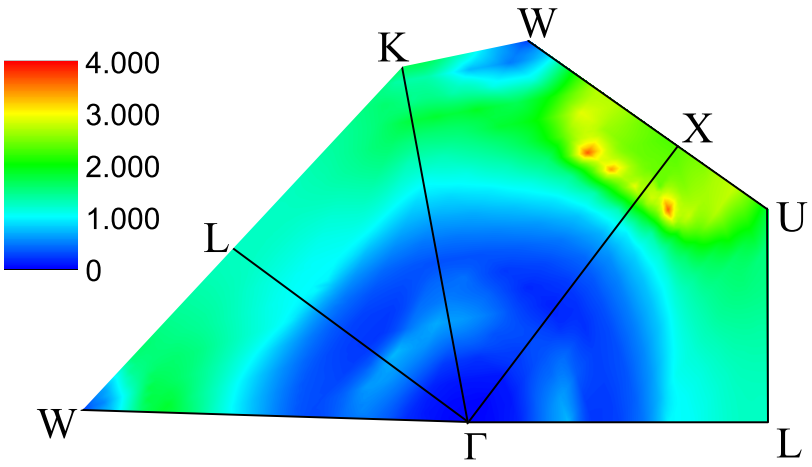

(a) 2Γ (meV) of LA modes

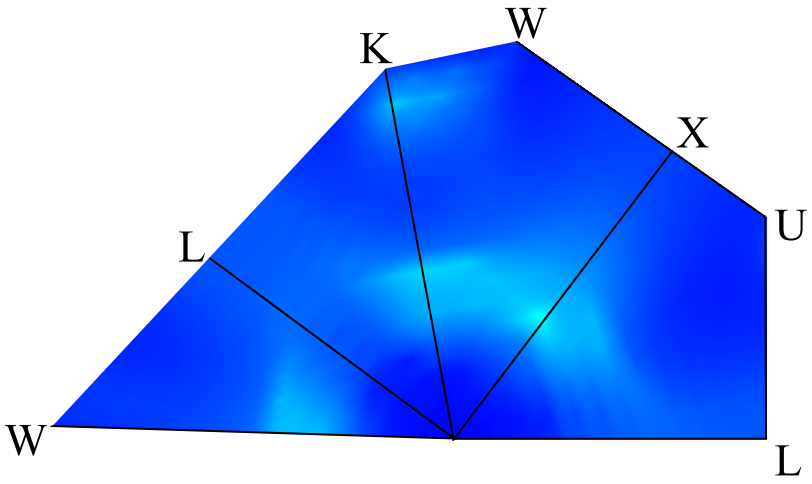

(b) 2Γ (meV) of TA_2 modes

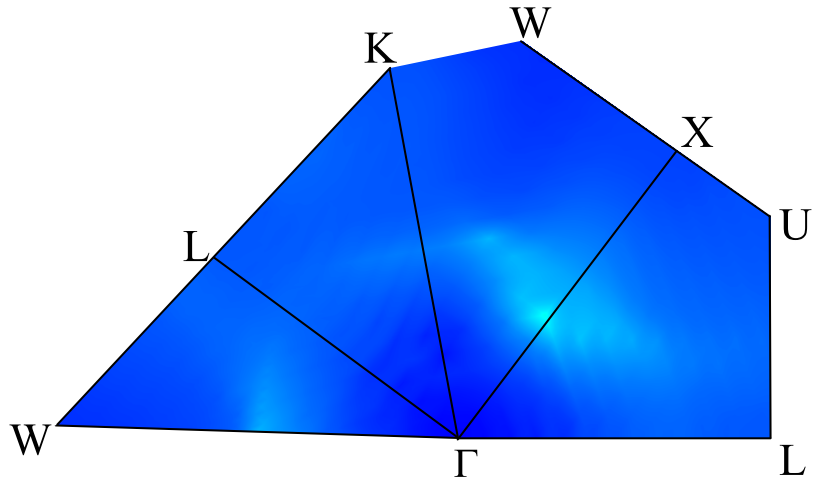

(c) 2Γ (meV) of TA_1 modes

Figure 9.3: Phonon linewidth distribution over high-symmetry planes are shown in (a), (b), and (c) for LA, TA_1, and TA_2 modes.

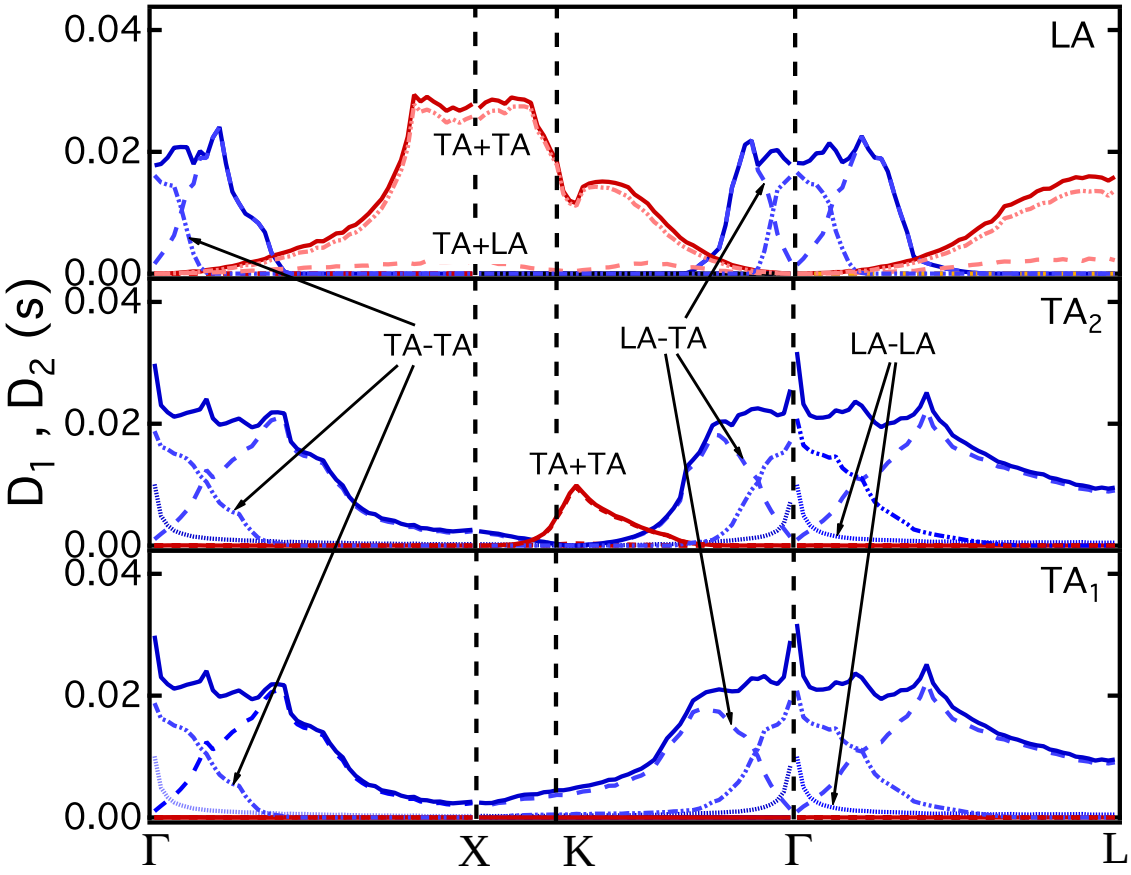

Figure 9.4: Up-conversion (D_1) processes in blue and down-conversion (D_2) processes in red for three branches along high-symmetry directions. Individual scattering channels are shown by dashed lines.

are expected to be TA↔LA–TA. Near the zone center, processes like TA↔TA–TA and TA↔LA–LA start to dominate. Large variations of the two-phonon density of states, especially those of LA modes, are clearly responsible for the large variation of phonon linewidth, as one can see by comparing Fig. 9.2b and 9.4.

Figure 9.5 shows the phonon linewidths at 300 K at all irreducible q-vectors for the different phonon energies. Phonons in the high-energy region have a much larger broadening than in the low-energy region. There is a splitting of the linewidth distribution in the high-energy region, associated with LA phonons near square and hexagonal surfaces of the Brillouin zone (evident from Fig. 9.3a). These LA phonons are primarily scattered by down-conversion into two TA phonons

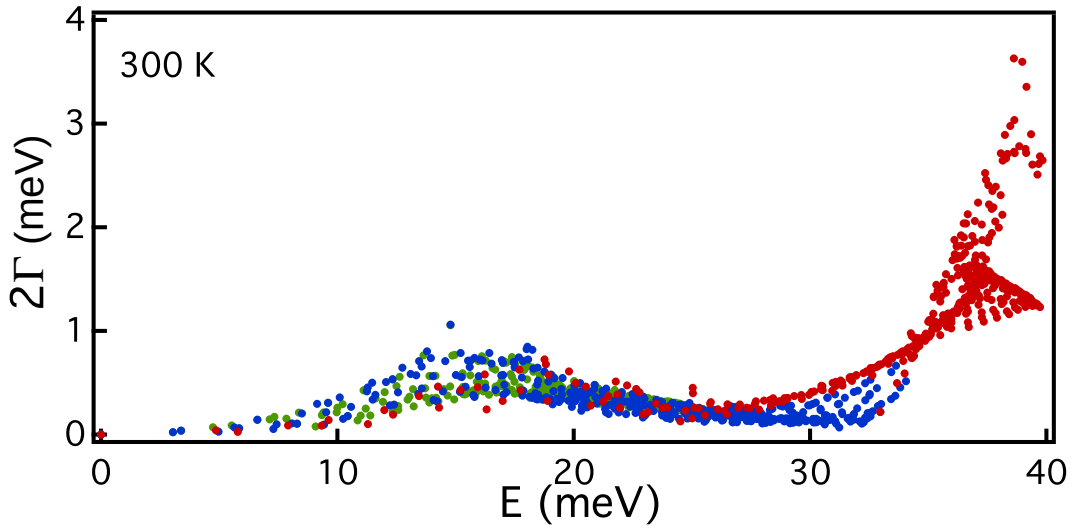

Figure 9.5: Distribution of phonon broadenings versus phonon energy at 300 K with TA_1 phonons shown in green, TA_2 phonons in blue, and LA phonons in red

(Fig. 9.4). The LA phonons with wavevectors near the square surface of the BZ have shorter lifetimes because there are more TA phonons available kinematically for their decay (note the similarity of the LA panels in Fig. 9.2b and Fig. 9.4). The LA phonons with wavevectors near the square surfaces decay into two TA phonons that are both in the middle-energy range where the DOS is high, but the LA phonons with wavevectors near hexagonal surfaces can decay into only one TA phonons in the middle energy range—the other TA phonon falls in the low-energy range near the zone center where the DOS is much lower.

To obtain the overall effect of phonon broadening on the phonon DOS, the linewidths of all the phonons at irreducible $\vec{q}$-points on a $24 \times 24 \times 24$ $\vec{q}$-grid were calculated from 0 K to 900 K. Phonon linewidths increase with temperature owing to phonon occupation numbers in Eq. 9.1, but different phonons broaden with temperature at different rates. Phonon DOS curves at a given temperature, $g(E, T)$, were calculated by considering the phonon broadening from third-order anharmonicity, and the phonon shifts caused by thermal expansion in the quasi-harmonic approximation. The energy lineshape of each phonon was modeled as

a damped harmonic oscillator [14]

$$g(E,T) = \int (B(E,E',T)g(E' - \triangle E'(T))\,\mathrm{d}E' \,, \tag{9.4}$$

where the damped harmonic oscillator function is

$$B(E,E',T) = \frac{2\Gamma'}{(\pi E'E)[(\frac{E}{E'} - \frac{E'}{E})^2 + (\frac{2\Gamma'}{E'})^2]} \,, \tag{9.5}$$

and the energy shift is

$$\triangle E' = E'\left[\exp\left(-3\gamma\int_0^T \alpha(T')dT'\right) - 1\right] \,, \tag{9.6}$$

where the mode Grüneisen parameter γ was calculated as $\mathrm{d}\ln\omega/\mathrm{d}\ln V$, and the coefficient of linear thermal expansion α was evaluated with an empirical relation between thermal expansion and heat capacity for aluminum. [177]

Figure 9.6 compares the calculated and measured phonon DOS curves. There is a significant broadening of the phonon DOS at higher temperatures, and the broader peak around 37 meV indicates that LA phonons decay faster than TA phonons. The large broadening of these LA phonons gives a prominent tail that extends to higher energies. The overall trend of a larger broadening of LA than TA phonons is in good agreement between computation and experiment. The good agreement between the quasiharmonic phonon shift due to thermal expansion and experiment suggest that the higher-order anharmonicity corrections to the phonon shifts are likely to be small. It is unlikely that the shifts from the third-order and fourth-order anharmonicity are canceling for all phonons in the BZ.

The overall agreement between computation and experiment is good, but there are discrepancies. Some may be associated with the accuracy of the DFT method for calculating the anharmonicity tensor, or from the limitations of perturbation theory when including only third-order phonon-phonon interactions. The lifetime broadening should, in principle, be calculated with phonons for a crystal volume corresponding to each temperature of interest. However, using phonons calculated

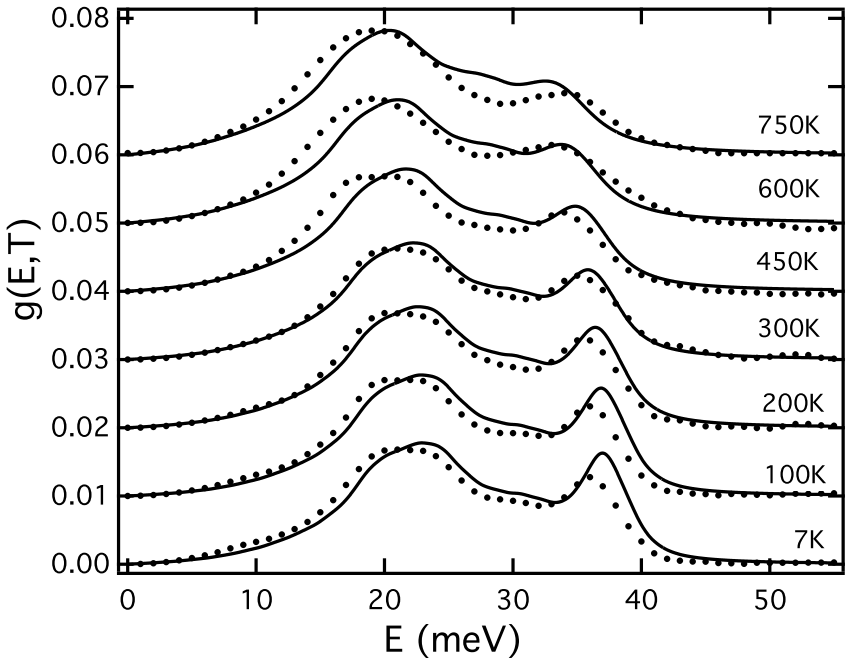

Figure 9.6: Comparison of phonon DOS between calculation (solid lines) and inelastic neutron scattering measurements (points)

for an expanded crystal at 600 K altered the results for most phonon lifetimes by less than 1%, and 5% for near-zone boundary modes. A major discrepancy comes from the limitations of the analysis of the experimental broadenings when the phonon linewidth is comparable to the energy resolution of the instrument. In principle, the phonon linewidth must approach zero as q goes to zero, and this trend is not seen in the experimental data of Fig. 9.2b.

9.4 Conclusions

In summary, the linewidths of all phonons in aluminum were obtained from first-principles density functional theory with methods using interacting phonon theory in second-order perturbation theory. The good agreement between the calculated phonon linewidths and previous linewidth measurements at 300 K, and the shapes of the phonon DOS curves to 750 K, not only demonstrate that our method can successfully predict the anharmonicity tensor with DFT, but also indicate that

the third-order phonon-phonon interactions are primarily responsible for the lifetime broadening of phonons in aluminum to approximately 80% of its melting temperature. The most anharmonic phonons in aluminum are found to be those LA phonons near square and hexagonal surfaces of the first Brillouin zone. The major scattering channels for these LA phonons are their decay into two TA phonons. At lower $\vec{q}$, the kinematics favor the up-conversion of both LA phonons and TA phonons. Because the phonon dispersions of FCC metals tend to be similar, phonon lifetimes show similar systematics for other FCC metals, such as the nobel metals, although the $\vec{q}$ of the most anharmonic LA phonons will differ somewhat. [178] We look forward to more extensive applications of these computational methods to account for the effects of phonon-phonon interaction in anharmonic solids, thereby isolating nonharmonic effects from adiabatic electron phonon interactions, for example.

Part VI

Future Work

Chapter 10

Progress in Phonon Anharmonicity and Future Work

The Raman spectroscopy studies of Γ phonons in hafnia and zirconia left some interesting ideas. Contrary to popular wisdom that a single macroscopic Grüneisen can approximately describe the phonon energy dependence on lattice volume, the physical picture proves more complicated. Due to the relatively low symmetry of these oxides, the microscopic Grüneisen parameters vary widely for different phonon modes, and change sign. Although averaged effects on macroscopic properties may seem consistent with quasiharmonic behavior, a significant fraction of the phonon modes are indeed quite anharmonic. Similar behaviors are expected for the majority of ionic compounds, especially those with low-symmetry structures. Follow-up studies on titania and cassiterite further confirmed the importance of mode geometry on the mode anharmonicity. Also, the discrepancy between the temperature and pressure Grüneisen parameters is surprisingly large, suggesting different mechanism for intrinsic and extrinsic anharmonicity. Previous studies have largely neglected these effects, and further exploration will advance the understanding of phonons and vibrational entropy.

Large anharmonicities of some phonon modes may not show up in macroscopic thermodynamical properties, as has been the case for hafnia and zirconia, but the case is quite different for other materials. In scandium fluoride, two phonon modes involving the transverse fluorine motions are purely quartic at some

high symmetry points in the Brillouin zone (BZ), and in more than two-thirds of the BZ, they also have large quartic components in their phonon potentials. These quartic modes result in the thermal stiffening of some low-energy phonons, and more dramatically an enormous isotropic negative thermal expansion over a temperature range 1100 K. Additionally, the vibrational entropy contribution from these phonon modes helps stabilize the delicate (open framework) cubic phase up to the melting point. Phonon anharmonicities, even from only a few phonon modes, have the potential in determining some macroscopic thermodynamical properties, such as negative thermal expansion, phase stability, and thermal transport. Besides the scientific interest, understanding phonon anharmonicities can benefit materials engineering and applications.

A wide range of energy-related challenges require materials with thermal transport properties tailored to specific applications. For energy production, there is a need to better understand thermal transport in nuclear fuels containing physical and chemical defects. For energy consumption, better thermal barrier coatings can improve fuel efficiencies of internal combustion and jet engines. For waste-heat harvesting, the development of improved thermoelectric compounds is limited by compromising between electrical and thermal transport properties. With the development of three-dimension silicon chips and increased leakage current owing to reduced component size, modern electronics are becoming progressively more energy intensive, making effective cooling a daunting task. All these challenges create a continuous pursuit of materials with improved thermal transport properties.

Most engineering applications require either good thermal conductors or good thermal insulators. Unlike electrical conductivity, which spans twenty orders of magnitude, thermal conductivity only ranges from about 0.01 to 1000 W/(m·K). For “good” metals and many semiconductors, the conduction electrons dominate thermal transport, but in most other systems, including some of the best thermal conductors and insulators, thermal transport by phonons is the main mechanism. Traditionally, phonon-related heat transport problems are solved using the phonon

mean-free-path approximation, but the phonon Boltzmann transport equation is becoming more common. This approach requires a detailed understanding of phonon scattering, including phonon-phonon, phonon-defect, and phonon-boundary processes. As a result, it is increasingly difficult to model large-scale systems, in which effects of grain size, interfaces, and disorders cannot be ignored.

Anharmonic phonon-phonon scattering is the key to a better understanding of thermal transport. While Raman spectroscopy has high energy resolution and gives insight into the rich variety of the phonon anharmonic effect in complex structures, it has access to only some of the optical phonon modes at the center of the Brillouin zone. For a more complete study of anharmonicity, neutron scattering studies using a time-of-flight or a triple-axis instrument are necessary. Time-of-flight inelastic neutron scattering is the ideal tool to capture the overall phonon DOS and its temperature dependence. Aside from the phonon frequency shift, which is typically used to understand vibrational thermodynamics, high resolution measurements of phonon energy broadening allow for an assessment of the origin of the anharmonic behavior. Heat is transported mostly by long-wavelength longitudinal modes, and thus it is important to examine trends in the phonons at low energies. The cold neutron spectrometer may be a better tool for detailed phonon linewidth studies of phonon dispersions at lower energies.

One of the projects in progress is an anharmonicity study of alkaline earth metal oxides (MgO, CaO, SrO, and BaO). The thermal transport properties of these materials are very important for geophysics, and theoretical calculations of the phonon anharmonicities due to phonon-phonon coupling are available. It is also interesting to study the change of anharmonicity from size effects and differences in chemical environments. The TOF inelastic neutron scattering measurements on these materials up to 1300 K were successfully performed with the ARCS spectrometer, and the initial results have very good quality and show interesting trends. Large, high-quality single crystals are readily available for many of the metal oxides, such as MgO and Al_2O_3. They are ideal subjects for studies of phonon anharmonicity with triple-axis neutron spectrometers.

Ongoing studies on transition-metal oxides, such as hafnia, zirconia, and yttria-stabilized zirconia (YSZ), which play vital roles in batteries and photovoltaics, will not only improve the understandings of their phonon behavior and thermal transport but also of other transport properties, such as ionic conductivity. YSZ is the top candidate for thermal barrier coating applications due to its high bulk modulus, high melting temperature, and surprisingly low thermal conductivity. YSZ has a slight increase of thermal conduction at higher temperature where oxygen vacancies may play the dominant role in transport properties. The phonon DOS of these materials up to 1300 K were obtained by inelastic neutron scattering, and the analysis is in progress.

Among other materials of interest, carbon materials include some of the best thermal conductors and insulators. Although graphite and graphene have metal-like properties, their heat conduction is generally dominated by phonons and can be tuned by disorders, defects, and grain size. Phonon anharmonicity also plays an important role in the negative thermal expansion of graphene. Another subject of interest are materials with anisotropic thermal properties, such as tungsten selenide. The highly anisotropic structure in tungsten selenide is believed to produce flat phonon dispersions along one axis, resulting in a slow sound velocity and a significant reduction (1/30) in thermal conductivity along this direction. It is possible that materials with similar structural characteristics will reduce heat conduction in a desired direction while providing good electric conductivity, making them ideal thermoelectrics. One example is oxide-based thermoelectric materials, which have the advantage of superior thermal stability.

With the advent of large computer clusters, first principles density functional theory is now able to accurately calculate phonon linewidths from phonon-phonon coupling using interacting phonon theory in second-order perturbation theory. Our recent calculations in aluminum show good agreement between calculated phonon linewidth and experimental results. In order to address the discrepancy between the theory and experiment at low Q values, and to examine the temperature effects, a triple-axis experiment was performed to measure the phonon

linewidth in an Al single crystal along high symmetry directions at 7, 300, 450, and 600 K. The data analysis is currently in progress.

The calculation of phonon linewidths also proves helpful for sorting out the electron-phonon interactions in materials. By subtracting the contribution of phonon-phonon interactions from the total phonon linewidth, it is possible to isolate the electron-phonon effects. Pd and Pt metals are similar electronically, but differ in the strengths of their electron-phonon interactions. Our group has recently shown large effects of the adiabatic EPI on the temperature dependence of phonons in V metal [1], which has an EPI not much bigger than that of Pd. Older work by Brockhouse and colleagues [179] reported the temperature dependence of Kohn anomalies in Pd and Pt, and these effects on the transverse phonon branches seem big enough to be important to the thermodynamics of Pd and Pt at elevated temperatures. To address these questions, the temperature dependence of the phonon DOS of Pd and Pt to 1600 K were measured with the ARCS spectrometer. It was a successful experiment, although the requirement for a very high sample temperature made it difficult. The measured phonon DOS were clean, and the temperature effects on phonon energy and linewidth were well quantified. Further computational analysis is still in progress.

First-principles molecular dynamics, also made practical only recently, is an intrinsically better representation of real materials than traditional phonon calculations at zero temperature. When executed well, this method provides the most complete and accurate information about the system (within the limit of density functional theory) including all thermodynamic properties. This is crucial for anharmonicity studies because extrinsic anharmonic effects will be missed otherwise. With knowledge of the phonon dynamics, bulk thermal conductivity can be calculated using the Boltzmann transport equation or Monte Carlo simulations. A multiple-scale simulation is necessary to address fully the thermal transport properties in real materials because interfaces must be modeled at a macro scale with acoustic mismatch or diffusion. Experimentally, the laser flash and pump-probe reflectivity techniques are mature and reliable to measure the

thermal conductivity in materials, especially for high-quality samples such as single crystals. A comparison between simulation and experiment will not only help to better understand the widely used materials, but may also help to improve them and develop new ones for various energy applications.

Phonon anharmonicity and the related vibrational entropy are often crucial for phase stability. For alloys of Cu and Zr, a peculiar B2 phase (CuZr) exists in equilibrium only at high temperatures, and it undergoes a eutectoid transformation below 715°C to two other intermetallic compounds of lower symmetry, so it must have relatively high entropy. Almost certainly there is some stabilization of this phase at high temperatures, owing to its vibrational entropy being greater than the lower-symmetry phases. This is unexpected and of great interest for study. Meanwhile, 50/50 CuZr easily forms metallic glass, and a dynamical study of the phonons through the glass transformation could also be interesting.

Part VII

Appendix

Appendix A

Publications Related to the Current Work

Ordered by the year of publication:

C. W. Li, X. Tang, J. A. Muñoz, J. Keith, S. Tracy, D. L. Abernathy, and B. Fultz, *Structural relationship between negative thermal expansion and anharmonicity of cubic ScF_3*, Physical Review Letters, 107, 195504 (2011)

J. A. Muñoz, M. S. Lucas, O. Delaire, M. L. Winterrose, L. Mauger, Chen W. Li, A. O. Sheets, M. B. Stone, D. L. Abernathy, Y. Xiao, P. Chow, and B. Fultz, *Positive vibrational entropy of chemical ordering in FeV*, Physical Review Letters, 107, 115501 (2011)

N. D. Markovskiy, J. A. Muoz, M. S. Lucas, Chen W. Li, O. Delaire, M. B. Stone , D. L. Abernathy, and B. Fultz, *Non-harmonic phonons in MgB_2 at elevated temperatures*, Physical Review B, 83, 174301, (2011)

C. W. Li, M. M. McKerns, and B. Fultz, *A Raman Spectrometry Study of Phonon Anharmonicity of Zirconia at Elevated Temperatures*, Journal of American Ceramic Society, 94, 1, 125–130 (2011)

X. Tang, C. W. Li, and B. Futlz, *Anharmonicity-induced phonon broadening in aluminum at high temperatures*, Physical Review B, 82, 184301 (2010)

J. B. Keith, J. R. Fennick, D. R. Nelson, C. E. Junkermeier, J. Y. Y. Lin, C. W. Li, M. M. McKerns, J. P. Lewis, and B. Fultz, *AtomSim: Web-deployed Atomistic Dynamics Simulator,* Journal of Applied Crystallography, 43, 1553–1559 (2010)

M. S. Lucas, J. A. Muñoz, L. Mauger, C. W. Li, A. O. Sheets, Z. Turgut, J. Horwath, D. L. Abernathy, M. B. Stone, O. Delaire, Y. Xiao, and B. Fultz, *Effects of chemical composition and B2 order on phonons in bcc Fe-Co alloys*, Journal of Applied Physics, 108, 2 (2010)

C. W. Li, M. M. McKerns, and B. Fultz, *Raman spectrometry study of phonon anharmonicity of hafnia at elevated temperatures*, Physical Review B, 80, 5 (2009)

Appendix B

TOF Inelastic Scattering Sample Thickness

When planning for a TOF inelastic neutron-scattering experiment, one of the first things to consider is the amount of the sample to use. There are cases in which one has to use whatever is available. For example, the sample may be extremely expensive, so only a small amount is available, or the sample may be a single crystal. But most of the time it is possible choose a good compromise that minimizes multiple scattering while making good use of the available neutrons.

The neutron-scattering cross sections for coherent scattering, incoherent scattering, and absorption are available in many databases, such as the website of NCNR. [67] The common unit for these cross-sections is the barn, which is $10^{-28}\mathrm{m}^2$. The numbers are usually single- or two-digit, although some isotopes may have absorption cross sections of thousands of barns. These cross sections are actually quite small for most elements (different for isotopes) because a neutron has no charge and can only be scattered by nuclei through the strong force, which has a very short range. Samples with any element with an absorption cross section larger than 10 barn may suggest a problem, although sometimes an isotope can be used instead. For example, natural Boron has two isotopes: ^{10}B (20%) and ^{11}B (80%), and ^{10}B has a absorption cross section of 3836 barn. Any sample with a significant B concentration is hopeless for TOF inelastic neutron scattering. However, ^{11}B has almost no absorption (0.0055 barn), so the sample made with highly concentrated ^{11}B (modestly expensive) will work.

For a relatively thin sample, it is a good approximation that the scattered fraction (f_{scatt}) equals the ratio of the sum of all the total scattering (coherent plus incoherent) cross sections of the atoms in the neutron beam (σ_i) to the physical cross section of the sample in the neutron beam (A)

$$f_{\mathrm{scatt}} = \frac{\sum_i \sigma_i}{A}. \tag{B.1}$$

Assume the sample has an even thickness of d, a density of ρ, and a molar mass of $M = \sum_j n_j M_j$, where M_j and n_j are the molar mass and quantities of the jth element in the chemical formula, the number of jth atom in the neutron beam

is

$$N_j = \frac{dA\rho n_j N_{\mathrm{A}}}{M}, \tag{B.2}$$

and where N_{A} is the Avogadro constant. The the scattered fraction is

$$f_{\mathrm{scatt}} = \frac{\sum_j \sigma_j N_j}{A} = \frac{d\rho N_A}{M} \sum_j \sigma_j n_j, \tag{B.3}$$

where σ_j is the total scattering cross section of the jth element.

The result (Eq. B.3) is intuitive. The scattering fraction is proportional to the thickness, density, and atom-weighted total cross section of the material. For a 5% ~ 10% scattering cross section, as discussed in Section 4.3.5, and a neutron beam size of 5×5 cm^2 (the ARCS spectrometer), a typical sample needs and weigh somewhere between a few grams to a few hundred grams. This is sometimes one of the major obstacles of TOF inelastic neutron scattering, because a large amount of sample can be prohibitively expensive or challenging to make.

There are also a few other things to be considered when planning the sample. Firstly, the sample is usually placed at 45 degrees to the neutron beam to avoid casting the "dark angle" onto the detectors. This does not alter the required sample amount but does change the thickness and shape of the sample. Secondly, the sample environment may need to be taken into account, especially when it produces a large background. It is not a good idea to have the overall signal dominated by the neutrons scattered from the sample environment, but it is even worse if there is double scattering from both sample and sample environment. The latter will cause significant troubles for the multiphonon and multiple scattering corrections. Lastly, when a sample can is used, it is hard to estimate an average sample thickness. In those cases, it is always a good idea to use less sample, especially if the background is low.

Appendix C

Folding Sample Sachet

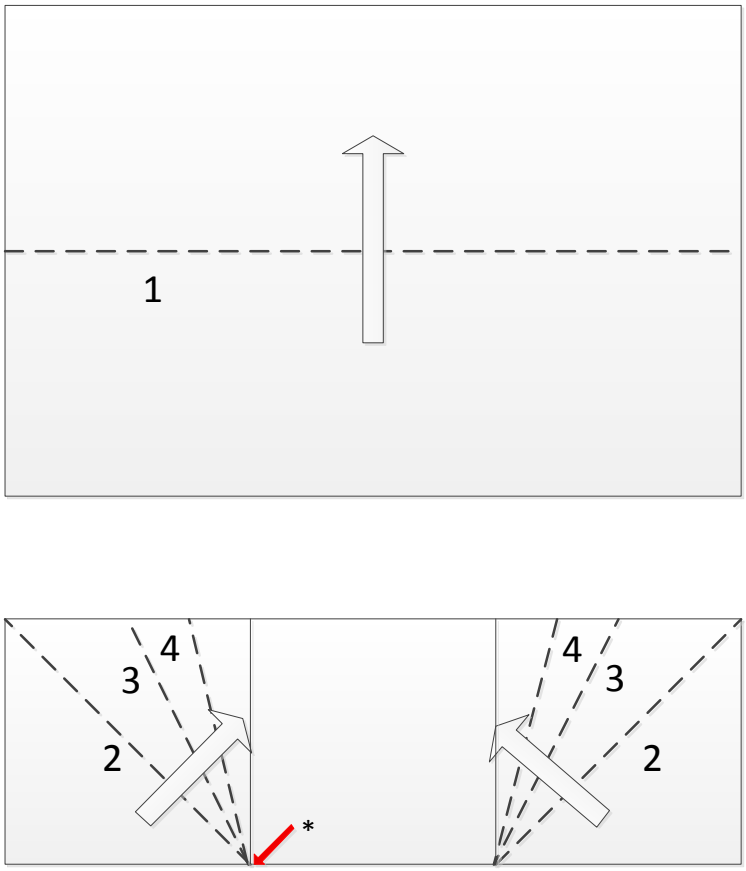

Figure C.1: Fold a sample sachet from one piece of foil. Follow the numbers and fold at the dashed lines, then cut off excessive pieces on the top. The thick side edges need to be shielded by a neutron-absorbing BN frame. It may be a good idea to slightly shift the part marked by the red arrow to avoid breaking brittle metal foil.

Part VIII

Bibliography and Index

Bibliography

[1] O. Delaire, M. S. Lucas, J. A. Muñoz, M. Kresch, and B. Fultz, "Adiabatic Electron-Phonon Interaction and High-Temperature Thermodynamics of A15 Compounds," *Physical Review Letters*, vol. 101, no. 10, p. 105504, 2008.

[2] O. Delaire, M. Kresch, J. A. Muñoz, M. S. Lucas, J. Y. Y. Lin, and B. Fultz, "Electron-phonon interactions and high-temperature thermodynamics of vanadium and its alloys," *Physical Review B*, vol. 77, no. 21, p. 214112, 2008.

[3] *Wikipedia*. http://en.wikipedia.org/wiki/Phonon.

[4] J. M. Ziman, *Electrons and phonons: the theory of transport phenomena in solids*. Oxford: Clarendon Press, 2001.

[5] M. T. Dove, *Introduction to lattice dynamics*. Cambridge: Cambridge University Press, 1993.

[6] M. I. Kaganov, *Electrons, phonons, magnons*. Moscow: Mir, 1981.

[7] D. Wallace, *Thermodynamics of crystals*. New York: Wiley, 1972.

[8] G. Venkataraman, *Dynamics of perfect crystals*. Cambridge: MIT Press, 1975.

[9] J. M. Ziman, *Principles of the theory of solids*. Cambridge [Eng.]: University Press, 1972.

[10] N. D. Ashcroft, Neil W. Mermin, *Solid state physics*. New York: Holt Rinehart and Winston, 1976.

[11] C. Hammond, *The basics of crystallography and diffraction*. Oxford: Oxford University Press, 2009.

[12] *Wikipedia*. http://en.wikipedia.org/wiki/Bravais_lattice.

[13] C. Kittel, *Introduction to solid state physics*. Hoboken, NJ: Wiley, 2005.

[14] A. P. French, *Vibrations and waves*. New York: Norton, 1971.

[15] M. G. Kresch, *Temperature dependence of phonons in elemental cubic metals studied by inelastic scattering of neutrons and X-rays*. PhD thesis, Caltech, 2008.

[16] B. Fultz, T. Kelley, M. Mckerns, J. Lee, O. Delaire, and M. Kresch, *Experimental inelastic neutron scattering: introduction to DANSE*. http://docs.danse.us/DrChops/ExperimentalInelasticNeutronScattering.pdf, 2011.

[17] J. Slater, *Introduction to chemical physics*. New York; London: McGraw-Hill Book Company, Inc., 1939.

[18] C. Booth and J. S. Rowlinson, "The influence of lattice vibrations on the order-disorder transitions of alloys," *Transactions of the Faraday Society*, vol. 51, pp. 463–467, Jan. 1955.

[19] L. Anthony, J. K. Okamoto, and B. Fultz, "Vibrational entropy of ordered and disordered Ni_3Al," *Physical Review Letters*, vol. 70, pp. 1128–1130, Feb. 1993.

[20] D. C. Wallace, *Statistical physics of crystals and liquids: A guide to highly accurate equations of state*. River Edge, NJ: World Scientific, 2002.

[21] P. D. Bogdanoff, B. Fultz, J. L. Robertson, and L. Crow, "Temperature dependence of the phonon entropy of vanadium," *Physical Review B*, vol. 65, p. 014303, Dec. 2001.

[22] O. Delaire and B. Fultz, "Charge redistribution and phonon entropy of vanadium alloys," *Physical Review Letters*, vol. 97, p. 245701, Dec. 2006.

[23] P. Bruesch, *Phonons: Theory and experiments I: Lattice dynamics and models of interatomic forces*. Berlin: Springer-Verlag, 1982.

[24] A. Maradudin, *Theory of lattice dynamics in the harmonic approximation*. New York: Academic Press, 1971.

[25] M. Born, *Dynamical theory of crystal lattices*. Oxford: Clarendon Press, 1954.

[26] G. Srivastava, *The physics of phonons*. Bristol; Philadelphia: A. Hilger, 1990.

[27] A. A. Maradudin and S. H. Vosko, "Symmetry properties of the normal vibrations of a crystal," *Reviews of Modern Physics*, vol. 40, pp. 1–37, Jan. 1968.

[28] J. L. Warren, "Further considerations on the symmetry properties of the normal vibrations of a crystal," *Reviews of Modern Physics*, vol. 40, pp. 38–76, Jan. 1968.

[29] D. Griffiths, *Introduction to quantum mechanics*. Englewood Cliffs, N.J.: Prentice Hall, 1995.

[30] A. A. Maradudin and A. E. Fein, "Scattering of neutrons by an anharmonic crystal," *Physical Review*, vol. 128, p. 2589, 1962.

[31] R. A. Cowley, "Anharmonic crystals," *Reports on Progress in Physics*, vol. 31, p. 123, 1968.

[32] M. Zoli, "Temperature-dependent frequency shifts and broadening of phonon linewidths in lead," *Journal of Physics: Condensed Matter*, vol. 3, p. 6249, 1991.

[33] M. Zoli, G. Santoro, V. Bortolani, A. A. Maradudin, and R. F. Wallis, "Anharmonic damping of phonon modes in the fcc metals," *Physcal Review B*, vol. 41, p. 7507, 1990.

[34] J. G. Lee, *Computational materials science: an introduction*. Boca Raton, FL: CRC Press, 2012.

[35] J. Kohanoff, *Electronic structure calculations for solids and molecules: theory and computational methods*. Cambridge: Cambridge University Press, 2006.

[36] F. Ercolessi, *A molecular dynamics primer*. http://www.fisica.uniud.it/ ercolessi/md/.

[37] D. Frenkel, *Understanding molecular simulation: from algorithms to applications*. San Diego, CA: Academic Press, 1996.

[38] M. Finnis, *Interatomic forces in condensed matter*. Oxford; New York: Oxford University Press, 2003.

[39] R. Martin, *Electronic structure: basic theory and practical methods*. Cambridge; New York: Cambridge University Press, 2004.

[40] D. Sholl, *Density functional theory: a practical introduction*. Hoboken, N.J.: Wiley, 2009.

[41] C. Fiolhais, *A primer in density functional theory*. Berlin; New York: Springer, 2003.

[42] W. Koch, *A chemist's guide to density functional theory*. Weinheim; New York: Wiley-VCH, 2001.

[43] M. Marques, *Time-dependent density functional theory*. Berlin: Springer, 2006.

[44] D. Marx and J. J. Hutter, *Ab Initio Molecular Dynamics: Basic Theory and Advanced Methods*. Cambridge: Cambridge University Press, 2009.

[45] P. Deuflhard, *Computational molecular dynamics: challenges, methods, ideas: proceedings of the 2nd International Symposium on Algorithms for*

Macromolecular Modelling, Berlin, May 21–24, 1997. Berlin; New York: Springer-Verlag, 1999.

[46] C. Lubich, *From quantum to classical molecular dynamics*. European Mathematical Society, 2008.

[47] M. Griebel, *Numerical simulation in molecular dynamics*. Berlin: Springer, 2007.

[48] D. Raabe, *Continuum scale simulation of engineering materials: fundamentals, microstructures, process applications*. Weinheim: Wiley-VCH, 2004.

[49] A. R. Leach, *Molecular modelling: principles and applications*. Harlow, England: Longman, 1996.

[50] A. Hinchliffe, *Molecular modelling for beginners*. Chichester, West Sussex, England; Hoboken, NJ: Wiley, 2003.

[51] J.-R. Hill, L. Subramanian, and A. Maiti, *Molecular modeling techniques in material sciences*. Boca Raton, FL: Taylor & Francis, 2005.

[52] J. M. Haile, *Molecular dynamics simulation: elementary methods*. New York: Wiley, 1997.

[53] K. Jorge, "Phonon spectra from short non-thermally equilibrated molecular dynamics simulations," *Computational Materials Science*, vol. 2, pp. 221–232, Mar. 1994.

[54] G. Kresse and J. Furthmüller, "Efficiency of ab-initio total energy calculations for metals and semiconductors using a plane-wave basis set," *Computational Materials Science*, vol. 6, p. 15, 1996.

[55] *Vienna Ab initio Simulation Package (VASP)*. http://www.vasp.at/.

[56] P. G. et al., "Quantum espresso: a modular and open-source software project for quantum simulations of material," *Journal of Physics: Condensed Matter*, vol. 21, p. 395502, 2009. http://www.quantum-espresso.org.

[57] *ABINIT*. http://www.abinit.org.

[58] *WIEN2k*. http://www.wien2k.at/index.html.

[59] J. Gale and A. Rohl, "The general utility lattice program," *Molecular Simulation*, vol. 29, p. 291, 2003. http://projects.ivec.org/gulp/.

[60] *Large-scale Atomic/Molecular Massively Parallel Simulator (LAMMPS)*. http://lammps.sandia.gov/.

[61] *PHONON*. http://wolf.ifj.edu.pl/phonon/.

[62] *Phonopy*. http://phonopy.sourceforge.net/.

[63] *PHON*. http://www.homepages.ucl.ac.uk/~galeucfbdxa/phon/.

[64] *Wikipedia*. http://en.wikipedia.org/wiki/Neutron.

[65] G. Squires, *Introduction to the theory of thermal neutron scattering*. Cambridge; New York: Cambridge University Press, 1978.

[66] S. W. Lovesey, *Theory of neutron scattering from condensed matter*. Oxford: Clarendon Press, 1984.

[67] *NIST Center for Neutron Research*. http://www.ncnr.nist.gov/resources/nlengths/.

[68] G. Placzek and L. Van Hove, "Crystal dynamics and inelastic scattering of neutrons," *Physical Review*, vol. 93, pp. 1207–1214, Mar. 1954.

[69] L. Van Hove, "Time-dependent correlations between spins and neutron scattering in ferromagnetic crystals," *Physical Review*, vol. 95, no. 6, pp. 1374–1384, 1954.

[70] *DrChops*. http://danse.us/trac/DrChops.

[71] W. Sturhahn, "Nuclear resonant spectroscopy," *Journal of Physics: Condensed Matter*, vol. 16, pp. S497–S530, Feb. 2004.

[72] V. F. Sears, E. C. Svensson, and B. M. Powell, "Phonon density of states in vanadium," *Canadian Journal of Physics*, vol. 73, pp. 726–734, Nov. 1995.

[73] *getdos*. http://code.google.com/p/getdos/.

[74] G. Shirane, S. M. Shapiro, and J. M. Tranquada, *Neutron scattering with a triple-axis spectrometer: basic techniques*. New York: Cambridge University Pres, 2002.

[75] M. J. Cooper and R. Nathans, "The resolution function in neutron diffractometry. I. The resolution function of a neutron diffractometer and its application to phonon measurements," *Acta Crystallographica*, vol. 23, pp. 357–367, Sept. 1967.

[76] N. J. Chesser and J. D. Axe, "Derivation and experimental verification of the normalized resolution function for inelastic neutron scattering," *Acta Crystallographica Section A*, vol. 29, pp. 160–169, Mar. 1973.

[77] A. Zheludev, *Reslib*. http://neutron.ornl.gov/~zhelud/reslib/.

[78] *Wikipedia*. http://en.wikipedia.org/wiki/Rayleigh_scattering.

[79] E. Smith, *Modern Raman spectroscopy: a practical approach*. Hoboken, NJ: J. Wiley, 2005.

[80] F. Rull and J. Martínez-Frías, "Raman spectroscopy goes to Mars," *Spectroscopy Europe*, vol. 18, no. 1, p. 18, 2006.

[81] M. Fayer, *Ultrafast infrared and Raman spectroscopy*. New York: Marcel Dekker, 2001.

[82] E. Wilson, *Molecular vibrations the theory of infrared and Raman vibrational spectra*. New York: McGraw-Hill, 1955.

[83] R. Salzer, *Infrared and Raman spectroscopic imaging*. Weinheim: Wiley-VCH, 2009.

[84] K. Nakamoto, *Infrared and Raman spectra of inorganic and coordination compounds.* Hoboken, N.J.; Oxford: Wiley; Wiley-Blackwell distributor, 2009.

[85] J. R. Ferraro, K. Nakamoto, and C. W. Brown, *Introductory Raman Spectroscopy*. Academic Press, 2003.

[86] D. Long, *The Raman effect*. New York; Chichester: Wiley, 2001.

[87] D. Mayo, *Course notes on the interpretation of infrared and Raman spectra*. Hoboken, N.J.: Wiley-Interscience, 2003.

[88] B. Schrader, *Infrared and Raman Spectroscopy, Method and Applications*, vol. 11. Wiley-VCH, May 1996.

[89] K. Kneipp, *Surface-enhanced raman scattering physics and applications*. Berlin; New York: Springer, 2006.

[90] S. Wartewig, *IR and Raman spectroscopy: fundamental processing*. Weinheim: Wiley-VCH, 2003.

[91] I. R. Lewis and H. G. M. Edwards, *Handbook of Raman spectroscopy*. Cleveland, OH: CRC Press, 1974.

[92] J. Laserna, *Modern techniques in Raman spectroscopy*. Chichester; New York: Wiley, 1996.

[93] W. Weber, *Raman scattering in materials science*. Berlin; New York: Springer, 2000.

[94] D. Harris, *Symmetry and spectroscopy: an introduction to vibrational and electronic spectroscopy*. New York: Dover Publications, 1989.

[95] J. Salthouse, *Point group character tables and related data*. London: Cambridge University Press, 1972.

[96] H. A. Szymanski, *Raman spectroscopy: theory and practice*. 1967–1970.

[97] G. D. Wilk, R. M. Wallace, and J. M. Anthony, "High-κ gate dielectrics: Current status and materials properties considerations," *Journal of Applied Physics*, vol. 89, p. 5243, 2001.

[98] E. Gusev, E. Cartier, D. Buchanan, M. Gribelyuk, M. Copel, H. Okorn-Schmidt, and C. D'Emic, "Ultrathin high-κ metal oxides on silicon: processing, characterization and integration issues," *Microelectronic Engineering*, vol. 59, p. 341, 2001.

[99] J. Wang, H. P. Li, and R. Stevens, "Hafnia and hafnia-toughened ceramics," *Journal of Materials Science*, vol. 27, p. 5397, 1991.

[100] Q. E. Pierre, P. Barbéris, A. P. Mirgorodsky, and T. Merle-Méjean, "Comparative lattice-dynamical study of the raman spectra of monoclinic and tetragonal phases of zirconia and hafnia," *Journal of the American Ceramic Society*, vol. 85, p. 1745, 2002.

[101] R. Ruh and P. W. R. Corfield, "Crystal structure of monoclinic hafnia and comparison with monoclinic zirconia," *Journal of the American Ceramic Society*, vol. 53, p. 126, 1970.

[102] C. Carlone, "Raman spectrum of zirconia-hafnia mixed crystals," *Physical Review B*, vol. 45, p. 2079, 1992.

[103] E. Anastassakis, B. Papanicolaou, and I. M. Asher, "Lattice dynamics and light scattering in hafnia and zirconia," *Journal of Physics and Chemistry of Solids*, vol. 36, p. 667, 1975.

[104] A. Jayaraman, S. Y. Wang, S. K. Sharma, and L. C. Ming, "Pressure-induced phase transformations in hfo_2 to 50 gpa studied by raman spectroscopy," *Physical Review B*, vol. 48, p. 9205, 1993.

[105] G. A. Kourouklis and E. Liarokapis, "Pressure and temperature dependence of the raman spectra of zirconia and hafnia," *Journal of the American Ceramic Society*, vol. 74, p. 502, 1991.

[106] X. Zhao and D. Vanderbilt, "First-principles study of structural, vibrational, and lattice dielectric properties of hafnium oxide," *Physical Review B*, vol. 65, p. 233106, 2002.

[107] A. A. Demkov, "Investigating alternative gate dielectrics: A theoretical approach," *Physica Status Solidi (b)*, vol. 226, p. 57, 2001.

[108] G. Morell, W. Pérez, E. Ching-Prado, and R. S. Katiyar, "Anharmonic interactions in beryllium oxide," *Physical Review B*, vol. 53, p. 5388, 1996.

[109] C. D. Pears, *Southern Res. Inst., USAF ASD-TDR-62-765*. 1962.

[110] C. Wang, M. Zinkevich, and F. Aldinger, "The zirconia-hafnia system: dta measurements and thermodynamic calculations," *Journal of the American Ceramic Society*, vol. 89, p. 3751, 2006.

[111] L. M. Bollinger, S. P. Harris, C. T. Hibdon, and C. O. Muehlhause, "Neutron absorption and scattering by hafnium," *Physical Review*, vol. 92, p. 1527, 1953.

[112] G. V. Lewis and C. R. A. Catlow, "Potential models for ionic oxides," *Journal of Physics C: Solid State Physics*, vol. 18, p. 1149, 1985.

[113] H. Arashi, "Pressure-induced phase transformation of hfo_2," *Journal of the American Ceramic Society*, vol. 75, p. 844, 1992.

[114] C. Grain and W. Campbell, *U.S. Bur. Mines, Rept. Invest.* 1962. No. BM-RI-5982.

[115] J. Serrano, F. J. Manjón, A. H. Romero, F. Widulle, R. Lauck, and M. Cardona, "Dispersive phonon linewidths: the e_2 phonons of zno," *Physical Review Letters*, vol. 90, p. 055510, 2003.

[116] J. Serrano, F. Widulle, A. Romero, A. Rubio, R. Lauck, and M. Cardona, "Dependence of phonon widths on pressure and isotopic mass: zno," *Physica Status Solidi (b)*, vol. 235, p. 260, 2003.

[117] D. M. Adams, S. Leonard, D. R. Russell, and R. J. Cernik, "X-ray diffraction study of hafnia under high pressure using synchrotron radiation," *Journal of Physics and Chemistry of Solids*, vol. 52, p. 1181, 1991.

[118] P. G. Klemens, "Anharmonic decay of optical phonons," *Physical Review*, vol. 148, p. 845, 1966.

[119] M. Balkanski, R. F. Wallis, and E. Haro, "Anharmonic effects in light scattering due to optical phonons in silicon," *Physical Review B*, vol. 28, p. 1928, 1983.

[120] C. Li and M. Li, "Uv raman spectroscopic study on the phase transformation of zro_2, y_2o_3-zro_2 and so_4^2/zro_2," *Journal of Raman Spectroscopy*, vol. 33, p. 301, 2002.

[121] J. P. Coughlin and E. G. King, "High-temperature heat contents of some zirconium-containing substances," *Journal of the American Chemical Society*, vol. 72, p. 2262, 1950.

[122] P. P. Bose, R. Mittal, N. Choudhury, and S. L. Chaplot, "Inelastic neutron scattering and lattice dynamics of zro_2, y_2o_3 and $thsio_4$," *Pramana–Journal of Physics*, vol. 71, p. 1141, 2008.

[123] C. W. Li, M. M. McKerns, and B. Fultz, "Raman spectrometry study of phonon anharmonicity of hafnia at elevated temperatures," *Physical Review B*, vol. 80, p. 054304, 2009.

[124] R. Storn and K. Price., "Differential evolution, a simple and efficient heuristic strategy for global optimization over continuous spaces," *Journal of Global Optimization*, vol. 11, pp. 341–359, 1997.

[125] M. McKerns, P. Hung, and M. Aivazis, "Mystic: A simple model-independent inversion framework," http://dev.danse.us/trac/mystic.

[126] L. J. Lucas, H. Owhadi, and M. Ortiz, "Rigorous verification, validation, uncertainty quantification and certification through concentration-of-measure

inequalities," *Computer Methods in Applied Mechanics and Engineering*, vol. 197(51–52), pp. 4591–4609, 2008.

[127] T. J. Sullivan, U. Topcu, M. McKerns, and H. Owhadi, "Uncertainty quantification via codimension-one partitioning," *International Journal for Numerical Methods in Engineering*, vol. 85(12), p. 14991, 2011.

[128] X. Tang and J. Dong, "Lattice thermal conductivity of mgo at conditions of earth's interior," *Proceedings of the National Academy of Sciences USA*, vol. 107(10), p. 4539, 2010.

[129] P. Söderlind, "Ambient pressure phase diagram of plutonium: A unified theory for α-pu and δ-pu," *Europhysics Letters*, vol. 55 (4), pp. 525–531, 2001.

[130] A. W. Sleight, "Negative thermal expansion materials," *Current Opinion in Solid State and Materials Science*, vol. 3, pp. 128–131, 1998.

[131] A. W. Sleight, "Isotropic negative thermal expansion," *Annual Review of Materials Research*, vol. 28, pp. 29–43, 1998.

[132] T. A. Mary, J. S. O. Evans, T. Vogt, and A. W. Sleight, "Negative thermal expansion from 0.3 to 1050 kelvin in zrw_2o_8," *Science*, vol. 272, p. 90, 1996.

[133] G. Ernst, C. Broholm, G. R. Kowach, and A. P. Ramirez, "Phonon density of states and negative thermal expansion in zrw_2o_8," *Nature*, vol. 396, p. 147, 1998.

[134] D. Cao, F. Bridges1, G. R. Kowach, and A. P. Ramirez, "Frustrated soft modes and negative thermal expansion in zrw_2o_8," *Physical Review Letters*, vol. 89, p. 215902, 2002.

[135] J. N. Hancock, C. Turpen, Z. Schlesinger, G. R. Kowach, and A. P. Ramirez, "Unusual low-energy phonon dynamics in the negative thermal expansion compound zrw2o8," *Physical Review Letters*, vol. 93, p. 225501, 2004.

[136] M. G. Tucker, A. L. Goodwin, M. T. Dove, D. A. Keen, S. A. Wells, and J. S. O. Evans, "Negative thermal expansion in zrw_2o_8: Mechanisms, rigid unit modes, and neutron total scattering," *Physical Review Letters*, vol. 95, p. 255501, 2005.

[137] G. D. Barrera, J. A. O. Bruno, T. H. K. Barron, and N. L. Allan, "Negative thermal expansion," *Journal of Physics: Condensed Matter*, vol. 17, pp. R217–R252, 2005.

[138] Z. Schlesinger, J. A. Rosen, J. N. Hancock, and A. P. Ramirez, "Soft manifold dynamics behind negative thermal expansion," *Physical Review Letters*, vol. 101, p. 015501, 2008.

[139] M. E. Simon and C. M. Varma, "Dynamics of some constrained lattices," *Physical Review Letters*, vol. 86, p. 1781, 2001.

[140] A. L. Goodwin and C. J. Kepert, "Negative thermal expansion and low-frequency modes in cyanide-bridged framework materials," *Physical Review B*, vol. 71, p. 140301, 2005.

[141] S. S. Han and W. A. Goddard, "Metal-Organic Frameworks Provide Large Negative Thermal Expansion Behavior," *J. Phys. Chem. C*, vol. 111, no. 42, pp. 15185–15191, 2007.

[142] A. L. Goodwin, M. Calleja, M. J. Conterio, M. T. Dove, J. S. O. Evans, D. A. Keen, L. Peters, and M. G. Tucker, "Colossal Positive and Negative Thermal Expansion in the Framework Material Ag3[Co(CN)6]," *Science*, vol. 319, pp. 794–797, Feb. 2008.

[143] B. K. Greve, K. L. Martin, P. L. Lee, P. J. Chupas, K. W. Chapman, and A. P. Wilkinson, "Pronounced negative thermal expansion from a simple structure: cubic scf_3," *Journal of the American Chemical Society*, vol. 132 (44), pp. 15496–15498, 2010.

[144] K. S. Aleksandrov, V. N. Voronov, A. N. Vtyurin, A. S. Krylov, M. S. Molokeev, M. S. Pavlovskii, S. V. Goryainov, A. Y. Likhacheva, and A. I. Ancharov, "Pressure-induced phase transition in the cubic scf_3 crystal," *Physics of the Solid State*, vol. 51, pp. 810–816, 2009.

[145] P. P. Fedorov, G. A. Lovetskaya, and B. P. Sobolev, "Phase diagram of the scf_3-luf_3 system," *Zhurnal Neorganicheskoi Khimii*, vol. 40, pp. 1561–1562, 1995.

[146] M. Dapiaggi and A. N. Fitch, "Negative (and very low) thermal expansion in reo_3," *Journal of Applied Crystallography*, vol. 42, pp. 253–258, 2009.

[147] E. E. Rodriguez, A. Llobet, T. Proffen, B. C. Melot, R. Seshadri, P. B. Littlewood, and A. K. Cheetham, "The role of static disorder in negative thermal expansion in reo_3," *Journal of Applied Physics*, vol. 105, p. 114901, 2009.

[148] V. I. Zinenko and N. G. Zamkova, "Lattice dynamics of mf3 crystals (m = al, ga, and in)," *Physics of the Solid State*, vol. 42, p. 1348, 2000.

[149] M. Kresch, M. Lucas, O. Delaire, J. Y. Lin, and B. Fultz, "Phonons in aluminum at high temperatures studied by inelastic neutron scattering," *Physical Review B*, vol. 77, p. 024301, 2008.

[150] P. E. Blöchl, "Projector augmented-wave method," *Physical Review B*, vol. 50, p. 17953, 1994.

[151] K. Kunc and R. M. Martin, "Ab initio force constants of gaas: A new approach to calculation of phonons and dielectric properties," *Physical Review Letters*, vol. 48, p. 406, 1982.

[152] T. Chatterji, P. G. Freeman, M. Jimenez-Ruiz, R. Mittal, and S. L. Chaplot, "Pressure-and temperature-induced m_3 phonon softening in reo_3," *Physical Review B*, vol. 79, p. 184302, 2009.

[153] P. Dorey and R. Tateo, “Anharmonic oscillators, the thermodynamic bethe ansatz and nonlinear integral equations,” *Journal of Physics A: Mathematical and General*, vol. 32, pp. L419–L425, 1999.

[154] A. Kash and J. C. Tsang, *Light scattering in solids VI—topics in applied physics*. 1991.

[155] R. A. Cowley, “Raman scattering from crystals of the diamond structure,” *Journal de Physique (Paris)*, vol. 26, p. 659, 1965.

[156] E. Haro, M. Balkanski, R. F. Wallis, and K. H. Wanser, “Theory of the anharmonic damping and shift of the raman mode in silicon,” *Physical Review B*, vol. 34, p. 5358, 1986.

[157] D. Vanderbilt, S. G. Louie, and M. L. Cohen, “Calculation of anharmonic phonon couplings in c, si, and ge,” *Physical Review B*, vol. 33, p. 8740, 1986.

[158] J. Zarestky, C. Stassis, B. N. Harmon, K. M. Ho, and C. L. Fu, “Temperature dependence of the vibrational modes of molybdenum,” *Physical Review B*, vol. 28, p. 697, 1983.

[159] Y. Y. Ye, Y. Chen, K. M. Ho, B. N. Harmon, and P. A. Lindgard, “Phonon-phonon coupling and the stability of the high-temperature bcc phase of zr,” *Physical Review Letters*, vol. 58, p. 1769, 1987.

[160] A. Debernardi, S. Baroni, and E. Molinari, “Anharmonic phonon lifetimes in semiconductors from density-functional perturbation theory,” *Physical Review Letters*, vol. 75, p. 1819, 1995.

[161] A. Debernardi, “Phonon linewidth in iii-v semiconductors from density-functional perturbation theory,” *Physical Review B*, vol. 57, p. 12847, 1998.

[162] A. Debernardi, C. Ulrich, K. Syassen, and M. Cardona, “Raman linewidths of optical phonons in 3c-sic under pressure: First-principles calculations and experimental results,” *Physical Review B*, vol. 59, p. 6774, 1999.

[163] G. Lang, K. Karch, M.Schmitt, P. Pavone, A. P. Mayer, R. K. Wehner, and D. Strauch, "Anharmonic line shift and linewidth of the raman mode in covalent semiconductors," *Physical Review Letters*, vol. 59, p. 6182, 1999.

[164] S. Narasimhan and D. Vanderbilt, "Anharmonic self-energies of phonons in silicon," *Physical Review B*, vol. 43, p. 4541, 1991.

[165] G. Deinzer, G. Birner, and D. Strauch, "Ab initio calculation of the linewidth of various phonon modes in germanium and silicon," *Physical Review B*, vol. 67, p. 144304, 2003.

[166] X. Tang and J. Dong, "Pressure dependence of harmonic and anharmonic lattice dynamics in mgo: A first-principles calculation and implications for lattice thermal conductivity," *Physics of the Earth and Planetary Interiors*, vol. 174, p. 33, 2009.

[167] R. Stedman and G. Nilsson, "Dispersion relations for phonons in aluminum at 80 and 300k," *Physical Review*, vol. 145, p. 492, 1966.

[168] W. J. L. Buyers, G. Dolling, G. Jacucci, M. L. Klein, and H. R. Glyde, "Anharmonic phonon response in aluminum: A neutron-scattering test of computer-simulation calculations," *Physical Review B*, vol. 20, p. 4859, 1979.

[169] T. Hogberg and R. Sandstrom, "Anharmonic effects on phonons in aluminium," *Physica Status Solidi (b)*, vol. 33, p. 169, 1969.

[170] T. R. Koehler, N. S. Gillis, and D. C. Wallace, "Anharmonic interaction in aluminum. i," *Physical Review B*, vol. 1, p. 4521, 1970.

[171] M. M. Dacorogna, M. L. Cohen, and P. K. Lam, "Self-consistent calculation of the q dependence of the electron-phonon coupling in aluminum," *Physical Review Letters*, vol. 55, p. 837, 1985.

[172] N. Bock, D. Coffey, and D. C. Wallace, “Nonadiabatic contributions to the free energy from the electron-phonon interaction in na, k, al, and pb,” *Physical Review B*, vol. 72, p. 155120, 2005.

[173] N. Bock, D. C. Wallace, and D. Coffey, “Adiabatic and nonadiabatic contributions to the free energy from the electron-phonon interaction for na, k, al, and pb,” *Physical Review B*, vol. 73, p. 075114, 2006.

[174] A. S. Cooper, “Precise lattice constants of germanium, aluminum, gallium arsenide, uranium, sulphur, quartz and sapphire,” *Acta Crystallographica*, vol. 15, p. 578, 1962.

[175] X. Tang, J. Dong, P. Hutchins, O. Shebanova, J. Gryko, P. Barnes, J. K. Cockcroft, M. Vickers, and P. F. McMillan, “Thermal properties of si136: Theoretical and experimental study of the type-ii clathrate polymorph of si,” *Physical Review B*, vol. 74, p. 014109, 2006.

[176] K. Okubo and S. I. Tamura, “Two-phonon density of states and anharmonic decay of large-wave-vector la phonons,” *Physical Review B*, vol. 28, p. 4847, 1983.

[177] F. C. Nix and D. MacNair, “The thermal expansion of pure metals: Copper, gold, aluminum, nickel, and iron,” *Physical Review*, vol. 60, p. 597, 1941.

[178] X. Tang and B. Fultz, “First-principles study of phonon linewidths in noble metals,” *Physical Review B*, vol. 84, pp. 1–7, Aug. 2011.

[179] D. Jackson, T. Jackman, J. Davies, W. Unertl, and P. Norton, “Vibrational properties of Au and Pt(110) surfaces deduced from rutherford backscattering data,” *Surface Science*, vol. 126, no. 1–3, pp. 226–235, 1983.

Index